



저작자표시-비영리-변경금지 2.0 대한민국

이용자는 아래의 조건을 따르는 경우에 한하여 자유롭게

- 이 저작물을 복제, 배포, 전송, 전시, 공연 및 방송할 수 있습니다.

다음과 같은 조건을 따라야 합니다:



저작자표시. 귀하는 원저작자를 표시하여야 합니다.



비영리. 귀하는 이 저작물을 영리 목적으로 이용할 수 없습니다.



변경금지. 귀하는 이 저작물을 개작, 변형 또는 가공할 수 없습니다.

- 귀하는, 이 저작물의 재이용이나 배포의 경우, 이 저작물에 적용된 이용허락조건을 명확하게 나타내어야 합니다.
- 저작권자로부터 별도의 허가를 받으면 이러한 조건들은 적용되지 않습니다.

저작권법에 따른 이용자의 권리는 위의 내용에 의하여 영향을 받지 않습니다.

이것은 [이용허락규약\(Legal Code\)](#)을 이해하기 쉽게 요약한 것입니다.

[Disclaimer](#)

공학박사 학위논문

**Studies on Self-Assembly and Structure-Property
Relationship of Functional Supramolecules: Unique
Optoelectronic Functions of Dicyanodistyrylbenzene
Derivative Crystal, and Their Charge-Transfer Complex**

독특한 광전자 기능성을 보이는 다이사이아노다이스티릴벤젠계
결정과 이를 포함한 전하이동 복합체의 자기조립 현상 및 구조-
특성 간의 상관관계에 관한 연구

2016 년 2 월

서울대학교 대학원

재료공학부

박 상 규

**Studies on Self-Assembly and Structure-Property
Relationship of Functional Supramolecules: Unique
Optoelectronic Functions of Dicyanodistyrylbenzene
Derivative Crystal, and Their Charge-Transfer Complex**

A THESIS SUBMITTED IN PARTIAL FULFILLMENT OF
THE REQUIREMENTS FOR THE DEGREE OF
DOCTOR OF PHILOSOPHY
IN ENGINEERING AT THE GRADUATE SCHOOL OF
SEOUL NATIONAL UNIVERSITY

FEBRUARY 2016

By
Sang Kyu Park

Supervisor
Prof. Soo Young Park

**Studies on Self-Assembly and Structure-Property
Relationship of Functional Supramolecules: Unique
Optoelectronic Functions of Dicyanodistyrylbenzene
Derivative Crystal, and Their Charge-Transfer Complex**

독특한 광전자 기능성을 보이는 다이사이아노다이스티릴벤젠계
결정과 이를 포함한 전하이동 복합체의 자기조립 현상 및 구조-
특성 간의 상관관계에 관한 연구

지도 교수 박 수 영

이 논문을 공학박사 학위논문으로 제출함

2015 년 12 월

서울대학교 대학원

재료공학부

박 상 규

박상규의 공학박사 학위논문을 인준함

2015 년 12 월

위 원 장 _____ (인)

부위원장 _____ (인)

위 원 _____ (인)

위 원 _____ (인)

위 원 _____ (인)

Abstract

Studies on Self-Assembly and Structure-Property Relationship of Functional Supramolecules: Unique Optoelectronic Functions of Dicyanodistyrylbenzene Derivative Crystal, and Their Charge-Transfer Complex

Sang Kyu Park

Department of Materials Science and Engineering

The Graduate School

Seoul National University

Organic semiconductors based on π -conjugated molecules have emerged as one of the promising materials systems attributed to the advantageous features, such as chemical versatility, light-weight, transparency, low-temperature processability, and flexibility, compared to the inorganic counterparts. It has been revealed that the optoelectronic functionalities of organic semiconductor solids are governed not only by electronic features of constituents but also by their supramolecular arrangements. In this regard, rapid progresses in structure-property correlations have been achieved; in addition, strategies for controlling supramolecular assembly and thereby to modulate properties have also been regarded as an important research subject. Meanwhile, remarkable research interest has arisen on multi component donor-acceptor (D-A) complexes, heterojunctions, and interfaces; since wholly new physicochemical

functionalities can be promoted – i.e., photovoltaic effect, charge-transfer induced transport enhancement, and excited complex luminescence. In particular, D-A charge-transfer (CT) complexes have long been regarded as one of the most pulsating research subjects by their prominent (metallic-)conductivities. However, studies on charge-transfer complexes with neutral characters are not much conducted by now, particularly with precise structure-property correlation. This class of CT complexes however exhibit great possibilities for their semiconducting properties and peculiar luminescence features by characteristic electronic and structural properties.

Among the promising π -conjugated organic semiconductors, I have paid particular attention on multifunctional dicyanodistyrylbenzene (DCS) based torsion spring molecules which give rise to the unique optoelectronic characteristics – i.e., bright solid-state luminescence and favorable charge transport property. Among the DCS based semiconductors, elaborately designed (2Z,2'Z)-3,3'-(1,4-phenylene)bis(2-(3,5-bis(trifluoromethyl)phenyl)acrylonitrile), CN-TFPA, facilitated to form millimeter scaled two-dimensional (2D) n-type supramolecules driven from the panoply of well-balanced π - π and cyano-induced hydrogen bonding interactions, as two important supramolecular synthons. Attributed to the both electronic and structural factors, the 2D layered self-assembled structure provided distinguished aggregation induced enhanced emission ($\Phi_F = \text{ca. } 80\%$) and n-type transporting nature ($0.5 \text{ cm}^2 \text{ V}^{-1} \text{ s}^{-1}$) in OFET devices. The supramolecular features of the material rendered exfoliation and transfer capability similar to the graphene 2D layers case, affording novel way to

constitute ultra-thin crystalline OFETs.

Beside its unique supramolecular optoelectronic features, CN-TFPA was found to be an interesting A material to establish unique CT complexes for advanced optoelectronic functions. Considering favorable ambipolar charge-transporting nature combined with desired CT fluorescence, I rationally designed isometric D material (1,4-bis(3,5-dimethylstyryl)benzene, 4M-DSB) based on distyrylbenzene (DSB) molecular backbone structure; manifesting minimized structural mismatch with CN-TFPA, thus established regular quasi-1D mixed stack assembly with densely packed molecular arrangement. The indirect electronic coupling from superexchange mechanism indeed rendered peculiar ambipolar charge-transport (p-/n-channel mobility up to $6.7 \times 10^{-3} \text{ cm}^2 \text{ V}^{-1} \text{ s}^{-1}$ and $6.7 \times 10^{-2} \text{ cm}^2 \text{ V}^{-1} \text{ s}^{-1}$, respectively). Moreover, the electronic and structure character gave rise to high CT fluorescence quantum yield ($\Phi_F = \text{ca. } 30\text{-}40\%$) by configuration interaction and minimized exciton trap density, which gave a great possibility for advanced CT optoelectronics by bridging charge transport and emission characteristics.

As a next step toward developing mixed-stack CT based advanced optoelectronic devices, i.e. realization of electroluminescence (EL) during OFETs operation, further studies are greatly required to promote increment of fluorescence quantum yield of D-A CT systems. Introduction of DCS type D ((2Z,2'Z)-2,2'-(1,4-phenylene)bis(3-p-tolylacrylonitrile), 2MDCS) as an isometric donor counterpart for DCS based acceptor (CN-TFPA) facilitated great increase in CT emission quantum yield ($\Phi_F = \text{ca. } 60\%$).

The highly efficient CT luminescence is attributed to the molecular orbital mixing character of the lowest singlet transition and reduced nonradiative decay constant by energy gap law. Furthermore, densely packed 2:1 (D:A) molecular arrangement was exhibited with anomalous two-dimensional supramolecular growth; the 2D assembly can be promoted by supramolecular synthons of DCS based D/A molecules (CT interaction and $-\text{CN}$ induced H-bonding interaction). In virtue of ambipolar transporting nature (balanced p-/n-channel mobility of ca. $10^{-4} \text{ cm}^2 \text{ V}^{-1} \text{ s}^{-1}$) and unprecedentedly high fluorescence quantum yield, CT based light-emitting OFETs devices could successfully be demonstrated (EQE up to 1.5% in true ambipolar regime); suggesting the great potential of mixed stack CT complexes for futuristic organic optoelectronics applications.

In the meantime, effort has also been devoted for developing stimuli-responsive multi-color fluorescence switching systems comprised of mixed D-A CT complex. It was highly envisioned that high-contrast fluorescence switching with anticipatable emission energies (red \leftrightarrow blue) can be implemented by the distinctive luminescence properties of constituents (D: 4M-DSB; A: 3,3'-(1,4-phenylene)bis(2-(3,5-bis(trifluoromethyl)phenyl)acrylonitrile, Thio-Y) and their mixed CT phase, if the phase alternation can be promoted by strategic external stimulation. Due to the non-centrosymmetric design of the acceptor molecule, somewhat attenuated intermolecular interaction networks in CT phase can be attained; thus, lead to superior stimuli responsive features. The electrostatic supramolecular synthons, i.e., CT and H-bonding

interactions, was found to be greatly affected by polar aprotic solvent vapor exposure which promoted D/A segregated structure formation. On the other hand, non-polar solvent and polar protic solvent induced mixed D-A CT phase formation by electrostatic and solvophobic effect governing procedure, respectively. Combined with peculiar biphasic solvent property dependence, thermal and mechanical stimuli can also be utilized to form CT phase for multi-stimuli responsive features due to the spontaneity of CT formation; establishing a unique way to develop stimuli-responsive fluorescence memory system.

In this dissertation, I have focused on structure – property correlation in particular about the fluorescence and/or charge transport characteristics of the dicyanodistyrylbenzene based supramolecule and CT complexes, supported by precise quantum-chemical calculations based on well-defined structures. As in the case of single-component semiconductor solids, the molecular arrangements of this class of CT materials are revealed to derive great impact on their optoelectronic functions in CT complexes, combined with electronic properties of individual constituents. Through the conative regulations of such molecular/supramolecular parameters, in this respect, manifestation of unprecedented features or improvement of optoelectronic properties can successfully be achieved. The CT complex comprised of DCS and/or DSB molecules can thereby be understood as promising candidate for organic optoelectronics applications among the countless organic semiconducting materials.

Keyword: dicyanodistyrylbenzene, distyrylbenzene, supramolecule, charge-transfer complex, optoelectronic property, charge-transport, fluorescence, organic field-effect transistor, electroluminescence, stimuli-responsiveness.

Student Number: 2010-20601

Contents

Abstract	i
Contents	vii
List of Tables	x
List of Scheme	xii
List of Figures	xiii
Chapter 1. Introduction	1
1.1. Functional Supramolecules based on π -Conjugated Molecules	1
1.2. Charge-Transfer Complexes and Functional Supramolecules based on Charge-Transfer Interactions	9
1.3. Supramolecular Optoelectronics: Basics of Charge Transport, and Photophysics in Semiconducting Supramolecules and Charge-Transfer Complexes	16
1.3.1. Charge Transport in Semiconducting Supramolecules	17
1.3.2. Charge Transport in Semiconducting Charge-Transfer Complexes	30
1.3.3. Photophysics in Semiconducting Supramolecules	37
1.3.4. Photophysics in Charge-Transfer Complexes	46
1.3.5. Organic Light-Emitting Transistors	51
1.4. Contents of Thesis	57
1.5. References	60

Chapter 2. High-Performance n-Type Organic Transistor with a Solution-Processed and Exfoliation-Transferred Two-Dimensional Crystalline Layered Film	70
2.1. Introduction	70
2.2. Experimental.....	72
2.3. Results and Discussion	78
2.4. Conclusions	96
2.5. References	97
Chapter 3. Tailor-Made Highly Luminescent and Ambipolar Transporting Organic Mixed Stacked Charge-Transfer Crystals: an Isometric Donor-Acceptor Approach	100
3.1. Introduction	100
3.2. Experimental.....	104
3.3. Results and Discussion	111
3.4. Conclusions	136
3.5. References	137
Chapter 4. Bridging Highly Luminescent – Ambipolar Transport Characters: Light-Emitting Organic Field-Effect Transistors Based on Two Dimensionally Growing Charge-Transfer Complex Cocrystals.....	143
4.1. Introduction	143

4.2. Experimental.....	147
4.3. Results and Discussion	153
4.4. Conclusions	176
4.5. References	177
Chapter 5. Stimuli-Responsive Reversible Fluorescence Switching in a Crystalline Donor-Acceptor Mixture Films: Mixed Stacked Charge-Transfer Emission vs. Segregated Stack Monomer Emission	182
5.1. Introduction	182
5.2. Experimental.....	186
5.3. Results and Discussion	189
5.4. Conclusions	209
5.5. References	209
Abstract in Korean	212
List of Publications.....	218
List of Presentations.....	222
List of Patents	226

List of Tables

Table 2-1. Characterized Electrical Properties of CN-TFPA SC-OFETs.....	90
Table 3-1. Frontier MO energies, adiabatic and vertical electron affinities (EA) and ionization potentials (IP) of the 4M-DSB (D) and CN-TFPA (A) molecules as calculated by DFT (B3LYP). Vertical transition energies Evert(S0→S1) as calculated by TD-DFT (B3LYP).....	113
Table 3-2. Crystal data and structure refinement for D•A (1:1) CT co-crystal.....	119
Table 3-3. Vertical transition energies Evert of 4M-DSB (D), CN-TFPA (A) and D•A (1:1) as calculated by TD-DFT(CAM-B3LYP/6-311G*)//DFT(B3LYP/6-311G*).....	126
Table 4-1. Crystal data and structure refinement for D1-A1 (2:1) CT cocrystal in 100 K and 293 K.....	158
Table 4-2. Summarized optical characteristics of D1 , A1 , and CT complex cocrystal.	164
Table 4-3. Vertical transition energies of D1-A1 CT pair calculated by TD-DFT (CAM-B3LYP/6-311G*).....	167
Table 4-4. Summarized field-effect transistors properties from top-contact bottom-gate and bottom-contact bottom-gate device geometries.....	173
Table 5-1. Optical properties of CT complex and constituent compounds in the solid state: absorption (λ_{abs}) and emission (λ_{em}) wavelengths, absolute quantum yields (Φ_F), intensity-weighted average fluorescence lifetimes	

(τF), radiative rates (kr), and non-radiative rates (knr).	192
Table 5-2. Experimental frontier MO energies as estimated by UPS and optical bandgap. Frontier MO energies, adiabatic and vertical electron affinities (EA) and ionization potentials (IP) of the D1 , and A1 molecules as calculated by DFT (B3LYP). Vertical transition energies Evert(S0→S1) as calculated by TD-DFT (B3LYP).....	194
Table 5-3. Vertical transition energies Evert of 4M-DSB (D1), Thio-Y (A1) and D1-A1 (1:1) as calculated by TD-DFT(CAM-B3LYP/6-11G*)//DFT(B3LYP/6-311G*).....	195
Table 5-4. Crystal data and structure refinement for CT-P1 cocrystal.	200

List of Schemes

Scheme 2-1. Synthetic Procedure to Obtain CN-TFPA	75
Scheme 3-1. The synthetic route for obtaining 4M-DSB (D).....	109
Scheme 4-1. Synthetic procedure to obtain 2MDCS (D1).....	151
Scheme 5-1. The synthetic route for obtaining Thio-Y (A1).....	185

List of Figures

Figure 1-1. Representative supramolecular synthons.....	5
Figure 1-2. Representative π -conjugated materials.....	6
Figure 1-3. Molecular arrangements of (a) pentacene, (b) perfluoropentacene, (c) TIPS-pentacene, (d) C8-BTBT, and (e) C18-PTCDI. The crystallographic data are obtained from (a) CCDC 145333, (b) 234729, (c) 172476, (d) 679293, and (e) 738649, respectively.....	7
Figure 1-4. (a) Molecular structures of hosts/aldehydes of room temperature phosphorescent supramolecules. In solution, negligible intermolecular -O \cdots Br-interaction results in fluorescence; however, intermolecular -O \cdots Br-interaction in crystalline state induces phosphorescence by efficient spin-orbit coupling. (b) Molecular structures of hexabenzocoronene – TNF based functional molecules and the schematic drawings depicting supramolecular assembly.....	8
Figure 1-5. (a) Representative molecular structures of donors and acceptors in (TTF) – (TCNQ) based charge-transfer complexes. (b) Ionicity diagram for (TTF) – (TCNQ) based charge-transfer complexes. (c) Schematic illustrations of binary mixed and segregate stack.....	14
Figure 1-6. Schematic illustrations of supramolecular assemblies based on donor-acceptor charge-transfer interactions.....	15

Figure 1-7. Schematic illustrations of the four representative organic field-effect transistors structures.	20
Figure 1-8. (a) Output characteristic, and (b) transfer characteristic of PTCDI-C8 field-effect transistor.....	21
Figure 1-9. Schematic carrier concentration diagram of (a) linear, (b) pinch-off, and (c) saturation regime during field-effect transistor operations.	22
Figure 1-10. (a) Schematic description of reorganization energy, in neutral ($\lambda_{\text{rel}}^{(1)}$) and charged ($\lambda_{\text{rel}}^{(2)}$) molecular state. (b) Calculated transfer integral of anthracene dimer pair by as a function of the intermolecular separation (R12).....	27
Figure 1-11. Four representative molecular arrangements found from molecular crystals.	28
Figure 1-12. Transfer integral calculated along three distinctive molecular stacking directions of DNNT molecule. Calculated frontier molecular orbitals and reorganization energies of DNNT and its analogues.....	29
Figure 1-13. (a) Representatives of TTF – TCNQ based charge-transfer complexes exhibiting semiconducting behaviors in specific conditions. (b) Field-effect transistor characteristics of Mott-insulator (BEDT-TTF) – (TCNQ) complex showing ambipolar transport and metallic transporting nature above 240 K.....	34
Figure 1-14. Indirect (effective) coupling calculated by energy-splitting in D-A-D and A-D-A trimer stacks of (DMQ _t T) – (F4TCNQ) pair.	35

Figure 1-15. Examples of charge-transfer complex systems manifesting semiconducting properties.....	36
Figure 1-16. The state energy (Jablonski) diagram describing transitions between electronic states. The arrows and numbered denotations are indicating, ①: absorption; ②: internal conversion, vibrational relaxation; ③: intersystem crossing; ④: fluorescence; and ⑤: phosphorescence.	38
Figure 1-17. Schematic drawing of the Davydov splitting; indicating relationships between molecular arrangement and transition dipole moment coupling for defining favored optical transitions.....	44
Figure 1-18. Absorption and photoluminescence spectra in solution (dotted line) and in solid-state (solid line) of representative (a) J-type and (b) H-type stacking molecules.	45
Figure 1-19. Examples of luminescent charge-transfer complex systems and their fluorescent microscope images. (a) (naphthalene) – (TCNB) with varying pyrene dopant concentrations; (b) (Bpe) – (IFB) charge-transfer complex (left image), and (Bpe) – (F4DIB) multi-component cocrystal (right image); (c) (Bpe) – TCNQ charge-transfer complex.	50
Figure 1-20. Plots of $V_G - V_{ch}$ vs. horizontal distance with varied V_G and fixed V_D and schematic illustration of hole and electron density of corresponding charge transport regime. (a) saturation regime for p-channel transport, (b) true	

ambipolar regime, and (c) saturation regime for n-channel transport.	56
.....	56
Figure 2-1. Schematic illustration of the solvent evaporation crystal growth technique.	75
.....	75
Figure 2-2. (a) Fluorescent image of a single CN-TFPA crystal, taken using an optical microscope (circled image insets: birefringence image of same crystal using polarized optical microscope). (b) AFM image (scale bar: 1 μm) of a single CN-TFPA crystal (inset: thickness profile along dashed line). (c, d) Molecular stacking observed from single-crystal XRD analysis (the directions of the intermolecular interactions are illustrated using white arrows).	81
.....	81
Figure 2-3. (a) The calculated optimized geometry of the CN-TFPA molecule using the B3LYP functional and 6-31+G** basis set at the density functional theory with the Gaussian 03 software. (b) The molecular geometry of CN-TFPA in the bulk single-crystal phase, based on results from the single crystal XRD analysis.	82
.....	82
Figure 2-4. (a, b) Fluorescent images of 2D crystalline CN-TFPA layers grown by solution evaporation crystal growth (scale bar: (a) 100 μm , (b) 50 μm). (c) Molecular monolayer and bilayer from B-phase 2D sheet, measured using AFM (scale bar: 1 μm , inset: thickness profile along white dashed line). (d) Out-of-plane XRD analysis of the B-phase (blue line), G-phase (green line) and bulk single crystal (red line) (insets: schematic drawings of molecular	

stacks of each phase, with slipped angles to the plane bc).	83
.....	83
Figure 2-5. (a) UV-visible absorption spectra of CN-TFPA solution, nanoparticle, and vacuum deposited film. (b) PL spectra of CN-TFPA solution, G-phase, B-phase, and bulk single-crystal.	84
Figure 2-6. (a, b) Fluorescent image taken from SC-OFETs fabricated using the solvent evaporation technique (a: G-phase, b: B-phase). Insets indicate the birefringence of each device.	87
Figure 2-7. (a, b) Measured n-type characteristics of the CN-TFPA SC-OFETs devices (a: G-phase, b: B-phase).	87
Figure 2-8. (a-c) Transfer characteristics of CN-TFPA poly-crystalline vacuum thermal deposited film (a: $T_{SUB}=RT$, b: $T_{SUB}=50^{\circ}C$ and c: $T_{SUB}=70^{\circ}C$). (d-f) AFM images of films by varying substrate temperatures (d: RT, e: $50^{\circ}C$, f: $70^{\circ}C$) (scale bar: $2\mu m$).	88
Figure 2-9. Out-of-plane XRD analysis on CN-TFPA vacuum deposition films (square line: RT, circle line: $50^{\circ}C$, triangle line: $70^{\circ}C$). (n, 0, 0) peaks of G/B-phase were designated above the each XRD pattern.	89
Figure 2-10. (a) Schematic illustrating the measurement of the anisotropic field-effect mobility of the B-phase SC-OFETs (scale bar: $200\ \mu m$). (b) Eight n-channel mobility values from the single crystalline B-phase 2D layer were measured every 45° (the value at 315° was not obtained) (solid arrow in (b): speculated direction of the π -stacking direction).	93

Figure 2-11. (a, b) Fluorescent images of exfoliated B-phase 2D crystal on Scotch tape, and on SiO ₂ substrate after the retransfer process (scale bar of a: 30 μm, and of b: 20 μm). (c) Schematic illustration of the mechanical cleavage method.	94
Figure 2-12. (a) AFM image (scale bar: 1 μm) of an exfoliated B-phase 2D crystal on a SiO ₂ substrate (inset: thickness profile along dashed white line). (b) Measured n-type transfer characteristics of the exfoliated B-phase 2D crystal.....	95
Figure 3-1. Nanoparticle suspension preparation. (a) Images taken under ambient light, and (b) UV on nanoparticle suspension by varying THF:water v:v ratio (10:0, 9:1, 8:2, 7:3, 6:4, 5:5, 4:6, 3:7, 2:8 and 1:9) with a fixed total concentration of 5×10 ⁻⁶ M.	109
Figure 3-2. FE-SEM images of dropcasted nanoparticle suspensions (5×10 ⁻⁶ M in THF:water 1:9, v:v). (a) 4M-DSB (D), (b) CN-TFPA (A), and (c,d) D · A (1:1).....	110
Figure 3-3. Chemical structures of 4M-DSB (D) and CN-TFPA (A).....	110
Figure 3-4. (a) Normalized UV-vis absorption and PL spectra of 4MDSB (D), CN-TFPA (A), and D + A mixture in THF solution (5 × 10 ⁻⁶ M). (b) Calculated vertical electronic transition energies of D , A , and a D - A (1:1) dimer (broadened by a Gaussian); for D - A , transitions are also indicated as bars. (c) Normalized UV-vis absorption and PL spectra of D , A , and D - A (1:1) NP suspensions in THF:water (1:9, v:v). (d) PL spectra of the	

D–A (1:1) CT cocystal at room temperature and 77 K with minimized reabsorption. 114

Figure 3-5. (a) Optical microscope image of **D–A** (1:1) CT cocystal under ambient light irradiation (insets: images under $\pm 45^\circ$ rotating polarizer). (b) Single-crystal XRD structure of the **D–A** (1:1) CT cocystal; blue molecule: **D**, green molecule: **A**. (c) Counter pitch angle ($90^\circ - \text{pitch angle}$), and (d) counter roll angle ($90^\circ - \text{roll angle}$) and $\pi-\pi$ distance (interlayer distance) measured from single-crystal XRD results. 117

Figure 3-6. Molecular conformation in mixed stacked **D•A** (1:1) CT co-crystal. (a) The molecular geometry of **D**, and (b) **A** found from single-crystalline **D•A** (1:1) CT co-crystal state. The conformational angle of each single bond is denoted with black arrows. 118

Figure 3-7. (a, b) Interstack H-bonding interaction promoted by CN in mixed stacked **D•A** (1:1) CT co-crystal and in pure **A** crystal. (a) The number of intermolecular interactions branched out from CN units in CT co-crystal: 4 H-bonding, and (b) pure **A** crystal: 8 H-bonding, per molecule. Intermolecular bonding lengths are indicated in the each figure. See also differently positioned hydrogens are participated in H-bonding interactions ((a) 1 central phenyl and 1 vinylene hydrogens for CT co-crystal / (b) 2 central phenyl hydrogens for pure **A** crystal). 120

Figure 3-8. Static dipole moment of the dimer pair in mixed stacked **D•A** (1:1) CT co-crystal. Single-crystalline structure of the **D•A** (1:1) CT co-crystal with

unit cell axis a, b, c. Calculated ground state static dipole moments (SDM) of the dimer pair are indicated in black arrows.....	121
Figure 3-9. Molecular stacking structure in pure A crystal.....	121
Figure 3-10. (a) MO diagram for the D - A (1:1) system as calculated by DFT(CAM-B3LYP); the main CI contribution for the $S_1 \leftarrow S_0$ transition is indicated; the orientation of the respective TDM is depicted on the left. (b) DFT calculated transfer integrals for electrons (t_e) and holes (t_h) along the b -axis based on the energy-splitting method.....	125
Figure 3-11. The electron-hole wave function plot. Description of the first four excited states for the D • A pair as calculated at the ZINDO/S//DFT:B3LYP(6-311G*) level of theory. The numbering follows the C-atoms of the molecular backbone (D : 1-22, A : 23-44).....	127
Figure 3-12. Experimental and calculated Raman spectra of pure D , A and D • A (1:1) CT co-crystal. (a) Experimental non-resonant Raman spectra of the D , A and D • A (1:1) CT co-crystals. (b) Calculated Raman spectra of the D and A compounds as calculated at the DFT(B3LYP/6-311G*) level of theory. The frequencies were scaled by a factor of 0.97 to be compared to the experimental spectrum.....	128
Figure 3-13. (a) Transfer and (b) output characteristics of the single-crystal OFET, fabricated by SVA. I_D , V_D , V_G , and L/W indicate drain current, drain voltage, gate voltage and length-to-width ratio of the active channel cocrystal. Inset: schematic drawing of the device structure. (c) Optical	

microscope image of a single-crystal OFET (left: under ambient light, right: under UV).	133
Figure 3-14. The colligative capacitance values of SiO ₂ / PMMA layer.	134
Figure 3-15. (a) Out-of-plane XRD measured on D•A (1:1) CT co-crystal, inset table: 2 theta values compared with values found in single-crystal XRD analysis. (b) AFM measured on D•A (1:1) CT co-crystal, inset shows height profile between adjacent layers.	134
Figure 3-16. (a) measured PL intensity anisotropy of the D–A (1:1) CT cocrystal. (b) Schematic drawings of the molecular packing structure with respect to the macroscopic crystal morphology; crystallographic axes are indicated.....	135
Figure 4-1. (a) Chemical structures of 2MDCS (D1) and CN-TFPA (A1). (b) DFT (B3LYP, 6-31G(d,p)) calculated frontier molecular orbitals of D1 , A1 , and D1-A1 and experimentally determined frontier molecular orbitals of D1 and A1 . (c, d) Images of self-assembled D1 and A1 supramolecular structures, and (e) image of physical vapor transport grown two-dimensional CT cocrystal taken under UV using optical microscope. (f) Atomic force microscope image of CT cocrystal surface (5 μm × 5 μm). ..	175
Figure 4-2. (a) Molecular arrangement of D1-A1 2:1 CT cocrystal from simulated single-crystal X-ray diffraction analyses. (b,c) roll and slip angle views. (d) Speculated local dipole alignment induced from –CN functionalities. (e)	

Summarized characteristic intermolecular interactions and slip-/roll-angle of molecular arrangement. Green arrow in (b, e): **D1-D1** π - π interaction; purple arrow in (b, e) **D1-A1** π - π interaction; red arrow in (b, e): **D1-D1** -CN \cdots HC- interaction; orange arrow in (b, e) **D1-A1** -CF \cdots HC- interaction; blue arrow in (c, e): **D1-A1** -CF \cdots HC- interaction. 157

Figure 4-3. ^1H NMR analysis of physical vapor transport grown CT cocrystal. The peak positions (circle: **D1**, triangle: **A1**) are assigned from individual ^1H NMR analyses results. The integrated values indicate 2:1 stoichiometry of **D1:A1**. 159

Figure 4-4. Coplanarized molecular geometries of 2MDCS (**D1**) and CN-TFPA (**A1**) found from SC-XRD analyses. The dihedral angle of each single bond twisting is indicated. 159

Figure 4-5. DSC curves of PVT grown single-crystals, **D1-A1** 2:1 mixture powder, **D1** powder, and **A1** powder samples; (a): the first cycle, and (b): the second cycle. 160

Figure 4-6. (a) Normalized UV-vis absorption and photoluminescence (PL) spectra of dilute **D1**, **A1**, and **D1-A1** (2:1) THF solution. (b) Normalized UV-vis absorption and PL spectra of **D1**, **A1**, and **D1-A1** (2:1) nanoparticle suspension (water:THF, 0.98:0.02). The solid and open circle: **D1** absorption and PL; the solid and open diamond: **A1** absorption and PL; the solid and open triangle: **D1-A1** CT pair absorption and PL spectra in solution (a) and nanoparticle suspension (b). (c) PL (solid circle) and

electroluminescence spectra (open circle) of physical vapor transport grown D1-A1 CT cocrystal.....	165
Figure 4-7. Solid-state PL lifetime spectra of D1 single crystal (a), A1 single crystal (b), and D1-A1 2:1 CT cocrystal (c).....	166
Figure 4-8. (a) MO alignment and descriptions of D1-A1 CT pair calculated by TD-DFT (CAM-B3LYP/6-311G*). The characteristic configuration interaction terms comprising $S_0 \rightarrow S_1$ transition and their portions are indicated by red arrows. (b) Extinction coefficient spectrum of 2:1 D1-A1 CT nanoparticle suspension (black line) and oscillator strength of each characteristic transition calculated from TD-DFT (red bar), and extracted from experimental values (green bar).....	168
Figure 4-9. (a, b) optical microscope images of bottom-contact bottom-gate SC-OFETs device, taken under ambient light and UV, respectively. (c, d) p-channel and n-channel transfer characteristic (black square) and external quantum efficiency (red hexagon). (e, f) p-channel and n-channel output characteristic.....	174
Figure 4-10. (a) DFT (CAM-B3LYP) calculated indirect electronic coupling of D1-A1-D1-D1 and A1-D1-D1-A1 tetramer stacks for p-channel and n-channel carrier, respectively. (b) DFT calculated direct electronic coupling between nearest inter stack D1-D1 and A1-A1 pairs.....	175
Figure 5-1. (a) Chemical structures of donor (D1 : 4M-DSB) and acceptor (A1 : Thio-	

Y). (b) Frontier molecular orbital diagrams of mixed and demixed phases.
..... 185

Figure 5-2. (a) Normalized UV/Vis absorption of **D1**, **A1**, and **D1-A1** nanoparticles, and normalized PL spectra of **D1-A1** nanoparticle. (b) Normalized PL spectra of **D1**, **A1**, CT-P1, and CT-P2 single crystals. (c) Calculated absorption spectrum of **D1-A1** dimer by TD-DFT. 191

Figure 5-3. Calculated molecular orbital diagram for CT dimer pair by DFT(CAM-B3LYP/6-311G*). 193

Figure 5-4. (a–c) Molecular arrangement of CT-P1 (solvent-included structure) from SC-XRD. **D1**: blue molecule; **A1**: yellow molecule; and solvent (C-Cl): red molecule. (b) Roll-angle view with information of the **D1-A1** π - π distance (black arrow) and the **A1-A1** –CN \cdots HC– distance (red arrow). (c) Slip-angle view showing dimer-pair brick-wall geometry. Black dotted box: **D1-A1** dimer pair; red cube: lattice free volume. 199

Figure 5-5. Powder XRD (a), TGA (b), and ^1H NMR (c) analyses of CT-P1 (black trace) and CT-P2 (red trace) single-crystalline powder obtained *via* recrystallization procedure. The main peak of CT-P1 is assigned to (002) at two theta value of 11.38° ; two theta position of CT-P2 (002) is assumed to be 11.72° due to the structure similarity (a). Inclusion of solvent molecules is only observed in case of CT-P1 by TGA analyses; additional ca. 2.6% weight loss at 139.6°C indicates solvent exclusion by lattice reorganization (b). Additional solvent peaks (THF and EtOH) are only

detected in CT-P1 case from ^1H NMR; the stoichiometry of D1:A1:solvent are found to be ca. 1:1:0.35 (c).....	201
Figure 5-6. Solid-state PL lifetime spectra for D1 : 4M-DSB (circle), A1 : Thio-Y (diamond), CT-P1 (square), and CT-P2 (triangle), respectively.....	202
Figure 5-7. Digital images of CT spin-coated films taken under 365 nm UV irradiation.	205
Figure 5-8. (a) Normalized PL spectra of pristine (black open diamond), DCE-SVA (red open circle), and MeCN-SVA (blue open hexagon) spin-coated films. Each state is compared with CT-P1 (black diamond), CT-P2 (red circle), and D1 (blue hexagon), respectively. (b) XRD data of D1 , A1 , CT-P1, and CT-P2 single crystals, and spin-coated films of the DCE- and MeCN-SVA states. (C) The blue triangle, black diamond, and red star indicate characteristic peaks of D1 , CT-P1, and CT-P2, respectively. The relative PL intensity transition during repetitive SVA processes using MeCN and DCE at ca. 471 nm (blue open square), and ca. 622 nm (red open circle).	205
Figure 5-9. Out-of-plane XRD of D1-A1 CT SVA film with consecutive MeCN \leftrightarrow DCE annealing procedures.	206
Figure 5-10. FE-SEM images and AFM images of pristine D1-A1 spincoated film (a, b), MeCN SVA film (c, d), and DCE SVA film (e, f).	206
Figure 5-11. Optical memory demonstration of D1-A1 CT spin-coated film consisting of three components (i.e., D1 , A1 , and PMMA), utilizing various external	

stimuli. The thermal erasing process that took place after piezo writing exhibited an inevitable stain.208

Figure 5-12. DSC curves of **D1-A1** mixture powder (black: 1st cycle, red: 2nd cycle), **A1** single-crystal (blue), **D1** single-crystal (turquoise blue), and CT-P1 single-crystal (magenta). The featured transition peaks are indicated above the curves. Inset digital images indicate fluorescence characters after applying 20 min thermal stimulus using DSC instrument.208

Chapter 1. Introduction

1.1. Functional Supramolecules based on π -Conjugated Molecules

Supramolecular chemistry - and its synonym crystal engineering, has been emerged as one of the major research fields in chemistry, emphasizing the importance of non-bonding interactions beyond covalent bonding interaction for comprising molecular solids.^[1] Can be differentiated from the simple aggregated structures, the supramolecules of given organic materials exhibit distinctive properties based on their stacking structures.^[2] In virtue of enormous expeditions on various functional units, important supramolecular synthons and intermolecular interaction species have been characterized and versatilely utilized to design functional supramolecules, see **Figure 1-1**.

In the recent years, in particular, supramolecules based on π -conjugated materials have grasped much attention, due to the prominent possibilities for next-generation optoelectronics devices applications, such as organic light-emitting diode (OLED), organic field-effect transistor (OFET), and organic photovoltaic (OPV).^[3-5] The π -conjugated materials basically can adopt two distinctive molecular arrangements. For instance, the hydrocarbons with high C : H ratios mainly manifest $\text{CH}\cdots\pi$ interactions;

thus result in namely herringbone type stacking. Such herringbone type stacking supramolecules are easily found in p-channel materials such as (oligo-)acenes (e.g., pentacene) and heteroacenes (e.g., benzothienobenzothiophene derivative, C8-BTBT).^[6,7] However, substituents with large steric effect can also lead to π - π stacking arrangement even with the hydrocarbons with high C : H ratio, the benchmarks of such supramolecules are rubrene and 6,13-bis(triisopropylsilylethynyl)pentacene (TIPS-pentacene).^[8,9] Meanwhile, the π -conjugated materials with stabilized frontier molecular orbitals by electron withdrawing substituents give rise to C \cdots C interactions by π - π stacking molecular arrangement. Fluorination of pentacene (perfluoropentacene), for instance, drives significant structural changes from herringbone structure to π - π stack.^[10] In addition, π -conjugated hydrocarbons with strong electron accepting units, e.g., derivatives of naphthalene tetracarboxylic diimide, perylene tetracarboxylic diimide, and cyanostilbene, have exhibited characteristic π - π stacking molecular arrangements, see **Figure 1-2** and **1-3**.^[11-14]

In addition to the characteristic supramolecular synthons in π -conjugated materials, i.e., CH \cdots π , and π \cdots π (C \cdots C) interactions, further derivatizations of materials by supramolecular synthons and/or intermolecular interaction motifs have resulted in remarkable optical, and electrical performances and/or even interesting optoelectronic features. Gsänger et al., reported 1,2,5,6,7,8,11,12-octachloroperylene-3,4:9,10-tetracarboxylic diimide (Cl₈-PTCDI), which exhibited brickstone arrangement with substantial π -orbital interaction by highly twisted perylene backbone (**Figure 1-3e**).^[15]

In addition to the molecular orbitals stabilization effect of Cl and imide functionality; open NH imide groups facilitated tight binding structure by strong H-bonding interaction (-NH...O-), giving rise to remarkable n-channel mobility of ca. $1 \text{ cm}^2 \text{ V}^{-1} \text{ s}^{-1}$. Ajayaghosh et al., have extensively been working on functional organogel comprised of oligophenylenevinylene derivatives, of which the supramolecular nanostructures are achievable by strategic intermolecular interaction networks particularly utilizing strong H-bonding and π - π stacking supramolecular synthons.^[16] Indeed, various optoelectronic functionalities could be rendered such as fluorescent, light-harvesting, electrical conductivity in this unique system.^[17] Kim et al., have successfully established the way to promote pure organic room-temperature phosphorescence *via* heavy halogen atom – lone pair electron interaction, **Figure 1-4a**.^[18] In particular, diluted aromatic ketone containing phosphors in a tightly stacked isostructural bi-halogenated analogue's medium not only increased intersystem crossing rate but also effectively reduced self-quenching and vibrational deactivation for high phosphorescence quantum yield (ca. 55%). In the meantime, Aida et al. have established versatile route to design supramolecular polymers for unique optoelectronic functions, utilizing strong π - π interaction of hexabenzocoronene (HBC), the graphene-like π -conjugated molecule, **Figure 1-4b**. By appending various functional moieties to HBC molecule, e.g., trinitrofluorenone (TNF), C60, bipyridine (bpy), and etc., unique optoelectronic features could be attained such as ambipolar transport, photoconducting behavior, photovoltaic effect, and controlled photo-induced charge-carrier

recombination in coaxial molecular heterojunction supramolecular polymers.^[19-21]

Consensus has been made that such intriguing optoelectronic features are not only the factor of molecular character itself but also their stacking nature; thus, desired properties of supramolecules shall be derived by molecular/supramolecular engineering considering both electronic and structure effects. In this regard, it is worth to emphasize that proper understanding of the structure-property correlation is the kernel of the subject: *supramolecular optoelectronics*. For this, it is essential to comprehend electronic and structural effect of substituents from the aspect of supramolecular chemistry; furthermore, it is required to understand relationship between molecular stacking mode and resulting electronic (or excitonic) interaction between adjacent molecules.

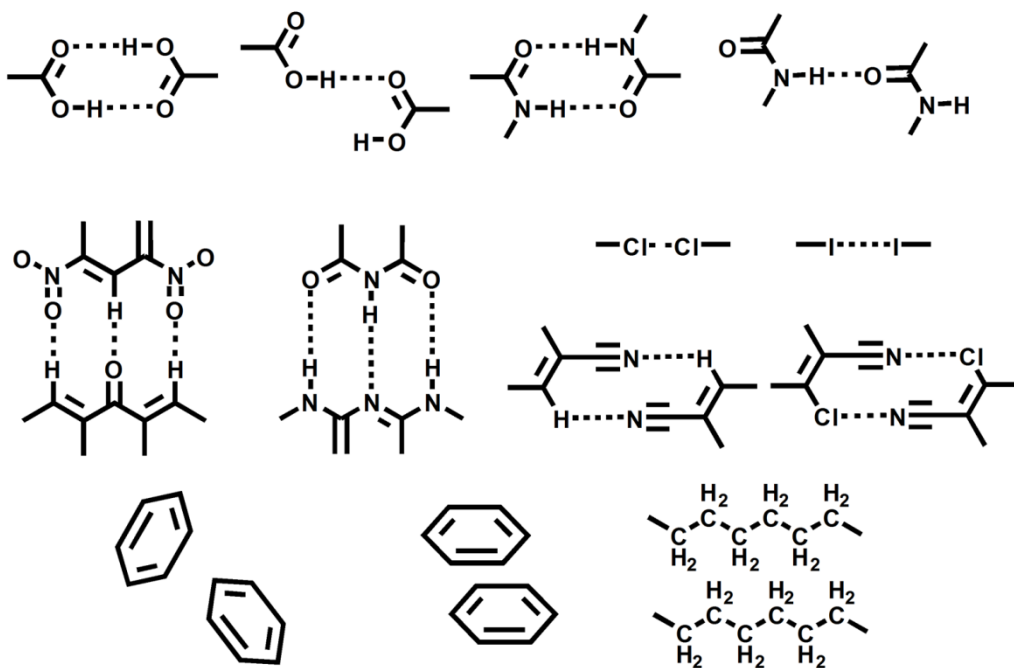


Figure 1-1. Representative supramolecular synthons.^[2]

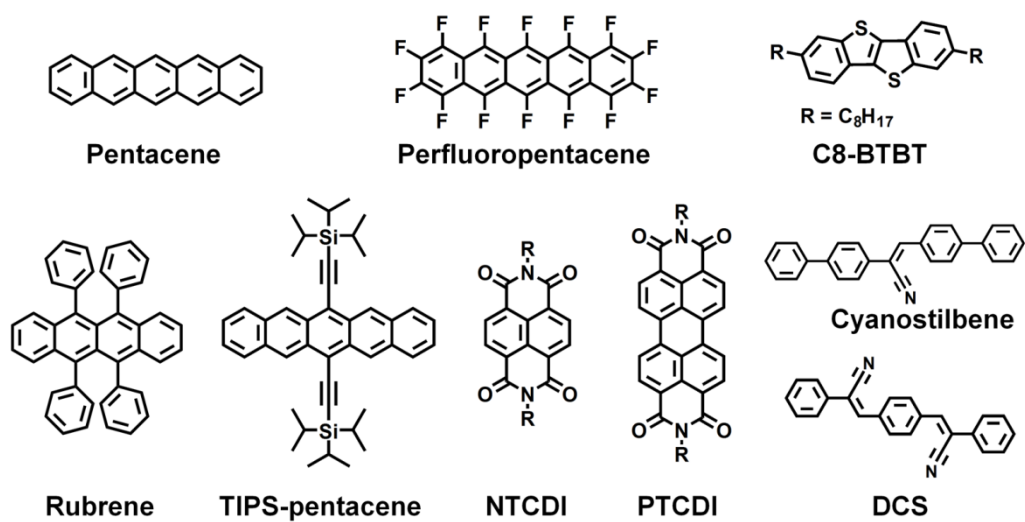


Figure 1-2. Representative π -conjugated materials.

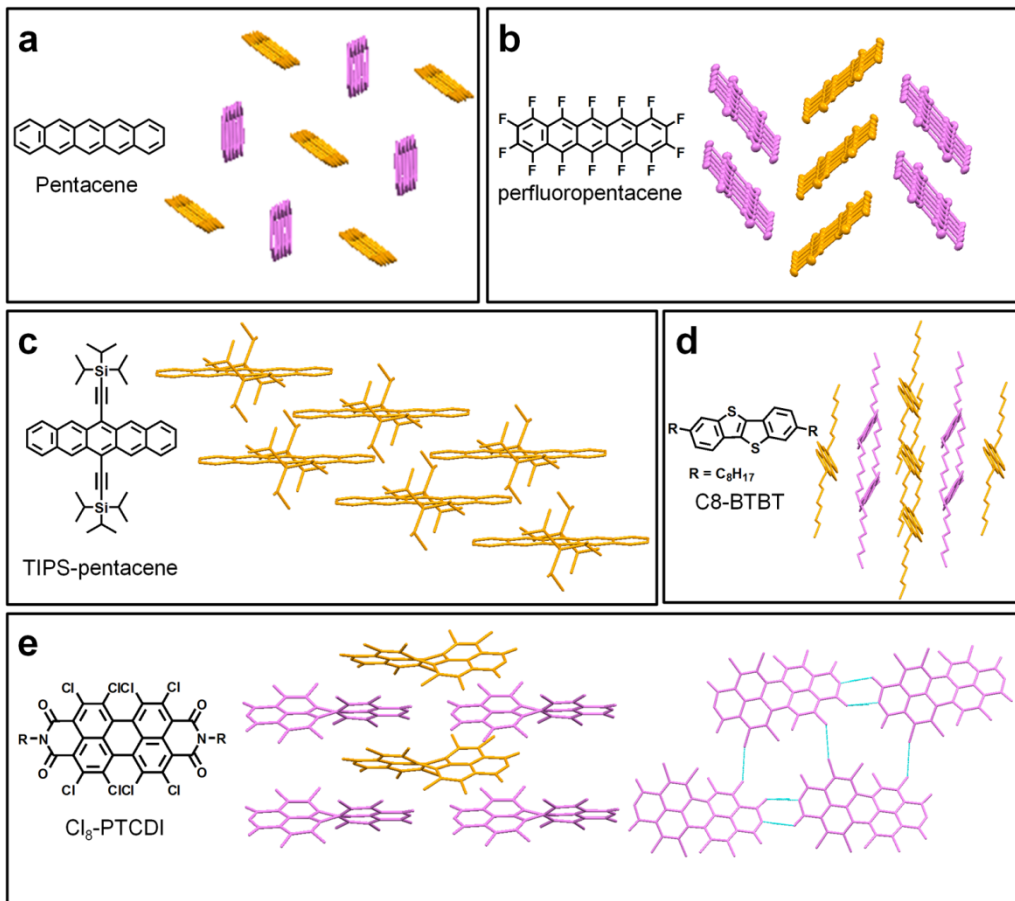


Figure 1-3. Molecular arrangements of (a) pentacene, (b) perfluoropentacene, (c) TIPS-pentacene, (d) C8-BTBT, and (e) Cl₈-PTCDI. The crystallographic data are obtained from (a) CCDC 145333, (b) 234729, (c) 172476, (d) 679293, and (e) 738649, respectively.

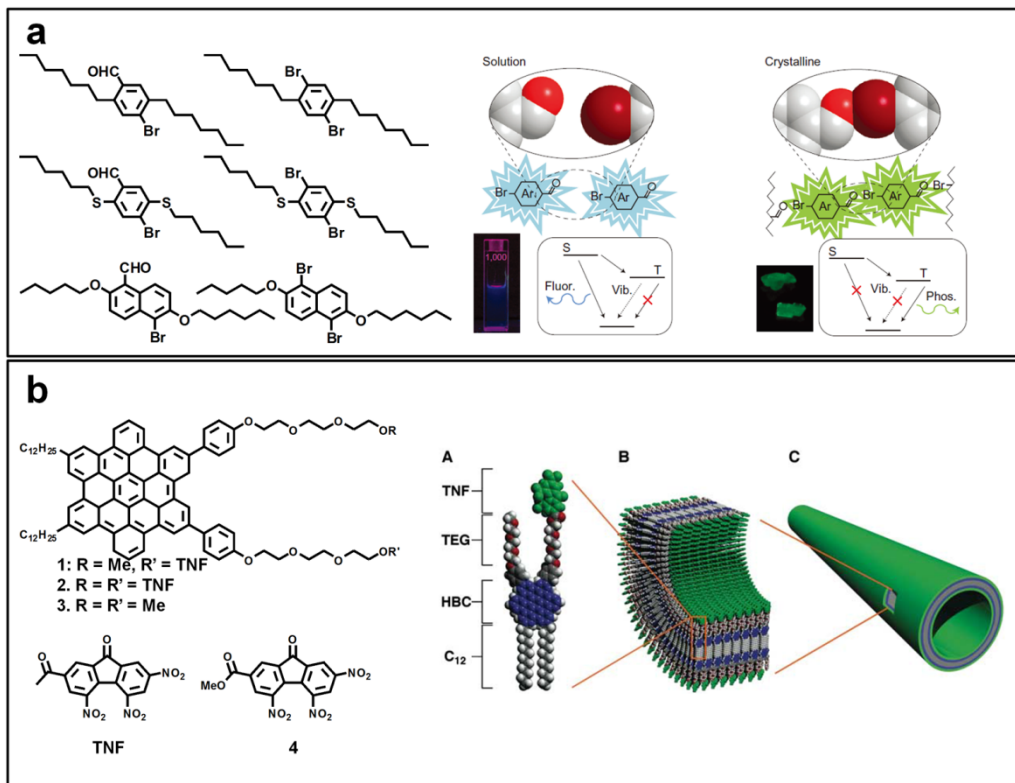


Figure 1-4. (a) Molecular structures of hosts/aldehydes of room temperature phosphorescent supramolecules. In solution, negligible intermolecular $-O\cdots Br$ -interaction results in fluorescence; however, intermolecular $-O\cdots Br$ -interaction in crystalline state induces phosphorescence by efficient spin-orbit coupling.^[18] (b) Molecular structures of hexabenzocoronene – TNF based functional molecules and the schematic drawings depicting supramolecular assembly.^[19]

1.2. Charge-Transfer Complexes and Functional Supramolecules based on Charge-Transfer Interactions

The charge-transfer (CT) complexes and their highly conducting features based on electron donor (D) and acceptor (A) pair have been regarded as an important subject in chemistry and physics for several decades. As Mulliken et al. described in his earlier literature,^[22] even though researchers had been aware of molecular complexes based on electron D-A pairs, much attention have been received after the discovery of newly generated CT absorption band in a solution of benzene and I₂.^[23,24] The metallic conductivity also found from pioneering molecular complexes based on aromatic electron donor materials with halogen anions, e.g., (perylene-bromine complex, electrical conductivity of ca. $1 \cdot 10^{-3} \text{ ohm}^{-1} \text{ cm}^{-1}$),^[25] which generated gradual increase of expectancy for developing pure organic metals. The first discovery of unprecedentedly high conductivity (in room-temperature ca. $500\text{-}1000 \text{ ohm}^{-1} \text{ cm}^{-1}$, in low K ca. $10^4 \text{ ohm}^{-1} \text{ cm}^{-1}$) in tetrathiafulvalene (TTF) – tetracyanoquinodimethane (TCNQ);^[26] the representative class of CT system, indeed have accelerate many physicists and chemists to develop and evaluate its analogous pairs, **Figure 1-5a**. In this revolutionary movement, remarkable metallic conducting, superconducting, ferroelectric, and ferromagnetic behaviors could be attained, and could successfully be elucidated by both theoretical and experimental efforts.^[27-32]

It is well known that the physicochemical properties of CT complexes are greatly determined by the electronic properties of constituents, stoichiometry, and molecular arrangements, **Figure 1-5**.^[33,34] Basically, the ionization potential of D and electron affinity of A determines ionicity of CT complex, i.e., δ in $(D^{\delta+})_m(A^{\delta'-})_n$, the CT complex with ionic, mixed-valence, and neutral character can generally be classified by the range of δ ($\delta, \delta' = 1$ for ionic, $1 > \delta, \delta' > \delta_c$ for mixed valence, and $\delta_c > \delta, \delta' \geq 0$ for neutral case, δ_c corresponds to critical degree of CT).^[34] In addition to the electronic features, the molecular stacking structures – i.e., the segregated stack vs. mixed stack, greatly determine the characteristics of CT complexes, see **Figure 1-5b, c**. It is well described that mixed valence character with segregated stack gives rise to highly conducting state of CT, due to the charge delocalization through one-dimensionally stacked D and A. This could be elucidated by band theory that partially filled band states of CT lead to metallic conduction. However, not all the complexes which exhibit partially filled band states are conductive; since charges occupied in frontier molecular orbitals and their periodicity can lead to such as on-site and off-site Coulombic repulsion, thus lead to insulator formation e.g., Mott, and charge-ordered insulators.^[35] Such insulators with mixed valence characters however exhibited field-effect transistor characteristics, memristor property, actuation, antiferromagnet, and conductivity in certain circumstances, thus, theoretical and technological interest have also been paid on such peculiar system.^[36-39] On the other hand, relatively little endeavor has been devoted to CT system with mixed stacked and neutral characters, particularly by

insulating or semiconducting character with rather limited conductivity. Only recently, however, various types of such systems have been developed and utilized for active channel for field-effect transistors and luminescence systems; also rendering a great opportunity for next-generation optoelectronics applications.^[40-42]

The CT phenomenon has also provided elegant strategies for designing functional supramolecules, **Figure 1-6**. Differentiated from multi-component assembly using electronically inactive co-formers – which lead to structural changes induced electronic and excitonic coupling modulations by specific interaction species;^[43] the CT interaction directly affects electronic and structural properties of complexed matters. Attributed from electronic interaction between electron D-A pair, D-A interaction exhibited similarities compared to H-bonding interaction based supramolecular synthons. H-bonding interaction, constructed by acidic hydrogen atom donor and hydrogen atom acceptor (or lone pair donor), shows complementary and directional nature; which all can be observed in mixed D-A complex as summarized in recent review by Ghosh.^[44] Between electron D-A pairs, spontaneous non-bonding interaction can be established by Coulombic interaction; in many cases highly directed by one-dimensional (1D) D-A-D-A mixed molecular arrangement along π -plane direction. In spite of such similarities, CT interaction exhibits rather weak or moderate binding strength compared to the H-bonding interaction and generally requires other strategic interaction motifs to establish robust multi-component assembly. However, CT interaction is still considered as an essential and promising motif for designing

supramolecules, due to the novel functionalities which shall be deduced from the peculiar electronic interactions along the stacking direction.

For an instance, mixed stacked D-A CT complex (D: (oligo)phenylenevinylene derivative, A: perylenebisimide derivative) utilizing amphiphilic designing strategies successfully rendered 1D self-assembled supramolecular structure showing high conductivity (in the order of $10^{-2} \text{ S cm}^{-1}$).^[45] Mixed stacked 1:2 ionic D-A pair (D: pyrene derivative, A: viologen derivative) exhibiting photoconductivity with reversible and fast switching behavior was also demonstrated, which could be attained by photocurrent generation and facile charge transport within molecular heterojunction between D-A stacking direction.^[46] Persec et al, reported on coassembly of donor and acceptor type liquid crystalline mesophases forming electron D-A complex which presented peculiar ambipolar transport by time-of-flight measurement in the D-A columnar stack.^[47] Meanwhile, segregately stacked discotic liquid crystalline D (hexabenzocoronene derivative) and A (perylenebisimide derivative) was also claimed to show photovoltaic effect, however without ground state CT character.^[48] As found from the literatures, D-A supramolecular system especially with CT character indeed have exhibited distinctive optoelectronic features with great opportunities for diverse applications. Such systems beyond classical TTF-TCNQ based molecular pairs are still remained at a premature stage; however, it is believed that chemical and supramolecular engineering strategies for designing D-A CT systems would resolve elusive but promising features such as room-temperature superconductivity, room-

temperature ferroelectricity, and novel optoelectronic properties for promising organic optoelectronics applications.

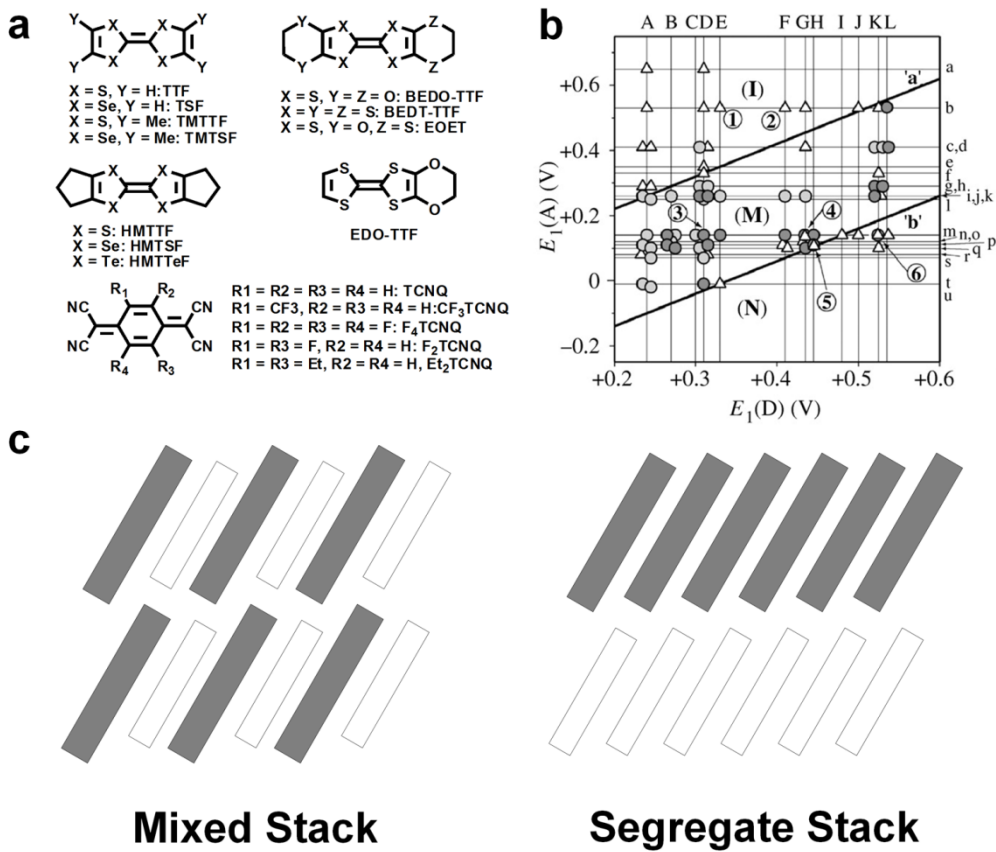


Figure 1-5. (a) Representative molecular structures of donors and acceptors in (TTF) – (TCNQ) based charge-transfer complexes.^[34] (b) Ionicity diagram for (TTF) – (TCNQ) based charge-transfer complexes.^[34] (c) Schematic illustrations of binary mixed and segregate stack.

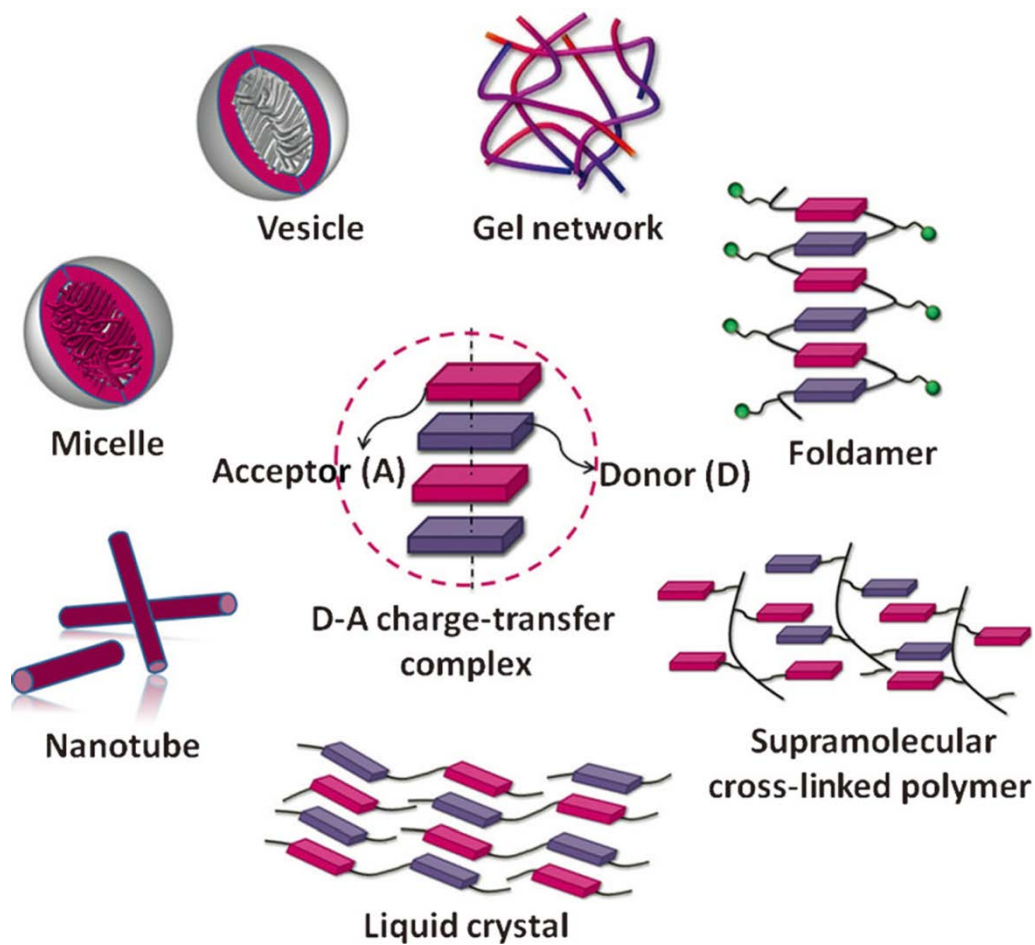


Figure 1-6. Schematic illustrations of supramolecular assemblies based on donor-acceptor charge-transfer interactions.^[44]

1.3. Supramolecular Optoelectronics: Basics of Charge Transport, and Photophysics in Semiconducting Supramolecules and Charge-Transfer Complexes

Since prominent electrical conductivity from doped polyacetylene as well as charge-transfer complexes has been unearthed, the subject – organic π -conjugated materials and optoelectronics applications has been pulsating for several decades.^[26,49] Tremendous efforts indeed have been made to realize optoelectronic devices such as OFET, OLED, and OPV; and in particular market success has already been achieved in the case of OLEDs.^[3-5] Simultaneously, in-depth understanding of charge-transport nature and exciton dynamics has been achieved and presented instructive structure-property correlations, which promoted marked enhancement of device efficiency. Such exertions are still in the present progression state; moreover, it is obvious that precise understanding of such consecutive efforts is essential to establish further advances in organic optoelectronics. Herein, therefore, basics and progresses on charge-transport and photophysics of organic supramolecular systems will be provided as well as those from charge-transfer complexes – one of the promising concepts that can attain breakthroughs for establishing next-generation organic optoelectronics applications.

1.3.1. Charge Transport in Semiconducting Supramolecules

Charge-transport characteristics of π -conjugated molecular (or polymeric) solids are greatly governed by electronic interaction as well as electron-phonon interaction within their stacking structures.^[50] Organic field-effect transistors (OFETs) – the device constructed with organic semiconducting active layer, gate insulator, source-drain, and gate electrodes; have attracted much attention not only for the practical applications but also for their fundamental importance i.e., understanding charge-carrier transport nature of supramolecular solids based on precise structure-property correlation. The four device configurations are generally utilized, i.e., bottom gate - bottom contact, bottom gate - top contact, top gate - top contact, and top gate - bottom contact, **Figure 1-7**.^[51] Those configurations can be utilized by proper device fabrication strategies considering contact between active layer and electrodes, interface engineering issues, and materials processing; since, the devices performances shall greatly be affected by the device structures.

The performances of OFETs devices are characterized or determined mainly by their field-effect mobility (μ), on/off current ratio, and threshold voltage (V_{th}). The three distinctive factors are generally characterized by two different measurement modes, i.e., transfer, and output characteristics (**Figure 1-8**).^[52] As visualized in output characteristics of n-channel organic semiconductor (PTCDI-C₈), the drain current (I_D)

exhibits drain voltage (V_D) and gate voltage (V_G) dependence, showing linear I_D - V_D dependence in $V_G - V_T \gg V_D$, pinch-off phenomenon in $V_G - V_T \sim V_D$, and saturation I_D - V_D dependence in $V_G - V_T < V_D$, see **Figure 1-8**, and **1-9**.^[52] Meanwhile, from the transfer characteristics, one can easily calculate aforementioned parameters.^[52,53] The standard linear and saturation regime I-V equation can be derived by Ohm's law:

$$J = \sigma E$$

where, J is current flux, σ is conductivity, and E is electric field. By substituting each parameter by its definition, i.e., $J = I/W\delta$, $\sigma = e\mu n$, and $E = \partial V_{ch}/\partial x$, the equation can be rearranged into:

$$I(x)dx = W\mu C[V_G - V_{th} - V_{ch}(x)]dV_{ch}(x)$$

In this equation, W is channel width, C is capacitance per unit area, V_{th} is the threshold voltage and μ is mobility of charge-carrier. Simplified by $\partial V_{ch}(x)/\partial x = V_D/L$, the integration form of above equation becomes:

$$\frac{\int_0^L I(x)dx}{\int_0^L dx} = \left[\frac{W}{L}\right] \times \mu \times \left[\frac{\int_0^L C[V_G - V_{th} - V_{ch}(x)]dx}{\int_0^L dx}\right] \times V_D$$

In linear transport regime (i.e., $V_D \ll V_G - V_{th}$), I-V characteristic can be derived by above equation:

$$I_D = \frac{W}{L} \mu C \left(V_G - V_{th} - \frac{V_D}{2}\right) V_D$$

Meanwhile, saturation occurs and can be observed from output curves of $V_D > V_G - V_{th}$ caused from pinch-off phenomenon at $V_D \sim V_G - V_{th}$. Thus by substituting V_D of above

equation to $V_G - V_{th}$, the I-V characteristic for saturation regime can be derived as:

$$I_D = \frac{W}{2L} \mu C (V_G - V_{th})^2$$

From these equations, one can extract field-effect mobility values from both linear and saturation regime. The linear field-effect mobility can be extracted from transconductance (g_m):

$$g_m = \left. \frac{\partial I_D}{\partial V_G} \right|_{V_D} = \frac{W}{L} C \mu V_D$$

and in constant V_D ,

$$\frac{dg_m}{dV_D} = \frac{W}{L} C \mu$$

Meanwhile, the mobility in saturation regime can easily be obtained from transfer characteristic by $\sqrt{I_D}$ vs. V_G .

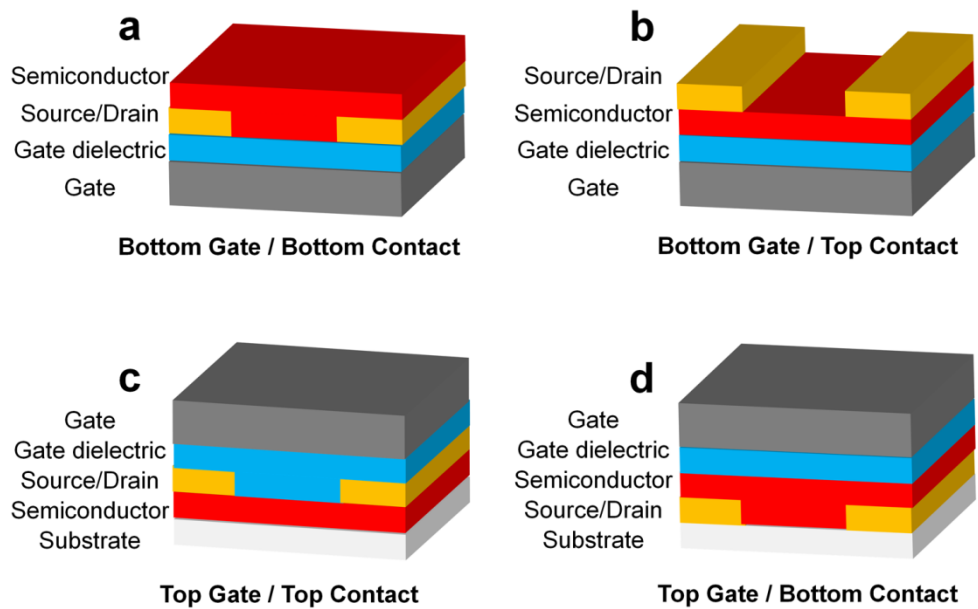


Figure 1-7. Schematic illustrations of the four representative organic field-effect transistors structures.

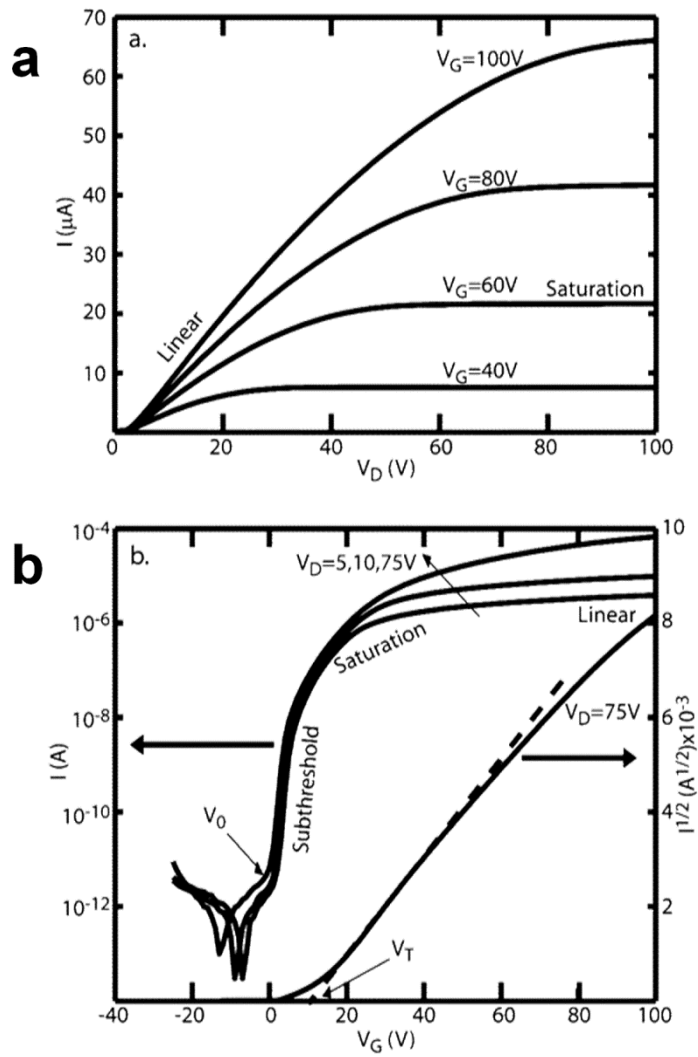


Figure 1-8. (a) Output characteristic, and (b) transfer characteristic of PTCDI-C₈ field-effect transistor.^[52]

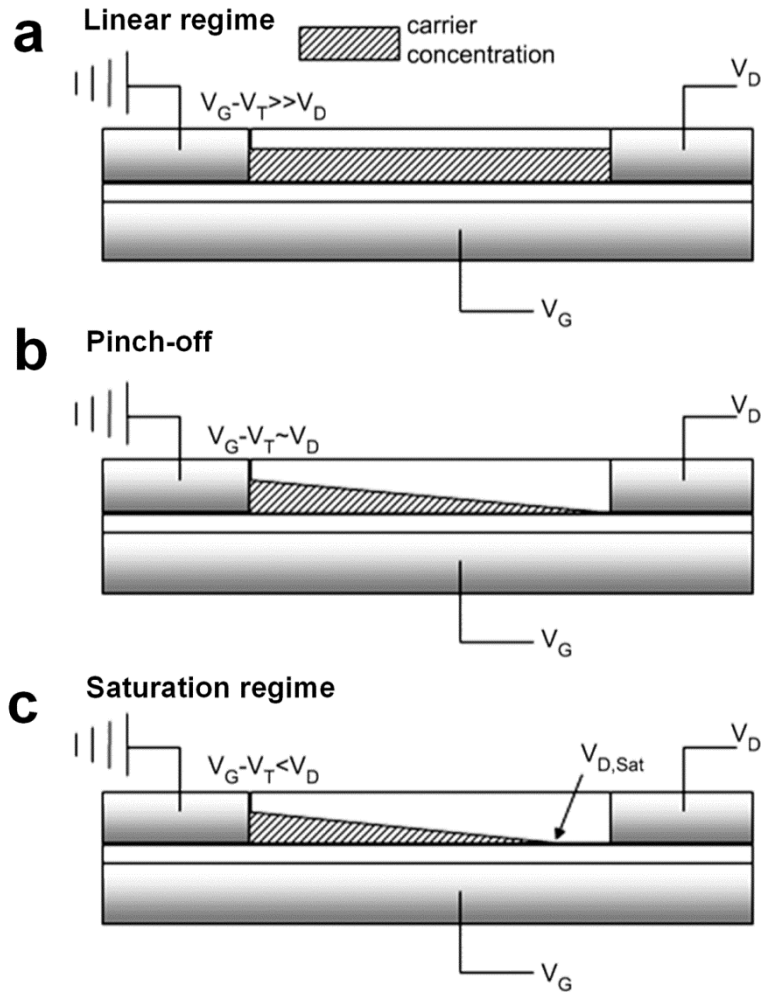


Figure 1-9. Schematic carrier concentration diagram of (a) linear, (b) pinch-off, and (c) saturation regime during field-effect transistor operations.^[52]

The on/off current ratio is another important performance determining parameter, which shows close dependence on charge-carrier mobility, charge density, and etc. It can be deduced from I-V characteristic, typically from transfer curve. The off current state can be defined by the lowest I_D value when there is negligible amount of accumulated charge-carriers by low V_G (in principle, 0 V); however, the on current refers to the (saturated) I_D for a given non-zero bias condition. The threshold voltage (V_{th}) and subthreshold swing can also be extracted from transfer characteristic; the former can be calculated from intercept of linear region of the $\sqrt{I_D}$ vs. V_G plot, the latter can be extracted by $S=dV_G/d(\log I_D)$.

In the typical polycrystalline thin-films of organic semiconductors, the charge-carrier mobility values are not satisfactorily high (therefore, low current values) to be utilized as practical on/off switching elements applications, mainly attributed from to the structural defects e.g., grain boundaries, and impurities. Such disorders in structures acting as charge-carrier trap sites, together with traps distributed throughout semiconductor/insulator interface crucially limit the performances of OFETs devices.^[a] On the other hand, OFETs based on single crystalline materials, the utmost form of the supramolecules with minimized defect, have opened a new horizon for next-generation electronic devices attributed to the superior electrical performances.^[54,55] For instance, physical vapor transport method grown rubrene single-crystal OFETs (SC-OFET) devices exhibited unprecedentedly high charge-carrier mobility i.e., ca. 15-40 cm² V⁻¹

s⁻¹.^[56,57] Meanwhile, recent advances in both materials developments and device fabrication methods resulted in remarkable transistors performance, e.g., ink-jet printed C8-BTBT SC-OFETs exhibited field-effect mobility up to ca. 30 cm² V⁻¹ s⁻¹, and C8-BTBT SC-OFETs based on off-center spin-coating method manifested mobility even exceeding 40 cm² V⁻¹ s⁻¹.^[58,59]

Besides the possibility of SC-OFETs for practical applications, investigations on SC-OFETs have facilitated in-depth understanding of structure to charge transport property correlation. As previously discussed from **Section 1.1.**, the molecular stacking structure of the given organic semiconductor greatly influences the charge-transport properties. Electronic coupling of nearest dimer pair is greatly governed by molecular orbital overlap between dimer pair; therefore, spatial distribution of dimer pair as well as molecular orbital defined by primary chemical structure determines the charge-transport efficiency of the supramolecular system, which is describable with below equation.^[50]

$$H = H_e + H_{ph} + H_{e-ph}^l + H_{e-ph}^{nl}$$

The electronic Hamiltonian H_e is defined as:

$$H_e = \sum_m \epsilon_m^{(0)} a_m^\dagger a_m + \sum_{mn} t_{mn}^{(0)} a_m^\dagger a_n$$

where, ϵ_m is site energy of the lattice site m (i.e., HOMO and LUMO) and t_{mn} is transfer integral. As well described in ref. 50, the molecular solid constructed by van der Waals interaction is essentially different from inorganic crystals – structures

comprised of strong covalent bonds; therefore, the electron and vibration coupling can also greatly modulate the charge-transport natures in semiconducting supramolecules. The local electron-phonon coupling (H_{e-ph}^l) stands for the site energy interaction between both intra-/ inter-molecular vibrations (**Figure 1-10a**). The electronic coupling between m , and n sites can also be affected by electron-vibration coupling, such dependence is refer to as non-local electron-phonon coupling (H_{e-ph}^{nl}) in above equation, see **Figure 1-10b** which theoretically describes effects of non-local phonon coupling.

Indeed, the electronic coupling effects can be well elucidated in previous literatures. Well summarized by Wang et. al., organic supramolecules adopt basic stacking motif among the four benchmark packing modes by characteristic supramolecular synthons (i.e., $\text{CH}\cdots\pi$, and $\pi\cdots\pi$ interaction), see **Figure 1-11**.^[51] Based on the packing modes of molecules, the degree of electronic interaction might significantly differ; in particular, the stacking modes including strong π - π interaction have been regarded as desired molecular arrangement for charge-carrier transport efficiency by favorable π -orbital overlap. Among these, two-dimensional (2D) π -stacking materials containing quasi 2D electronic interaction have exhibited efficient charge-transport natures, the representatives of 2D stacking organic semiconductors are TIPS-pentacene and Cl_8 -PTCDI, see also **Figure 1-2**, and **1-3** in **Section 1.1**.^[9,15] Meanwhile, the herringbone motif can also give rise to remarkable charge-mobility; for instance,

benzothienobenzothiophene (BTBT) analogue DNTT with small counter slip angle maximizes electronic interaction by characteristic sulfur atoms with high HOMO density, showing noteworthy transfer integral values toward $\text{CH}\cdots\pi$ direction, see calculated transfer integral values in **Figure 1-12**.^[60,61] The favorable electronic interaction of BTBT derivatives indeed gives rise to unprecedentedly high field-effect mobility even in solution processed OFETs.^[58,59] The results imply the importance of electronic interaction not just spatial distribution and orientation of nearest dimers, which in turn suggests the importance of subtle interplay of intermolecular interaction of molecular arrangement.

In addition to electronic coupling, consideration of the reorganization energy factors for effective charge-transport also has been proceeded. The reorganization energy (local electron-phonon coupling factor), i.e. energy required during charging and discharging the molecules, indeed greatly governs measured field-effect mobility values, see λ^h of **Figure 1-10a**, and **Figure 1-12**.^[60] The lattice reorganization energy (non-local electron-phonon interaction factor), moreover, is known as crucial factor for the mobility,^[a] which might render a great impact on distance and orientation between the nearest dimer pair (**Figure 1-10b**).^[50] From this line of idea, it is obvious that various factors of molecular and supramolecular structures should also be considered for charge-transport efficiency.

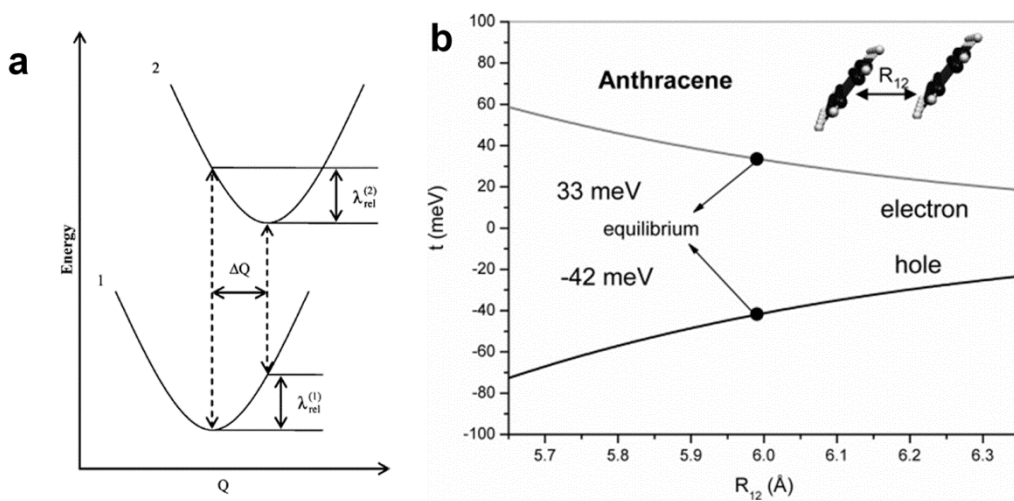


Figure 1-10. (a) Schematic description of reorganization energy, in neutral ($\lambda_{\text{rel}}^{(1)}$) and charged ($\lambda_{\text{rel}}^{(2)}$) molecular state. (b) Calculated transfer integral of anthracene dimer pair by as a function of the intermolecular separation (R_{12}).^[50]

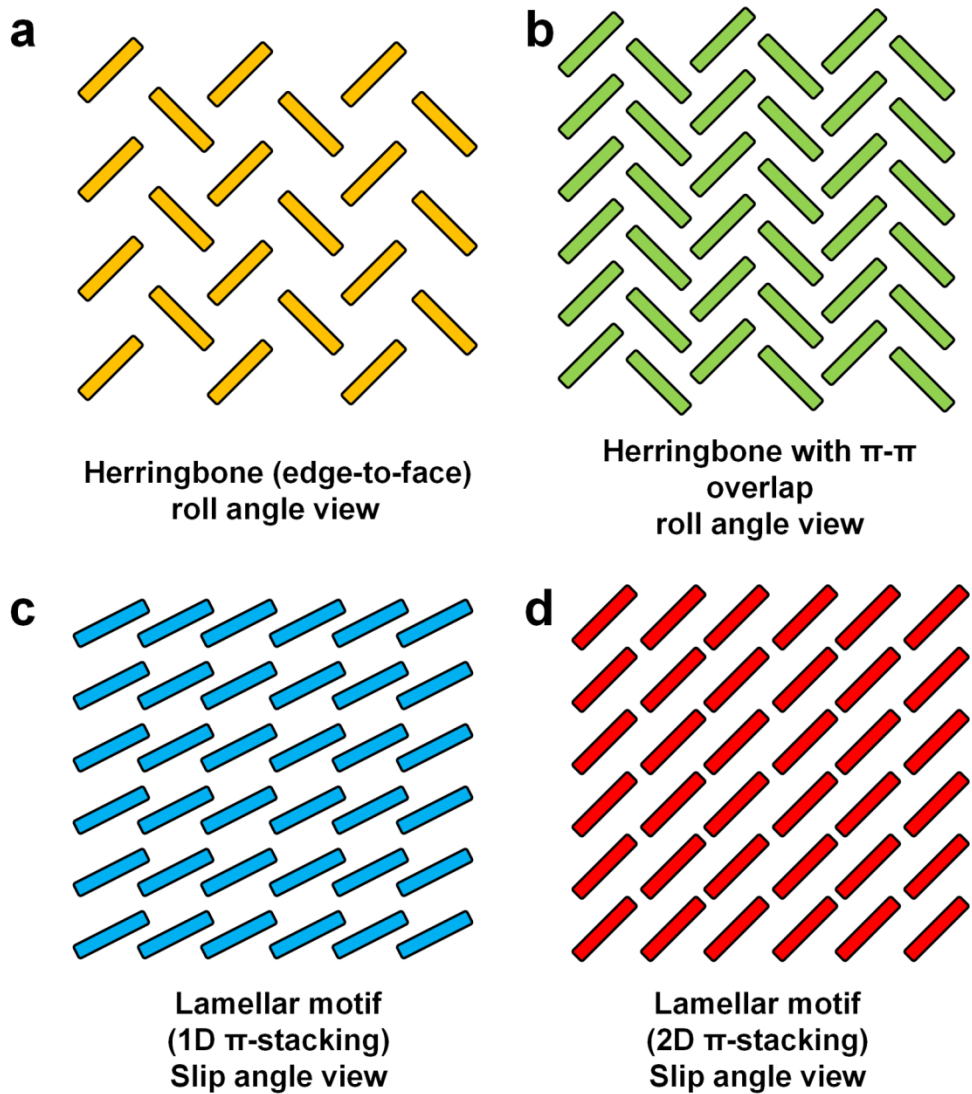


Figure 1-11. Four representative molecular arrangements found from molecular crystals.^[51]

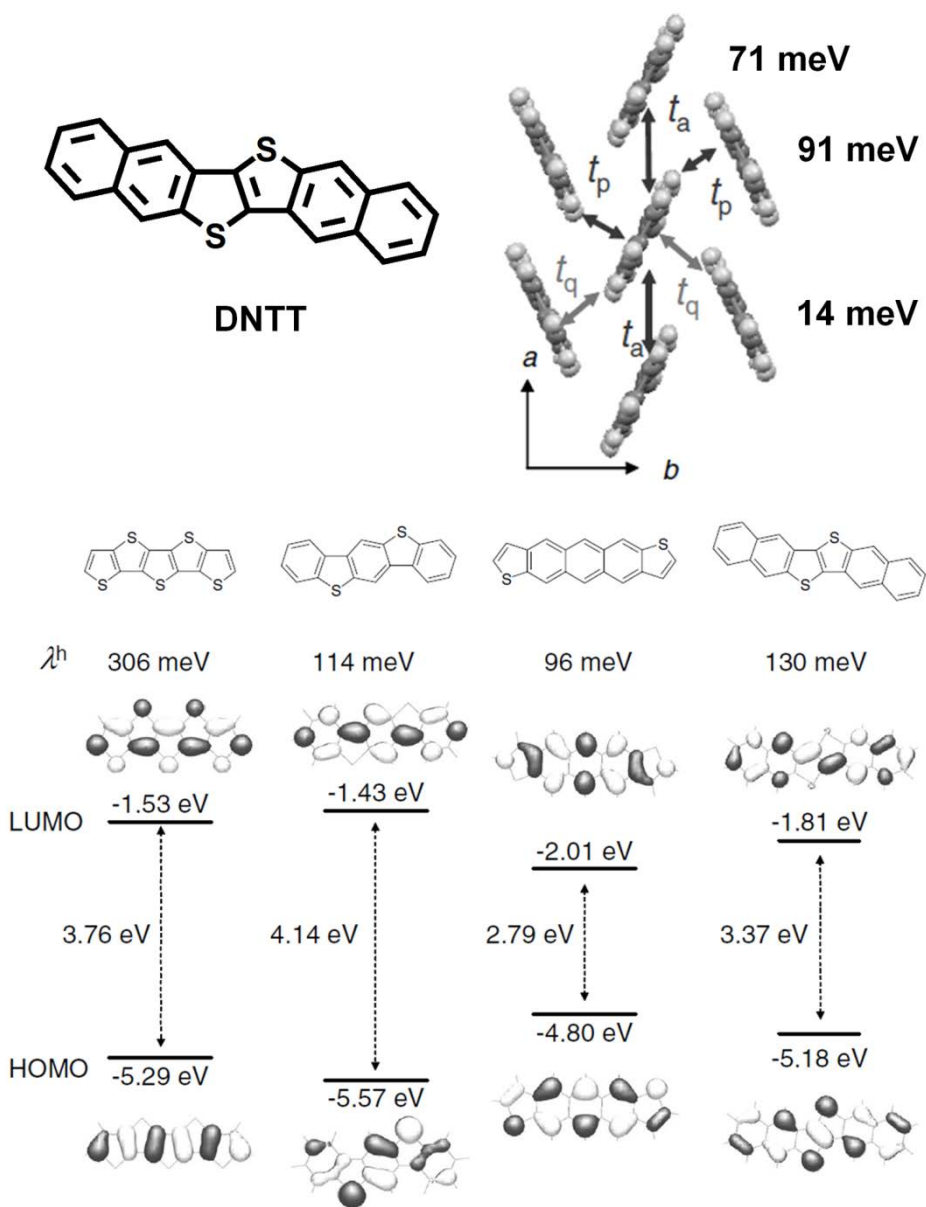


Figure 1-12. Transfer integral calculated along three distinctive molecular stacking directions of DNTT molecule. Calculated frontier molecular orbitals and reorganization energies of DNTT and its analogues.^[60]

1.3.2. Charge Transport in Semiconducting Charge-Transfer Complexes

In the meantime, efforts have also been provided to scrutinize possibilities of CT complexes for the semiconducting active channel elements of OFETs. As aforementioned in **Section 1.2.**, such consideration has been initiated from the use of classical TTF-TCNQ based CT systems (**Figure 1-13a**).^[62] The first attempt was based on TTF-TCNQ showing electron-like transport at 12 K by external gate field.^[63] Among the Mott insulators, the bis(ethylenedithio)tetrathiafulvalene (BEDT-TTF) – TCNQ exhibited peculiar ambipolar charge transport, of which the mobility increased by lowering temperature toward 240 K by metallic conducting behavior.^[64] The segregated stacked (BEDT-TTF)-(TCNQ) CT complex manifests metal-insulator phase transition at 330 K, thus shows semiconducting property at room-temperature.^[65] Well known superconducting CT system with layered structure i.e., κ -(BEDT-TTF)₂Cu[N(CN)₂]Br exhibited Mott insulating behavior in a specific condition (i.e., strain-induced negative pressure and/or field-induced phase transition), which showed n-channel conduction or ambipolarity.^[66,67] In addition, the charge-ordered insulating state (metal-insulator transition at 135 K) of layer stacked α -(BEDT-TTF)₂I₃ also manifested FET characteristic (some of devices showed ambipolarity); while, charge-ordered electronic state was rather robust to electrostatic charge carrier injection.^[68]

Ionic CT system, (BEDT-TTF)-(F₂TCNQ) complex, showing Mott insulating state also exhibited peculiar ambipolar transport only with limited circumstances (low temperature, 2-60 K).^[69] By the efforts – reillumination of insulating mixed valence or ionic CT complexes, possibilities have been remarked for versatile semiconductors applications, particularly with ambipolar transporting nature.

As aforementioned, on the other hand, only recently mixed stacked CT complexes with somewhat neutral characters have been regarded as promising candidates for semiconducting charge-transporting materials. By systematic theoretical analyses conducted by Brédas and coworkers, it has been revealed that mixed D-A arrangement indeed shows a great potential for ambipolar transport by non-direct (effective) electronic coupling by superexchange mechanism (**Figure 1-14**).^[70] From the literature, it is rationalized that when valence and conduction band shows symmetry along the mixed stacking direction, electronic coupling for both hole and electron becomes highly similar due to the frontier MOs mixing between D and A. Moreover, it has also been suggested that the direct coupling along the other directions might results in useful 2-dimensional electronic coupling for efficient charge transport. Meanwhile, Geng et al. have made a particular emphasis on the role of other bridging MOs for electronic coupling.^[71] In principle, the mixed stacked D-A CT should reflect similar transfer integral values for hole and electron due to the contribution of HOMO – LUMO interaction between D and A, which dominates effective electronic coupling. However, the effective transfer integral may differ by contribution of non-frontier

bridging MOs leading to inequivalent electronic coupling by constructive or destructive effects. In these systems, the reorganization factors also influence charge transporting nature as in the case of single-component semiconducting molecular solids.^[70]

Advances for developing D-A materials have proceeded in parallel, see **Figure 1-15**. Sagade et al., have discussed the electrical properties of molecular pair comprising coronene tetracarboxylate based D (CS) and methyl viologen based A (MV), manifesting promising hole transporting property (μ_h up to $0.53 \text{ cm}^2 \text{ V}^{-1} \text{ s}^{-1}$, low operation bias condition $\sim 2 \text{ V}$).^[72] Zhu and coworkers have developed novel D molecule (meso-diphenyl tetrathia[22]annulene[2,1,2,1], DPTTA) which was delicately designed to develop D-A complexes with various types of acceptor, such as TCNQ, fullerenes, and 4,8-bis(dicyanomethylene)-4,8-dihydrobenzo[1,2-b:4,5-b']-dithiophene, (DTTCNQ).^[40,73,74] The D-A complexes based on DPTTA exhibited ambipolarity during FETs operation; among these, (DPTTA) – (DTTCNQ) showed unprecedentedly high field-effect mobility values with fairly balanced character ($\mu_h \sim 0.77$, $\mu_e \sim 0.24 \text{ cm}^2 \text{ V}^{-1} \text{ s}^{-1}$) by unique quasi 2D electronic coupling comprised of direct and effective transfer integral.^[74] Park et al. have developed CT complex utilizing isometric D (4M-DSB) – A (CN-TFPA) pair based on distyrylbenzene derivative, showing not only ambipolar transport ($\mu_h \sim 4.3 \times 10^{-3} \text{ cm}^2 \text{ V}^{-1} \text{ s}^{-1}$, $\mu_e \sim 5.4 \times 10^{-2} \text{ cm}^2 \text{ V}^{-1} \text{ s}^{-1}$) but also highly luminescent character (CT emission quantum yield of 30 – 40%).^[75,76] The unique optoelectronic features of the result indicated possibility of light-emitting OFET

(LE-OFET) application. Study on stoichiometry effect on CT system has also been conducted, i.e., 1:1, 2:1, and 3:1 stoichiometry of perylene (D) – TCNQ (A).^[77] The theoretical calculation on each stoichiometry clearly revealed that effective mass of electron become larger in A-D-D-A stack by D dimer between adjacent A molecules in the case of 3:1; on the other hand, the 1:1, and 2:1 stoichiometry exhibited comparably low effective mass along stacking direction by A-D-A-D stacks. Such differentiated electronic features combined with coupling toward other directions significantly altered the charge-transport characters.

In fact, it is relatively difficult to develop such multi-component CT system, since one should consider all steric effect, electronic effect, and molecular shape matching of constituent molecules. However, the mixed stacked CT renders great advantages over single-component molecular solid, e.g., anticipatable ambipolar transport, and peculiar CT emission by pronounce and characteristic MO interactions.

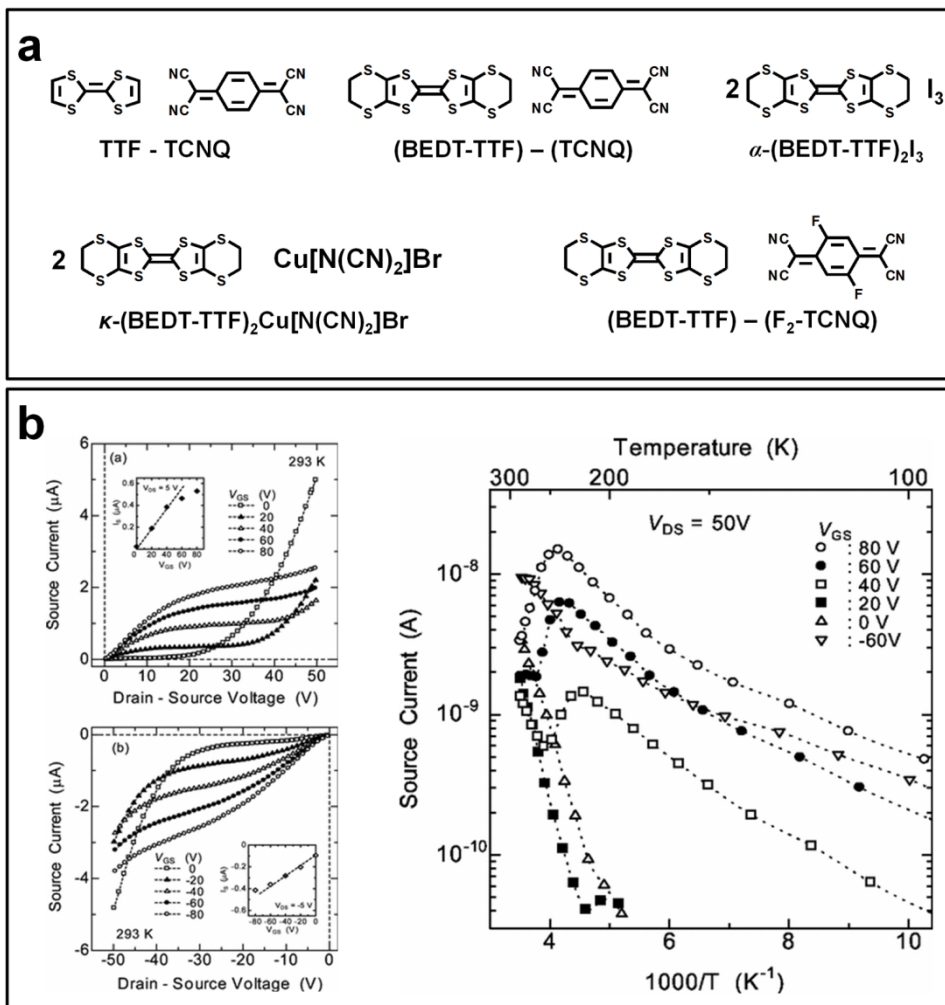


Figure 1-13. (a) Representatives of TTF – TCNQ based charge-transfer complexes exhibiting semiconducting behaviors in specific conditions. (b) Field-effect transistor characteristics of Mott-insulator (BEDT-TTF) – (TCNQ) complex showing ambipolar transport and metallic transporting nature above 240 K.^[64]

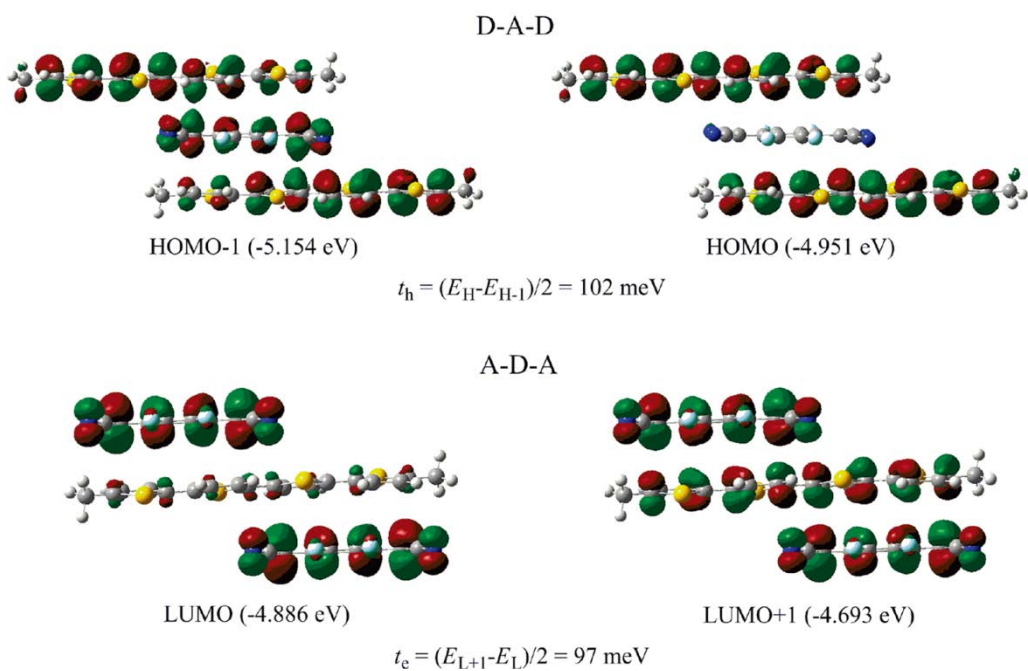
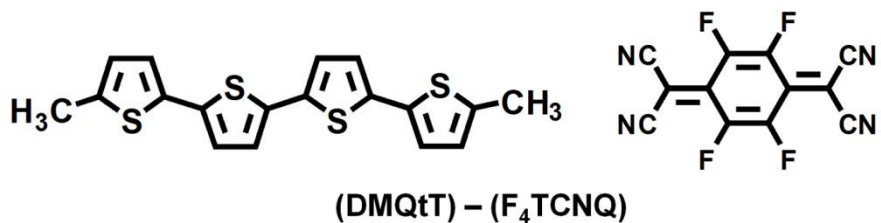


Figure 1-14. Indirect (effective) coupling calculated by energy-splitting in D-A-D and A-D-A trimer stacks of (DMQdT) – (F₄TCNQ) pair.^[70]

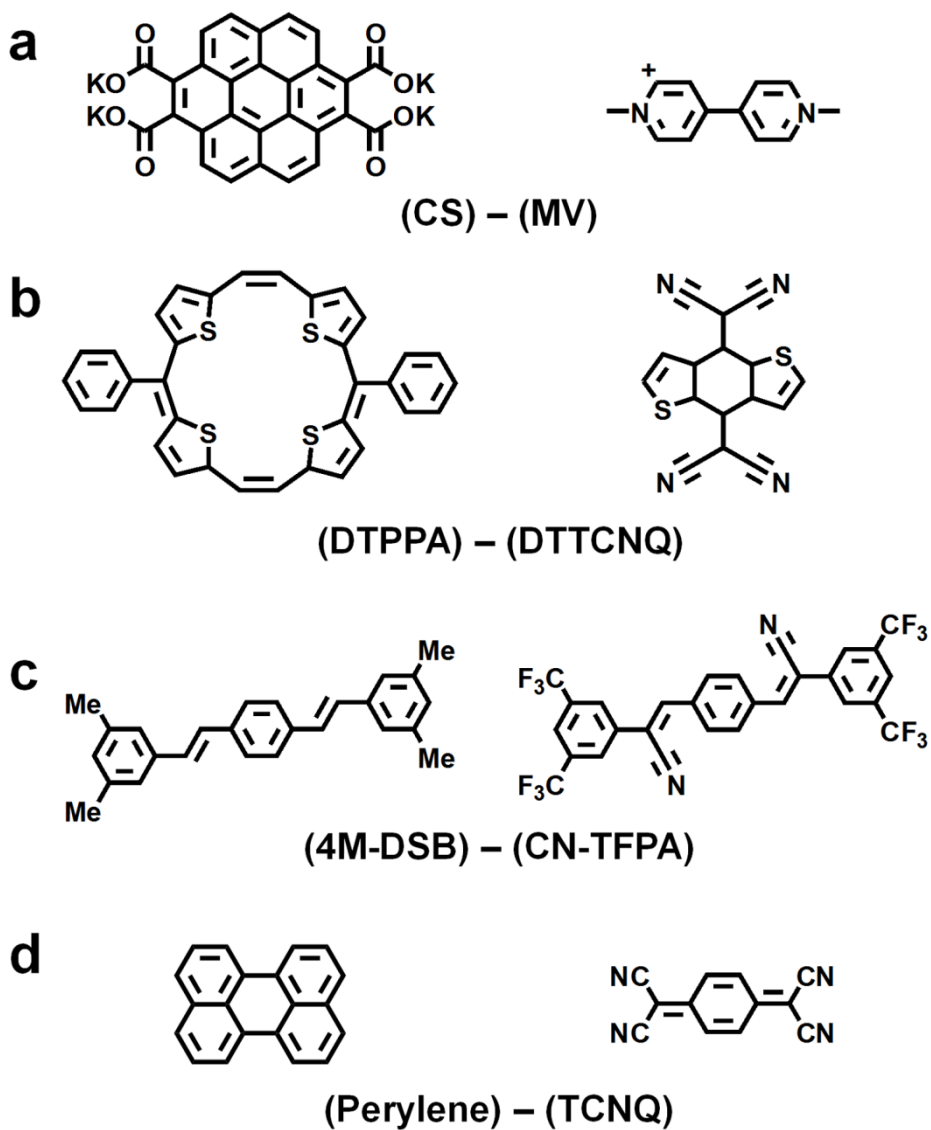


Figure 1-15. Examples of charge-transfer complex systems manifesting semiconducting properties.

1.3.3. Photophysics in Semiconducting Supramolecules

Likewise the case of charge-transport properties in π -conjugated supramolecular systems, intermolecular electronic interaction greatly influences the photophysical process compared to the intrinsic photophysics of molecular species. The highly crystalline supramolecules with proper molecular arrangements manifest highly luminescent character by radiative processes (e.g., fluorescence, phosphorescence, delayed fluorescence, and etc.); affording great opportunities to be applied in sensor, optical recording, laser, and optical memory system. Before discussing the structural influences on optical and photophysical properties of self-assembled supramolecular systems, it is worthwhile to briefly discuss the photophysical processes of (isolated) molecular systems. The state energy diagram (also known as Jablonski diagram) well elucidates molecular photophysical process, see **Figure 1-16**.^[78]

Each transition process in **Figure 1-16** refer to as,

- ① absorption (10^{15} s^{-1})
- ② internal conversion/vibrational relaxation (10^{11} - 10^{14} s^{-1})
- ③ intersystem crossing (10^7 - 10^8 s^{-1})
- ④ fluorescence (10^7 - 10^8 s^{-1})
- ⑤ phosphorescence (10^1 - 10^4 s^{-1})

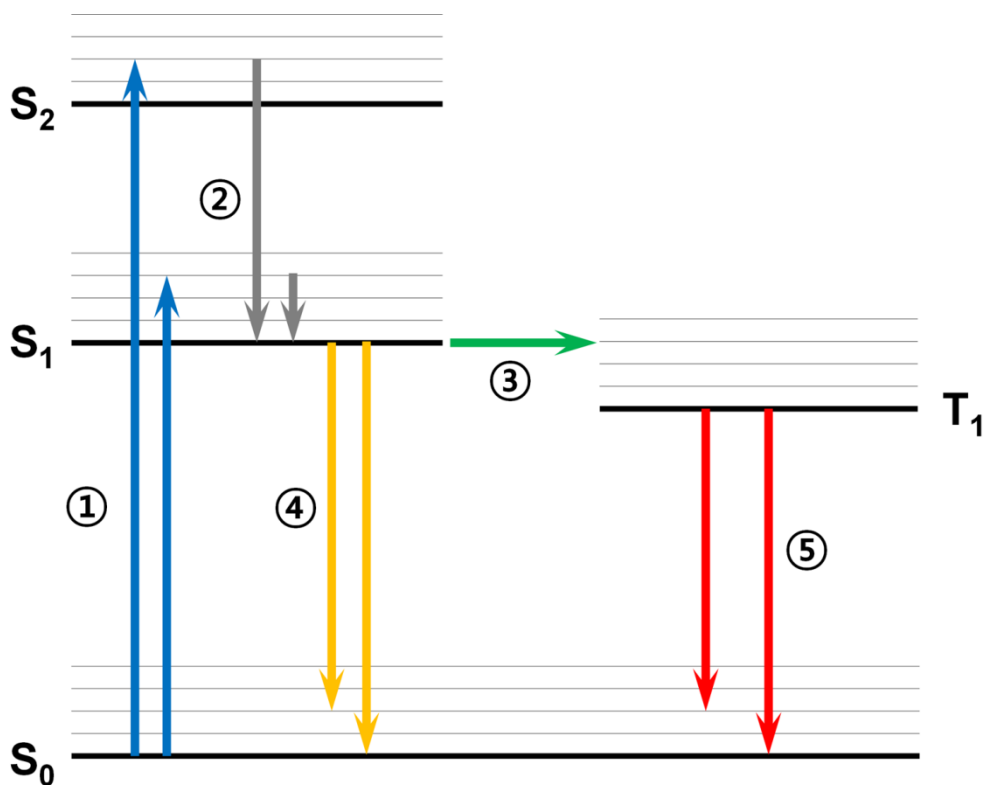


Figure 1-16. The state energy (Jablonski) diagram describing transitions between electronic states. The arrows and numbered denotations are indicating, ①: absorption; ②: internal conversion, vibrational relaxation; ③: intersystem crossing; ④: fluorescence; and ⑤: phosphorescence.

The rate (or probability) of each transition is indicated in the parenthesis. When a ground state (S_0) molecule absorbs light, resonances in specific frequencies between the ground and excited states give rise to vertical transition toward excited states, in general with same multiplicity, see process ① in **Figure 1-16**. The lowest excited singlet state (S_1) can be attained through direct excitation from the ground state (S_0) or by relatively fast internal conversion rate (k_{IC}) and vibrational relaxation processes from higher excited singlet state (S_n) by Kasha's rule, see process ② in **Figure 1-16**. Meanwhile, the excited triplet states can be reached from intersystem crossing process from corresponding singlet excited state, see process ③ **Figure 1-16**. The energy of S_1 and T_1 states destined to dissipate either by radiative or nonradiative deactivation process; the radiative decay transition in the former case with same multiplicity refers to as fluorescence (process ④ **Figure 1-16**). The fluorescence usually manifest relatively fast decay rate of $10^7 - 10^9 \text{ s}^{-1}$. The radiative transition from the latter case, called phosphorescence, however shows relatively slow transition rate of $10^4 - 10^1 \text{ s}^{-1}$, attributed from the spin-forbidden character of $T_1 \rightarrow S_0$ transition, see process ⑤ **Figure 1-16**.

The photophysical processes can be theoretically comprehended by correlating experimental quantities to the theoretical ones.^[78] Classically, electron can be understood as negatively charged harmonic oscillator; therefore, harmonically oscillating electromagnetic wave (i.e., light) can oscillate such charged species by

resonance interaction for an optical transition. The strength of oscillation, i.e., oscillator strength (f), is the theoretical measure for describing probability of electronic transition, as well described in following equations:

$$f \equiv 4.3 \times 10^{-9} \int \varepsilon d\bar{\nu}$$

$$k_e^0 = 3 \times 10^{-9} \bar{\nu}_0^2 \int \varepsilon d\bar{\nu} \cong \bar{\nu}_0^2 f$$

where, $\int \varepsilon d\bar{\nu}$ is integrated molar extinction coefficient by wavenumber, k_e^0 is radiative rate constant, and $\bar{\nu}_0$ is the maximum wavelength of absorption in wavenumber. From the equations, it is easily understood that oscillator strength of given transition can directly correlated to the molar extinction coefficient (absorption) and radiation process. The transition between given states also lead to the transition dipole moment (μ),

$$\mu = er$$

where, e is elemental charge, and r is vectorial distance of dipole. The relationship between f and μ is defined by below equations:

$$f \propto \mu_i^2 = (er)^2$$

$$f = \left(\frac{8\pi m_e \bar{\nu}}{3he^2} \right) \mu_i^2 \cong 10^{-5} \bar{\nu} |er_i|^2$$

thus, the transition probability is again the function of transition dipole moment.

Meanwhile, to attain desired luminescence property of a given π -electronic system, the quantum yield of fluorescence should be satisfactorily high; for this, it is favorable

to manifest high fluorescence (radiative) constant but low internal conversion and low intersystem crossing rate constant by:

$$\Phi_f = \frac{k_f}{(k_f + k_{IC} + k_{ISC})} = \frac{k_f}{(k_f + k_{nr})}$$

where, k_f is fluorescence rate constant, k_{IC} is rate constant of internal conversion, k_{ISC} is intersystem crossing rate, and k_{nr} is rate constant of non-radiative deactivation. In the case of molecular fluorescent materials, high k_f but low k_{nr} can be achieved by using rigid molecular structures with appropriate conjugation lengths. The significance of molecular design should thus be stressed out, not only high transition dipole but also less vibrational and rotational relaxation can be attained through molecular engineering strategies for high Φ_f .

When it comes to the supramolecular solid-state case, interesting features are observable, however become rather complex by the intermolecular factors.^[78-80] In a high concentration solution condition or in a self-assembled state, fluorophores may manifest transition dipole moments interaction between nearest molecules. The interaction results in excited energy splitting, which also refers to as Davydov splitting, see **Figure 1-17**. Based on the relative orientation (x-/y-slip) between the nearest dimer molecular pair, the phase of electronic transition greatly differs by constructive or destructive transition dipole moment coupling. As Kasha revealed from his earlier literatures, parallel molecular arrangement (small y-slip, $\alpha > 32^\circ$) exhibits net dipole moment value of zero (or small value) at the lower excited state; thus, the transition

probability to this state is small.^[81] Therefore the transition toward the higher excited state is favored, which shows net dipole of higher value; hence blue shifted absorption spectrum is envisioned in such H-type stacking arrangement (**Figure 1-18**). On the other hand, head-to-tail molecular arrangement with large y-slip ($\alpha < 32^\circ$) manifests the opposite tendency. In this type of stacking structure, so called J-type stacking, exhibits higher transition probability toward the lower excited state due to the non-zero net dipole condition of the state; however, the higher excited state transition is minimized by negligible net dipole (**Figure 1-18**). Such characteristic influences of dipole coupling also greatly affect emission characters.^[79] In a H-type aggregate state, radiative transition from the lowest excited state is rather forbidden, thus generally leads to low k_f . In comparison, J-type aggregation normally exhibits high k_f due to the dipole allowed condition for the lowest excited state. Moreover, the strong electronic coupling by substantial π -orbital overlap gives rise to excited state dimer (excimer) formation, typically in co-facial H-type stacked molecular arrangement; thus, emission spectrum shows bathochromic shift with increasing k_{nr} (**Figure 1-18**). In this regard, the photophysics can be greatly influenced by structural factors in supramolecular state.

Meanwhile, the supramolecular structure itself also highly affects the photophysical processes by influencing nuclei motions in the solid-state. In particular in case of fluorescent molecules with less rigidity, the radiative transition goes highly

restricted by vibrational and rotational energy relaxation. However, when such molecules are placed in rigid matrix or become molecular solids, the emission quantum yield can remarkably be enhanced by restricted nuclei motion; thus, highly luminescent in these condition.^[82,83] Cyanostilbene and silole based fluorescent molecules have been served as two representative materials showing high emission quantum yield exclusively in their solid-states. There is similarity between two different molecular systems; however, underlying emission enhancement mechanisms can easily be differentiated. The increased radiative transition of propeller-shaped silole based compounds are much focused on intramolecular factors by aggregation induced emission (AIE) mechanism;^[83] in contrast, the aggregation induced enhanced emission (AIEE) mechanism of the cyanostilbene derivative pay much attention on unique self-assembling features.^[82, 85-87] The cyano (-CN) substitution on vinylene bridge induces highly twisted molecular conformation by steric effects, which avoids planar conformation in the S_1 state and results in the low radiative transition probability. However, intermolecular interactions result in co-planarized molecular geometry in supramolecular state, thus leads to increment of k_f and favorable electronic interaction for highly luminescent feature. In this respect, the AIEE mechanism can be rationalized by considering the distinctive intramolecular, electronic, and excitonic parameters, all of which are highly relevant to the supramolecular factors.

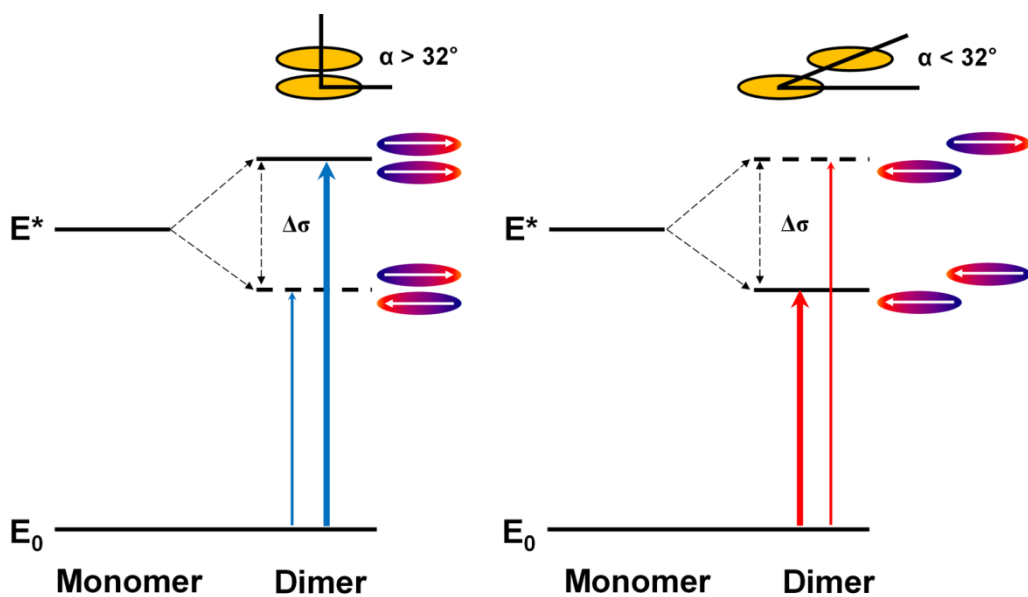


Figure 1-17. Schematic drawing of the Davydov splitting; indicating relationships between molecular arrangement and transition dipole moment coupling for defining favored optical transitions.

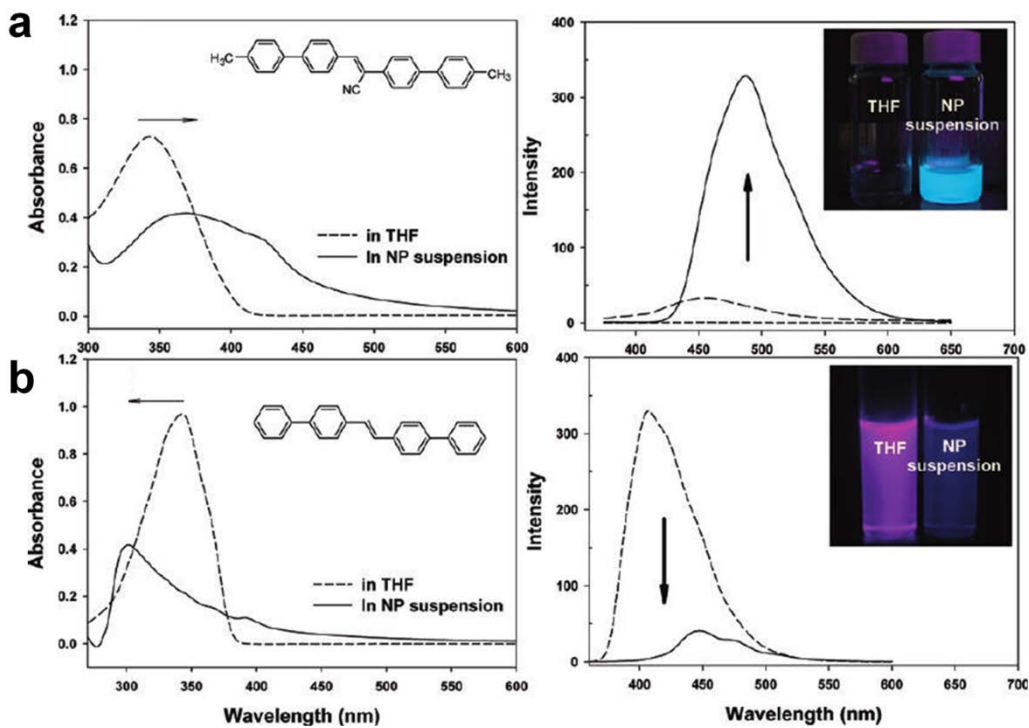


Figure 1-18. Absorption and photoluminescence spectra in solution (dotted line) and in solid-state (solid line) of representative (a) J-type and (b) H-type stacking molecules.^[82]

1.3.4. Photophysics in Charge-Transfer Complexes

Photophysical properties in D-A CT systems are somewhat complicated compared to those from single-component systems, by peculiar structure and electronic effects.^[78,88] The neutral CT complexes with large CT gap in general give rise to mixed stacked D-A arrangement showing distinctive absorption energy compared to those from individual constituents. The first singlet transition energy (S_1 or ${}^1CT^*$) in the visible region can empirically described by,

$$h\nu_{CT} = IP(D) - EA(A) - W$$

where, $h\nu_{CT}$ is CT absorption energy, $IP(D)$ is ionization potential of D, $EA(A)$ is electron affinity of A, and W is electrostatic stabilization factor in excited state. The equation gives linear relationship between $h\nu_{CT}$ vs. $IP(D) - EA(A)$; however, the W value is again a function of $IP(D) - EA(A)$ therefore precise picture of the relationship render parabolic dependence.

During absorption, the neutral character in ground state (typically, $\delta \leq 0.1$) however becomes highly ionic by charge-transfer, i.e., $[A, D] \rightarrow [A^-, D^+]$. The wave function of peculiar electronic situation therefore can be described as below,

$$\psi_N = a \psi(A, D) + b \psi(A^-, D^+)$$

$$\psi_V = a' \psi(A^-, D^+) - b' \psi(A, D)$$

where, ψ_N is wave function of the ground state, ψ_V is wave function of the excited

state. In the ground state (ψ_N), relationship $a \gg b$ can be envisioned by neutral character of the state; however, $a' \gg b'$ by ionic character in the excited state accompanied by substantial charge-transfer from D to A.

As discussed in the previous section 1.3.3., transition dipole moment (μ) describes the transition probability; thus is an important figure to analyze given transition. In fact, one can envisage that the transition dipole moment for CT transition might be high due to the substantial static dipole moment between D-A pair. However, in general, transition dipole moment (therefore, oscillator strength) of CT transition renders relatively low value, attributed from the limited orbital overlap integral between the ground and excited states. This in turn gives diminished radiative rate and high non-radiative rate; therefore, low fluorescence quantum yield in CT complexes are observed. Nevertheless, CT complexes have been regarded as an important class of emitter, due to the unique electronic features such as small ΔE_{ST} by small exchange integral which results in high availability of triplet manifolds e.g., phosphorescence, triplet-triplet annihilation, and thermally activated delayed fluorescence (TADF).^[89-91] Moreover, excited complex intermediates, i.e., exciplex, have manifested useful white-emission, or facilitated to design highly efficient OLEDs by strategic utilization of triplet manifolds (e.g. TADF, and phosphorescence).^[92-97]

In the recent years, few novel CT complexes featuring intriguing fluorescent characters have been reported, see **Figure 1-19**. Zhu et al. have carried out

experimental and theoretical works to establish structure – property correlation on CT exciton dynamics based on 1,2-bis(4-pyridyl)ethylene (Bpe as D) and 1,3,5-trifluoro-2,4,6-triiodobenzene (IFB as A) pair; as well as molecular pair of Bpe and 1,4-diiidotetrafluorobenzene (F₄DIB).^[98] Bpe-IFB exhibited segregated stacked with CT electronic states, however, Bpe-F₄DIB showed mixed stacked arrangement without CT characters. The former CT pair manifested relatively high quantum yield ($\Phi_F = 26.1\%$) in violet-blue emission range, 1D waveguide property, and semiconducting behavior *via* formation of CT electronic state with rather neutral character. On the contrary, the latter pair exhibited characteristic white-emission attributed to the innate luminescence natures of constituting molecules by non-CT feature but act as co-formers in respect to each other. They further made effort for scrutinizing CT emission feature using similar CT system, i.e., Bpe (as a D) and 1,2,4,5-tetracyanobenzene (TCNB, as an A).^[99] By strategic supramolecular engineering approach, unique 2D structure of the segregated stacked D-A complex could be established and exhibited blue CT fluorescence ($\Phi_F = 19\%$) with 2D optical waveguide property. Lee and coworkers, established intriguing route to design color tunable CT complexes, by CT doping and Förster resonance energy transfer (FRET) strategy.^[100,101] They successfully achieved 1D microtubular self-assembled structure by etching-assisted CT-induced assembly technique using blue emissive naphthalene-TCNB D-A pair ($\Phi_F = 17.5\%$); in addition, by substituting naphthalene to pyrene with varying doping ratio, the fluorescence color can effectively be modulated from blue-to-orange; thus white emission can also be achieved in a

doping ratio of 0.015%. Similar approach has been applied to (anthracene)_x(phenanthrene)_{1-x}(TCNB), and (carbazole)_x(fluorene)_{1-x}(TCNB) CT systems, exhibiting attractive emission alteration characters with relatively high quantum yield of ca. 27 – 40% depending on doping ratio. The intriguing exciton dynamics of fluorescence CT systems with versatile nanostructures indeed suggest next-generation photonics applications in addition to the peculiar charge-transporting natures.

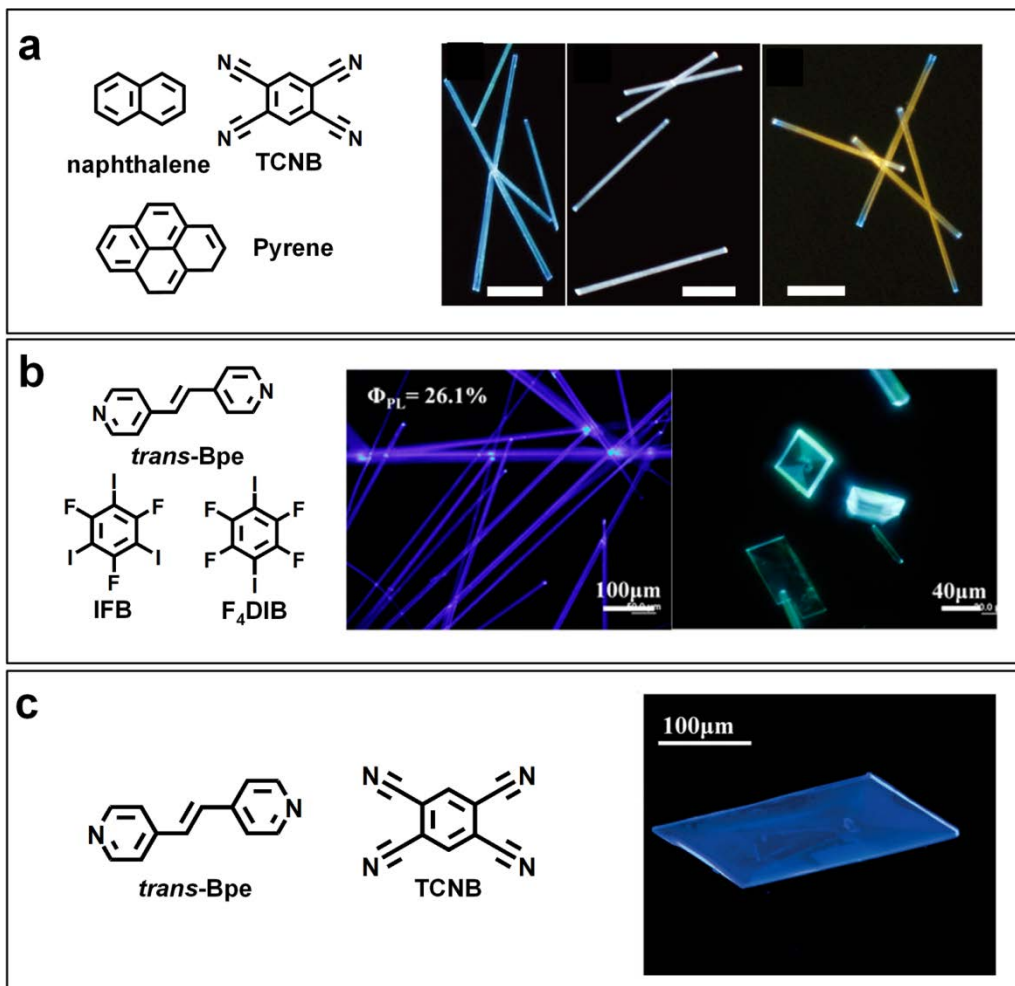


Figure 1-19. Examples of luminescent charge-transfer complex systems and their fluorescent microscope images. (a) (naphthalene) – (TCNB) with varying pyrene dopant concentrations;^[100] (b) (Bpe) – (IFB) charge-transfer complex (left image), and (Bpe) – (F₄DIB) multi-component cocrystal (right image);^[98] (c) (Bpe) – TCNQ charge-transfer complex.^[99]

1.3.5. Organic Light-Emitting Transistors

Notable charge-transport characters combined with highly luminescent natures in appropriately designed organic π -conjugated materials and their supramolecules are promising candidates for next-generation electroluminescent devices applications. Organic light-emitting diodes (OLEDs), multilayers structured devices typically comprised of hole-/electron transporting layers (HTL and ETL, respectively), emitting layer (EML), and cathode/anode electrodes, already have achieved great market success owing to the beneficial features such as high quantum efficiency, inherently thin device structure, and flexibility. Moreover, recent progresses in the concepts to utilize triplet manifolds by reverse intersystem crossing and exciplex phenomena open up new horizons to achieve high quantum efficiencies even exceeding theoretical limit.^[96,97,102]

In the meantime, studies on realization of electroluminescence (EL) under OFETs operations – the light-emitting OFETs (LE-OFETs) or organic light-emitting transistors (OLETs) have grasped particular attentions due to their advantageous features, i.e., simpler device structures by coupling EL and on/off switching functions of transistors.^[103] The working principle of LE-OFET is depicted in **Figure 1-20**. As depicted in **Figure 1-20a**, low V_G initially results in unipolar transport of counter charges (hole, for the n-channel enhancement mode), where the electron injection is

greatly limited by V_{th}^e . By increasing V_G , electron can be injected simultaneously with hole injection; thus leads to true ambipolar transport in an appropriate bias condition (**Figure 1-20b**). Finally, at a high V_G condition, the hole injection from a source electrode diminishes; thus, accumulated charge-carriers in the semiconductor channel exclusively became electrons (**Figure 1-20c**). As previous studies have presented, the highest value of external quantum efficiency (EQE) can be generated in true ambipolar regime, attributed to the separation of emitting zone from source/drain electrodes. Indeed, the exciton-metal interaction and electrode-induced photon losses significantly lower the EQE values of LE-OFET devices in unipolar regimes. Therefore, it is obvious that the device performances of ambipolar semiconductors shall outperform those from unipolar transporting materials by controlling emitting zone by varying V_G .

The first LE-OFET characteristics was observed using tetracene as an active channel material, due to the benchmark transport and EL characters found from this long-time studied organic semiconductor.^[104] Due to the p-channel unipolar character of tetracene, the light could be observed exclusively at the drain electrode (electron injecting electrode) however with low efficiency (1×10^{-5} photons per charge). Unipolar semiconductor active channel with doping concept have also been utilized to promote enhanced EL intensity. The device comprised of tetraphenylpyrene (TPPy) as charge-carrier transporting material and rubrene as dopant indeed effectively increased external quantum efficiency (EQE) by a factor of 10, compared to the undoped TPPy device.^[105] Meanwhile, LE-OFETs based on ambipolar transporting organic

semiconductors have been much extensively studied due to their innate benefit, i.e., bipolar carrier injection from source and drain electrodes. For instance, polyphenylene vinylene (PPV) based polymer (SuperYellow) with work function tuned source (Ag) and drain (Ca) electrodes exhibited maximum light intensity at a gate bias condition where electron current became greater than that from hole; as indicated by light-emitting zone analyses.^[106] The study on poly(2-methoxy-5-(3,7-dimethyloctoxy)-*p*-phenylene-vinylene) (OC1C10-PPV) based LE-OFETs was also conducted showing EQE of 0.35%.^[107] The literature provided precise elucidation of the bias effects for controlling the emissive region as aforementioned; which is the important features for realizing desired device efficiency. Besides, single-crystalline materials based on oligomeric semiconductors have also been utilized for LE-OFETs studies (e.g., thiophene/phenylene cooligomers (TPCOs), and distyrylbenzene (DSB) oligomers, doped single crystals), which facilitate to understand structure-property correlation as well as for realization of futuristic electrically excited lasers.^[108-110] For bipolar carrier injection, however, LE-OFETs devices in general adopt asymmetric source/drain electrodes which provide effective carrier injection by favorable energy matching between frontier molecular orbitals to work function of metal electrodes.

As an alternative way to fabricate LE-OFETs, hetero-structured devices (e.g., bulk heterojunctions, and layered structures) comprising p-/n-channel semiconductors have also been carried out. Rost et al. demonstrated coevaporated p-/n-channel heterojunction film containing α -quinoxithiophene (α -5T) as a hole-transport material

and *N,N'*-ditridecylperylene-3,4,9,10-tetracarboxylic diimide (P13) as an electron-transport material, showing smaller EL energy gap compared to frontier molecular orbital gap of constituting materials.^[111,112] Namdas et al. demonstrated bilayer structured device constructed with hole transporting polymer (poly(2,5-bis(3-tetradecylthiopen-2-yl)thieno[3,2-b]thiophene, PBTTT-C14) and emissive polymer (Super yellow).^[113] The device exhibited high brightness of 2500 cd/m², however with rather low EQE which is limited by tunneling injection of minor n-channel carriers (ca. 0.15%). Dinelli et al. reported LE-OFETs device based on p-/n-channel bilayer structure (p: α , ω -dihexyl-quaterthiophene, DH4T; n: P13), desired balanced ambipolar mobility were manifested for EL application (p-/n-channel μ of $\sim 10^{-2}$ cm² V⁻¹ s⁻¹).^[114] The effect of bilayer growth compatibility was remarked by in-depth correlation of device performance with uniform film continuity. Capelli et al., interestingly, have effectively surmounted typically low EQE value < 1% in LE-OFETs operation.^[115] Energetically aligned trilayer system comprised of HTL (dihexyl substituted quaterthiophene, DH-4T) / EML (tris(8-hydroxyquinolino)aluminium (Alq₃) : 4-(dicyanomethylene)-2-methyl-6-(p-dimethylaminostyryl)-4H-pyran DCM) / ETL (diperfluorohexyl substituted quaterthiophene, DFH-4T) successfully reduced exciton-charge quenching by introducing strategic emissive layer, which manifested EQE exceeding 5%. Besides, Kim et al. demonstrated LE-OFETs device using self-assembled p-/n-junction coaxial microcable comprising p-channel polymer (poly(3-hexylthiophene), P3HT) and n-channel supramolecule (1-cyano-trans-1,2-bis-(30,50-

bis-trifluoromethyl-biphenyl)ethylene, CN-TFMBE), which exhibited notable interfacial CT character and EL emission from efficient bipolar injection characteristics.^[116] In the meantime, LE-OFETs based on molecular p-/n-heterojunction i.e. CT complexes have not yet been reported, mainly due to the typical trivial PL efficiency by inefficient orbital overlap. However, highly balanced ambipolar transport in the mixed stack D-A arrangement by superexchange nature might promise EL emission, if the undesired low emission quantum yields are resolved.

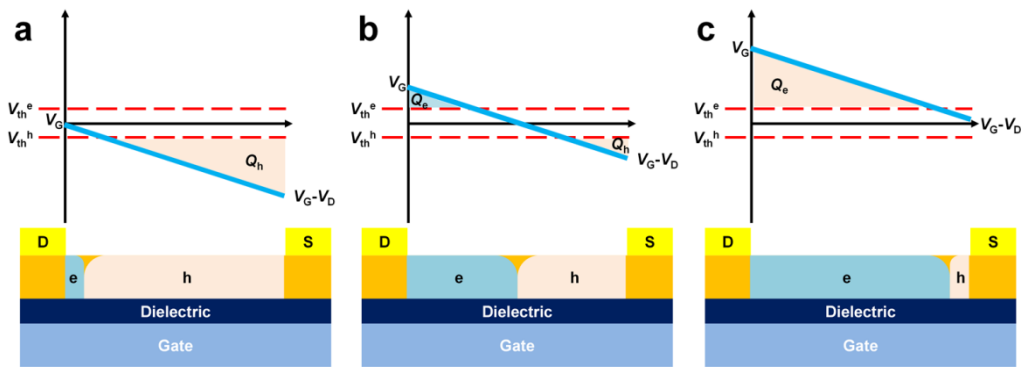


Figure 1-20. Plots of $V_G - V_{ch}$ vs. horizontal distance with varied V_G and fixed V_D and schematic illustration of hole and electron density of corresponding charge transport regime. (a) saturation regime for p-channel transport, (b) true ambipolar regime, and (c) saturation regime for n-channel transport.^[53]

1.4. Contents of Thesis

In this thesis, I will provide versatile route to design multi-functional supramolecules and charge-transfer (CT) complexes based on dicyanodistyrylbenzene (DCS) derivatives, rendering unique optoelectronic functions originated from strategic molecular/supramolecular design principles.

In *Chapter 2*, unique two-dimensionally (2D) self-assembling n-channel supramolecules will be presented for solution processable single-crystal organic field-effect transistors (SC-OFETs) applications. Highly balanced in-plane 2D intermolecular interaction network formation can be implemented by strategic introduction of supramolecular synthons (i.e., π - π interaction and -CN \cdots HC-), which simultaneously stabilized frontier molecular orbitals for efficient electron transport. Attributed to the attenuated out-of-plane intermolecular interaction of this DCS derivative, densely packed 2D layered structures can easily be exfoliated and transferred to substrates for few mono-layered 2D electronics applications.

In *Chapter 3*, design principle for achieving both ambipolar transport and highly luminescent CT emission will be introduced by establishing densely packed mixed stacked donor (D) – acceptor (A) CT complex. Strategic substituents patterns of the distyrylbenzene based D and dicyanodistyrylbenzene based A facilitate strong D-A assembly by adequate frontier molecular orbital offset as well as minimized molecular

structure mismatch (i.e., isometric D-A approach). The peculiar optoelectronic properties are not only originated from the molecular arrangement but also from characteristic electronic properties of the CT cocrystal, i.e., ambipolar transport *via* effective electronic coupling arose from superexchange nature, and bright CT emission *via* non-negligible oscillator strength induced from the role of high energy transition of $S_0 \rightarrow S_1$ (e.g., HOMO-1 \rightarrow LUMO).

In *Chapter 4*, a novel molecular/supramolecular designing approach will be introduced to realize electroluminescence of CT complex using an OFET configuration. Unprecedentedly high photoluminescence quantum yield (ca. 60%) is successfully attained by non-negligible oscillator strength by configuration interaction of the lowest singlet transition as well as desired tightly stacked molecular arrangement which greatly reduces exciton trap density. The dicyanodistyrylbenzene based D-A pair with isometric designs give rise to unique mixed stacked 2D co-assembly with 2:1 stoichiometry, which facilitate favorable ambipolar transport with highly balanced character. Combined highly CT fluorescence and ambipolar transporting natures indeed prove to render great possibilities of neutral mixed CT for next-generation organic lightings applications.

In *Chapter 5*, a stimuli-responsive high contrast fluorescence switching (i.e., red \leftrightarrow blue fluorescence) based on a 1:1 D-A CT complex will be reported, of which the emission modulation can be achieved by noteworthy reconfiguration behavior between

mixed D-A CT phase \leftrightarrow demixed D/A phase. A somewhat loosely packed molecular organization is obtained as a consequence of the noncentrosymmetric chemical structure of A, which gives rise to considerable free volume and weak intermolecular interactions for favorable stimuli responsive feature. Despite the loosen D-A arrangement, the CT complex manifests moderate fluorescence quantum yield; thus, suggesting a possibility of the mixed stacked CT for optical recording and sensors applications.

1.5. References

- [1] Lehn, J.-M. *Angew. Chem. Int. Ed. Engl.* **1988**, *27*, 89.
- [2] Desiraju, G. R. *Angew. Chem. Int. Ed.* **1995**, *34*, 2311.
- [3] Tang, C. W.; Van Slyke, S. A. *Appl. Phys. Lett.* **1987**, *51*, 913.
- [4] Siringhaus, H.; Brown, P. J.; Friend, R. H.; Nielsen, M. M.; Bechgaard, K.; Langeveld-Voss, B. M. W.; Spiering, A. J. H.; Janssen, R. A. J.; Meijer, E. W.; Herwig, P.; de Leeuw, D. M. *Nature* **1999**, *401*, 685.
- [5] Yu, G.; Gao, J.; Hummelen, J. C.; Wudl, F.; Heeger, A. J. *Science* **1995**, *270*, 1789.
- [6] Campbell, R. B.; Robertson, J. M.; Trotter, J. *Acta Crystal.* **1961**, *14*, 705.
- [7] Izawa, T.; Miyazaki, E.; Takimiya, K. *Adv. Mater.* **2008**, *20*, 3388.
- [8] Jurchescu, O. D.; Meetsma, A.; Palstra, T. T. M. *Acta Crystal.* **2006**, *B62*, 330.
- [9] Anthony, J. E.; Brooks, J. S.; Eaton, D. L.; Parkin, S. R. J. *Am. Chem. Soc.* **2001**, *123*, 9482.
- [10] Suzuki, T.; Kobayashi, M.; Gao, Y.; Fukai, Y.; Inoue, Y.; Sato, F.; Tokito, S. *J. Am. Chem. Soc.* **2004**, *126*, 8138.
- [11] Newman, C. R.; Frisbie, C. D.; da Silva Filho, D. A.; Brédas, J.-L.; Ewbank, P. C.; Mann, K. R. *Chem. Mater.* **2004**, *16*, 4436.
- [12] Laquindanum, J. G.; Katz, H. e.; Dodabalapur, A.; Lovinger, A. J. *J. Am. Chem. Soc.* **1996**, *118*, 11331.

- [13] Ostrick, J. R.; Dodabalapur, A.; Torsi, L.; Lovinger, A. J.; Kwock, E. W.; Miller, T. M.; Galvin, M.; Berggren, M.; Katz, H. E. *J. Appl. Phys.* **1997**, *81*, 6804.
- [14] An, B.-K.; Gihm, S. H.; Chung, J. W.; Park, C. R.; Kwon, S.-K.; Park, S. Y. *J. Am. Chem. Soc.* **2009**, *131*, 3950.
- [15] Gsänger, M.; Oh, J. H.; Könemann, M.; Höffken, H. W.; Krause, A.-M.; Bao, Z.; Würthner, F. *Angew. Chem. Int. Ed.* **2010**, *49*, 740.
- [16] Ajayaghosh, A.; George, S. J. *J. Am. Chem. Soc.* **2001**, *123*, 5148.
- [17] Babu, S. S.; Praveen, V. K.; Ajayaghosh, A. *Chem. Rev.* **2014**, *114*, 1973.
- [18] Bolton, O.; Lee, K.; Kim, H.-J.; Lin, K. Y.; Kim, J. *Nat. Chem.* **2011**, *3*, 205.
- [19] Yamamoto, Y.; Fukushima, T.; Suna, Y.; Ishii, N.; Saeki, A.; Seki, S.; Tagawa, S.; Taniguchi, M.; Kawai, T.; Aida, T. *Science* **2006**, *314*, 1761.
- [20] Yamamoto, Y.; Zhang, G.; Jin, W.; Fukushima, T.; Ishii, N.; Saeki, A.; Seki, S.; Tagawa, S.; Minari, T.; Tsukagoshi, K.; Aida, T. *Proc. Nat. Acad. Sci. USA* **2009**, *106*, 21051.
- [21] Zhang, W.; Jin, W.; Fukushima, T.; Saeki, A.; Aida, T. *Science* **2011**, *334*, 340.
- [22] Mulliken, R. S.; Person, W. B. *Annu. Rev. Phys. Chem.*, **1962**, *13*, 107.
- [23] Benesi, H. A.; Hildebrand, J. H. *J. Am. Chem. Soc.* **1948**, *70*, 2832.
- [24] Benesi, H. A.; Hildebrand, J. H. *J. Am. Chem. Soc.* **1949**, *71*, 2703.
- [25] Akamatu, H.; Inokuchi, H.; Matsunaga, Y. *Nature* **1954**, *173*, 168.
- [26] Ferraris, J.; Cowan, D. O.; Walatka, V., Jr.; Perlstein, J. H. *J. Am. Chem. Soc.* **1973**, *95*.

- [27] Jérôme, D.; Mazaud, A.; Ribault, M.; Bechgaard, K. *J. Phys. Lett.* **1980**, *41*, L95.
- [28] Jérôme, D. *Chem. Rev.* **2004**, *104*, 5565.
- [29] Miller, J. S.; Calabrese, J. C.; Rommelmann, H.; Chittipeddi, S. R.; Zhang, J. H.; Reiff, W. M.; Epstein, A. J. *J. Am. Chem. Soc.* **1987**, *109*, 769.
- [30] Tokura, Y.; Koshihara, S.; Iwasa, Y.; Okamoto, H.; Komatsu, T.; Koda, T.; Iwasawa, N.; Saito, G. *Phys. Rev. Lett.* **1989**, *63*, 2405.
- [31] Tayi, A. S.; Shveyd, A. K.; Sue, A. C.-H.; Szarko, J. M.; Rolczynski, B. S.; Cao, D.; Kennedy, T. J.; Sarjeant, A. A.; Stern, C. L.; Paxton, W. F.; Wu, W.; Dey, S. K.; Fahrenbach, A. C.; Guest, J. R.; Mohseni, H.; Chen, L. X.; Wang, K. L.; Stoddart, J. F.; Stupp, S. I. *Nature* **2012**, *488*, 485.
- [32] Batail, P. *Chem. Rev.* **2004**, *104*, 4887.
- [33] Schwoerer, M.; Wolf, H. C. *Organic Molecular Solids*; Wiley-VCH: Weinheim, Germany, 2007.
- [34] Saito, G.; Murata, T. *Phil. Trans. R. Soc. A* **2008**, *366*, 139.
- [35] Mori, T. *Chem. Rev.* **2004**, *104*, 4947.
- [36] Hasegawa, T.; Mattenberger, K.; Takeya, J.; Batlogg, B. *Phys. Rev. B* **2004**, *69*, 245115.
- [37] Driscoll, T.; Kim, H.-T.; Chae, B.-G.; Di Ventra, M.; Basov, D. N. *Appl. Phys. Lett.* **2009**, *95*, 043503.
- [38] Liu, K.; Cheng, C.; Cheng, Z.; Wang, K.; Ramesh, R.; Wu, J. *Nano Lett.* **2012**, *12*, 6302.

- [39] Epstein, A. J.; Etemad, S.; Garito, A. F.; Heeger, A. J. *Phys. Rev. B* **1972**, *5*, 952.
- [40] Zhang, J.; Geng, H.; Virk, T. S.; Zhao, Y.; Tan, J.; Di, C.-a.; Xu, W.; Singh, K.; Hu, W.; Shuai, Z.; Liu, Y.; Zhu, D. *Adv. Mater.* **2012**, *24*, 2603.
- [41] J.-Y. Wang, J. Yan, L. Ding, Y. Ma, J. Pei, *Adv. Funct. Mater.* **2009**, *19*, 1746.
- [42] Y. L. Lei, L. S. Liao, S. T. Lee, *J. Am. Chem. Soc.* **2013**, *135*, 3744.
- [43] Yan, D.; Evans, D. G. *Mater. Horiz.* **2014**, *1*, 46.
- [44] Das, A.; Ghosh, S. *Angew. Chem. Int. Ed.* **2014**, *53*, 2038.
- [45] Rao, K. V.; George, S. J. *Chem.-Eur. J.* **2012**, *18*, 14286.
- [46] Yu, W.; Wang, X.-Y.; Li, J.; Li, Z.-T.; Yan, Y.-K.; Wang, W.; Pei, J. *Chem. Commun.* **2013**, *49*, 54.
- [47] Percec, V.; Glodde, M.; Bera, T. K.; Miura, Y.; Shiyanovskaya, I.; Singer, K. D.; Balagurusamy, V. S. K.; Heiney, P. A.; Schnell, I.; Rapp, A.; Spiess, H.-W.; Hudson, S. D.; Duan, H. *Nature* **2002**, *419*, 384.
- [48] Schmidt-Mende, L.; Fechtenkötter, A.; Müllen, K.; Moons, E.; Friend, R. H.; MacKenzie, J. D. *Science* **2001**, *293*, 1119.
- [49] Chiang, C. K.; Fincher, C. R.; Park, Y. W.; Heeger, A. J.; Shirakawa, H.; Louis, E. J.; Gau, S. C.; MacDiarmid, A. G. *Phys. Rev. Lett.* **1977**, *39*, 1098.
- [50] Coropceanu, V.; Cornil, J.; da Silva Filho, D. A.; Olivier, Y.; Silbey, R.; Brédas, J.-L. *Chem. Rev.* **2007**, *107*, 926.
- [51] Wang, C.; Dong, H.; Hu, W.; Liu, Y.; Zhu, D. *Chem. Rev.* **2012**, *112*, 2208.
- [52] Newman, C. R.; Frisbie, C. D.; da Silva Filho, D. A.; Brédas, J.-L., Ewbank, P. C.;

- Mann, K. R. *Chem. Mater.* **2004**, *16*, 4436.
- [53] Kang, M. S.; Frisbie, C. D. *ChemPhysChem* **2013**, *14*, 1547.
- [54] Briseno, A. L.; Mannsfeld, S. C. B.; Ling, M. M.; Liu, S.; Tseng, R. J.; Reese, C.; Roberts, M. E.; Yang, Y.; Wudl, F.; Bao, Z. *Nature* **2006**, *444*, 913.
- [55] Li, R.; Hu, W.; Liu, Y.; Zhu, D. *Acc. Chem. Res.* **2010**, *43*, 529.
- [56] Sundar, V. C.; Zaumseil, J.; Podzorov, V.; Menard, E.; Willett, R. L.; Someya, T.; Gershenson, M. E.; Rogers, J. A. *Science* **2004**, *303*, 1644.
- [57] Yamagishi, M.; Takeya, J.; Tominari, Y.; Nakazawa, Y.; Kuroda, T.; Ikehata, S.; Uno, M.; Nishikawa, T.; Kawase, T. *Appl. Phys. Lett.* **2007**, *90*, 182117.
- [58] Minemawari, H.; Yamada, T.; Matsui, H.; Tsutsumi, J. Haas, S.; Chiba, R.; Kumai, R.; Hasegawa, T. *Nature* **2011**, *475*, 364.
- [59] Yuan, Y.; Giri, G.; Ayzner, A. L.; Zoombelt, A. P.; Mannsfeld, S. C. B.; Chen, J.; Nordlund, D.; Toney, M. F.; Huang, J.; Bao, Z. *Nat. Commun.* **2014**, *5*, 3005.
- [60] Takimiya, K.; Shinamura, S.; Osaka, I.; Miyazaki, E. *Adv. Mater.* **2011**, *23*, 4347.
- [61] Takimiya, K.; Osaka, I.; Mori, T.; Nakano, M. *Acc. Chem. Res.* **2014**, *47*, 1493.
- [62] Mori, T. *Chem. Lett.* **2011**, *40*, 428.
- [63] Brooks, J. S. *Adv. Mater. Opt. Electron.* **1998**, *8*, 269.
- [64] Sakai, M.; Sakuma, H.; Ito, Y.; Saito, A.; Nakamura, M.; Kudo, K. *Phys. Rev. B* **2007**, *76*, 045111.
- [65] Mori, T.; Inokuchi, H. *Solid State Commun.* **1986**, *59*, 355.
- [66] Kawasugi, Y.; Yamamoto, H. M.; Tajima, N.; Fukunaga, T.; Tsukagoshi, K.; Kato,

- R. Phys. Rev. Lett.* **2009**, *103*, 116801.
- [67] Kawasugi, Y.; Yamamoto, H. M.; Tajima, N.; Fukunaga, T.; Tsukagoshi, K.; Kato, R. *Phys. Rev. B* **2011**, *84*, 125129.
- [68] Kimata, M.; Ishihara, T.; Tajima, H. *J. Phys. Soc. Jpn.* **2012**, *81*, 073704.
- [69] Hasegawa, T.; Mattenberger, K.; Takeya, J.; Batlogg, B. *Phys. Rev. B* **2004**, *69*, 245115.
- [70] Zhu, L.; Yi, Y.; Li, Y.; Kim, E.-G.; Coropceanu, V.; Brédas, J.-L. *J. Am. Chem. Soc.* **2012**, *134*, 2340.
- [71] Geng, H.; Zheng, X.; Shuai, Z.; Zhu, L.; Yi, Y. *Adv. Mater.* **2015**, *27*, 1443.
- [72] Sagade, A. A.; Rao, K. V.; George, S. J.; Datta, A.; Kulkarni, G. U. *Chem. Comm.* **2013**, *49*, 5847.
- [73] Zhang, J.; Tan, J.; Ma, Z.; Xu, W.; Zhao, G.; Geng, H.; Di, C.; Hu, W.; Shuai, Z.; Singh, K.; Zhu, D. *J. Am. Chem. Soc.* **2013**, *135*, 558.
- [74] Qin, Y.; Zhang, J.; Zheng, X.; Geng, H.; Zhao, G.; Xu, W.; Hu, W.; Shuai, Z.; Zhu, D. *Adv. Mater.* **2014**, *26*, 4093.
- [75] Park, S. K.; Varghese, S.; Kim, J. H.; Yoon, S.-J.; Kwon, O. K.; An, B.-K.; Gierschner, J.; Park, S. Y. *J. Am. Chem. Soc.* **2013**, *135*, 4757.
- [76] Wykes, M.; Park, S. K.; Bhattacharyya, S.; Varghese, S.; Kwon, J. E.; Whang, D. R.; Cho, I.; Wannemacher, R.; Lüer, L.; Park, S. Y.; Gierschner, J. *J. Phys. Chem. Lett.* **2015**, *6*, 3682.
- [77] Vermeulen, D.; Zhu, L. Y.; Goetz, K. P.; Hu, P.; Jiang, H.; Day, C. S.; Jurchescu, O.

- D.; Coropceanu, V.; Kloc, C.; McNeil, L. E. *J. Phys. Chem. C* **2014**, *118*, 24688.
- [78] Turro, N. J.; Ramamurthy, V.; Scaiano, J. C. *Principles of Molecular Photochemistry: An Introduction*; University Science Books: Sausalito, California, 2009.
- [79] Gierschner, J.; Park, S. Y. *J. Mater. Chem. C* **2013**, *1*, 5818.
- [80] Davydov, A. S. *Theory of Molecular Excitons*; Plenum: New York, 1971.
- [81] Kasha, M.; Rawls, H. R.; Ashraf El-Bayoumi, M. *Pure Appl. Chem.*, **1965**, *11*, 371.
- [82] An, B.-K.; Gierschner, J.; Park, S. Y. *Acc. Chem. Res.* **2012**, *45*, 544.
- [83] Mei, J.; Hong, Y.; Lam, J. W. Y.; Qin, A.; Tang, Y.; Tang, B. Z. *Adv. Mater.* **2014**, *26*, 5429.
- [84] Luo, J.; Xie, Z.; Lam, J. W. Y.; Cheng, L.; Chen, H.; Qiu, C.; Kwok, H. S.; Zhan, X.; Liu, Y.; Zhu, D.; Tang, B. Z. *Chem. Commun.* **2001**, *18*, 1740.
- [85] An, B.-K.; Kwon, S.-K.; Jung, S.-D.; Park, S. Y. *J. Am. Chem. Soc.* **2002**, *124*, 14410.
- [86] An, B.-K.; Lee, D.-S.; Lee, J.-S.; Park, Y.-S.; Song, H.-S.; Park, S. Y. *J. Am. Chem. Soc.* **2004**, *126*, 10232.
- [87] An, B.-K.; Gihm, S. H.; Chung, J. W.; Park, C. R.; Kwon, S.-K.; Park, S. Y. *J. Am. Chem. Soc.* **2009**, *131*, 3950.
- [88] Jones, II G. In *Photoinduced Electron Transfer Part A*, Fox, M. A.; Chanon, M., Eds.; Elsevier: Amsterdam, 1988; pp 245-268.
- [89] Iwata, S.; Tanaka, J. Nagakura, S.; *J. Chem. Phys.* **1967**, *47*, 2203.

- [90] Kozankiewicz, B.; Prochorow, J. *Chem. Phys. Lett.* **1979**, *61*, 347.
- [91] Kozankiewicz, B.; Prochorow, J. *Chem. Phys.* **1989**, *135*, 307.
- [92] Tamoto, N.; Adachi, C.; Nagai, K. *Chem. Mater.* **1997**, *9*, 1077.
- [93] Kim, J. H.; An, B.-K.; Yoon, S.-J.; Park, S. K. Kwon, J. E.; Lim, C.-K.; Park, S. Y. *Adv. Funct. Mater.* **2014**, *24*, 2746.
- [94] Goushi, K.; Yoshida, K.; Sato, K.; Adachi, C. *Nat. Photon.* **2012**, *6*, 253.
- [95] Goushi, K.; Adachi, C. *Appl. Phys. Lett.* **2012**, *101*, 023306.
- [96] Kim, K.-H.; Lee, S.; Moon, C.-K.; Kim, S.-Y.; Park, Y.-S.; Lee, J.-H.; Lee, J. W.; Huh, J.; You, Y.; Kim, J.-J. *Nat. Commun.* **2014**, *5*, 4769.
- [97] Park, Y.-S.; Lee, S.; Kim, K.-H.; Kim, S.-Y.; Lee, J.-H.; Kim, J.-J. *Adv. Funct. Mater.* **2013**, *23*, 4914.
- [98] Zhu, W.; Zheng, R.; Zhen, Y.; Yu, Z.; Dong, H.; Fu, H.; Shi, Q.; Hu, W. *J. Am. Chem. Soc.* **2015**, *137*, 11038.
- [99] Zhu, W.; Zheng, R.; Fu, X.; Fu, H.; Shi, Q.; Zhen, Y.; Dong, H.; Hu, W. *Angew. Chem. Int. Ed.* **2015**, *54*, 6785.
- [100] Lei, Y.-L.; Jin, Y.; Zhou, D.-Y.; Gu, W.; Shi, X.-B.; Liao, L.-S.; Lee, S.-T. *Adv. Mater.* **2012**, *24*, 5345.
- [101] Sun, Y.-Q.; Lei, Y.-L.; Sun, X.-H.; Lee, S.-T.; Liao, L.-S. *Chem. Mater.* **2015**, *27*, 1157.
- [102] Uoyama, H. Goushi, K.; Shizu, K. Nomura, H.; Adachi, C. *Nature* **2012**, *492*, 234.

- [103] Cicoira, F.; Santato, C. *Adv. Funct. Mater.* **2007**, *17*, 3421.
- [104] Hepp, A.; Heil, H.; Weise, W.; Ahles, M.; Schmechel, R.; von Seggern, H. *Phys. Rev. Lett.* **2003**, *91*, 157 406.
- [105] Oyamada, T.; Uchiuzou, H.; Akiyama, S.; Oku, Y.; Shimoji, N.; Matsushige, K.; Sasabe, H.; Adachi, C. *J. Appl. Phys.* **2005**, *98*, 074 506.
- [106] Swensen, J. S.; Soci, C.; Heeger, A. J. *Appl. Phys. Lett.* **2005**, *87*, 253511.
- [107] Zaumseil, Z.; Friend, R. H.; Sirringhaus, H. *Nat. Mater.* **2006**, *5*, 69.
- [108] Hotta, S.; Yamao, T.; Bisri, S. Z.; Takenobu, T.; Iwasa, Y. *J. Mater. Chem. C* **2014**, *2*, 965.
- [109] Nakanotani, H.; Kabe, R.; Yahiro, M.; Takenobu, T.; Iwasa, Y.; Adachi, C. *Appl. Phys. Exp.* **2008**, *1*, 091801.
- [110] Nakanotani, H.; Saito, M.; Nakamura, H.; Adachi, C. *Adv. Funct. Mater.* **2010**, *20*, 1610.
- [111] Rost, C.; Karg, S.; Riess, W.; Loi, M. A.; Murgia, M.; Muccini, M. *Appl. Phys. Lett.* **2004**, *85*, 1613.
- [112] Loi, M. A.; Rost-Bietsch, C.; Murgia, M.; Karg, S.; Riess, W.; Muccini, M. *Adv. Funct. Mater.* **2006**, *16*, 41.
- [113] Namdas, E. B.; Ledochowitsch, P.; Yuen, J. D.; Moses, D.; Heeger, A. J. *Appl. Phys. Lett.* **2008**, *92*, 183304.
- [114] Dinelli, F.; Capelli, R.; Loi, M. A.; Murgia, M.; Muccini, M.; Facchetti, A.; Marks, T. J. *Adv. Mater.* **2006**, *18*, 1416.

[115] Capelli, R.; Toffanin, S.; Generali, G.; Usta, H.; Facchetti, A.; Muccini, M. *Nat. Mater.* **2010**, *9*, 496.

[116] Kim, J. H.; Watanabe, A.; Chung, J. W.; Jung, Y.; An, B.-K.; Tada, H.; Park, S. Y. *J. Mater. Chem.* **2010**, *20*, 1062.

Chapter 2.

High-Performance *n*-Type Organic Transistor with a Solution-Processed and Exfoliation-Transferred Two-Dimensional Crystalline Layered Film

2.1. Introduction

In recent years, single-crystalline organic semiconductors have been intensively studied as a promising alternative to amorphous silicon-based materials in a wide range of electronic applications, especially organic field-effect transistors (OFETs).^[1] Single-crystalline organic semiconductors are particularly suited to OFETs because of characteristics such as their high carrier mobility, which derives from the lack of grain boundaries and the minimal number of charge trap sites, and their merits in terms of ease of processing and deposition on flexible substrates. In addition, the solution-processed self-assembly of organic semiconductors offers opportunities for the low-cost and large-area processing of next-generation electronics. Simple solution-processed single-crystalline OFETs (SC-OFETs) have therefore attracted much interest;^[2] to date, a variety of high-performance *p*-type SC-OFETs fabricated *via* various solution processes have been successfully demonstrated, and some of them have shown performances far superior to that of amorphous silicon.^[3]

In contrast with solution-processed *p*-type SC-OFETs, however, it remains a

challenge to fabricate solution-processed *n*-type SC-OFETs, because the building blocks for high-performance *n*-type SC-OFETs inherently have much more complicated molecular design prerequisites; specifically, they should show not only dense molecular packing and good solubility, but also high electron affinity (or low lowest unoccupied molecular orbitals (LUMO)) for an efficient electron injection from electrodes. In particular, the electron-withdrawing groups essential for the lowering of the LUMO level in *n*-type building blocks may destroy the highly crystalline structure or decrease the degree of molecular ordering, owing to their bulkiness and the presence of electrostatic forces. As a result, only a limited number of *n*-type π -conjugated systems have been introduced so far; these include perylenediimide,^[4] naphthalenediimide,^[5] and oligothiophene.^[6] Very recently, π -conjugated dicyanodistyrylbenzene (DCS)-type derivatives with electron-withdrawing trifluoromethyl ($-\text{CF}_3$) units have also proven their promising application potential towards high-performance *n*-type OFETs, due to its unique structural features.^[7-9] The ‘twist elasticity’ behavior of the DCS backbone, which exhibits large torsional changes in the π -conjugated backbone from the isolated solution state to the aggregated solid state, played an important role in achieving a coplanar structure, leading to close π - π contacts in the self-assembled condensed state.^[10] In addition, the electron-withdrawing $-\text{CN}$ and $-\text{CF}_3$ groups not only decreased the LUMO to a suitable level, but also stabilized the laterally adjacent molecules by building up specific noncovalent intermolecular interactions, which led to tight and dense molecular packing.^[11]

In the course of the continuous systematic syntheses of the DCS- found that one of our newly synthesized DCS derivatives, (2Z,2'Z)-3,3'-(1,4-phenylene)bis(2-(3,5-bis(trifluoromethyl)phenyl)acrylonitrile) (CN-TFPA) (**Scheme 2-1**), possessed a strong tendency to form well-ordered two-dimensional (2D) crystals in large areas directly on the substrate, *via* a simple solution-processed self-assembly process. In this work, I report that the 2D crystalline layer structure of CN-TFPA, which is conceived as a new, advantageous feature of the DCS π -conjugated system to build up high *n*-type conducting channels, can serve as an effective scaffold for the fabrication of solution-processed, high-performance, ultra-thin *n*-type SC-OFETs; this is due to its dense molecular packing, low LUMO levels, and the fact that it can be easily exfoliated to give thin-layered molecular assembly sheets.

2.2. Experimental

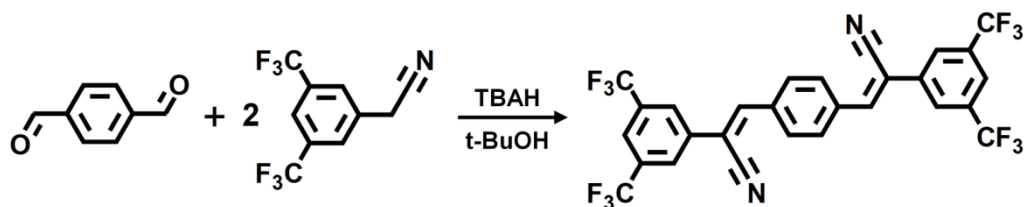
Synthesis (2Z,2'Z)-3,3'-(1,4-phenylene)bis(2-(3,5-bis(trifluoromethyl)phenyl)acrylonitrile) (CN-TFPA) was synthesized *via* Knoevenagel condensation between 2-(3,5-bis(trifluoromethyl)phenyl) acetonitrile and terephthalaldehyde, as shown in **Scheme 2-1**. All chemicals were purchased commercially and used without further purification. Terephthalaldehyde (0.8 g) and 2-(3,5-bis(trifluoromethyl)phenyl) acetonitrile (3.0 g) were dissolved in 50 ml of *t*-butyl alcohol. A 0.84 ml aliquot of

tetrabutylammonium hydroxide was slowly dropped into the solution, using a reaction temperature of 50° and a reaction time of 2 hours. The precipitated product, (2Z,2'Z)-3,3'-(1,4-phenylene)bis(2-(3,5-bis(trifluoromethyl)phenyl)acrylonitrile), was then filtered and purified by flash column chromatography with dichloromethane. For further purification, the product was recrystallized in a dichloromethane/methanol solution. Finally, sublimation purification was conducted under high vacuum (below 1×10^{-6} Torr), and a bright greenish-yellow powder was obtained as the product. The chemical structure of CN-TFPA was confirmed using ^1H NMR, ^{13}C NMR, elemental analysis (EA), and mass spectroscopy (*vide infra*).

^1H NMR (300 MHz, CDCl_3) δ [ppm]: 8.13 (s, 4H, Ar-H), 8.10 (s, 4H, Ar-H), 7.95 (s, 2H, Ar-H), 7.69 (s, 2H, vinyl-H). ^{13}C NMR (500 MHz, CDCl_3) δ [ppm]: 143.70, 136.55, 135.58, 133.60, 133.33, 133.06, 132.79, 130.55, 126.42, 124.20, 123.46, 122.02, 116.81, 111.23. MS (FAB) (m/z): Calculated for $\text{C}_{28}\text{H}_{12}\text{F}_{12}\text{N}_2$: 604.08, Found: 604.08. Anal. Calculated for $\text{C}_{28}\text{H}_{12}\text{F}_{12}\text{N}_2$: C, 55.64; H, 2.00; F, 37.72; N, 4.63. Found: C, 55.71; H, 1.98; N, 4.63.

Characterization ^1H NMR was recorded using a Bruker, Avance-300 (300 MHz) instrument, in a CDCl_3 solution. ^{13}C NMR was recorded using a Bruker, Avance-500 (500 MHz) instrument, in a CDCl_3 solution. Elemental analysis was conducted on CN-TFPA using a CE Instruments, EA1110 elemental analyzer. The mass spectrum of CN-TFPA was measured using a JEOL, JMS-600W mass spectrometer. Out-of-plane X-ray

diffraction measurements were performed using a D8-Advance X-ray diffractometer (Bruker Miller Co., Germany), and the operating conditions were a step size of 0.02, a scan rate of 3 degree/min, a 40 kV generator voltage, a 40 mA tube current, and room temperature (Cu std target $\lambda = 1.5418 \text{ \AA}$). AFM was performed using a PSIA instrument XE-150 and a Bruker instrument multimode with a NanoScope V controller. AFM topographic and phase images were recorded simultaneously in either contact or non-contact mode. UV-visible absorption spectra were recorded on a Shimadzu, UV-1650 PC spectrometer. The PL spectra of each solid-state phase were measured using a Varian, Cary Eclipse, fluorescence spectrophotometer. Differential scanning calorimetry (DSC) was recorded using a Perkin Elmer DSC7. The I-V characteristics of all of the OFETs were measured in a nitrogen-filled glove box, using a Keithley 4200 SCS instrument connected to a probe station.



Scheme 2-1. Synthetic Procedure to Obtain CN-TFPA

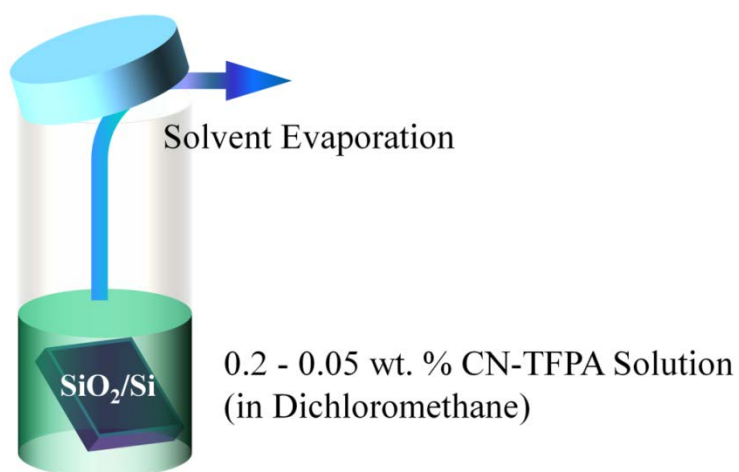


Figure 2-1. Schematic illustration of the solvent evaporation crystal growth technique.

Sample Preparation The nanoparticle suspension samples were prepared by typical simple precipitation method employing tetrahydrofurane and distilled water as solvent media. The CN-TFPA was dissolved in tetrahydrofurane with a concentration of $5 \times 10^{-3} \text{ mol L}^{-1}$. Then distilled water was slowly dropwised in various volume fractions with total concentration of $5 \times 10^{-6} \text{ mol L}^{-1}$. The suspensions were left for at least 2 hours before absorption spectra measurements. The bulk single-crystals of CN-TFPA were obtained *via* solvent diffusion crystal growth method using ethyl acetate / methanol.

Device Fabrication To prepare the substrates, the substrates were rinsed acetone and isopropyl alcohol for 10 minutes under ultra-sonication. After rinsing, 10 minutes of UV (360 nm) O^3 treatment was applied.

For simple solution processable single crystalline field-effect transistor fabrication, I employed the solvent evaporation crystal growth technique. an SiO_2/Si wafer was leand on the inner wall of a 20 ml vial containing a 0.05 wt% CN-TFPA solution (in dichloromethane), under ambient conditions, as depicted in **Figure 2-1**. CN-TFPA single crystal films were spontaneously grown (directly and slowly) on the substrates, which resulted in firm contact between substrates and the crystal films.^[12] The resulting crystals were found to have two different surface-induced solid-state packing structures (**G**-phase and **B**-phase, *vide infra*). After crystal formation, the substrates were annealed at 50°C for 1 hour, to eliminate any residual solvent. 50 nm-thick source-

drain Au electrodes were thermally deposited directly onto the crystalline layers through the metal mask, to fabricate top-contact SC-OFETs (the deposition rate was 0.1~0.2 k Å/s).

For thermally evaporated vacuum deposited poly-crystalline FETs fabrication, octadecyltrichlorosilane (ODTS) layer was introduced for reduced charge trap sites as well as for domain enlargement. ODTS was treated in vapor phase in vacuum oven, then the substrates were brought into nitrogen filled glove box. 30 nm thick CN-TFPA active layers were thermally deposited with deposition rate of 0.1–0.2 Å s⁻¹ and different substrate temperatures (T_{SUB}) (RT, 50°C and 70°C), under a vacuum of 7×10^{-7} Torr.

To fabricate the transfer-printed thin-crystal OFETs *via* mechanical cleavage method, mother crystals of 2D crystalline layers for the **G/B**-phase were prepared, using the solvent evaporation crystal growth technique. Scotch tape (3M) was attached to the top of the 2D crystalline layers, and pressed gently using fingers. By detaching the Scotch tape, exfoliated, flaky, thin crystals from the mother **G/B**-phase crystals could be obtained. Finally, I pressed the Scotch tape with the thin crystals onto the other SiO₂/Si substrate, so that the thin crystals could be transferred by detaching the Scotch tape. All of these procedures were carried out under ambient conditions. Finally, the samples were taken into the nitrogen-filled glove box, and thermally evaporated the Au electrodes, as presented in the fabrication of SC-OFETs section.

2.3. Results and Discussion

2.3.1. Self-Assembly and Solid-State Structure of CN-TFPA. Upon slow solvent evaporation, CN-TFPA molecules in a 0.20 wt.% 1,2-dichloroethane solution readily self-assembled into a large, green fluorescent single crystal with terraced surfaces (**Figure 2-2a**). The mono-layered step-terrace morphology was observed using atomic force microscopy (AFM), and was found to have a step size of approximately 1.4 nm, as shown in **Figure 2-2b**. The crystal films showed strongly anisotropic characteristics, as indicated by the uniform extinction of the reflected light intensity when the crystal films were rotated $\pm 45^\circ$ to the crossed polarizers (**Figure 2-2a**, inset).

To elucidate the 2D terrace structure of the CN-TFPA molecules in the single-crystal state, X-ray diffraction (XRD) analysis was performed on a single-crystal grown *via* solvent-diffusion crystal growth method. The molecular conformation and stacking structure of CN-TFPA are depicted in **Figure 2-2c, d**. It was clearly seen that the CN-TFPA had a quasi-planar molecular conformation in the condensed crystal state, although the twisted structure was more favored in the isolated state (see also **Figure 2-3**), owing to its unique ‘twist elasticity’ behavior. The quasi-planar CN-TFPA molecules bearing abundant electron-deficient groups were responsible for the strong π - π stacking interactions and the close interlayer distance of 3.09 Å along the *b*

direction.^[13] In addition, the continuously aligned H-bonding between the N of the cyano group and the two HC– of the laterally adjacent phenyl groups along direction *c* (8 different –N···HC– interactions (2.65, 2.72 Å) per molecule) (**Figure 2-2d**) played an essential role in producing the 2D crystal growth. The CN-TFPA molecules formed a layer-by-layer lamellar structure that was created *via* H-bonding between the F of the –CF₃ groups and the HC– of the adjacent phenyl groups along the direction *a* (4 different –F···HC– interactions (2.59 Å) per molecule), which was perpendicular to the plane *bc*. However, the intermolecular H-bonding along the direction *a* (out-of-plane) is predicted to be much weaker than that along the direction *c* (in-plane), because of the smaller number of H-bonding sites (8 vs. 4 for H-bonding along directions *c* and *a*, respectively), and the intrinsically weak nature of the H-bonding between the F in the –CF₃ group and the phenyl HC–.^[14] Consequently, this strong anisotropic intermolecular interaction between the plane *bc* and the direction *a* led to thin 2D lamellar CN-TFPA supramolecular structures with low-energy surfaced layers.

By solvent evaporation crystal growth technique (**Figure 2-1**), I could attain well-ordered 2D crystalline CN-TFPA layers. In addition to the green fluorescent 2D supramolecular structure of CN-TFPA (**Figure 2-4a**), it was also found that blue fluorescent polymorph (**Figure 2-4b**) could also be developed and isolated when dichloromethane or chloroform was used as a crystal growing medium; this was probably due to the different solvent properties, such as the polarity, boiling point, and vapor pressure.^[15] The obtained blue fluorescent CN-TFPA crystalline films also

exhibited a neat step-terrace structure (**Figure 2-4c**) (hereinafter green and blue fluorescent CN-TFPA crystalline layers are denoted as **G**-phase and **B**-phase, respectively). In the out-of-plane XRD analysis of the **G**-phase and **B**-phase crystalline layers, these two layers were found to have a different slipped angle for the DCS π -conjugated backbone (**Figure 2-4d**). The plane of the DCS backbone in the **G**-phase was slipped with respect to the plane *bc* with a dihedral angle of ca. 47.2° (d_{100} : 1.37 nm), whereas that in the **B**-phase was more perpendicular to the plane *bc*, with a dihedral angle of ca. 58.8° (d_{100} : 1.63 nm).

By comparing out-of-plane X-ray diffraction peaks of bulk single-crystal with peaks of 2D crystalline layers (**Figure 2-4d**), I could assign that the **G**-phase 2D terrace structure have same packing motif with that of bulk single-crystal. Moreover, coincidence between the photoluminescence spectra of bulk-crystals grown in solution and **G**-phase 2D terrace structure grown *via* solvent evaporation crystal growth technique could also be observe, due to the equivalent molecular packing states, as shown in **Figure 2-5b**.

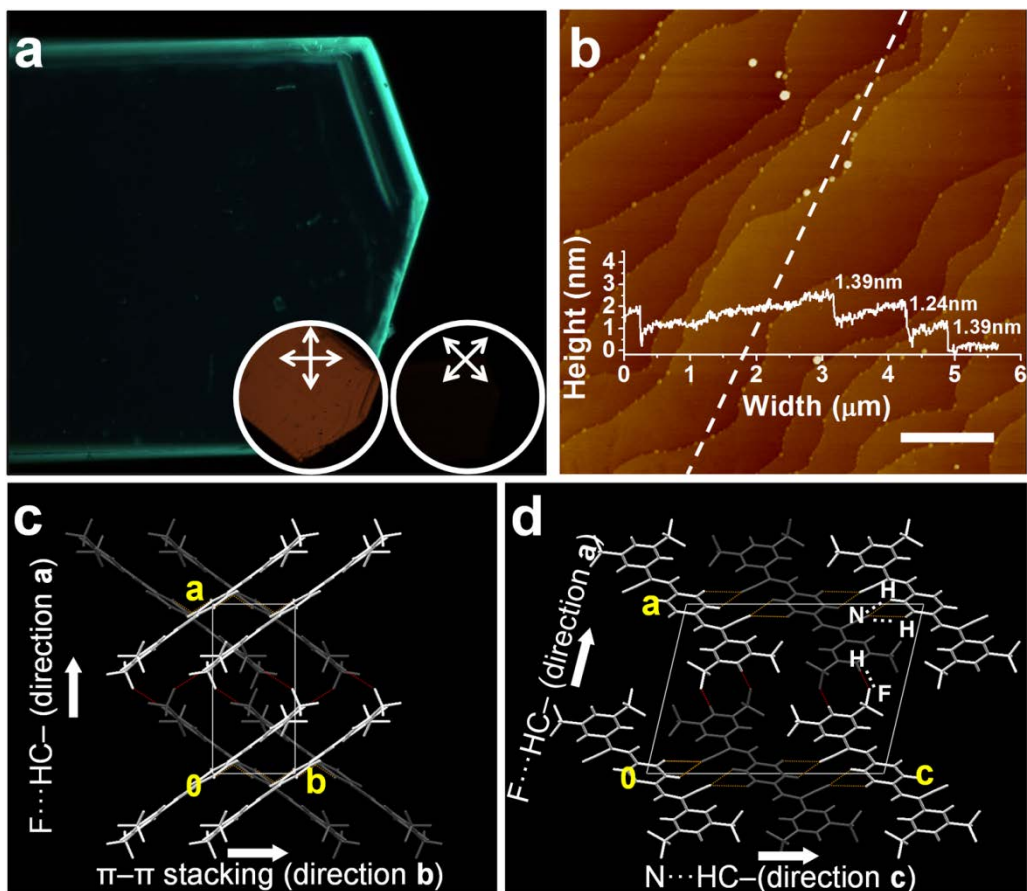
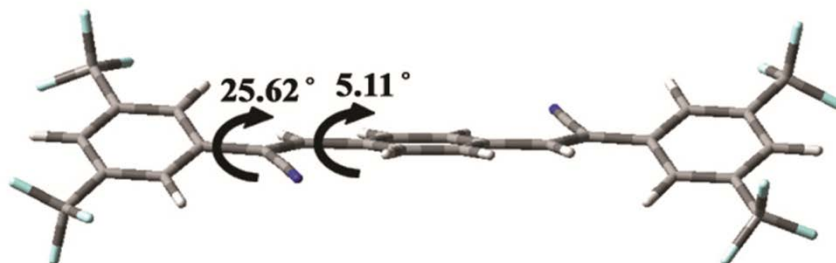


Figure 2-2. (a) Fluorescent image of a single CN-TFPA crystal, taken using an optical microscope (circled image insets: birefringence image of same crystal using polarized optical microscope). (b) AFM image (scale bar: 1 μm) of a single CN-TFPA crystal (inset: thickness profile along dashed line). (c, d) Molecular stacking observed from single-crystal XRD analysis (the directions of the intermolecular interactions are illustrated using white arrows).

a



b

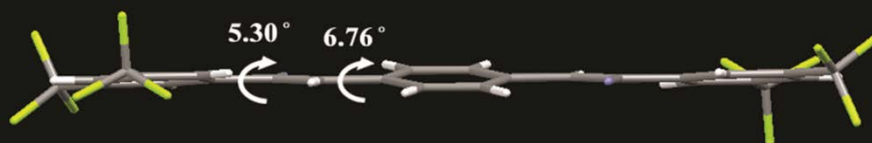


Figure 2-3. (a) The calculated optimized geometry of the CN-TFPA molecule using the B3LYP functional and 6-31+G** basis set at the density functional theory with the Gaussian 03 software. (b) The molecular geometry of CN-TFPA in the bulk single-crystal phase, based on results from the single crystal XRD analysis.

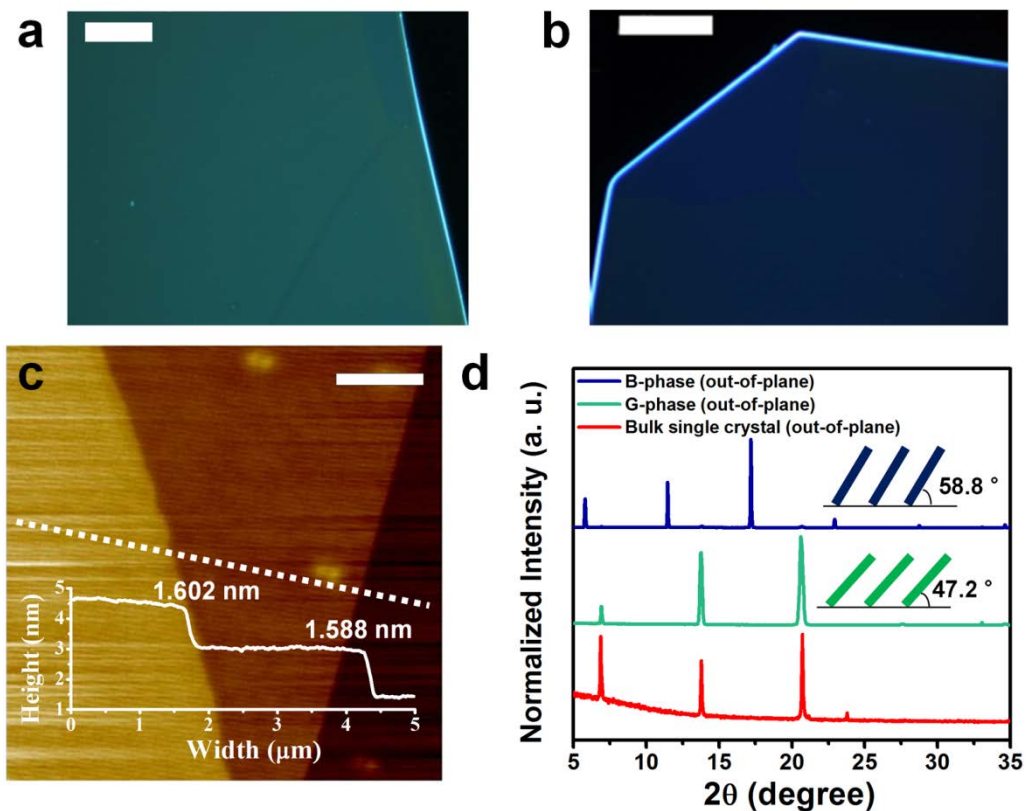


Figure 2-4. (a, b) Fluorescent images of 2D crystalline CN-TFPA layers grown by solution evaporation crystal growth (scale bar: (a) 100 μm , (b) 50 μm). (c) Molecular monolayer and bilayer from B-phase 2D sheet, measured using AFM (scale bar: 1 μm , inset: thickness profile along white dashed line). (d) Out-of-plane XRD analysis of the B-phase (blue line), G-phase (green line) and bulk single crystal (red line) (insets: schematic drawings of molecular stacks of each phase, with slipped angles to the plane bc).

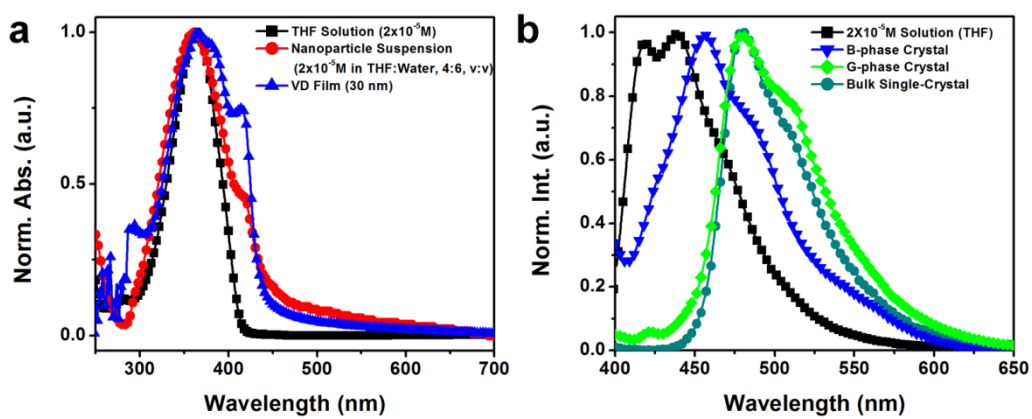


Figure 2-5. (a) UV-visible absorption spectra of CN-TFPA solution, nanoparticle, and vacuum deposited film. (b) PL spectra of CN-TFPA solution, G-phase, B-phase, and bulk single-crystal.

2.3.2. Charge Transport Properties. Moreover to the intermolecular interaction induced from $-\text{CN}$ and $-\text{CF}_3$ units for 2D assembly, those functionalities efficiently stabilize the LUMO level of CN-TFPA (HOMO: -6.98 eV, LUMO: -4.14 eV, bandgap: 2.84 eV, calculated from ultraviolet photoemission spectroscopy (UPS) and the optical band-gap of vacuum deposited film, see **Figure 2-5a**) *via* their electron-deficient characters. This stability is desirable for an efficient electron injection from the metal electrodes.

The 2D crystalline layered CN-TFPA films prepared by ‘solvent evaporation crystal growth technique’ were employed as active layers for SC-OFET applications with top-contact (Au) geometry (**Figure 2-6**). The SC-OFETs based on the **G**-phase 2D crystalline layer films showed typical *n*-type OFET behaviors, with electron mobility (μ_e) values as high as $0.03 \text{ cm}^2\text{V}^{-1}\text{s}^{-1}$, and an on/off current ratio of 10^4 (**Figure 2-7a**). However, μ_e was dramatically improved by more than 18 times in the **B**-phase SC-OFETs ($\mu_e = 0.55 \text{ cm}^2\text{V}^{-1}\text{s}^{-1}$), most likely because of the edge-on stacking structure of **B**-phase resulted in larger π - π overlaps, which led to enhanced electronic communication (**Figure 2-7b**). For comparison, the poly-crystalline FETs were also fabricated by vacuum thermal deposition and μ_e value as high as $0.34 \text{ cm}^2\text{V}^{-1}\text{s}^{-1}$ was obtained at T_{SUB} of 70°C , which is still lower than that from **B**-phase 2D layered film-based SC-OFETs due to the large amount of grain boundaries and possible impurities in poly-crystalline state (see **Figure 2-8, 2-9** and **Table 2-1** for detailed information).

The 2D crystalline characteristics of the **B**-phase SC-OFETs were further

confirmed in an anisotropic field-effect mobility study. **Figure 2-10** shows that the anisotropic dependence of the mobility values was clearly observed when varying the measuring directions; the μ_e in the direction indicated by the large red arrow was approximately 2 times higher than that in the direction indicated by the small blue arrow. The μ_e values in the directions indicated by the large red and small blue arrows were assumed to result from contributions from π - π stacking and H-bonding (–CN \cdots HC–), respectively. Importantly, the μ_e values along all directions exceeded $0.15 \text{ cm}^2\text{V}^{-1}\text{s}^{-1}$, indicating that the quasi 2D electronic interaction might arise in **B**-phase CN-TFPA structure, which is a very promising feature for practical OFET applications.

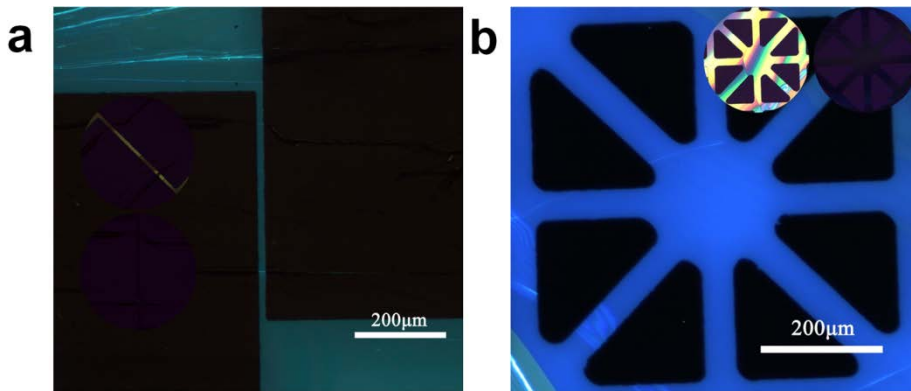


Figure 2-6. (a, b) Fluorescent image taken from SC-OFETs fabricated using the solvent evaporation technique (a: G-phase, b: B-phase). Insets indicate the birefringence of each device.

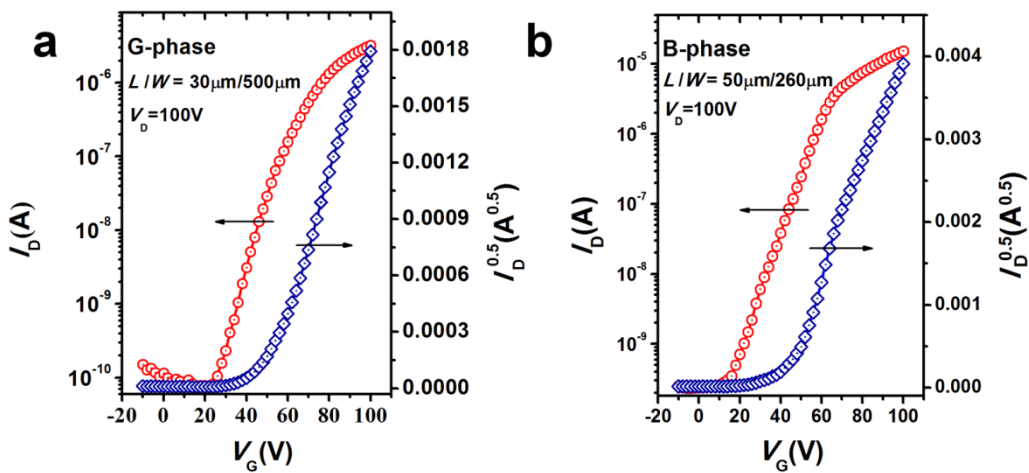


Figure 2-7. (a, b) Measured n-type characteristics of the CN-TFPA SC-OFETs devices (a: G-phase, b: B-phase).

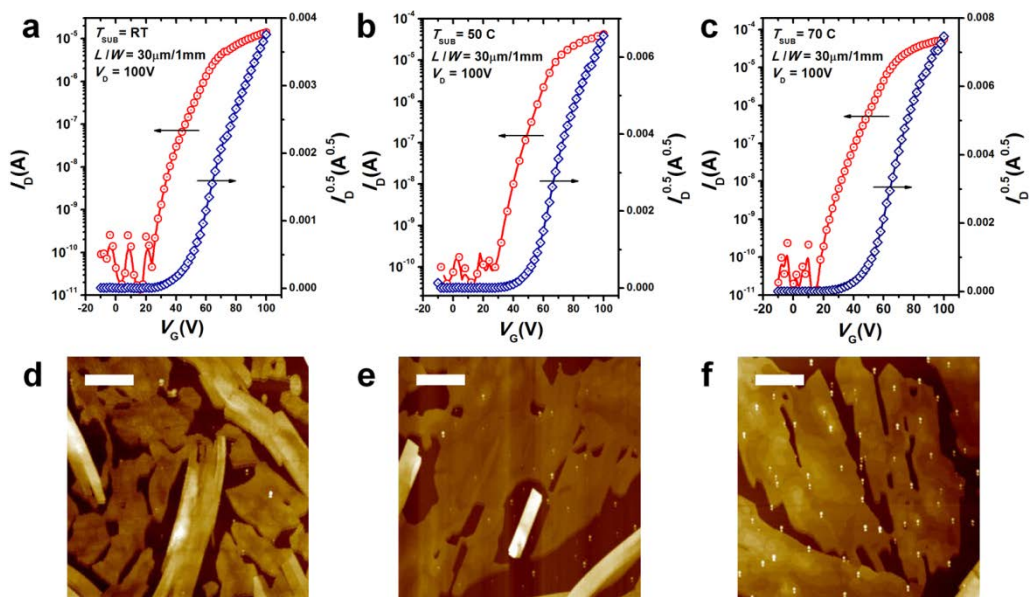


Figure 2-8. (a-c) Transfer characteristics of CN-TFPA poly-crystalline vacuum thermal deposited film (a: $T_{\text{SUB}} = \text{RT}$, b: $T_{\text{SUB}} = 50\text{C}$ and c: $T_{\text{SUB}} = 70\text{C}$). (d-f) AFM images of films by varying substrate temperatures (d: RT, e: 50C , f: 70C) (scale bar: $2\mu\text{m}$).

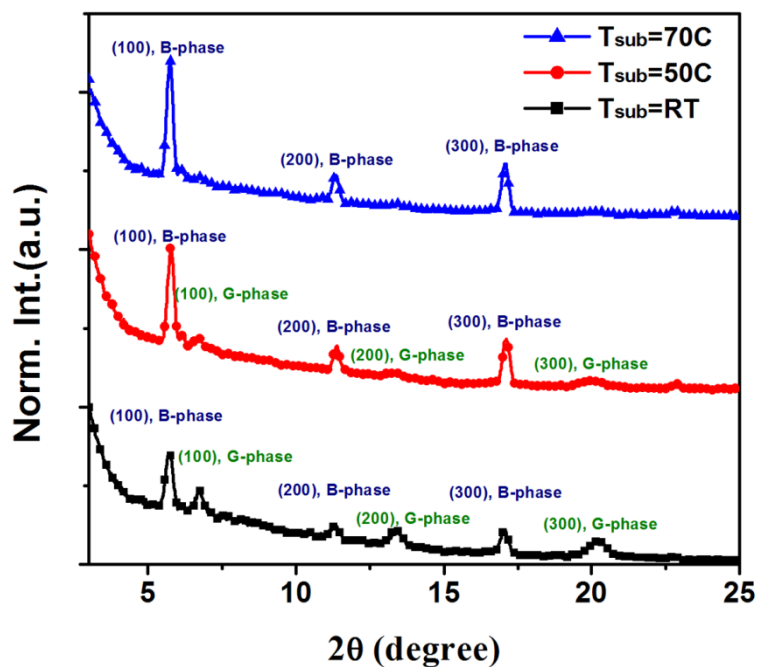


Figure 2-9. Out-of-plane XRD analysis on CN-TFPA vacuum deposition films (square line: RT, circle line: 50°C, triangle line: 70°C). (n, 0, 0) peaks of G/B-phase were designated above the each XRD pattern.

Table 2-1. Characterized Electrical Properties of CN-TFPA SC-OFETs

sample	μ_e [$\text{cm}^2 \text{V}^{-1} \text{s}^{-1}$] ^a	$I_{\text{on}}/I_{\text{off}}$	V_{th} [V] ^b	n ^c
G-phase 2D layered films ^d	3.0×10^{-2} (1.1×10^{-2})	10^4	41	10
B-phase 2D layered films ^d	5.5×10^{-1} (4.6×10^{-1})	10^5	45	10
exfoliated B-phase 2D layered films ^e	5.3×10^{-2} (2.9×10^{-2})	10^4 - 10^5	38	5
vacuum deposited films ($T_{\text{sub}} = \text{RT}$) ^f	5.9×10^{-2} (3.8×10^{-2})	10^6	44	9
vacuum deposited films ($T_{\text{sub}} = 50^\circ\text{C}$) ^f	2.3×10^{-1} (1.8×10^{-1})	10^6	51	9
vacuum deposited films ($T_{\text{sub}} = 70^\circ\text{C}$) ^f	3.4×10^{-1} (2.0×10^{-1})	10^6	50	9

^a Maximum and average electron mobility value. ^b Average threshold voltage. ^c Number of devices tested. ^d Devices fabricated by solvent evaporation crystal growth technique. ^e Device fabricated by mechanical cleavage method. ^f Device fabricated by vacuum deposition technique with ODTS treated SiO_2/Si substrate.

2.3.3. Exfoliation and Transferred Crystalline Layers for SC-OFETs

Demonstration. Besides the dense and tight molecular packing derived from the high-quality 2D crystals, the self-assembled CN-TFPA molecules possessed additional unique 2D crystalline layer properties, specifically strong in-plane but weak out-of-plane intermolecular interactions, which made it possible to exfoliate molecular sheets from the bulk 2D crystalline layers along the out-of-plane direction (direction *a*). The exfoliated thin 2D crystalline sheets could be used as an attractive platform for the construction of ultra-thin *n*-type SC-OFETs. To test this possibility, I tried to exfoliate molecular layers from the **B**-phase 2D crystalline layer films *via* the ‘mechanical cleavage method, using cellophane tape; this imitates the early-stage technique for obtaining graphene from graphite (details in Experimental Section, **Figure 2-11c**).^[16,17] It was found that 2–10 monolayers (ca. 3-15 nm thickness) of CN-TFPA with neat terrace structures were stripped and successfully transferred onto the target Si/SiO₂ substrates, binding tightly in the plane *bc* to maintain a large sheet area (ca. 100-200 μm) (**Figure 2-11**). The AFM image and surface profile in **Figure 2-12a** show that the CN-TFPA terrace films transferred onto the Si/SiO₂ substrates were of good quality, and had the same terrace height (1.64 nm) as the mother **B**-phase 2D crystalline films (1.60 nm, *d*₁₀₀: 1.63 nm). Top-contact OFETs based on these exfoliation-transferred crystalline layer films—and their mother crystals—were successfully fabricated, and their transistor properties were investigated. **Figure 2-11b** shows that the OFETs based on these exfoliated 2D crystalline layers with a thickness of ~30 nm exhibited good *n*-

type transistor behavior, with μ_e values of up to $0.053 \text{ cm}^2\text{V}^{-1}\text{s}^{-1}$; their mother crystals exhibited μ_e values of up to $0.30 \text{ cm}^2\text{V}^{-1}\text{s}^{-1}$ (**Figure 2-12**), which were comparable to the value shown by the intact **B**-phase 2D crystalline film. I believe that the lower μ_e values (compared with the OFETs based on the **B**-phase 2D crystalline layer films, for which $\mu_e = 0.55 \text{ cm}^2\text{V}^{-1}\text{s}^{-1}$) resulted from physical contact problems occurring during the retransfer procedures. Further experimental investigation is required to estimate the effects of changes in the thickness of the active organic semiconducting layers on μ_e . Nevertheless, the uniform 2D crystal formability and exfoliation capability of the material with moderate *n*-type charge carrier transporting characteristic suggest great potential for flexible electronics application. By combining mechanical cleavage methods with crystal patterning technique based on surface treatment,^[18] It is believed that repetitive formation of ultra-thin crystal patterns will be practicable which is suitable for flexible SC-OFETs with reasonable throughput device processing.

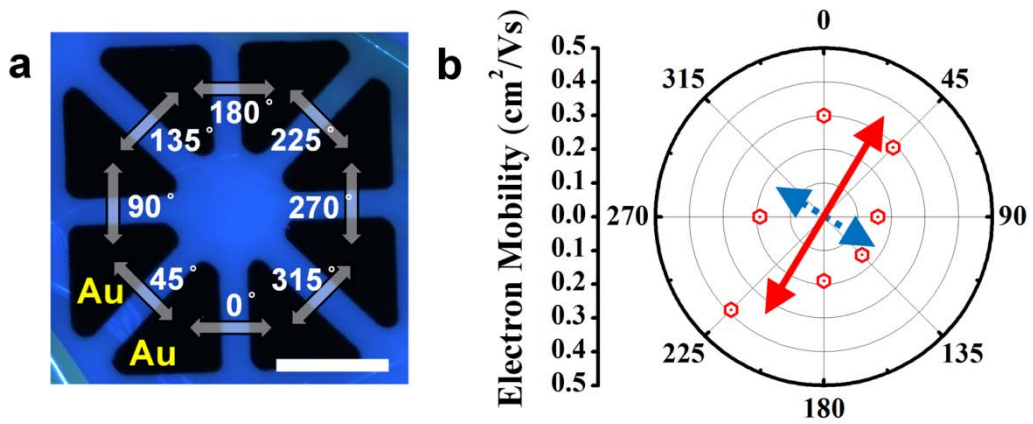


Figure 2-10. (a) Schematic illustrating the measurement of the anisotropic field-effect mobility of the B-phase SC-OFETs (scale bar: 200 μm). (b) Eight n-channel mobility values from the single crystalline B-phase 2D layer were measured every 45° (the value at 315° was not obtained) (solid arrow in (b): speculated direction of the π -stacking direction).

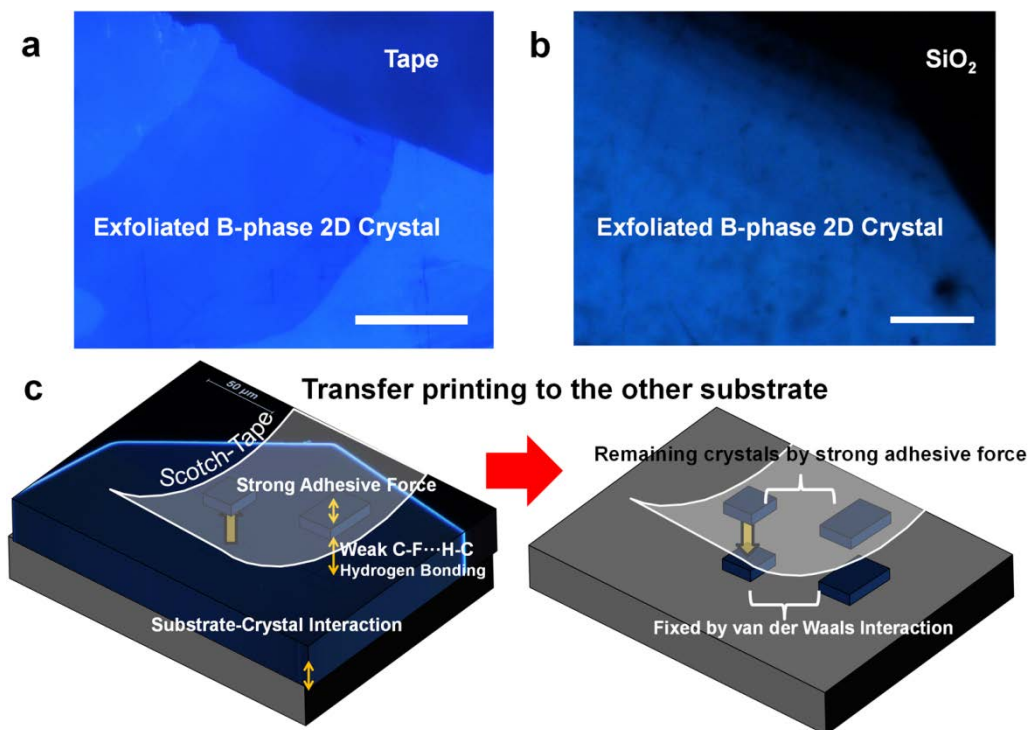


Figure 2-11. (a, b) Fluorescent images of exfoliated B-phase 2D crystal on Scotch tape, and on SiO₂ substrate after the retransfer process (scale bar of a: 30 μm, and of b: 20 μm). (c) Schematic illustration of the mechanical cleavage method.

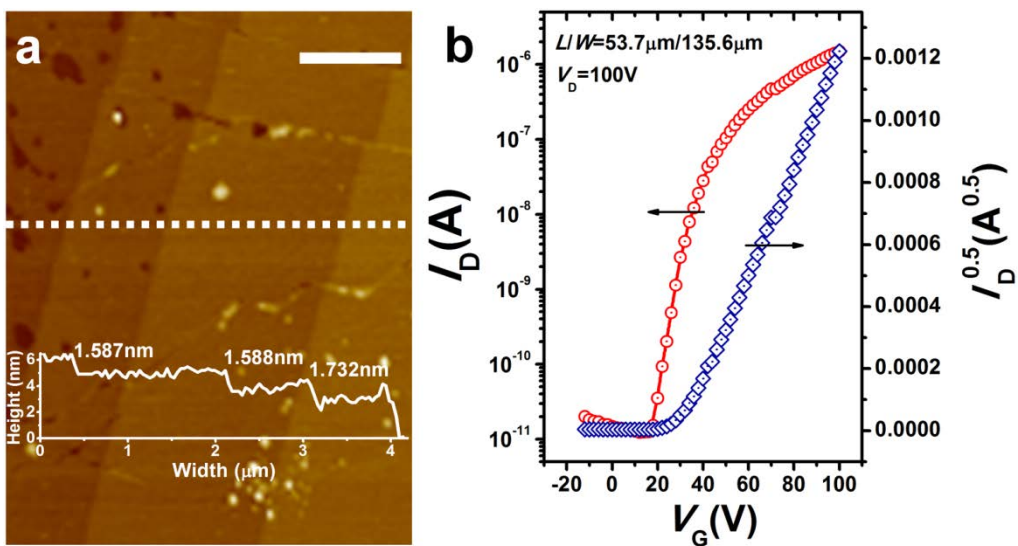


Figure 2-12. (a) AFM image (scale bar: 1 μm) of an exfoliated B-phase 2D crystal on a SiO₂ substrate (inset: thickness profile along dashed white line). (b) Measured n-type transfer characteristics of the exfoliated B-phase 2D crystal.

2.4. Conclusions

In conclusion, I report herein that CN-TFPA molecules acting as building blocks for high-performance *n*-type SC-OFETs showed a strong tendency to self-assemble into highly ordered 2D crystalline terrace structures with lowered LUMO levels; these structures are denoted here as **G**-phase and **B**-phase layers. These layers were deposited on substrates over a large area *via* a simple solution process that exploited the unique CF₃-substituted DCS molecular system. The SC-OFETs of the **B**-phase CN-TFPA 2D crystalline layer films showed electron mobilities (μ_e) of up to 0.55 cm²V⁻¹S⁻¹. Small numbers (2–10) of CN-TFPA monolayers with neat terrace structures could be exfoliated and transferred onto the target substrates using a simple ‘mechanical cleavage’ method. The top-contact OFETs based on the exfoliated CN-TFPA 2D ultra-thin crystalline layers (which had thicknesses of ~30 nm) also exhibited excellent *n*-type transistor behavior.

2.5. References

- [1] (a) Li, R.; Hu, W.; Liu, Y.; Zhu, D. *Acc. Chem. Res.* **2010**, *43*, 529. (b) Sundar, V. C.; Zaumseil, J.; Podzorov, V.; Menard, E.; Willett, R. L.; Someya, T.; Gershenson, M. E.; Rogers, J. A. *Science* **2004**, *303*, 1644. (c) Jiang, L.; Dong, H.; Hu, W. *J. Mater. Chem.* **2010**, *20*, 4994.
- [2] (a) Jiang, L.; Dong, H.; Meng, Q.; Li, H.; He, M.; Wei, Z.; He, Y.; Hu, W. *Adv. Mater.* **2011**, *23*, 2059. (b) Wu, Q.; Li, R.; Hong, W.; Li, H.; Gao, X.; Zhu, D. *Chem. Mater.* **2011**, *23*, 3138.
- [3] (a) Minemawari, H.; Yamada, T.; Matsui, H.; Tsutsumi, J.; Haas, S.; Chiba, R.; Kumai R.; Hasegawa, T. *Nature* **2011**, *475*, 364. (b) Nakayama, K.; Hirose, Y.; Soeda, J.; Yoshizumi, M.; Uemura, T.; Uno, M.; Li, W.; Kang, M. J.; Yamagishi, M.; Okada, Y.; Miyazaki, E.; Nakazawa, Y.; Nakao, A.; Takimiya, K.; Takeya, J. *Adv. Mat.* **2011**, *23*, 1626.
- [4] Gsänger, M.; Oh, J. H.; Könemann, M.; Höffken, H. W.; Krause, A.-M.; Bao, Z.; Würthner, F. *Angew. Chem. Int. Ed.* **2010**, *49*, 740.
- [5] Oh, J. H.; Suraru, S.-L.; Lee, W.-Y.; Könemann, M.; Höffken, H. W.; Röger, C.; Schmidt, R.; Chung, Y.; Chen, W.-C.; Würthner, F.; Bao, Z. *Adv. Funct. Mater.* **2010**, *20*, 2148.
- [6] Yoon, M.-H.; Facchetti, A.; Stern, C. E.; Marks, T. J. *J. Am. Chem. Soc.* **2006**, *128*,

5792.

[7] Shoji, K.; Nishida, J.-I.; Kumaki, D.; Tokito, S.; Yamashita, Y. *J. Mater. Chem.* **2010**, *20*, 6472.

[8] Yun, S. W.; Kim, J. H.; Shin, S.; Yang, H.; An, B.-K.; Yang, L.; Park, S. Y. *Adv. Mater.* **2012**, *24*, 911.

[9] Kim, J. H.; Chung, J. W.; Jung, Y.; Yoon, S. J.; An, B.-K.; Huh, H. S.; Lee, O. W.; Park, S. Y. *J. Mater. Chem.* **2010**, *20*, 10103.

[10] (a) An, B.-K.; Kwon, S.-K.; Jung, S.-D.; Park, S. Y. *J. Am. Chem. Soc.* **2002**, *124*, 14410. (b) An, B.-K.; Lee, D.-S.; Lee, J.-S.; Park, Y.-S.; Song, H.-S.; Park, S. Y. *J. Am. Chem. Soc.* **2004**, *126*, 10232. (c) An, B.-K.; Gierschner, J.; Park, S. Y. *Acc. Chem. Res.* **2012**, *45*, 544.

[11] Ando, S.; Murakami, R.; Nishida, J.-I.; Tada, H.; Inoue, Y.; Tokito, S.; Yamashita, Y. *J. Am. Chem. Soc.* **2005**, *127*, 14996.

[12] Yamao, T.; Miki, T.; Akagami, H.; Nishimoto, Y.; Ota, S.; Hotta, S. *Chem. Mater.* **2007**, *19*, 3748.

[13] (a) Hunter, C. A. *Angew. Chem. Int. Ed.* **1993**, *32*, 1584. (b) Cozzi, F.; Cinquini, M.; Annuziata, R.; Siegel, J. S. *J. Am. Chem. Soc.* **1993**, *115*, 5330.

[14] Desiraju, G. R. *Acc. Chem. Res.* **2002**, *35*, 565.

[15] (a) Weissbuch, I.; Addadi, L.; Leiserowitz, L. *Science* **1991**, *253*, 637. (b) Barbarella, G.; Zambianchi, M.; Antolini, L.; Ostojka, P.; Maccagnani, P.; Bongini, A.; Marseglia, E. A.; Tedesco, E.; Gigli, G.; Cingolani, R. *J. Am. Chem. Soc.* **1999**, *121*,

8920.

[16] Novoselov, K. S.; Geim, A. K.; Morozov, S. V.; Jiang, D.; Zhang, Y.; Dubonos, S. V.; Grigorieva, I. V.; Firsov, A. A. *Science* **2004**, *306*, 666.

[17] Jiang, H.; Tan, K. J.; Zhang, K. K.; Chen, X.; Kloc, C. *J. Mater. Chem.* **2011**, *21*, 4771.

[18] (a) Briseno, A. L.; Mannsfeld, S. C. B.; Ling, M. M.; Liu, S.; Tseng, R. J.; Reese, C.; Roberts, M. E.; Yang, Y.; Wudl, F.; Bao, Z. *Nature* **2006**, *444*, 913. (b) Briseno, A. L.; Aizenberg, J.; Han, Y.-J.; Penkala, R. A.; Moon, H.; Lovinger, A. J.; Kloc, C.; Bao, Z. *J. Am. Chem. Soc.* **2005**, *127*, 12164.

Chapter 3.

Tailor-Made Highly Luminescent and Ambipolar Transporting Organic Mixed Stacked Charge-Transfer Crystals: an Isometric Donor-Acceptor Approach

3.1. Introduction

Over several decades, much interest has been focused on organic solid-state semiconducting materials, due to their potential use in various (opto-)electronic device applications, such as the organic light emitting diode (OLED),^[1] organic photovoltaic devices (OPV),^[2] and organic field-effect transistors (OFETs).^[3] Among them, ambipolar charge carrier transport in organic semiconductors^[4] have raised much attention as potential alternatives for complementary metal oxide semiconductors (CMOS) in high-performing memory devices.^[5] However in the majority of the cases, organic semiconductors show only unipolar charge transport mainly due to the unbalanced electronic coupling of the frontier molecular orbitals (MOs).^[6] Therefore, several different approaches have been explored to realize ambipolar organic materials such as bridged electron donor (**D**) - acceptor (**A**) moieties,^[7] *p*-/*n*-channel semiconductor blends or bilayers^[8,9] and co-crystallization or co-assembly of **D** and **A** molecules.^[10,11] In some appropriate cases, such **D**·**A** structures form charge-transfer

(CT) complexes, opening a new prospect for realizing next generation (opto-)electronic applications.^[12] To this end, many supramolecular chemists have devoted their efforts to find predictable **D·A** stacking structures with prominent CT interaction from the extensive libraries of organic material systems.^[13] In spite of such efforts, (opto-)electronic application of such **D·A** co-crystal systems has rarely been achieved,^[12] especially for ambipolar OFETs application.

Organic CT complexes can exhibit two different types of binary molecular stacking structures, being segregated or mixed stacks. Most in-depth investigations so far have been focused on the former cases due to their unconventional metallic (super-)conductivities.^[14] Very recently, mixed stacked **D·A** CT complexes have also been reexamined theoretically and experimentally aiming at their promising features of ferroelectricity^[15] and ambipolar semiconductivity.^[11,16] The electronic properties of the CT structures are mainly driven by the frontier MO offsets of **D** and **A** as well as their specific molecular arrangement. Thus, careful selection of **D/A** pair with appropriate frontier MOs is necessary to achieve efficient CT co-crystal system. Up to now, only limited numbers of such ambipolar binary CT co-crystals were realized, all being based on bis(ethylenedithio)- (BEDT) or dibenzo- (DB) substituted tetrathiafulvalene (TTF) as donor and (fluorinated) tetracyanoquinodimethane (F₂)TCNQ or organometallic and ionic counter parts as acceptor (Cu[N(CN)₂]Br, I).^[11] Mixed stacked BEDT-TTF·F₂TCNQ exhibits distinct ambipolar charge transport only at low temperatures (2-60 K, metallic transport > 10 K) with drain voltage dependent mobilities of about 10⁻³

$\text{cm}^2\text{V}^{-1}\text{s}^{-1}$ for holes and electrons ($\mu_{\text{h}}/\mu_{\text{e}}: \sim 1.5$).^[11b] Mixed stacked DBTTF·TCNQ (prepared by co-sublimation) exhibited ambipolar behavior only when specific Fermi-level tuned electrodes were used.^[11c,11d] On the other hand, organic superconducting materials, such as layer-structured κ -(BEDT-TTF)₂Cu[N(CN)₂]Br^[11e,11f] and α -(BEDT-TTF)₂I₃^[11g] (formed by electrochemical process) crystals, exhibited negative pressure induced phase transition (Mott insulating or charge ordered states, respectively) when placed on SiO₂/Si substrate at low temperature, which resulted in mainly *n*-type field-effect transport but also weak ambipolarity depending on surface states of crystal samples. It has been reported that the segregated stacked BEDT-TTF·TCNQ (formed by solution casting) exhibited balanced ambipolar field-effect mobility $\sim 10^{-2} \text{ cm}^2\text{V}^{-1}\text{s}^{-1}$, even at room temperature,^[11h] while metal-like behavior was observed in the electron accumulation mode above 240 K. Very recently, remarkable and promising electronic properties of mixed stacked **D·A** CT-crystals were theoretically predicted via quantum chemical calculations by Brédas and coworkers,^[16] stressing the significance of superexchange along the stacking direction.

Unfortunately, however, ambipolar transporting CT crystals other than TTF·TCNQ based systems (the latter normally exhibit ambipolarity at low temperature) have rarely been demonstrated. While various π -conjugated **D·A** CT supramolecular structures have been investigated aiming at the (opto-)electronics device applications, only few of them exhibited ambipolarity, but of rather trivial performance.^[12c] Therefore, it would be of great impact to demonstrate high performance ambipolar CT

co-crystals at this moment, even better if combined with bright luminescence, which might pave the way to an advanced optoelectronic devices. Such alternative concepts require however tailor-made and energetically fine-tuned **D/A** pairs. In the past Park et al., and others have demonstrated that dicyanodistyrylbenzene (DCS) represent a class of molecules which are electronically significantly stabilized compared to the parent distyrylbenzene counterparts (DSB)^[17] and at the same time offer a versatile route to realize multifunctional, color variable, and brightly luminescent single-crystals.^[18] Thus, a combination of DSB/DCS derivatives as **D/A** pairs could be considered ideal *a priori*, especially since the similar chemical structure and size of **D** and **A** (*i.e.* isometric approach) should promote facile and regular co-crystallization.^[19,20] I thus designed a single-crystalline binary molecular co-crystal system comprising two isometric DSB- and DCS-based donor (4M-DSB, Figure 1) and acceptor (CN-TFPA, Figure 1),^[21] with appropriately tuned frontier MOs of the **D** and **A** molecules, to demonstrate unconventional bright emission together with outstanding ambipolar charge transport. As will be shown, the particular (opto-)electronic features of the newly designed **D·A** system are generated by a unique combination of the molecular electronic properties and the one-dimensional densely packed supramolecular arrangement driven by secondary bonding interactions. It should be noted that this design concept of isometric **D/A** pairs is conceptually different and advanced compared to the recently reported strategy of 'lock arm supramolecular ordering' (LASO),^[15] since the latter requires integrating additional supramolecular self-assembly motif to the **D** and **A** units. Due to

the remarkable structural characteristics of DCS derivatives (*i.e.* “twist elasticity”),^[18a] single-crystalline OFETs (SC-OFETs) of the **D·A** co-crystal could be easily prepared by solvent vapor annealing (SVA) from solution.^[5b,22] An in-depth structural, electrical, spectroscopic and theoretical study allowed for a full exploration of all relevant structure-property relationships in this unique class of ambipolar CT co-crystal systems.

3.2. Experimental

Synthesis 1,4-bis(3,5-dimethylstyryl)benzene, 4M-DSB, was synthesized by a 2-step procedure, see **Scheme 3-1**. (i) Commercially available 1,4-bis(bromomethyl)benzene and triethyl phosphite were used without further purification. 6.3 g of triethyl phosphite was added in 2.0 g of 1,4-bis(bromomethyl)benzene and refluxed with 115 °C overnight. After cooling to room temperature, the product was poured into distilled water and the organic layer was extracted with dichloromethane (DCM) and dried with anhydrous magnesium sulfate. After the residue solvent was removed by rotary evaporation, a white precipitate was obtained by column chromatography purification with ethyl acetate. For further purification, the product was reprecipitated in n-hexane/DCM and filtered to obtain tetraethyl 1,4-phenylenebis(methylene)diphosphonate (1,4-PBMDP, 2.55 g, Y= 88.9 %). ¹H NMR (300 MHz, CDCl₃) [δ ppm]: 7.26 (s, 4H), 4.05 – 3.96 (m, 8H), 3.16 (d, J=20.3, 4H),

1.26 (t, J=7.1, 12H). ^{13}C NMR (500 MHz, CDCl_3) [δ ppm]: 130.29, 129.94, 62.08, 33.97, 32.86, 16.35. MS (FAB) (m/z): Calculated for $\text{C}_{16}\text{H}_{28}\text{O}_6\text{P}_2$: 378.14, Found: 378.14. Anal. Calculated for $\text{C}_{16}\text{H}_{28}\text{O}_6\text{P}_2$: C, 50.79; H, 7.46; O, 25.37; P, 16.37. Found: C, 50.75; H, 7.49; O, 24.97.

(ii) 1.112 g of t-BuOK was added in 1,4-PBMDP (1.5 g) and 3,5-dimethylbenzaldehyde (1.064 g) tetrahydrofuran (THF) solution (40 ml) and refluxed at 70 °C, overnight. After cooling to room temperature, the product was poured into distilled water and the organic layer was extracted with DCM and dried with anhydrous magnesium sulfate. After the residue solvent was removed by rotary evaporation, flash column chromatography purification (ethyl acetate : n-hexane = 1 : 5) was carried out. For further purification, the product was recrystallized in DCM/n-hexane solution and finally **4M-DSB** was obtained as a white precipitate (1.2 g, Y= 89.4 %). ^1H NMR (300 MHz, CDCl_3) [δ ppm]: 7.49 (s, 4H), 7.15 (s, 4H), 7.07 (s, 4H), 6.91 (s, 2H), 2.34 (s, 12H). ^{13}C NMR (500 MHz, CDCl_3) [δ ppm]: 138.12, 137.28, 136.77, 129.44, 128.73, 127.93, 126.75, 124.43, 21.29. MS (FAB) (m/z): Calculated for $\text{C}_{26}\text{H}_{26}$: 338.20, Found: 338.20. Anal. Calculated for $\text{C}_{26}\text{H}_{26}$: C, 92.26; H, 7.74. Found: C, 92.19; H, 7.74.

(2Z,2'Z)-3,3'-(1,4-phenylene)bis(2-(3,5-bis(trifluoromethyl)phenyl)acrylonitrile), CN-TFPA, was synthesized by Knoevenagel condensation between 2-(3,5-bis(trifluoromethyl)phenyl) acetonitrile and terephthalaldehyde as previously

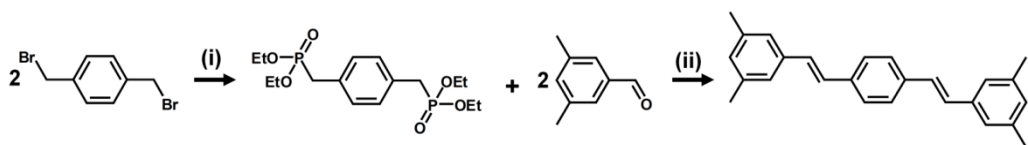
reported,^[21] see **Scheme 2-1** of *Part 2*.

Characterization ¹H NMR was recorded using a Bruker, Avance-300 (300MHz) in CDCl₃ solution for all materials. ¹³C NMR was recorded in CDCl₃ on a Bruker Avance-500 (500MHz). Elemental analyses were conducted with an EA1110 (CE Instruments). Mass spectra were measured using a JEOL, JMS-600W spectrometer. UV-Vis absorption spectra were done with a Shimadzu UV-1650 PC spectrometer. PL spectra were measured using a Varian, Cary Eclipse spectrophotometer. PL spectra on **D·A** (1:1) CT co-crystals were recorded using an Anton SP2500 series spectrometer equipped with a nitrogen cooled CCD camera and with 300 line/mm grating; the spectra were recorded with minimized self-absorption by proper crystal adjustment. Polarized measurements were done with a Glan–Thompson polarizer for the incident laser (405 nm); the analyzer was varied in intervals of 10°. The Φ_{PL} was measured in an integrating sphere (Hamamatsu C9920-01). AFM measurements were carried out in the Nanowizard scanning probe microscope (Version 1.3) of JPK instruments and the images were obtained in the contact mode using a soft cantilever. Single-crystal structure analysis was done with a SMART-APEX II ULTRA (Bruker). Out-of-plane X-ray diffraction (XRD) measurements were performed using PANalytical X’pert PRO system with a Bragg-Brentano geometry using CuK radiation with a graphite monochromator on the secondary side. Ground state geometries and MOs of the **D** and **A** compounds were calculated by DFT, imposing C_{2h} symmetry. Vertical EAs and IPs

were done on the radical anions and cations based on the neutral geometry, using DCM as a solvent as described by the polarizable continuum model (PCM); adiabatic IPs and EAs were obtained on optimized geometries of the radical ions. Excited states on the single molecular species were calculated at the TD-DFT level of theory. For all single molecules the B3LYP functional and 6-311G* basis set were employed as defined in the Gaussian09 program package.^[28] **D-A** dimer and trimer calculations were done by taking the X-ray coordinates from X-ray analysis, replacing the molecules by the DFT-optimized ones, Single point (TD-)DFT calculations employed the Coulomb-attenuated method (CAM) variant of the B3LYP functional^[29] as implemented in Gaussian09 to correctly account for long-range interactions. The orbital topologies were plotted with Molekel.^[30] The I-V characteristics of 6 individual devices were measured using a Keithley 4200 SCS. All procedures were carried out in a N₂-filled glove box.

Sample Preparation The **D·A** (1:1) NP suspension (5×10^{-6} mol L⁻¹) were obtained by re-precipitation from THF:water (1:9, v:v); for this, **D** and **A** were dissolved in THF in 1:1 molar ratio, then distilled water was slowly injected as a poor solvent, left for 2 hour before the optical studies, see **Figure 3-1**, and **3-2**. Pure **D** and **A** NP suspensions were prepared accordingly. Single-crystalline bulk **D·A** (1:1) CT co-crystals were prepared by solvent diffusion from a 1:1 mixture in dichloromethane/methanol.

Device Fabrication For substrates preparation, SiO₂/Si substrates (*p*-doped 300 nm) were rinsed with acetone and isopropyl alcohol respectively for 10 minutes in an ultrasonicator, followed by 15 minutes UV (360 nm) O₃ treatment. **D**, **A** compounds and PMMA (average M_w ~15000) were dissolved in 1,2-dichloroethane (0.5 wt. % of PMMA, 0.1 wt. % of **A** and **D**, 1:1). The solution was spin-coated at 2500 rpm for 1 min. For the SVA process, 4 ml of DCM were injected in 8 ml vial and covered with an as-casted film for 30 minutes to ensure full growth of the co-crystal. For the top-contact SC-OFETs, 50 nm of Au were thermally deposited through a metal mask in a vacuum chamber.



Scheme 3-1. The synthetic route for obtaining 4M-DSB (D).

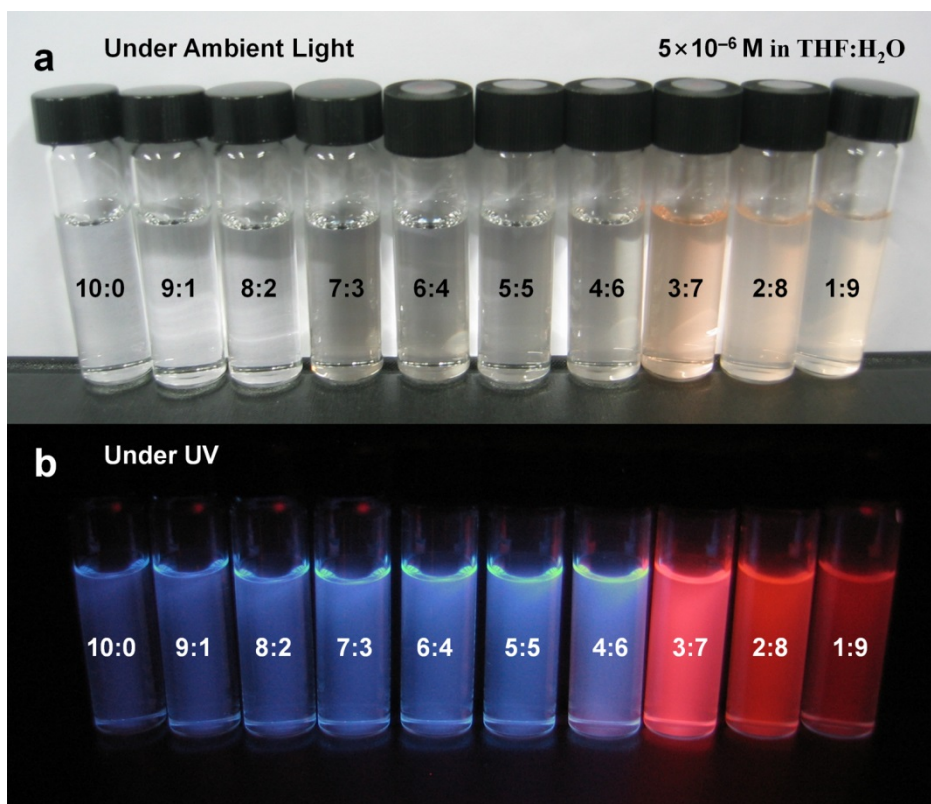


Figure 3-1. Nanoparticle suspension preparation. (a) Images taken under ambient light, and (b) UV on nanoparticle suspension by varying THF:water v:v ratio (10:0, 9:1, 8:2, 7:3, 6:4, 5:5, 4:6, 3:7, 2:8 and 1:9) with a fixed total concentration of 5×10^{-6} M.

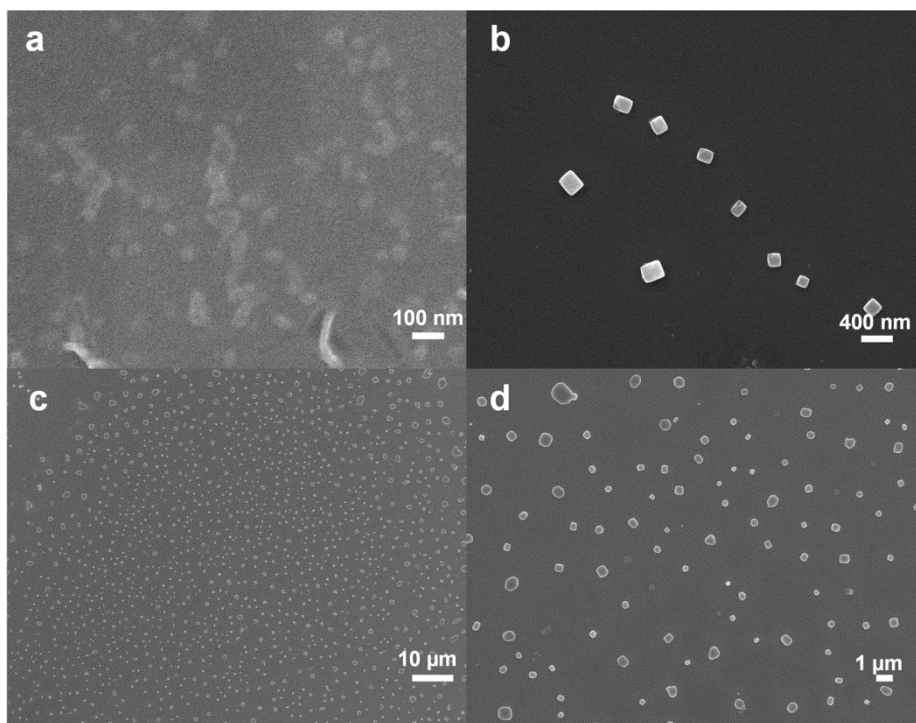


Figure 3-2. FE-SEM images of dropcasted nanoparticle suspensions ($5 \times 10^{-6} \text{M}$ in THF:water 1:9, v:v). (a) 4M-DSB (**D**), (b) CN-TFPA (**A**), and (c,d) **D·A** (1:1).

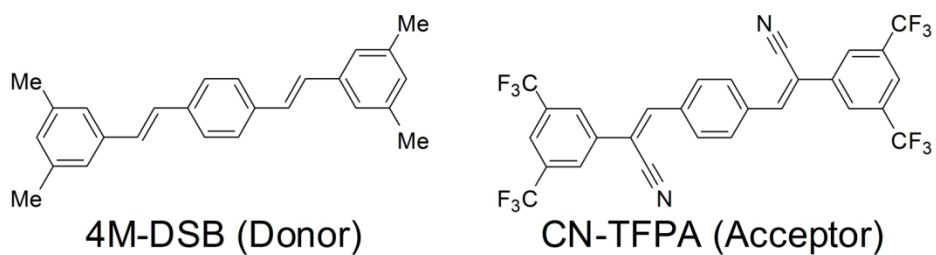


Figure 3-3. Chemical structures of 4M-DSB (**D**) and CN-TFPA (**A**).

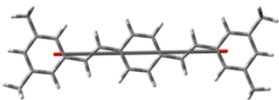
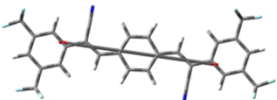
3.3. Results and Discussion

3.3.1. Molecular Design. The substitution pattern of 4M-DSB (**D**) and CN-TFPA (**A**) comprising electron donating (CH_3) and electron withdrawing (CF_3) groups was determined so that (i) the luminescence is bright and in the visible, (ii) the solubility is sufficiently large by using moderately small DSB backbone with multiple **D** or **A** substituents, (iii) dense packing is promoted by avoiding long or bulky substituents, (iv) the structural differences of **D** and **A** are as small as possible to favor mixed stacking, (v) the substituents of **D** (H , CH_3) and **A** (CN ; CF_3) are complementary to promote alternating π -stacking and extend H-bonding, and (vi) the MO offset of **D** and **A** is maximized, see **Figure 3-3**. The latter was effectively achieved by employing both CN and CF_3 functionality in **A**, which significantly lowered the frontier MOs against those in **D**. Indeed, density functional theory (DFT, for details see Experimental Section) calculations suggest stabilization of **A** by 1.6 eV (1.7 eV) for the highest(lowest) (un)occupied MOs, HOMO (LUMO), see **Table 3-1**, in qualitative agreement with our experimental results. The HOMO of **D** and **A** were estimated to -6.09 eV and -6.98 eV using ultraviolet photoelectron spectroscopy (UPS) and optical bandgap values obtained from absorption spectra of nanoparticle suspension were estimated to 3.05 eV and 2.84 eV, therefore, LUMO of **D** and **A** were estimated to -3.04 eV and -4.14 eV.^[21] Accordingly the electron affinity of **A** ($\text{EA}_{\text{calc}} = 3.8$ eV) is large enough to provide a

strong driving force for a direct charge-transfer from **D** (ionization potential $IP_{\text{calc}} = 5.2$ eV) to **A**, and to promote ambipolar charge carrier transport when composing a **D·A** (1:1 stoichiometric) mixed stacked CT co-crystal.

As a convenient method of realizing solid state CT structures from the **D** and **A** molecules, we prepared nanoparticle (NP) suspensions from a 1:1 binary mixture solution of **D** and **A** in tetrahydrofuran (THF) through re-precipitation into water.^[23] Uniform and stable NP suspension was obtained, whose absorption and photoluminescence (PL) spectra were significantly different from those of the pure **D** or **A** NP suspensions as shown in **Figure 3-4c**. In contrast to the rather small changes in the dilute solution system (**Figure 3-4a**), spectral changes due to the CT interaction and stacking are very prominent in the NP states. According to the strong CT interaction, new red-shifted absorption bands of moderate strength (533, 495 nm) coupled with intense orange PL (570 nm) strongly bathochromically shifted from those of **D** and **A** were newly observed in the **D·A** NPs. Based on such promising CT interaction in NPs, I could prepare high quality bright emissive, dark orange **D·A** (1:1) binary single-crystals with a strongly elongated hexagonal shape, see **Figure 3-5a**.

Table 3-1. Frontier MO energies, adiabatic and vertical electron affinities (EA) and ionization potentials (IP) of the 4M-DSB (**D**) and CN-TFPA (**A**) molecules as calculated by DFT (B3LYP). Vertical transition energies $E_{\text{vert}}(S_0 \rightarrow S_1)$ as calculated by TD-DFT (B3LYP).

	D	A
HOMO ^a	-5.30 eV	-6.86 eV
LUMO ^a	-1.93 eV	-3.70 eV
EA _{adiab} ^b	2.44 eV	3.91 eV
EA _{vert} ^b	2.31 eV	3.75 eV
IP _{adiab} ^b	5.11 eV	6.05 eV
IP _{vert} ^b	5.23 eV	6.14 eV
$E_{\text{vert}}(S_0 \rightarrow S_1)$ ^a	3.16 eV (H→L)	2.97 eV (H→L)
		
^a in vacuo	^b in dichloromethane (PCM)	

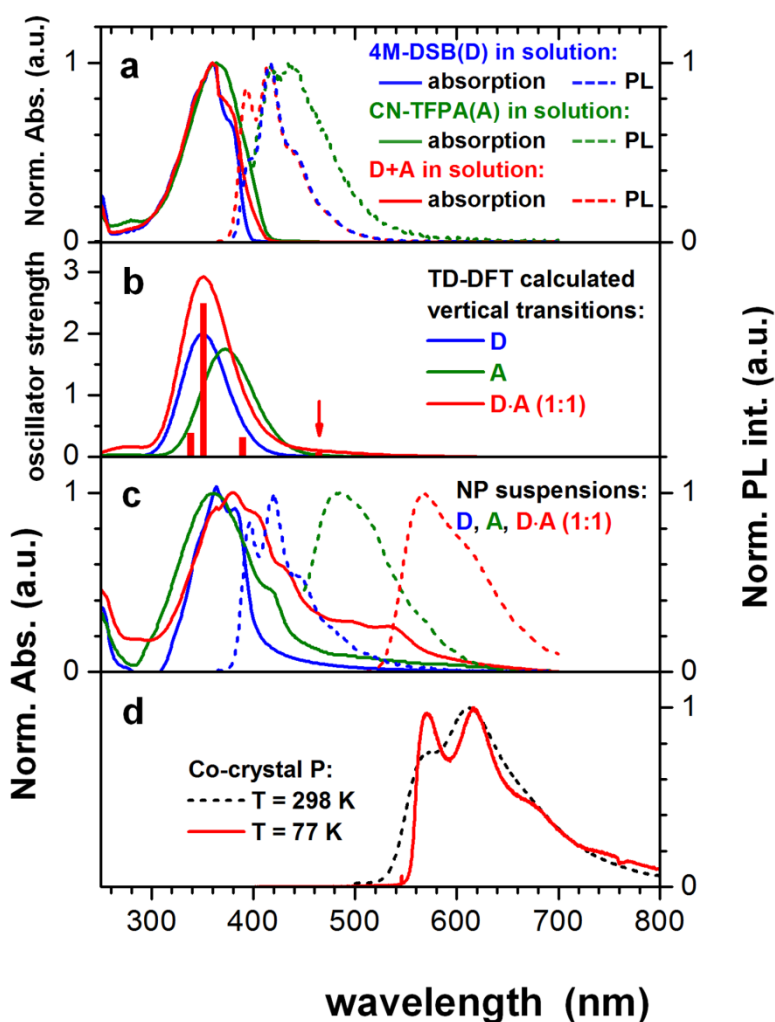


Figure 3-4. (a) Normalized UV-vis absorption and PL spectra of 4MDSB (**D**), CN-TFPA (**A**), and **D** + **A** mixture in THF solution (5×10^{-6} M). (b) Calculated vertical electronic transition energies of **D**, **A**, and a **D-A** (1:1) dimer (broadened by a Gaussian); for **D-A**, transitions are also indicated as bars. (c) Normalized UV-vis absorption and PL spectra of **D**, **A**, and **D-A** (1:1) NP suspensions in THF:water (1:9, v:v). (d) PL spectra of the **D-A** (1:1) CT cocrystal at room temperature and 77 K with minimized reabsorption.

3.3.2. Solid State Structure. X-ray analysis of the **D·A** CT co-crystal confirmed the 1:1 stoichiometry within a monoclinic system, space group P2(1)/c, see **Figure 3-5**, and **Table 3-2**. The crystal consist of regular 1-dimensional mixed **D-A-D-A** stacks with intermolecular distances of about 3.36 Å (**Figure 3-5d**) along the *b*-axis, attributed to the significant CT and subsequent Coulombic interaction between the **D** and **A** molecules, which automatically fulfilled positional locking unlike the recently reported LASO concept.^[15] The molecules are practically planar in the **D·A** CT co-crystal (**Figure 3-6**), consistent with the “twist elasticity behavior”^[18a] of the β -cyano-functionalized **A** molecules, which are further driven by intermolecular H-bonding (**Figure 3-7**). For a **D·A** pair, the electronic offset of the frontier MOs gives rise to a static dipole moment (SDM) of 1.22 D as calculated at the DFT(CAM-B3LYP) level of theory. The SDM of the **D·A** pair points in 45° angle against the long axis of the molecules, thus oriented exactly along the crystallographic *b*-axis as shown in **Figure 3-8**; therefore, in view of ensuring electro-neutrality in the crystalline state, 90° tilt between neighboring **D-A-D-A** stacks is well rationalized (**Figure 3-5b**), of which the driving force is the enthalpy gain to promote dense packing. This inter-stack arrangement is further assisted by considerable intermolecular H-bonding interactions (-N···HC-) along the *c*-axis, similar to the molecular stacking features in the pure **A** crystal, see **Figure 3-9**.^[21] This hinge-like arrangement of adjacent stacks minimizes the electronic interactions between neighboring stacks and gives rise to strongly anisotropic quasi-1D electronic characteristics of the densely packed planar **D-A-D-A**

stacks, which is considered favorable for both p -/ n -type charge transport.

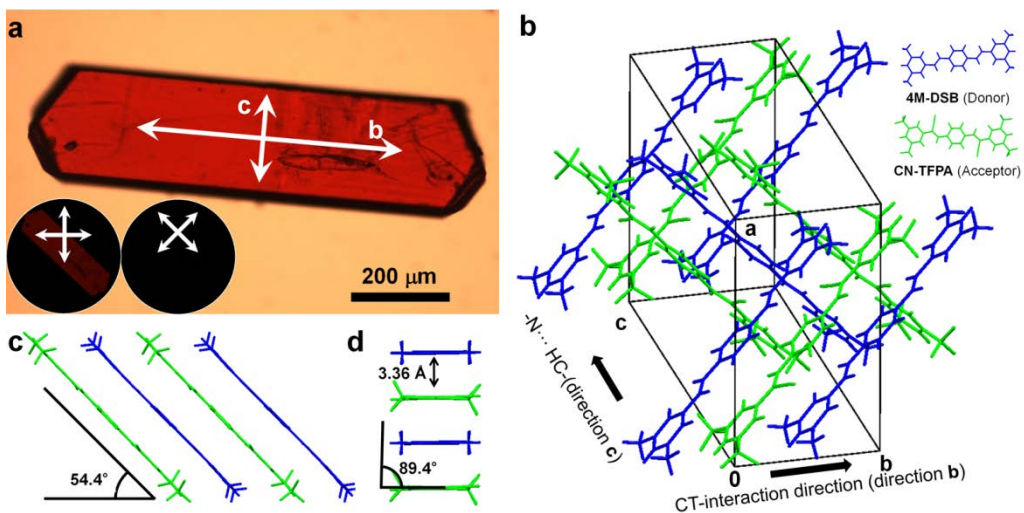


Figure 3-5. (a) Optical microscope image of D–A (1:1) CT cocrystal under ambient light irradiation (insets: images under $\pm 45^\circ$ rotating polarizer). (b) Single-crystal XRD structure of the D–A (1:1) CT cocrystal; blue molecule: D, green molecule: A. (c) Counter pitch angle ($90^\circ - \text{pitch angle}$), and (d) counter roll angle ($90^\circ - \text{roll angle}$) and π - π distance (interlayer distance) measured from single-crystal XRD results.

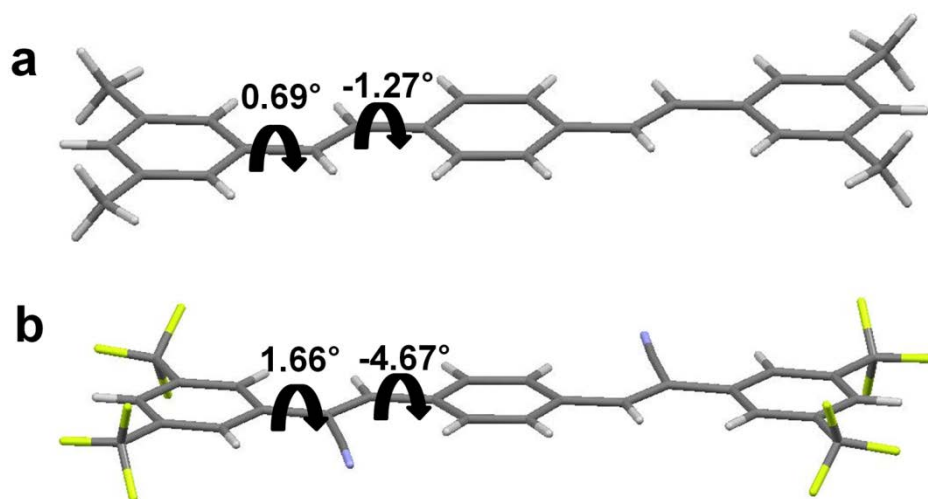


Figure 3-6. Molecular conformation in mixed stacked **D·A** (1:1) CT co-crystal. (a) The molecular geometry of **D**, and (b) **A** found from single-crystalline **D·A** (1:1) CT co-crystal state. The conformational angle of each single bond is denoted with black arrows.

Table 3-2. Crystal data and structure refinement for **D·A (1:1)** CT co-crystal.

Empirical formula	C ₂₇ H ₁₉ F ₆ N
Formula weight	471.43
Temperature	173(2) K
Wavelength	0.71073 Å
Crystal system	Monoclinic
Space group	P2(1)/c
Unit cell dimensions	a = 15.0774(8) Å α = 90° b = 9.3896 (6) Å β = 112.131(3)°. c = 16.7012 (9) Å γ = 90°
Volume	2190.2(2) Å ³
Z	4
Density (calculated)	1.430 Mg/m ³
Absorption coefficient	0.119 mm ⁻¹
F(000)	968
Crystal size	0.38 x 0.27 x 0.11 mm ³
Theta range for data collection	1.46 to 28.43°.
Index ranges	-17<=h<=20, -12<=k<=12, -22<=l<=21
Reflections collected	20771
Independent reflections	5444 [R(int) = 0.1647]
Completeness to theta = 27.49°	98.5 %
Absorption correction	None
Max. and min. transmission	0.9870 and 0.9562
Refinement method	Full-matrix least-squares on F ²
Data / restraints / parameters	5444 / 0 / 307
Goodness-of-fit on F ²	0.876
Final R indices [I>2σ(I)]	R1 = 0.0543, wR2 = 0.1371
R indices (all data)	R1 = 0.1129, wR2 = 0.1614
Largest diff. peak and hole	0.402 and -0.282 e.Å ⁻³

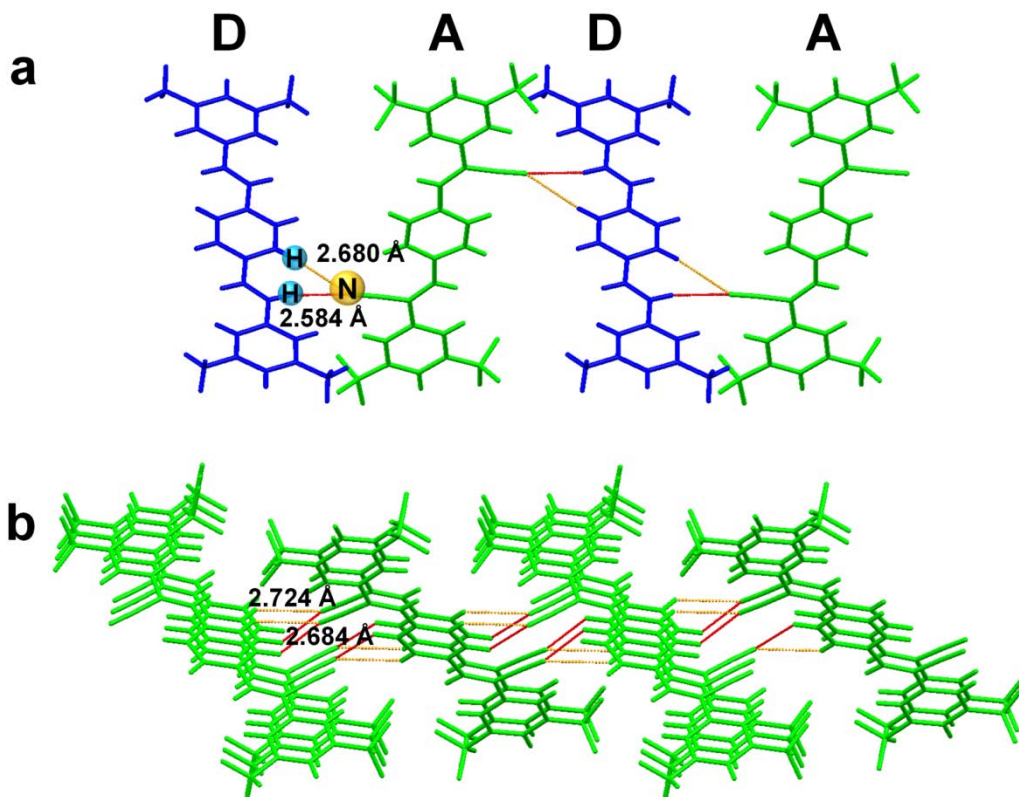


Figure 3-7. (a, b) Interstack H-bonding interaction promoted by CN in mixed stacked **D**·**A** (1:1) CT co-crystal and in pure **A** crystal. (a) The number of intermolecular interactions branched out from CN units in CT co-crystal: 4 H-bonding, and (b) pure **A** crystal: 8 H-bonding, per molecule. Intermolecular bonding lengths are indicated in the each figure. See also differently positioned hydrogens are participated in H-bonding interactions ((a) 1 central phenyl and 1 vinylene hydrogens for CT co-crystal / (b) 2 central phenyl hydrogens for pure **A** crystal).

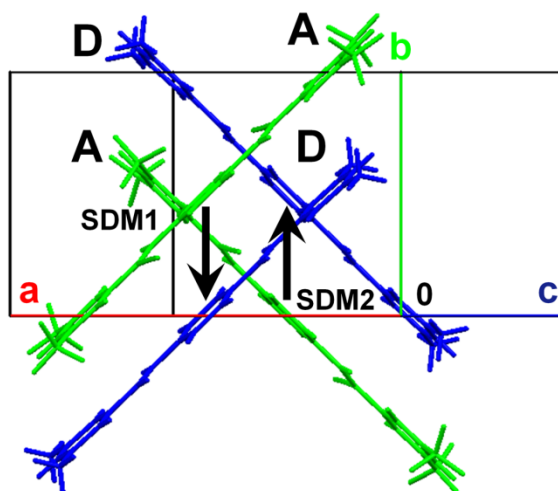


Figure 3-8. Static dipole moment of the dimer pair in mixed stacked **D·A** (1:1) CT co-crystal. Single-crystalline structure of the **D·A** (1:1) CT co-crystal with unit cell axis *a*, *b*, *c*. Calculated ground state static dipole moments (SDM) of the dimer pair are indicated in black arrows.

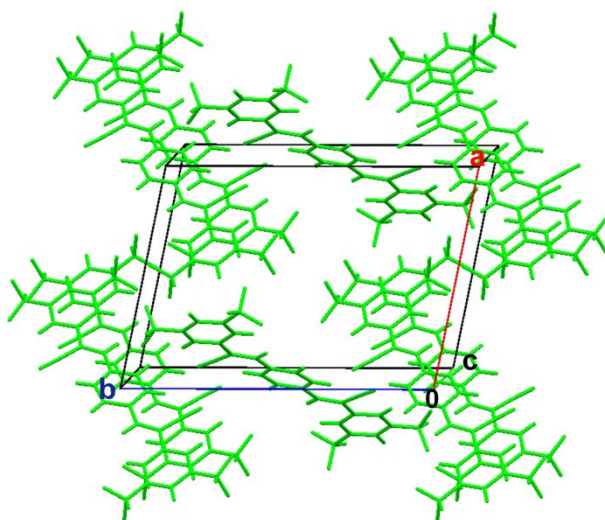


Figure 3-9. Molecular stacking structure in pure **A** crystal

3.3.3. Electronic and Optical Properties. The consequences of the close π -stacked **D**·**A** arrangements on the electronic and optical properties are conveniently and reliably elucidated by DFT calculations, by using the experimental molecular coordinates obtained from the X-ray structure analysis, see **Figure 3-10a**. It was found that the HOMO and LUMO of the stacks are totally localized on **D** and **A** moieties, respectively, as implied by the large MO offset between the designed molecules. Other MOs adjacent to the frontier orbitals, however, showed some MO delocalization with rather strong asymmetries.

The lowest electronic transition ($S_0 \rightarrow S_1$) arises mainly from a HOMO \rightarrow LUMO excitation (**Table 3-3**) and thus gives a significant red-shift against the absorption of **A** (**Figure 3-4b, c**). Due to the pronounced localized character of the frontier MOs, the transition reveals a strong CT character as visualized by the electron-hole wavefunction plot in **Figure 3-11**.^[19] Due to the strong CT character of the electronic transition, the transition dipole moment (TDM; with oscillator strength of 0.07) is oriented fairly along the direction of the SDM (**Figure 3-10a**), *i.e.* in the ***b***-direction of the crystal. The energy of the transition (2.67 eV; 464 nm) agrees quite well with experiment, assuming that the low-lying peaks at 532 nm (2.32 eV) and 494 nm (2.51 eV) of the experimental spectrum (**Figure 3-4c**) represent apparent vibronics of S_1 , so that the vertical transition might be around 2.5 eV. The observed band found at 428 nm (2.89 eV) should then correspond to S_2 , calculated at 3.19 eV (389 nm). The main absorption band (experimentally observed at 360 nm; 3.44 eV, see **Figure 3-4c**) is

assigned to the $S_0 \rightarrow S_3$ transition, calculated at 3.53 eV (351 nm). This transition of the **D·A** (1:1) CT co-crystal is described mainly by a HOMO \rightarrow LUMO+1 excitation (**Table 3-3**), thus essentially generated by the frontier orbitals of **D**; hence, the energetic position of $S_0 \rightarrow S_3$ as well as the orientation of the TDM agree well with the $S_0 \rightarrow S_1$ transition of **D** as indeed observed in **Figure 3-4c**.

The bright emission (PL quantum yield $\Phi_{\text{PL}} = 0.31$) and the rather well-structured PL spectrum of the **D·A** (1:1) CT co-crystal (which becomes especially obvious at low temperatures, see **Figure 3-4d**) might be a surprise at a first glance, since systems with significant CT character mostly show unstructured exciplex-like emissions of low intensity. I attribute the high PL efficiency of the **D·A** (1:1) CT co-crystal to the non-negligible oscillator strength of the S_1 state as discussed above and also to the low non-radiative decay often found in single crystals,^[24] which is most likely due to the low trapping probability of the originally formed CT exciton. With respect to the well resolved vibronics (which can be correlated to the respective Raman modes, see **Figure 3-12**), it is to be reminded that the decisive factor for vibronic coupling is the extent by which the normal coordinates of a considered vibration coincide with the geometrical change upon electronic de-/excitation. Hence, excimer- or exciplex-like PL spectra with strongly red-shifted, unstructured features in binary CT compounds are mainly obtained, when there is a significant change in the *intermolecular* separation during electronic de-/excitation.^[25] This change is suggested to be small in the present **D·A** (1:1) CT co-crystal case attributed to the localized nature of the frontier MOs. Due

to this strong localization, a pronounced change in the intermolecular coordinate upon electronic de-/excitation is not expected; therefore, intermolecular modes should have a minor influence in the vibronic structure, thus mimicking single molecular vibronics as apparently the case shown in **Figure 3-4**.

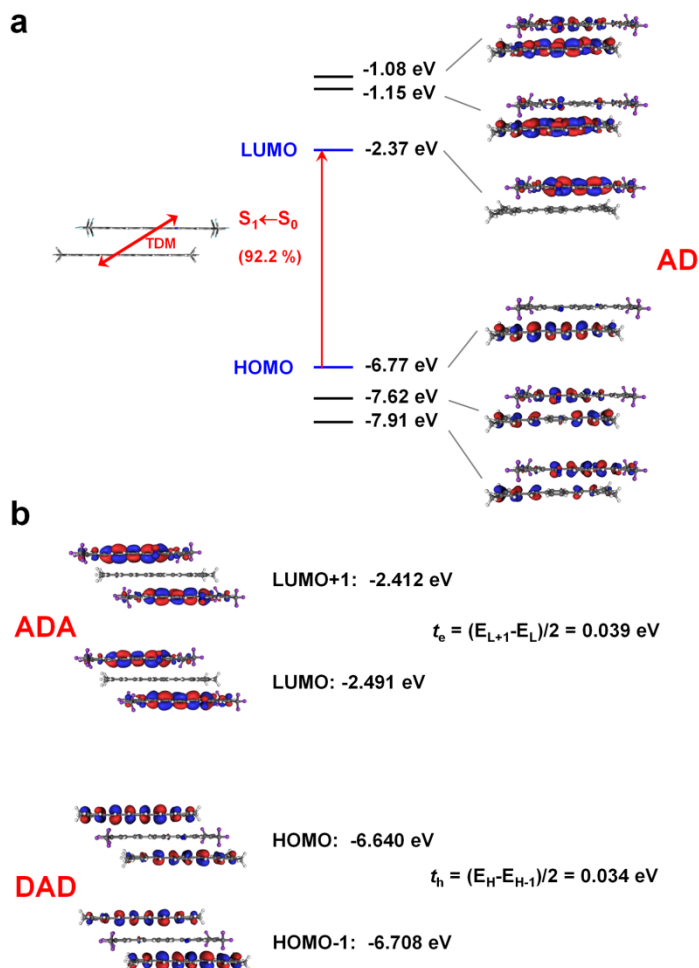


Figure 3-10. (a) MO diagram for the D-A (1:1) system as calculated by DFT(CAM-B3LYP); the main CI contribution for the $S_1 \leftarrow S_0$ transition is indicated; the orientation of the respective TDM is depicted on the left. (b) DFT calculated transfer integrals for electrons (t_e) and holes (t_h) along the b -axis based on the energy-splitting method.^[16]

Table 3-3. Vertical transition energies Evert of 4M-DSB (**D**), CN-TFPA (**A**) and **D·A** (1:1) as calculated by TD-DFT(CAM-B3LYP/6-311G*)//DFT(B3LYP/6-311G*).

E_{vert}	D	A	D:A (1:1)
S₁←S₀	3.54 eV (f = 2.00) H→L: 93% H-1→L+1: 5%	3.33 eV (f = 1.75) H→L: 95% H-1→L+1: 4%	2.67 eV (f = 0.07) H→L: 92 % H-1→L: 2% H-2→L: 2%
S₂←S₀			3.19 eV (f = 0.31) H-1→L: 56% H-2→L: 22% H→L+1: 14%
S₃←S₀			3.53 eV (f = 2.49) H→L+1: 53% H→L+2: 23% H-1→L: 15%
S₄←S₀			3.66 eV (f = 0.39) H-2→L: 47% H→L+2: 18% H→L+1: 15% H-1→L: 9%

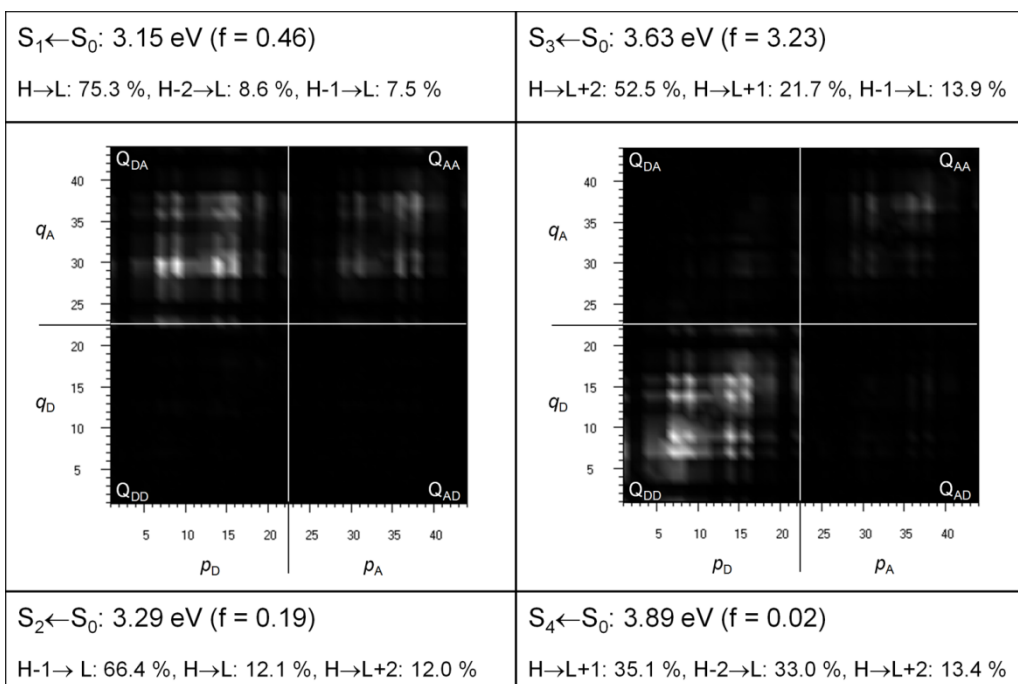


Figure 3-11. The electron-hole wave function plot. Description of the first four excited states for the **D**·**A** pair as calculated at the ZINDO/S//DFT:B3LYP(6-311G*) level of theory. The numbering follows the C-atoms of the molecular backbone (**D**: 1-22, **A**: 23-44).

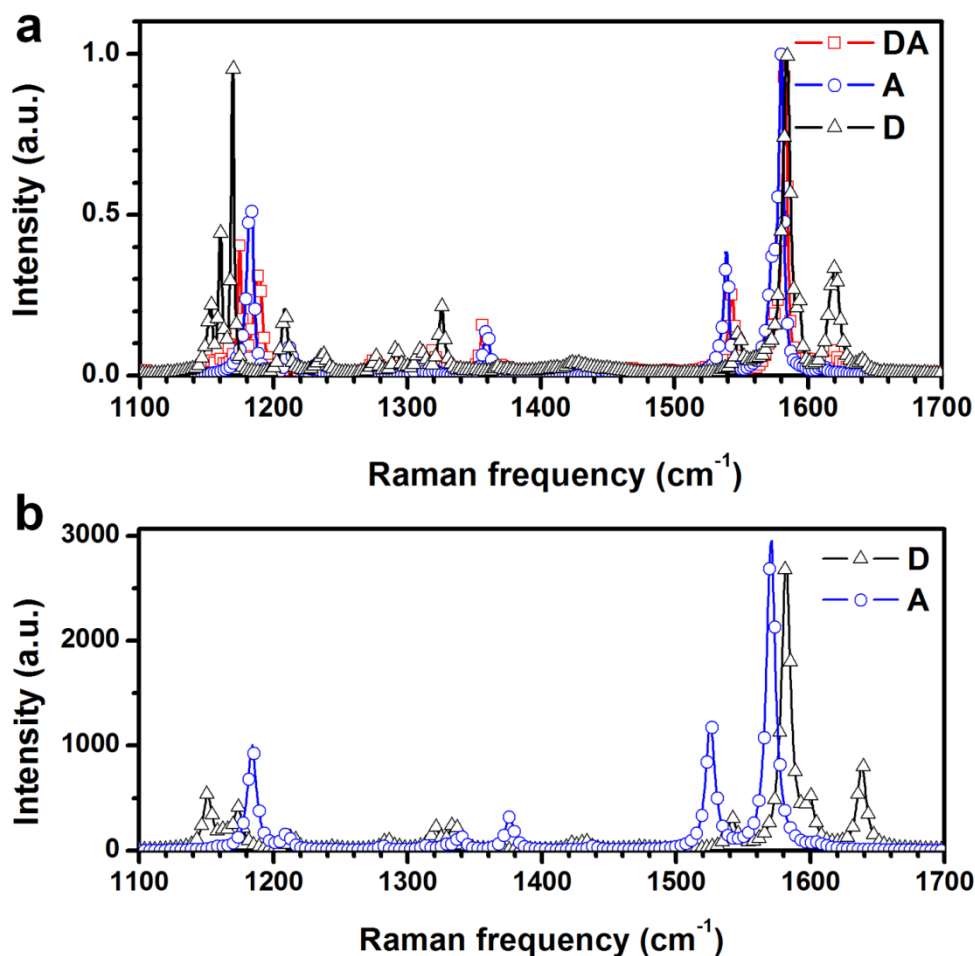


Figure 3-12. Experimental and calculated Raman spectra of pure **D**, **A** and **D·A** (1:1) CT co-crystal. (a) Experimental non-resonant Raman spectra of the **D**, **A** and **D·A** (1:1) CT co-crystals. (b) Calculated Raman spectra of the **D** and **A** compounds as calculated at the DFT(B3LYP/6-311G*) level of theory. The frequencies were scaled by a factor of 0.97 to be compared to the experimental spectrum.

3.3.4. Charge Transport Properties. The exclusive localization of the frontier MOs as discussed above are in fact an important prerequisite for favorable ambipolar charge transport. To estimate the potential of the binary CT co-crystal for electronics applications, I and coworkers have calculated the transfer integrals for both hole and electron (t_h , t_e) along the stacking direction (*i.e.* **b**-axis, **D-A-D-A**) based on single-crystal XRD analysis as shown in **Figure 3-10**. The transfer integral values are known to be strongly governed by the degree of orbital overlap and to affect the effective mass of the charge carrier.^[26] Following the method of Zhu et al,^[16] t_h and t_e were calculated from the MO differences in **D-A-D** and **A-D-A** stacks (**Figure 3-10**), giving $t_h = 0.034$ eV and $t_e = 0.039$ eV. The calculated values point to effective superexchange along the π -stacking direction,^[16] suggesting efficient and well-balanced ambipolar charge mobility, which supports the strategy of our CT stack design concept. Since the mobility scales with t^2 , the μ_e is suggested to be 30 % higher than μ_h within the frame of this rather simplistic computational model.

Based on these promising results, I have carried out electrical measurements for the bottom-gate and Au top-contact SC-OFETs, see inset of **Figure 3-13a,c**. For this, an efficient and simple solution process was employed, SVA,^[5b,22] which I use here to grow **D·A** (1:1) CT co-crystals based on a ternary solid-solution type spin-coated film (composed of **D**, **A** and poly(methylmethacrylate), PMMA, as insulating polymer binding material, see Experimental Section). Here, by exposing spin-coated blended layer to the organic solvent vapor (*e.g.* dichloromethane, DCM), high quality **D·A** (1:1)

mixed stacked single-crystals could be fabricated on the surface of PMMA film as shown in **Figure 3-13c**. Owing to the well-established advantages of introducing a polymer insulating layer, such as surface trap-site coverage and improvement of device operation stability, the SVA method allows for a precise evaluation of the charge transporting characteristics in solution-grown defect-free single-crystals. The red emissive characteristics of the SVA-grown crystals (**Figure 3-13c**) are inherent to the **D·A** binary CT co-crystals as described above and exclude the possibility of mixing separate **D** and **A** crystals.

As shown in **Figure 3-13a, c**, transfer and output characteristics of **D·A** (1:1) SC-OFET were measured in both hole-/electron-enhancement mode at ambient temperature. The V-shape transfer curves clearly indicate the transition from ambipolar to unipolar transport with increasing V_G in both hole-/electron-enhancement mode (see **Figure 3-13a**). In addition, diode-like behaviors are apparent at low V_G regimes due to the increased injection of the opposite charge-carriers; however, saturation characteristics for unipolar carrier at high V_G regimes are clearly seen in the output curves (see **Figure 3-13b**).^[27] Measurements along the long crystal axis gave hole and electron mobilities up to $6.7 \times 10^{-3} \text{ cm}^2 \text{V}^{-1} \text{s}^{-1}$ (avg. $4.3 \times 10^{-3} \text{ cm}^2 \text{V}^{-1} \text{s}^{-1}$) and $6.7 \times 10^{-2} \text{ cm}^2 \text{V}^{-1} \text{s}^{-1}$ (avg. $5.4 \times 10^{-2} \text{ cm}^2 \text{V}^{-1} \text{s}^{-1}$), respectively, for which the capacitance values of SiO_2/PMMA layer were separately measured and used, see **Figure 3-14**. Although the experimental ambipolar character ($\mu_e/\mu_h \sim 12.6$) is somewhat less balanced compared to the theoretical predictions ($\mu_e/\mu_h \sim 1.3$), the overall good charge transport characteristics

both for *p/n*-channel transport strongly support our strategy to design ambipolar **D·A** CT co-crystals which is ascribed to the superexchange nature along the stacking direction. As one can expect, the currently measured ambipolar mobility (μ_h up to $6.7 \times 10^{-3} \text{ cm}^2 \text{V}^{-1} \text{s}^{-1}$ and μ_e up to $6.7 \times 10^{-2} \text{ cm}^2 \text{V}^{-1} \text{s}^{-1}$) in this work is rather moderate compared to the large *n*-channel mobility of pure **A** crystal ($5.5 \times 10^{-1} \text{ cm}^2 \text{V}^{-1} \text{s}^{-1}$) in good agreement with the calculated transfer integral values of **D·A** mixed stack ($t_h = 0.034 \text{ eV}$ and $t_e = 0.039 \text{ eV}$) and pure **A** arrangement ($t_e = 0.079 \text{ eV}$);^[21] however it is still good and well-balanced, due to the fact that the isometric **D/A** pairs with rationally designed substituents on them actually gave rise to the most tight **D-A-D-A** packing, revealing high counter role and counter pitch angle (89.4 and 54.4, respectively) with close π -stacking distance (3.36 Å), to ensure excellent ambipolar transporting characteristics, see **Figure 3-5c, d**.

In order to prove whether the favored charge transport direction (along the long crystal axis) indeed coincides with the stacking direction (**b**-axis), the absolute orientation of the molecules with respect to the crystal facets were investigated. Combined out-of-plane XRD measurements (**Figure 3-15a**) and height profile from atomic force microscopy (AFM) (**Figure 3-15b**) evidence that the crystal facet coincides with the (1 0 0) plane. To determine the orientation of the stacking direction (**b**-axis) against the long crystal axis, polarized PL experiments were carried out, since the TDM of the emitting dipole is pointing into the stacking direction (*vide supra*) and thus provides the optimal tool to determine the absolute orientation of the **b**-axis.

According to the results in **Figure 3-16**, maximum PL intensity was observed along the elongated crystal axis (further support came from pronounced optical birefringence, see inset of **Figure 3-5a**). Thus, the spectroscopic measurements indeed confirmed that the molecular stack direction along the *b*-axis coincides with the long crystal axis and thus explains the favorable, efficient and ambipolar charge transport in this direction.

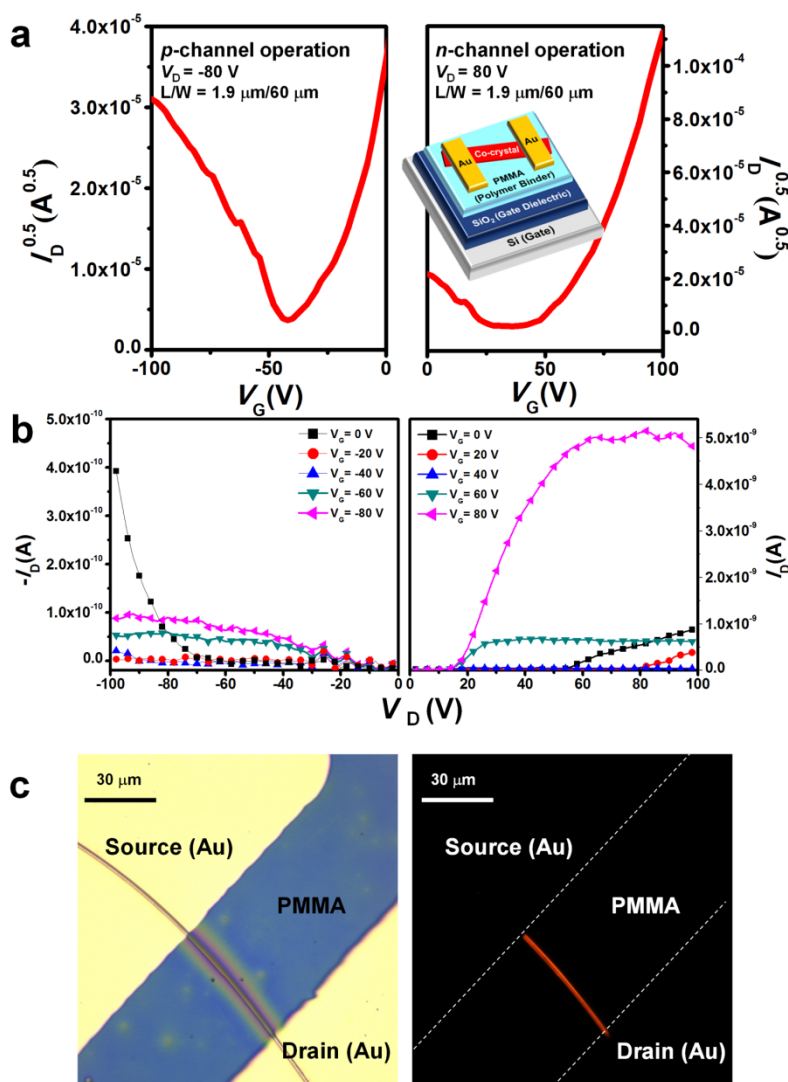


Figure 3-13. (a) Transfer and (b) output characteristics of the single-crystal OFET, fabricated by SVA. I_D , V_D , V_G , and L/W indicate drain current, drain voltage, gate voltage and length-to-width ratio of the active channel cocrystal. Inset: schematic drawing of the device structure. (c) Optical microscope image of a single-crystal OFET (left: under ambient light, right: under UV).

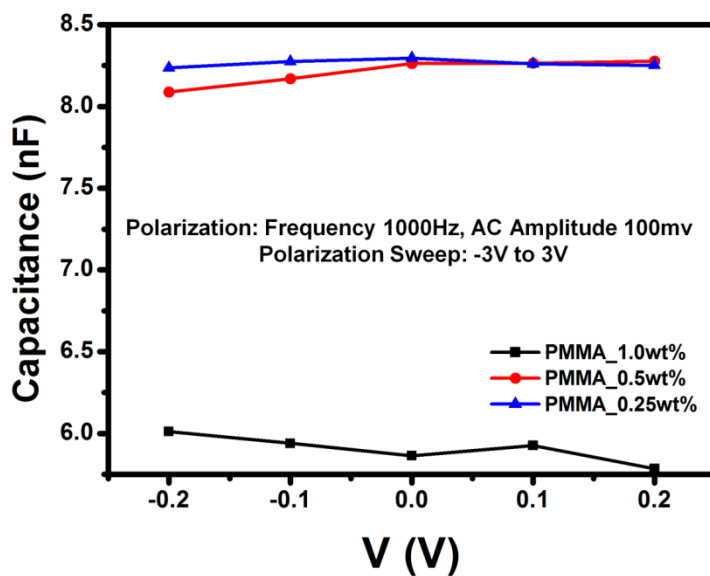


Figure 3-14. The colligative capacitance values of SiO₂ / PMMA layer.

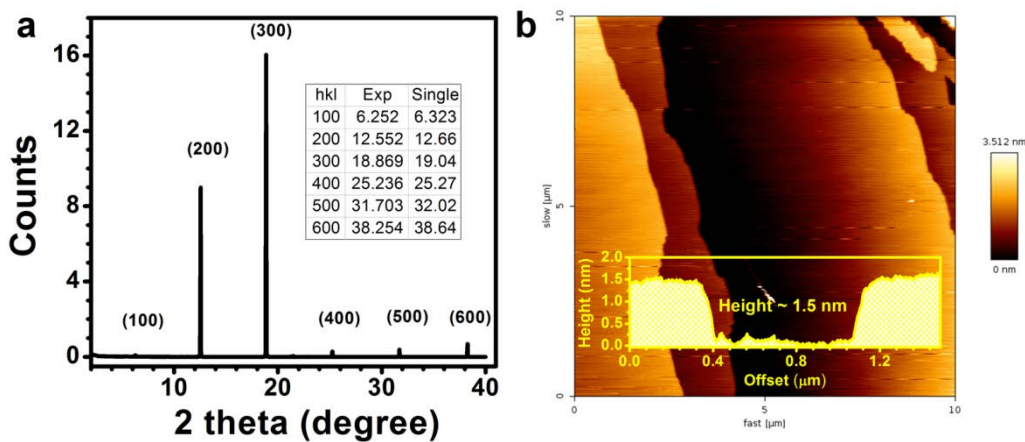


Figure 3-15. (a) Out-of-plane XRD measured on **D·A** (1:1) CT co-crystal, inset table: 2 theta values compared with values found in single-crystal XRD analysis. (b) AFM measured on **D·A** (1:1) CT co-crystal, inset shows height profile between adjacent layers.

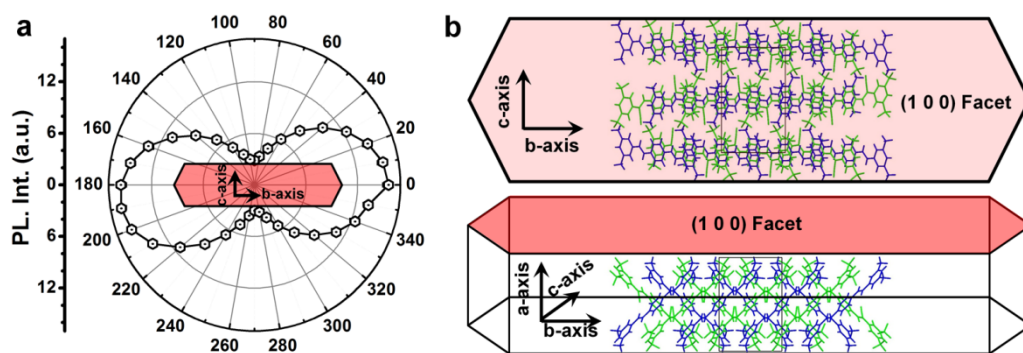


Figure 3-16. (a) measured PL intensity anisotropy of the **D–A** (1:1) CT cocrystal. (b) Schematic drawings of the molecular packing structure with respect to the macroscopic crystal morphology; crystallographic axes are indicated.

3.4. Conclusions

In conclusion, I have comprehensively investigated the rational design of a mixed stack single-crystalline CT system with efficient red luminescence ($\Phi_{\text{PL}}=31\%$) and ambipolar quasi-1D charge transport properties (μ_{h} up to $6.7\times 10^{-3}\text{ cm}^2\text{V}^{-1}\text{s}^{-1}$ and μ_{e} up to $6.7\times 10^{-2}\text{ cm}^2\text{V}^{-1}\text{s}^{-1}$). To this end, an isometric **D** and **A** pair with appropriately tuned frontier MOs were successfully designed and synthesized; distyrylbenzene (DSB) and dicyanodistyrylbenzene (DCS) based **D** and **A** molecules, respectively.

Our combined in-depth structural, electric, spectroscopic and computational analysis allowed for a full exploration of all relevant structure-property relationships in this unique system, which can be summarized as follows.

(i) The molecules could be self-assemble into a 1:1 **D**·**A** mixed columnar structures driven by the tailor-made electronic and geometric properties of **D** and **A**, *i.e.* isometric geometry, favorable Coulomb and H-bonding interactions, and the requirements for electro-neutrality and enthalpic arguments.

(ii) The lowest excited state in the **D**·**A** (1:1) CT co-crystal is mainly ascribed by a HOMO→LUMO excitation, where the HOMO and LUMO are entirely localized on the **D** and **A** moiety, respectively. The distinct CT character of the transition gives rise to a strong red-shifted absorption band with moderately small oscillator strength which allows for bright and highly polarized red emission.

(iii) Solution-processed single-crystalline OFETs shows efficient anisotropic and ambipolar charge carrier transport behavior, with hole and electron mobilities up to $6.7 \times 10^{-3} \text{ cm}^2 \text{V}^{-1} \text{s}^{-1}$ and $6.7 \times 10^{-2} \text{ cm}^2 \text{V}^{-1} \text{s}^{-1}$. The transport was proven to occur along the direction of **D-A-D-A** mixed stacks promoted by the densely packed, planar molecules with localized frontier MOs, which follows a superexchange mechanism to give rise to high *p*- and *n*-channel behavior.

Summing up the remarkable properties of the investigated system, our isometric **D·A** approach opens a new and versatile route towards highly efficient ambipolar and at the same time bright luminescent materials, which holds important implications for next-generation (opto-)electronic applications.

3.5. References

- [1] Tang, C. W.; Van Slyke, S. A. *Appl. Phys. Lett.* **1987**, *51*, 913.
- [2] Yu, G.; Gao, J.; Hummelen, J. C.; Wudl, F.; Heeger, A. J. *Science* **1995**, *270*, 1789.
- [3] Sirringhaus, H.; Brown, P. J.; Friend, R. H.; Nielsen, M. M.; Bechgaard, K.; Langeveld-Voss, B. M. W.; Spiering, A. J. H.; Janssen, R. A. J.; Meijer, E. W.; Herwig, P.; de Leeuw, D. M. *Nature* **1999**, *401*, 685.
- [4] (a) Liu, Y.-Y.; Song, C.-L.; Zeng, W.-J.; Zhou, K.-G.; Shi, Z.-F.; Ma, C.-B.; Yang, F.; Zhang, H.-L.; Gong, X. *J. Am. Chem. Soc.* **2010**, *132*, 16349. (b) Zhang, Y.; Kim, C.;

- Lin, J.; Nguyen, T.-Q. *Adv. Funct. Mater.* **2012**, *22*, 97.
- [5] (a) Meijer, E. J.; De Leeuw, D. M.; Setayesh, S.; Van Veenendaal, E.; Huisman, B.-H.; Blom, P. W. M.; Hummelen, J. C.; Scherf, U.; Klapwijk, T. M. *Nature Mater.* **2003**, *2*, 678. (b) Babel, A.; Wind, J. D.; Jenekhe, S. A. *Adv. Funct. Mater.* **2004**, *14*, 891.
- [6] Sakamoto, Y.; Suzuki, T.; Kobayashi, M.; Gao, Y.; Fukai, Y.; Inoue, Y.; Sato, F.; Tokito, S. *J. Am. Chem. Soc.* **2004**, *126*, 8138.
- [7] (a) Mativetsky, J. M.; Kastler, M.; Savage, R. C.; Gentilini, D.; Palma, M.; Pisula, W.; Müllen, K.; Samorì, P. *Adv. Funct. Mater.* **2009**, *19*, 2486. (b) Yamamoto, Y.; Zhang, G.; Jin, W.; Fukushima, T.; Ishii, N.; Saeki, A.; Seki, S.; Tagawa, S.; Minari, T.; Tsukagoshi, K.; Aida, T. *Proc. Natl. Acad. Sci. U.S.A.* **2009**, *106*, 21051.
- [8] Babel, A.; Zhu, Y.; Cheng, K.-F.; Chen, W.-C.; Jenekhe, S. A. *Adv. Funct. Mater.* **2007**, *17*, 2542.
- [9] Alves, H.; Molinari, A. S.; Xie, H.; Morpurgo, A. F. *Nature Mater.* **2008**, *7*, 574.
- [10] (a) Zhang, J.; Geng, H.; Virk, T. S.; Zhao, Y.; Tan, J.; Di, C.-a.; Xu, W.; Singh, K.; Hu, W.; Shuai, Z.; Liu, Y.; Zhu, D. *Adv. Mater.* **2012**, *24*, 2603. (b) Wakahara, T.; D'Angelo, P.; Miyazawa, K.; Nemoto, Y.; Ito, O.; Tanigaki, N.; Bradley, D. D. C.; Anthopoulos, T. D. *J. Am. Chem. Soc.* **2012**, *134*, 7204. (c) Jonkheijm, P.; Stutzmann, N.; Chen, Z.; de Leeuw, D. M.; Meijer, E. W.; Schenning, A. P. H. J.; Würthner, F. *J. Am. Chem. Soc.* **2006**, *128*, 9535.
- [11] (a) Mori, T. *Chem. Lett.* **2011**, *40*, 428. (b) Hasegawa, T.; Mattenberger, K.; Takeya, J.; Batlogg, B. *Phys. Rev. B* **2004**, *69*, 245115. (c) Takahashi, Y.; Hasegawa, T.;

- Abe, Y.; Tokura, Y.; Nishimura, K.; Saito, G. *App. Phys. Lett.* **2005**, *86*, 063504. (d) Takahashi, Y.; Hasegawa, T.; Abe, Y.; Tokura, Y.; Saito, G. *App. Phys. Lett.* **2006**, *88*, 073504. (e) Kawasugi, Y.; Yamamoto, H. M.; Tajima, N.; Fukunaga, T.; Tsukagoshi, K.; Kato, R. *Phys. Rev. Lett.* **2009**, *103*, 116801. (f) Kawasugi, Y.; Yamamoto, H. M.; Tajima, N.; Fukunaga, T.; Tsukagoshi, K.; Kato, R. *Phys. Rev. B* **2011**, *84*, 125129. (g) Kimata, M.; Ishihara, T.; Tajima, H. *J. Phys. Soc. Jpn.* **2012**, *81*, 073704. (h) Sakai, M.; Sakuma, H.; Ito, Y.; Saito, A.; Nakamura, M.; Kudo, K. *Phys. Rev. B* **2007**, *76*, 045111. (i) Hinderhofer, A.; Schreiber, F. *ChemPhysChem* **2012**, *13*, 628.
- [12] (a) Rao, K. V.; George, S. J. *Chem. Eur. J.* **2012**, *18*, 14286. (b) Schmidt-Mende, L.; Fechtenkötter, A.; Müllen, K.; Moons, E.; Friend, R. H.; MacKenzie, J. D. *Science* **2001**, *293*, 1119. (c) Percec, V.; Glodde, M.; Bera, T. K.; Miura, Y.; Shiyanovskaya, I.; Singer, K. D.; Balagurusamy, V. S. K.; Heiney, P. A.; Schnell, I.; Rapp, A.; Spiess, H.-W.; Hudson, S. D.; Duan, H. *Nature* **2002**, *419*, 384. (d) Sagade, A. A.; Rao, K. V.; Mogera, U.; George, S. J.; Datta, A.; Kulkarni, G. U. *Adv. Mater.* **2013**, *25*, 559.
- [13] (a) Wang, C.; Yin, S.; Chen, S.; Xu, H.; Wang, Z.; Zhang, X. *Angew. Chem.* **2008**, *120*, 9189. (b) Wang, C.; Guo, Y.; Wang, Y.; Xu, H.; Wang, R.; Zhang, X. *Angew. Chem.* **2009**, *121*, 9124. (c) Rao, K. V.; Jayaramulu, K.; Maji, T. K.; George, S. J. *Angew. Chem.* **2010**, *122*, 4314. (d) Dössel, L. F.; Kamm, V.; Howard, I. A.; Laquai, F.; Pisula, W.; Feng, X.; Li, C.; Takase, M.; Kudernac, T.; De Feyter, S.; Müllen, K. *J. Am. Chem. Soc.* **2012**, *134*, 5876.
- [14] (a) Ferraris, J. P.; Poehler, T. O.; Bloch, A. N.; Cowan, D. O. *Tetrahedron Lett.*

- 1973, 14, 2553. (b) Jérôme, D.; Mazaud, A.; Ribault, M.; Bechgaard, K. *J. Phys. Lett.* **1980**, 41, 95. (c) Batail, P. *Chem. Rev.* **2004**, 104, 4887.
- [15] Tayi, A. S.; Shveyd, A. K.; Sue, A. C.-H.; Szarko, J. M.; Rolczynski, B. S.; Cao, D.; Kennedy, T. J.; Sarjeant, A. A.; Stern, C. L.; Paxton, W. F.; Wu, W.; Dey, S. K.; Fahrenbach, A. C.; Guest, J. R.; Mohseni, H.; Chen, L. X.; Wang, K. L.; Stoddart, J. F.; Stupp, S. I. *Nature* **2012**, 488, 485.
- [16] Zhu, L.; Yi, Y.; Li, Y.; Kim, E.-G.; Coropceanu, V.; Brédas, J.-L. *J. Am. Chem. Soc.* **2012**, 134, 2340.
- [17] Döttinger, S. E.; Hohloch, M.; Segura, J. L.; Steinhüher, E.; Hanack, M.; Tompert, A.; Oelkrug, D. *Adv. Mater.* **1997**, 9, 233.
- [18] (a) An, B.-K.; Gierschner, J.; Park, S. Y. *Acc. Chem. Res.* **2012**, 45, 544. (b) Yoon, S.-J.; Chung, J. W.; Gierschner, J.; Kim, K. S.; Choi, M.-G.; Kim, D.; Park, S. Y. *J. Am. Chem. Soc.* **2010**, 132, 13675.
- [19] Gierschner, J.; Ehni, M.; Egelfaaf, H.-J.; Medina, B. M.; Beljonne, D.; Benmansour, H.; Bazan, G. C. *J. Chem. Phys.* **2005**, 123, 144914.
- [20] Bartholomew, G. P.; Bu, X.; Bazan, G. C. *Chem. Mater.* **2000**, 12, 2311.
- [21] Park, S. K.; Kim, J. H.; Yoon, S.-J.; Kwon, O. K.; An, B.-K.; Park, S. Y. *Chem. Mater.* **2012**, 24, 3263.
- [22] (a) Lee, W. H.; Lim, J. A.; Kwak, D.; Cho, J. H.; Lee, H. S.; Choi, H. H.; Cho, K. *Adv. Mater.* **2009**, 21, 4243. (b) Liu, C.; Minari, T.; Lu, X.; Kumatani, A.; Takimiya, K.; Tsukagoshi, K. *Adv. Mater.* **2011**, 23, 523.

- [23] An, B.-K.; Kwon, S.-K.; Jung, S.-D.; Park, S. Y. *J. Am. Chem. Soc.* **2002**, *124*, 14410.
- [24] Kabe, R.; Nakanotani, H.; Sakanoue, T.; Yahiro, M.; Adachi, C. *Adv. Mater.* **2009**, *21*, 4034.
- [25] Gierschner, J.; Mack, H.-G.; Oelkrug, D.; Waldner, I.; Rau, H. *J. Phys. Chem. A* **2004**, *108*, 257.
- [26] (a) Coropceanu, V.; Cornil, J.; da Silva Filho, D. A.; Olivier, Y.; Silbey, R.; Brédas, J.-L. *Chem. Rev.* **2007**, *107*, 926. (b) Giri, G.; Verploegen, E.; Mannsfeld, S. C. B.; Atahan-Evrenk, S.; Kim, D. H.; Lee, S. Y.; Becerril, H. A.; Aspuru-Guzik, A.; Toney, M. F.; Bao, Z. *Nature* **2011**, *480*, 504.
- [27] Zaumseil, J.; Sirringhaus, H. *Chem. Rev.* **2007**, *107*, 1296.
- [28] Frisch, M. J.; Trucks, G. W.; Schlegel, H. B.; Scuseria, G. E.; Robb, M. A.; Cheeseman, J. R.; Scalmani, G.; Barone, V.; Mennucci, B.; Petersson, G. A.; Nakatsuji, H.; Caricato, M.; Li, X.; Hratchian, H. P.; Izmaylov, A. F.; Bloino, J.; Zheng, G.; Sonnenberg, J. L.; Hada, M.; Ehara, M.; Toyota, K.; Fukuda, R.; Hasegawa, J.; Ishida, M.; Nakajima, T.; Honda, Y.; Kitao, O.; Nakai, H.; Vreven, T.; Montgomery, Jr., J. A.; Peralta, J. E.; Ogliaro, F.; Bearpark, M.; Heyd, J. J.; Brothers, E.; Kudin, K. N.; Staroverov, V. N.; Kobayashi, R.; Normand, J.; Raghavachari, K.; Rendell, A.; Burant, J. C.; Iyengar, S. S.; Tomasi, J.; Cossi, M.; Rega, N.; Millam, J. M.; Klene, M.; Knox, J. E.; Cross, J. B.; Bakken, V.; Adamo, C.; Jaramillo, J.; Gomperts, R.; Stratmann, R. E.; Yazyev, O.; Austin, A. J.; Cammi, R.; Pomelli, C.; Ochterski, J. W.; Martin, R. L.;

Morokuma, K.; Zakrzewski, V. G.; Voth, G. A.; Salvador, P.; Dannenberg, J. J.; Dapprich, S.; Daniels, A. D.; Farkas, Ö.; Foresman, J. B.; Ortiz, J. V.; Cioslowski, J.; Fox, D. J. Gaussian 09, Revision A.02, Gaussian, Inc., Wallingford CT, 2009.

[29] Yanai, T.; Tew, D. P.; Handy, N. C. *Chem. Phys. Lett.* **2004**, *393*, 51.

[30] Flukiger, P.; Luthi, H. P.; Portmann, S.; Weber, J. MOLEKEL, Version4.3; Swiss National Computing Centre CSCS, Manno, Switzerland, 2000, <<http://www.cscs.ch/molkel/>>

Chapter 4.

Bridging Highly Luminescent – Ambipolar Transport Characters: Light-Emitting Organic Field-Effect Transistors Based on Two Dimensionally Growing Charge-Transfer Complex Cocrystals

4.1. Introduction

Molecular heterosystems such as complexes and interfaces based on organic π -conjugated molecules have raised enormous research interest due to the great opportunities of novel optoelectronic functionalities beyond the individual characters of constituting materials.^[1] Bestowing unconventional electronic features, such as (super-)conductivity,^[2a-c] ferroelectricity,^[2d,e] and magnetic properties,^[2f] charge-transfer (CT) phenomenon based on electron donor (D) - acceptor (A) complexes or interfaces is highly attracting and paves the way toward developing next-generation organic devices applications. As theoretically and experimentally revealed, the characteristics of such complexes are strongly determined not only from their molecular arrangements (i.e., segregated and mixed stacks) but also from the energetic offset between ionization potential of D ($IP(D)$) and electron affinity of A ($EA(A)$);^[2g] until now, however, much devote has been focused on unconventional metallic (super-)conductivity typically from segregately stacked systems with mixed valence

characters. Only recently, mixed stacked semiconducting CT systems grasped further attention due to the intriguing behavior of such complex, for example ambipolar transport in organic field-effect transistor (OFET) devices, distinctive photoconductivity, and photoluminescent (PL) character.^[3] These electrical and optical features of mixed stacked CT indeed offer elegant ways for realizing high performing balanced ambipolar transport, light propagation, and smart luminescence CT, of which the performances are highly controlled by chemical-/crystal-engineering strategies regulating electronic coupling between nearby molecules.

Indeed, it is currently well-established that mixed stack CT can transport both p-/n-type charge carriers by characteristic superexchange mechanism; i.e., despite absence of direct coupling between nearest donors or acceptors by intercalated counter constituent, frontier molecular orbital (MO) mixing between D-A can give rise to non-direct (effect) electronic coupling for hole and electron with highly balanced character in appropriate conditions.^[4] First evaluation of CT complex as semiconducting active channel was conducted in charge density wave state of quasi-1D organic metal tetrathiafulvalene (TTF) - tetracyanoquinodimethane (TCNQ). Further evaluations of field-effect charge transport natures in band insulators (e.g., Mott insulator, and charge-ordered insulator) or ionic CT system have been successively carried out, some of which manifested characteristic ambipolar transport under metal-insulator transition conditions.^[5] Recent advances in respect of developing materials have opened new horizon for achieving favorable ambipolar transport in ambient temperature condition

using CT systems with neutral character.^[3] Among these notable results, Qin et al. have successfully surmounted low field-effect mobility values ($\mu_h \sim 0.77$, and $\mu_e \sim 0.24 \text{ cm}^2 \text{ V}^{-1} \text{ s}^{-1}$) utilizing appropriate D-A pair – i.e., meso-diphenyl tetrathia[22]annulene[2,1,2,1] (DPTTA) as a donor, and 4,8-bis(dicyanomethylene)-4,8-dihydrobenzo[1,2-b:4,5-b']-dithiophene (DTTCNQ) as an acceptor, offering unique quasi 2D electronic coupling comprised of both effective and direct coupling in two distinctive directions.^[3d]

In addition to the ambipolarity, neutral CT complexes with adequate electronic as well as structural factors render great opportunities for realizing luminescent CT systems.^[3h-k] In this class of materials, newly generated CT gap in a visible range can be manifested, dictated by $IP(D)$ and $EA(A)$ with electrostatic stabilization factor.^[6] The vertical transition from ground state S_0 to the lowest excited singlet state S_1 (i.e., ^1CT state) results in pronounced CT character due to the localized highest occupied MO (HOMO, H) and lowest unoccupied MO (LUMO, L) to D and A, respectively; which gives rise to bathochromic shift of CT fluorescence against those from individual D/A emission. The transition dipole moment (and oscillator strength f) of CT transition, however, is expected to show somewhat diminishing value, attributed to the negligible orbital overlap integral; thus, should lead to low radiative constant (k_F). In this regard, realization of electroluminescence (EL) during OFETs operations (i.e., light-emitting OFET, LE-OFET) is greatly hampered by limited k_F , despite notable optoelectronic functionalities (e.g., ambipolarity and fluorescence) of this class of CT systems.

In this study, therefore, I gave a particular attention on possibility for bridging peculiar ambipolar transport with CT emission character to design unique CT semiconductor for LE-OFET application. For this, I emphasize the significances of both high luminescence quantum yield and balanced ambipolarity in CT cocrystal. To implement both important parameters, herein, further attention is addressed to molecularly tailored dicyanodistyrylbenzene (DCS) based CT system which manifested prominent CT luminescence with remarkable ambipolar transport.^[7] In this study, a novel aggregation induced enhanced emission (AIEE) based CT system is reported, which comprised of DCS based donor (2MDCS, **D1**),^[8] and acceptor (CN-TFPA, **A1**) with 2:1 stoichiometry;^[9] manifesting unprecedentedly high CT emission PLQY ($\Phi_F = \text{ca. } 60\%$). From in-depth explorations on structure-property relationship, not only tightly packed structure originated from minimized chemical structure mismatch (i.e., isometric approach) effectively reduced exciton trap density to lower the non-radiative decay rate (k_{nr}) but also higher energy transitions in $S_0 \rightarrow S_1$ by configuration interaction with partial CT character promoted efficient radiative transition. In addition to the favorable CT emission, highly balanced ambipolar transport (μ_h and μ_e in the range of $10^{-4} \text{ cm}^2 \text{ V}^{-1} \text{ s}^{-1}$) is promoted in a programmed densely packed two-dimensional CT cocrystal sheet; which gives rise to notable EL emission during transistor action. The in-depth expedition of highly correlated structure, electronic, and optoelectronic properties of this 2D mixed stacked CT well rationalizes the potentialities of this class of CT materials for next-generation

electroluminescence devices applications.

4.2. Experimental

Synthesis Both (2Z,2'Z)-2,2'-(1,4-phenylene)bis(3-p-tolylacrylonitrile) (2MDCS, **D1**) and (2Z,2'Z)-3,3'-(1,4-phenylene)bis(2-(3,5-bis-(trifluoromethyl)phenyl)acrylonitrile), (CN-TFPA, **A1**) were synthesized by one-step Knoevenagel condensation reaction as previous reports, see **Scheme 2-1**, and **Scheme 4-1**.^[8,9] 2,2'-(1,4-phenylene)diacetonitrile (1.50 g, 0.0096 M) and 4-methylbenzaldehyde (2.31 g, 0.0192 M) were dissolved in a mixture of t-butyl alcohol (35 ml) and tetrahydrofuran (15 ml) using 100 ml round bottom flask (RBF). Tetrabutylammonium hydroxide (1.92 ml of 1 molar concentration in methanol) was dropped into the stirred reactants solution. The reaction was undergone at 50°C for 2 hours. After cooling the RBF, the precipitated product was filtered and washed with methanol, and carried out column chromatography purification. Further purification was conducted by recrystallization (chloroform/MeOH, yield 2.30 g) and sublimation purification (ca. 190°C, 5×10^{-6} torr). The chemical structure of 2MDCS was confirmed by ¹H NMR (300 MHz, CDCl₃) δ [ppm]: 7.84 (d, 4H), 7.74 (s, 4H), 7.57 (s, 2H), 2.43 (s, 6H).

Sample Preparation. The single crystals of **D1** and **A1** were grown by physical

vapor transport (PVT) under high purity Ar gas flow, at 285°C and 280°C, respectively for PLQY measurements. The two-dimensional 2:1 **D1-A1** CT complex cocrystals were also grown by PVT, the optimized temperature condition was 285°C. For optical properties measurement, the solutions of **D1**, and **A1** were prepared with concentration of 1×10^{-5} M, using tetrahydrofuran (THF). The 2:1 **D1-A1** THF solution was prepared with concentration of 5×10^{-6} M in respect of **A**. The nanoparticle suspension of **D1**, **A1**, and 2:1 **D1-A1** was prepared using water:THF (9.8:0.2, v:v), with same concentration of corresponding solution state. To obtain nanoparticle suspension with minimized scattering effects, the THF master solution was rapidly injected into water containing bial under vigorously stirred condition. The supramolecular structures of **D1** and **A1** in **Figure 4-1** were obtained through dropcasting method using 1,2-dichloroethane 0.05 wt% solution.

Characterization. The ^1H nuclear magnetic resonance (NMR) spectra were obtained using a Bruker Avance-300 (300 MHz, CDCl_3 solution). The cyclovoltametry (CV) measurements were carried out using a Princeton Applied Research Potentiostat/Galvanostat Model 273A with Ar bubbling condition; the LUMO of **D1** and **A1** were defined by the results, and HOMO of **D1** and **A1** were extracted by optical bandgaps. The absorption and PL spectra were attained by Shimadzu UV-1650 PC spectrometer and Photon Technology International QM-40 spectrophotometer, respectively. The PLQY values were obtained through a 3.2-in. integrating sphere

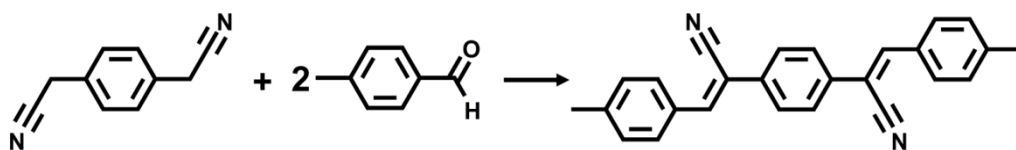
equipped QM-40 spectrometer. The lifetime results at PL λ_{\max} were recorded using a Picoquant FluoTime 200 instrument by time-correlated single photon counting method. The atomic force microscope (AFM) results were obtained by a Bruker Nanoscope III multimode SPM using tapping mode RTESP cantilevers. The thermogravimetric analyses (TGA) were conducted using a TA Instruments Q-5000 IR, with a heating rate of 5°C/min. The single-crystal X-ray analyses were conducted using a Bruker D8 Kappa diffractometer and a SMART APEX II CCD detector, with microsource MoK α radiation ($\lambda = 0.071073$ nm). The measurement were carried out under T condition of 100, and 293 K; the structure solution and refinement was carried out by SHELXS-97^[10] and space group assignment by PLATON.^[11]

Quantum Chemical Calculation. Ground-state MOs of the **D1**, **A1** compounds and **D1-A1** dimer pair were calculated by density functional theory (DFT) with B3LYP functional and 6-31G(d,p) basis set, in the Gaussian09 program package.^[12] Excited states of the **D1-A1** dimer pair were estimated by TD-DFT calculation using Coulomb-attenuated method (CAM)-B3LYP functional with 6-311G* basis set in a **D1-A1** pair arrangement dictated from the single-crystal XRD analysis. Transfer Integral values for both hole and electron in intrastack and interstack direction was calculated by energy splitting method, using CAM-B3LYP functional and 6-311G* basis set. The (HOMO – HOMO-1)/2 and (LUMO – LUMO+1)/2 were calculated for estimation of transfer integral for hole, and electron, respectively.

Device Characterization. For top-contact devices fabrication, p-doped SiO₂/Si

(thermally grown, 300 nm thick SiO₂ layer) substrates were used after piranha solution treatment and cleaned by acetone/isopropylalcohol (sonication, 10 min). The self-assembled monolayer of octadecyltrichlorosilane (ODTS) was formed by vacuum phase treatment in a vacuum oven (80 °C, 150 min), after 20 min of UV O₃ treatment applied to cleaned substrates. The aforementioned PVT grown CT cocrystals were laminated onto the ODTS treated substrates using a strand of hair; then, 50 nm thick Au source-drain electrodes were thermally deposited through a patterned shadow mask, with a high vacuum condition (ca. 1×10^{-6} torr, and the deposition rate of 0.2 Å/s). The electrical properties of prepared devices were measured by Keithley 4200 SCS instrument in a nitrogen-filled glovebox.

For bottom-contact device fabrication, SiO₂/Si substrates with prepatterned source-drain Au electrodes were used with identical cleaning procedure (*vide supra*). CT cocrystal laminated devices were taken into a vacuum probe station and characterized using Keithley 6517A electrometer and Keithley 487 Picoammeter/Voltage Source. The photoconductivity was measured using a Hamamatsu S1226-8bk photodiode. Electroluminescence spectrum of **D1-A1** CT cocrystal was recorded using an Andor Du420 spectroscopy CCD camera and Spectra-Physics Oriel Instruments USA (Model 77441).



Scheme 4-1. Synthetic procedure to obtain 2MDCS (**D1**).

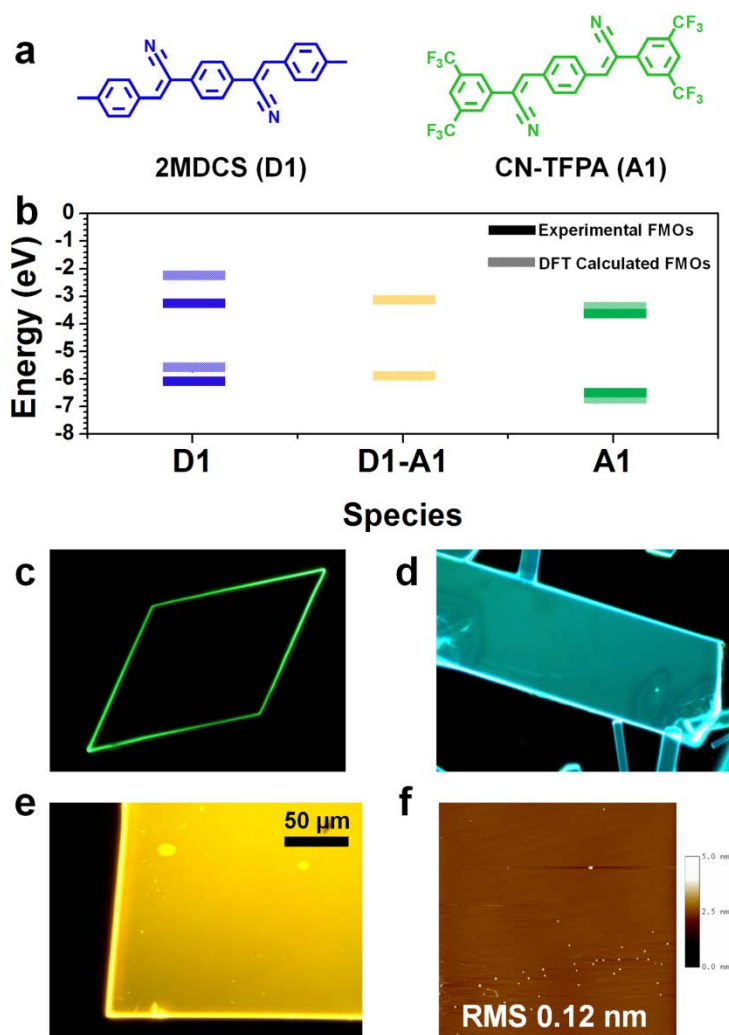


Figure 4-1. (a) Chemical structures of 2MDCS (**D1**) and CN-TFPA (**A1**). (b) DFT (B3LYP, 6-31G(d,p)) calculated frontier molecular orbitals of **D1**, **A1**, and **D1-A1** and experimentally determined frontier molecular orbitals of **D1** and **A1**. (c, d) Images of self-assembled **D1** and **A1** supramolecular structures, and (e) image of physical vapor transport grown two-dimensional CT cocrystal taken under UV using optical microscope. (f) Atomic force microscope image of CT cocrystal surface (5 μm × 5 μm).

4.3. Results and Discussion

4.3.1. Materials. DCS based donor (2MDCS, **D1**) and acceptor (CN-TFPA, **A1**) were prepared by simple Knoevenagel condensation reaction as previous reports (**Figure 4-1a**),^[8,9] see **Experimental Section**. Both **D1** and **A1** present centrosymmetric DCS backbone structure with varied substitution patterns. The isometric **D1** and **A1** design minimized molecular structure mismatch, therefore rendered simultaneous charge-transfer complexation despite somewhat small deviation of FMOs between the constituents, *vide infra*. The moderate energetic differences are achieved by substituting electron donating (methyl, -CH₃) and electron withdrawing (trifluoromethyl, -CF₃) functionalities to **D1** and **A1**, respectively. The frontier MOs i.e., HOMO and LUMO of **D1** are experimentally determined to -6.1 eV and -3.3 eV; however, further stabilization occurred in **A1** case (-6.5 eV and -3.6 eV), see **Figure 4-1b**. The DFT calculation results quantitatively well-reflect electronic properties of **D1** and **A1**, see **Figure 4-1b** and **Experimental Section**. The tailor-made molecular designs and electronic properties give rise to facile mixed stacked charge-transfer (CT) complex formation with unique optoelectronic and structural features.

4.3.2. Structure Analyses. Unique 2D hierarchical structure of **D1-A1** based CT complex is envisioned by supramolecular synthons of the constituents, i.e., -CN···HC- which Park et al. previously gave particular emphasize of laterally aligned -CN for

achieving tightly stacked 2D molecular arrangement. Indeed, the centrosymmetric DCS structures of **D1** and **A1** engender 2D hierarchical assembly during drop casting of 1,2-dichloroethane solutions, **Figure 4-1c** and **1d**. Our previous reports on CT complexes comprised of –CN containing acceptors also manifested the supramolecular synthon (-CN···HC-) during CT complexation; however, prominent Coulombic interaction along stacking direction (i.e., quasi 1D mixed stack) and/or noncentrosymmetric acceptor design effectively impeded 2D assembly.^[31,7] In fact, the 2D supramolecular structures in mixed stack CT complexes have rarely been obtained, due to the 1D anisotropic D-A interaction along stacking direction; however, ultrathin (< 1 μm) 2D geometries are especially beneficial for desired interfacial adhesion, sufficient drain current supply, and uniform performances by large-area single-crystalline active-channel formability.^[13]

Indeed, it was able to attain genuine 2D CT nanosheet structures by PVT crystal growth method with great uniformity (**Figure 1e, f**, see Experimental Section). The CT complex cocrystals manifest desirable supramolecular dimensions, i.e., several millimeters in length and width, but only few hundred nanometers in height (ca. 200 – 800 nm); thus are considered to be favorable for OFETs application, *vide infra*.

The peculiar structural characters could be well elucidated by single-crystal X-ray diffraction result (**Figure 4-2**). As described in **Figure 4-2**, the CT complex exhibited regular 2 (**D1**) : 1 (**A1**) mixed stacked molecular arrangement within a triclinic unit cell at 100 K (a: 0.89 nm, b: 1.12 nm, c: 1.64 nm; α : 103.2°, β : 95.1°, γ : 92.2°), the 2:1

stoichiometry was further analyzed by ^1H NMR analysis (**Figure 4-3**). In room temperature (293 K), it is expected to show only slight enlargement in the lattice constants of the crystal; since no changes in the symmetry is observed by temperature increment. The detailed structural analyses are available in **Table 4-1**. The intermolecular interactions could be categorized by three characteristic directions (i.e., molecular short axis, long axis, and π -plane facet directions). The unique 2D structure formation can easily be correlated by balanced 2D intermolecular interactions, see **Figure 4-2**. The 2:1 **D1-A1** alignment showed substantial π -overlap between adjacent molecular pairs (ca. 3.5 Å for both **D1-D1** and **D1-A1** dimer pairs, slightly shorter in the latter case; counter slip angle of 47.5°, and counter roll angle of 88.0°, see **Figure 4-2e**), facilitated by spontaneous **D1-A1** Coulombic interaction. Meanwhile, noteworthy intermolecular interaction networks are presented between adjacent molecular stacks (along molecular short axis direction), by $-\text{CN}$ and $-\text{CF}_3$ (**Figure 4-2b**, and **2e**). As depicted in **Figure 4-2d**, $-\text{CN}$ units not only result in H-bonding interaction between laterally aligned **D1** molecules but also promote local dipole alignment. In addition, multiple $-\text{CF}_3$ induced H-bonding interactions strongly sustain the 2D scaffold. Such balanced intermolecular interaction network with densely packed structure comprehensively gives rise to coplanarized molecular conformations (**Figure 4-4**), hence promotes favorable electronic coupling with non-negligible wavefunction overlap by configuration interaction, *vide infra*. In contrast, only few weak $-\text{CF}_3$ induced H-bonding interactions are detectable in molecular long axis direction; thus

effectively restricts 3D growth of the current CT complex.

The spontaneity of CT complexation is confirmed by DSC analyses, the 2:1 mixture powder of **D1/A1** shows characteristic exothermal transition at 247.9°C and completely new melting transition at 254.8°C (i.e., melting of CT complex) during the first heating regime; the thermal property essentially becomes identical to that of **D1-A1** CT cocrystal during the second cycle (**Figure 4-5**).

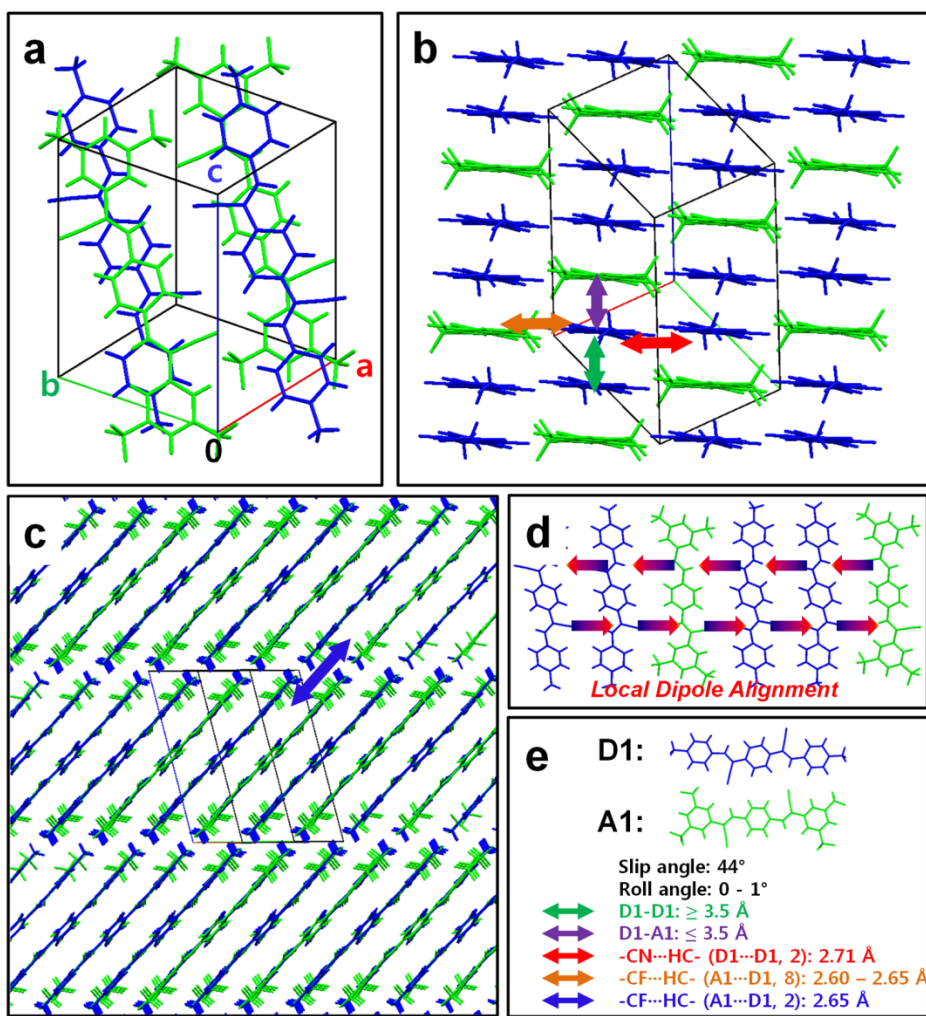


Figure 4-2. (a) Molecular arrangement of **D1-A1** 2:1 CT cocrystal from simulated single-crystal X-ray diffraction analyses. (b,c) roll and slip angle views. (d) Speculated local dipole alignment induced from $-CN$ functionalities. (e) Summarized characteristic intermolecular interactions and slip-/roll-angle of molecular arrangement. Green arrow in (b, e): **D1-D1** π - π interaction; purple arrow in (b, e) **D1-A1** π - π interaction; red arrow in (b, e): **D1-D1** $-CN \cdots HC-$ interaction; orange arrow in (b, e) **D1-A1** $-CF \cdots HC-$ interaction; blue arrow in (c, e): **D1-A1** $-CF \cdots HC-$ interaction.

Table 4-1. Crystal data and structure refinement for **D1-A1** (2:1) CT cocrystal in 100 K and 293 K.

Temperature	100 K	293 K
Stoichiometry 2MDCS:CN-TFPA	2:1	2:1
Crystal appearance	Yellow plate	Yellow pate
Crystal system	Triclinic	Triclinic
Space group	P2(1)/c	
Unit cell dimensions	a = 8.898 Å $\alpha = 103.245^\circ$ b = 11.162 Å $\beta = 95.134^\circ$ c = 16.400 Å $\gamma = 92.214^\circ$	a = 8.910 Å $\alpha = 104.380^\circ$ b = 11.387 Å $\beta = 95.963^\circ$ c = 16.870 Å $\gamma = 92.048^\circ$
Volume	1576 Å ³	1646 Å ³
Z	2	2
Density (calculated)	1.396 g cm ⁻³	1.337 g cm ⁻³
Reflection measured	5840	
Number of parameters	444	
R (F) (all reflections)	0.0897	
wR (F) (all reflections)	0.1526	
Packing motif	Parallel stacing	Not solved
Refinement method	Full-matrix least-squares on F ²	

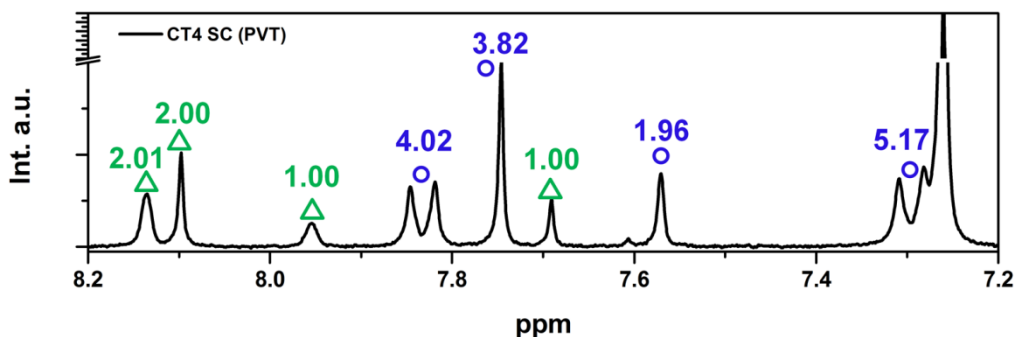


Figure 4-3. ¹H NMR analysis of physical vapor transport grown CT cocrystal. The peak positions (circle: **D1**, triangle: **A1**) are assigned from individual ¹H NMR analyses results. The integrated values indicate 2:1 stoichiometry of **D1**:**A1**.

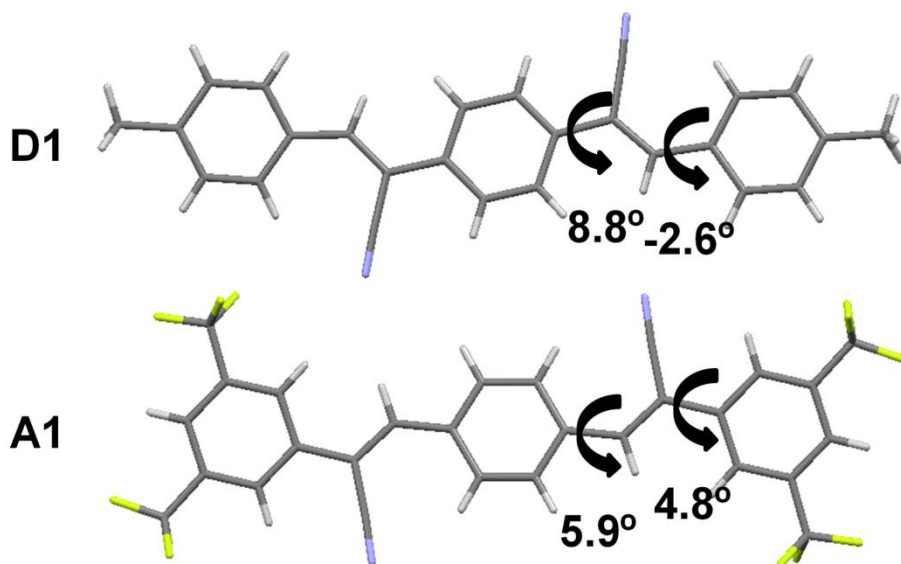


Figure 4-4. Coplanarized molecular geometries of 2MDCS (**D1**) and CN-TFPA (**A1**) found from SC-XRD analyses. The dihedral angle of each single bond twisting is indicated.

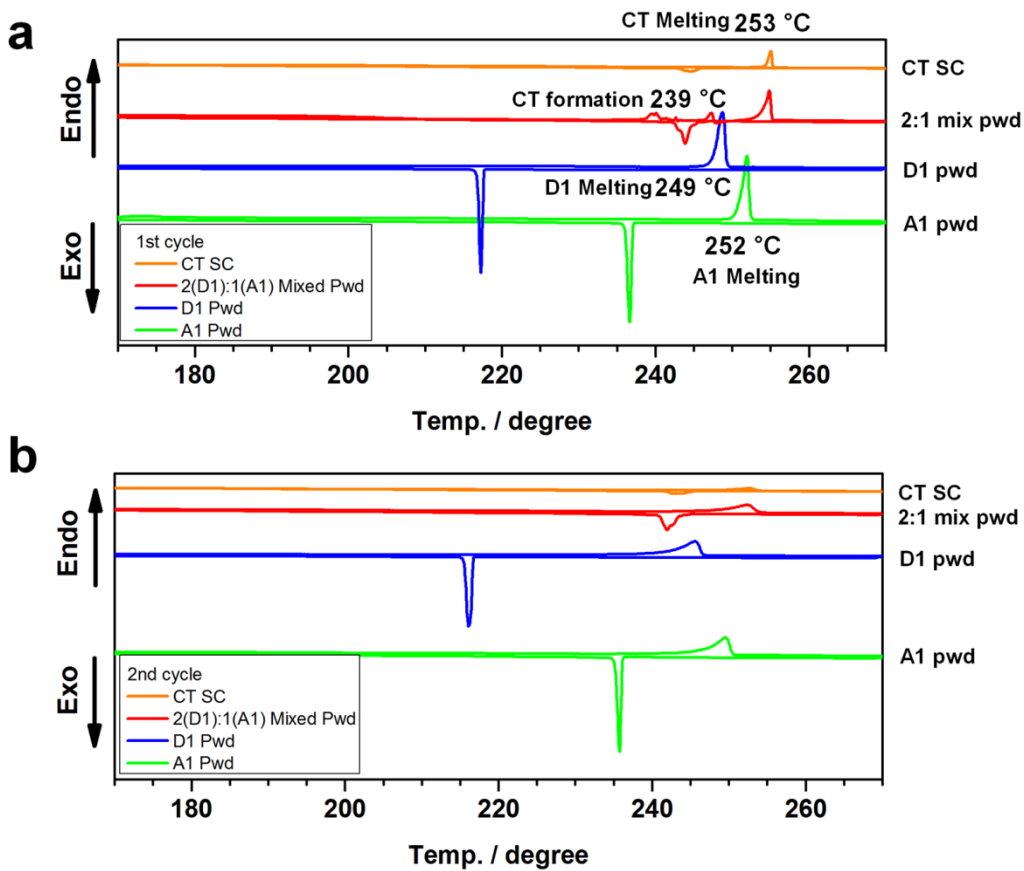


Figure 4-5. DSC curves of PVT grown single-crystals, **D1-A1** 2:1 mixture powder, **D1** powder, and **A1** powder samples; (a): the first cycle, and (b): the second cycle.

4.3.3. Electronic Properties and Photophysics. The steady-state absorption and PL spectra on **D1/A1** solution and nanoparticle suspension were recorded as stated in the **Experimental Section**, see **Table 4-2** and **Figure 4-6**. As can be predicted from calculated electronic properties of 2MDCS and CN-TFPA, the isolated states of **D1/A1** in solution (tetrahydrofuran, THF) exhibit similar absorption and emission energies; however with negligible emission by molecular torsion induced non-radiative deactivation. On the other hand, both compounds exhibit bright solid-state fluorescence with similar energies in their nanoparticle states (**D1**: $\lambda_{em} = 526$ nm, and **A1**: $\lambda_{em} = 514$ nm). The absorption spectra from **D1** and **A1** nanoparticle suspensions show stacking induced shoulder at around 415 nm, suggesting fine crystallinity even in kinetically controlled nanoparticle states. This high PL enhancement can be attributed from programmed (intra- / intermolecular) structural factors of 2MDCS and CN-TFPA, i.e., coplanarization and tightly stacked molecular arrangement; resulting in typical AIEE characteristics.^[14] Indeed, single crystals of both constituents exhibited high absolute photoluminescence quantum yield (PLQY, Φ_F ; **D1**: $\Phi_F = 89\%$, and **A1**: $\Phi_F = 83\%$); thus gives rise to considerably high radiative rate constant (k_F) of 27.0×10^7 s⁻¹ and, 13.2×10^7 s⁻¹, respectively (**Figure 4-7**). The relevant photophysical measures are summarized in **Table 4-2**.

The 2:1 CT nanoparticle suspension could facily be achieved using **D1-A1** mixture solution, which represents **D1-A1** CT state with minimized optical density in

its solid-state. Apparent CT band is observed from low lying energy absorption (2.72 eV, 455 nm). The molar extinction coefficient of CT absorption maximum is extracted to $\epsilon_m = 1.14 \times 10^4 \text{ M}^{-1} \text{ cm}^{-1}$, and gives oscillator strength (f) of 0.15 by.

$$f = 4.319 \times 10^{-9} [M \cdot \text{cm}^2] \int \epsilon_m(\nu) d\nu$$

The oscillator strength of S_1 transition, which is comparable to that from reference luminescent CT, infers possibility for highly luminescent character.^[7] The absorption transition characters are qualitatively reproduced by TD-DFT calculation of **D1-A1** dimer, see **Table 4-3**, **Figure 4-8**, and **Experimental Section**. The lowest vertical transition at 2.72 eV essentially corresponds to calculated energy at 3.11 eV ($S_0 \rightarrow S_1$); the following at 3.07 eV and 3.56 eV thus correspond to the calculated energy at 3.39 eV ($S_0 \rightarrow S_2$) and 3.60 eV ($S_0 \rightarrow S_3$) transition. The calculated singlet transitions represent CT, partial CT, and local excited (LE) states, respectively; however, the transition energies except for ($S_0 \rightarrow S_3$) somehow are overestimated in calculation result from TD-DFT with CAM-B3LYP functional. The lowest singlet transition, in particular, offers remarkable emission properties with novel CT AIEE characteristic, *vide infra*.

As depicted in **Figure 4-8a**, $S_0 \rightarrow S_1$ transition is mainly ascribed to the $H \rightarrow L$ (83 %) excitations; the H is distributed onto the **D1** molecule in **D1-A1** dimer pair. Similarly, the L state is exclusively localized at **A1** molecule by apparent CT character of the lowest singlet transition. It should however be noted that higher energy

contributions in $S_0 \rightarrow S_1$, i.e., $H-2 \rightarrow L$, and $H \rightarrow L+1$ by configuration interaction, which indeed provide non-negligible orbital overlap and oscillator strength *via* partial CT and LE characters, respectively. Furthermore, it should also be reminded that the PLQY do not solely dictated by oscillator strength, but other factors, e.g., k_F , k_{nr} , and τ_F , should be carefully dealt with for evaluating emission properties. Indeed, current CT system manifests unprecedentedly high PLQY ($\Phi_F = \text{ca. } 60\%$, see **Table 4-2**), which is among the highest value found from CT cocrystals. The remarkable emission character can be elucidated not only by configuration interaction factors but also by high k_F and moderate k_{nr} . Attributed to the small energetic offset between **D1** and **A1**, relatively large energy gap is presented ($\lambda_{\text{abs}} = 455 \text{ nm}$), which significantly reduces k_{nr} (ca. $1.5 \times 10^{-7} \text{ s}^{-1}$) compared to the relatively high k_F (ca. $2.3 \times 10^{-7} \text{ s}^{-1}$), which are experimentally determined by fluorescence lifetime measurement, see **Figure 4-7**. Furthermore, it is obvious that the structural factors - tightly stacked molecular arrangement with noteworthy uniformity of the single crystal, render minimized trap density. This can be evidenced from comparably lower PLQY value found from nanoparticle ($\Phi_F = 17 - 18\%$). Such notable luminescence features indeed enable EL emission from LE-OFETs operation.

Table 4-2. Summarized optical characteristics of **D1**, **A1**, and CT complex cocrystal.

	D1	A1	CT
$\lambda_{\text{abs},S1}$ [nm]	340	361	455
ϵ_{m} [$10^4 \text{ M}^{-1} \text{ cm}^{-1}$]	2.38	3.9	1.14
f_{exp}	-	-	0.15
f_{cal}	-	-	0.16
$\lambda_{\text{em},S1}$ [nm]	526	514	555
Φ_{F}	0.89	0.83	0.6
$\tau_{\text{F,Avg}}$ [ns]	3.3	6.3	26.3
k_{F} [$\times 10^7 \text{ s}^{-1}$]	27	13.2	2.3

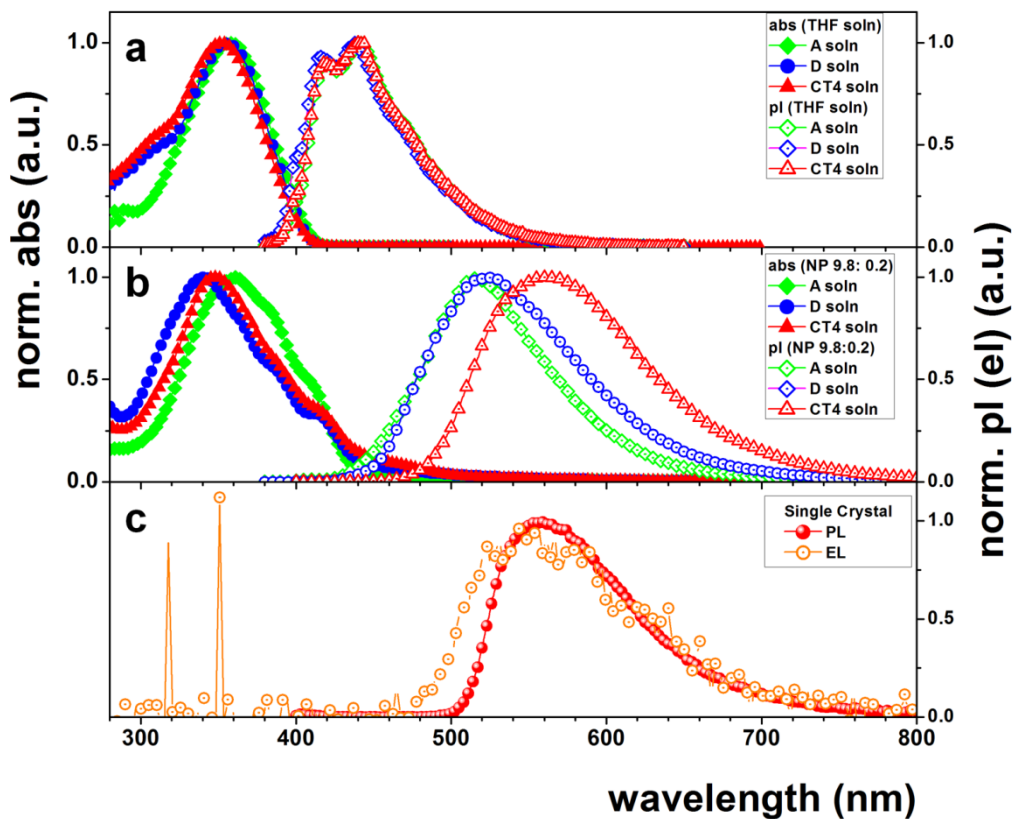


Figure 4-6. (a) Normalized UV-vis absorption and photoluminescence (PL) spectra of dilute **D1**, **A1**, and **D1-A1** (2:1) THF solution. (b) Normalized UV-vis absorption and PL spectra of **D1**, **A1**, and **D1-A1** (2:1) nanoparticle suspension (water:THF, 0.98:0.02). The solid and open circle: **D1** absorption and PL; the solid and open diamond: **A1** absorption and PL; the solid and open triangle: **D1-A1** CT pair absorption and PL spectra in solution (a) and nanoparticle suspension (b). (c) PL (solid circle) and electroluminescence spectra (open circle) of physical vapor transport grown **D1-A1** CT cocrystal.

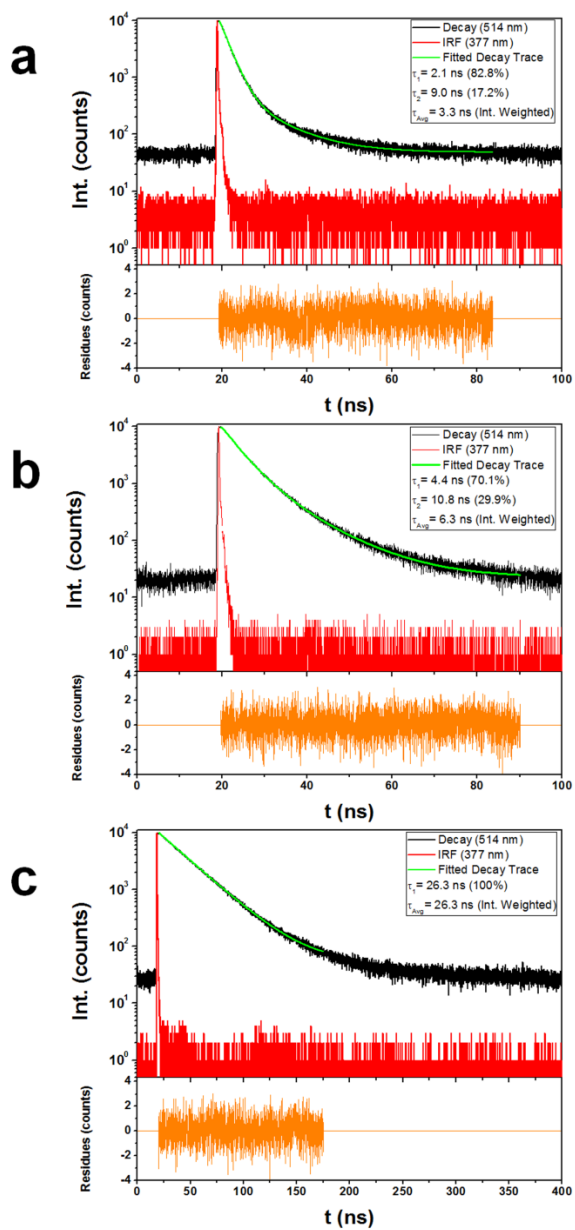


Figure 4-7. Solid-state PL lifetime spectra of **D1** single crystal (a), **A1** single crystal (b), and **D1-A1** 2:1 CT cocystal (c).

Table 4-3. Vertical transition energies of **D1-A1** CT pair calculated by TD-DFT (CAM-B3LYP/6-311G*).

E_{vert}	D1-A1			
	MO Description	H-2 → L	H-1 → L	H → L
S₁←S₀ 3.11 eV (f = 0.16)	6.8%	2.5%	82.9%	3.8%
S₂←S₀ 3.39 eV (f = 0.16)	-	56.3%	7.3%	28.7%
S₃←S₀ 3.60 eV (f = 0.16)	4.9%	30.2%	-	56.0%

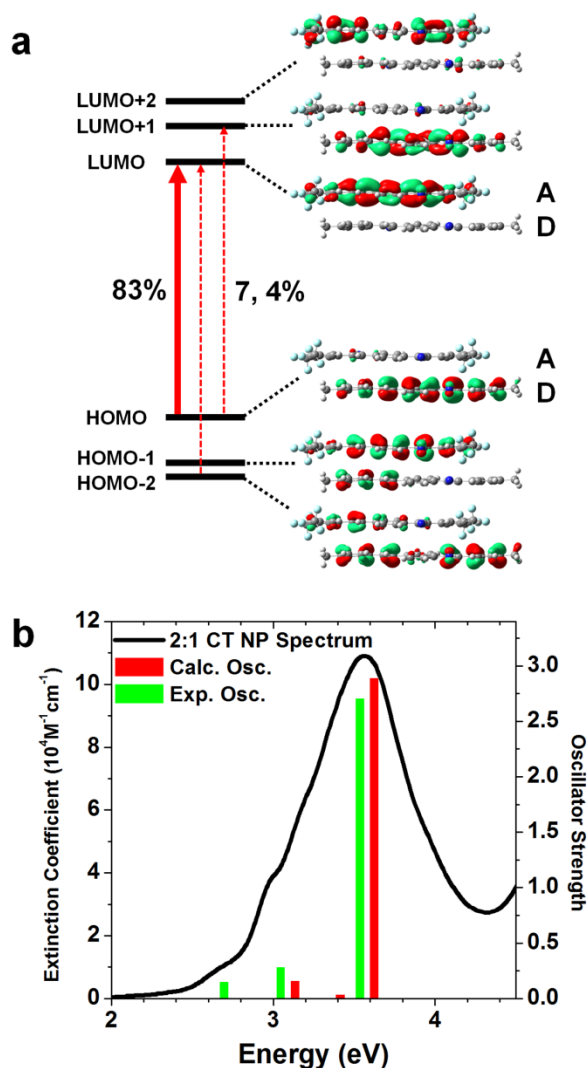


Figure 4-8. (a) MO alignment and descriptions of **D1-A1** CT pair calculated by TD-DFT (CAM-B3LYP/6-311G*). The characteristic configuration interaction terms comprising $S_0 \rightarrow S_1$ transition and their portions are indicated by red arrows. (b) Extinction coefficient spectrum of 2:1 **D1-A1** CT nanoparticle suspension (black line) and oscillator strength of each characteristic transition calculated from TD-DFT (red bar), and extracted from experimental values (green bar).

4.3.4. Charge-Transport Properties. Single-crystalline OFETs (SC-OFETs) devices were fabricated either by top-contact bottom-gate (TCBG) or bottom-contact bottom-gate (BCBG) OFETs geometry using PVT grown CT cocrystals, see **Experimental Section**. The symmetric Au source-drain electrodes were formed by vacuum thermal evaporation deposition in TCBG case, after laminating crystals onto the octadecyltrichlorosilane (ODTS) treated SiO₂/Si substrates particularly for reduced electron trap density. Prepatterned Au electrodes on SiO₂/Si substrates were utilized in the BCBG case. The TCBG devices exhibit highly balanced ambipolar characteristics (p-channel: $4.6 \times 10^{-4} \text{ cm}^2 \text{ V}^{-1} \text{ s}^{-1}$; n-channel: $2.9 \times 10^{-4} \text{ cm}^2 \text{ V}^{-1} \text{ s}^{-1}$); the mobility value of p-channel (n-channel) charge-carrier is extracted from saturation regime of p-channel (n-channel) carrier enhancement mode, see **Table 4-4**. Rather low device performance can be attributed from large CT gap i.e., 2.5 eV from H: 6.1 and L: 3.6 eV, and energetic difference between the FMOs and work function of Au (4.9 eV). However, the transport nature indeed indicates possibility of LE-OFETs applications due to the balanced bipolar mobility as well as high luminescence quantum efficiency.

The LE-OFETs characteristics were evaluated in large-area BCBG device geometry with prepatterned interdigitated Au electrodes (**Figure 4-9a, b**). Ultrathin 2D crystal sheets were addressed on to the ODTS treated source-drain prepatterned SiO₂/Si substrates; since the thinner crystals tend to render favorable physical contact by flexible nature thus resulted in higher charge density.^[13a] BCBG devices have also manifested apparent V-shape transfer characteristics as well as peculiar ambipolar

output characteristic (transition from superlinear to saturation by increasing gate bias ($|V_G|$)), see **Figure 4-9**. The output character clearly revealed existence of true ambipolar regime; for instance at $V_G = 90$ V in **Figure 4-9f**, after the saturation occurred by pinch-off of electron, further current increment is apparently observed due to the hole injection from the source electrode. The current minima found from p-/n-channel carrier enhancement modes (V_G at ca. -18 V and 25 V, respectively) thus correspond to the true ambipolar transport regime. Such ambipolar transport bias conditions shall result in maximum EQE values by reduced exciton-metal electrode interaction by separating emissive zone from source/drain electrodes.

Indeed EL character was apparently observed, the EL spectrum (**Figure 4-6c**) highly coincides with PL characters of **D1-A1** 2:1 nanoparticle and cocrystal. The result indicates CT excitons of S_1 state can exclusively be generated by bipolar charge injection in this tailor-made intermolecular CT complex. Realization of EL emission from p-/n-channel materials based heterostructures or host-guest systems has frequently been reported,^[15] however, LE-OFET based on molecular D-A heterojunction (i.e., CT complex) has not been described yet. The photocurrent and drain current of each device was simultaneously measured during obtaining transfer curve; and external quantum efficiency (EQE) could be extracted by:

$$\text{EQE} = \frac{e\lambda}{Rch} \times \frac{I_P}{I_D}$$

where, e is elementary charge, R is responsivity of photodiode, h is Planck constant,

and c is speed of light. Both p-/n-channel enhancement modes show EQE maxima at drain current minima, suggesting that the colligative influence of exciton-electrode, photon-electrode interaction as well as exciton-charge interaction resulted in such behaviors as can frequently be observed in LE-OFETs based on ambipolar semiconductor active channels. The EQE reaches as high as 1.5% from n-channel operation as depicted in **Figure 4-9d**, which is among the highest values observed from single-layered active-channel based LE-OFETs.^[16]

To scrutinize the peculiar transporting natures of the current CT complex, quantum chemical calculation was performed to estimate electronic coupling (transfer integral, t), see **Figure 4-10** and Experimental Section. For an exploration of possibility of indirect electronic coupling by superexchange mechanism, transfer integral of both types of charge-carriers were calculated by energy splitting method, along the stacking direction (i.e., **D1-A1-D1-D1** and **A1-D1-D1-A1** stack for the p- and n-channel carrier, respectively).^[3f] The intermolecular coordinates of the stacks were dictated from SC-XRD result however with optimized **D1** and **A1** geometries. From the definition of superexchange mechanism, i.e., mixing of the frontier molecular orbitals of two closest D (A) molecules with the orbitals of the bridging A (D) molecules, transfer integral values are extracted from $H - H-3$ ($L - L+2$) splitting; since H , $H-1$, and $H-2$ (L , and $L+1$) are fully localize onto the **D1** (**A1**) with rather small energetic separation between states. The 2:1 **D1-A1** mixed molecular arrangement render comparably large effective electronic coupling for both hole ($t_{h,eff} =$

357 meV) and electron ($t_{e,\text{eff}} = 303$ meV). On the other hand, direct coupling between nearest **D1-D1** and **A1-A1** dimers reflected low coupling efficiency ($t_h = 2$ meV and $t_e = 9$ meV) attributed from quasi 1D nature of the CT complex structure; thus, the charge-transport pathway should be along the mixed stacking direction. In this respect, the experimentally extracted ambipolar mobility can be resulted from favorable effective electronic coupling by superexchange mechanism. However, somewhat low field-effect mobility as well as the nonlinear current increase in the linear regime of output characteristic indicate the limitation of charge-injection especially in BCBG device structure, due to the large energetic separation between HOMO (LUMO) and work function of Au electrode.

Table 4-4. Summarized field-effect transistors properties from top-contact bottom-gate and bottom-contact bottom-gate device geometries.

		$\mu_{\text{Max}} [\text{cm}^2 \text{V}^{-1} \text{s}^{-1}]$	$\mu_{\text{Avg}} [\text{cm}^2 \text{V}^{-1} \text{s}^{-1}]$	$V_{\text{T}} [\text{V}]$	on/off	n
TCBG	p	5.5×10^{-4}	3.8×10^{-4}	-54	10^2 - 10^3	6
	n	2.9×10^{-4}	1.4×10^{-4}	55	10^1 - 10^3	6
BCBG	p	1.8×10^{-5}	9.2×10^{-6}	5	10^1 - 10^2	4
	n	4.9×10^{-5}	2.7×10^{-5}	30	10^1 - 10^3	4

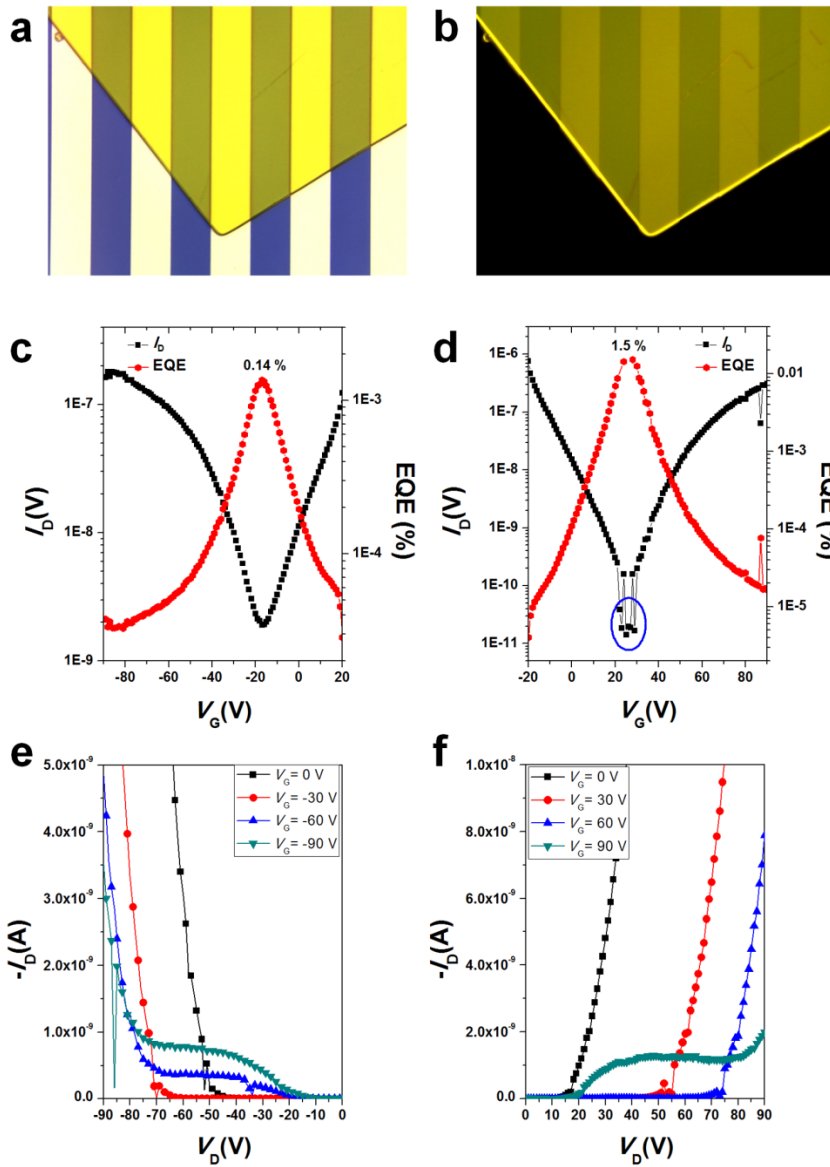


Figure 4-9. (a, b) optical microscope images of bottom-contact bottom-gate SC-OFETs device, taken under ambient light and UV, respectively. (c, d) p-channel and n-channel transfer characteristic (black square) and external quantum efficiency (red hexagon). (e, f) p-channel and n-channel output characteristic.

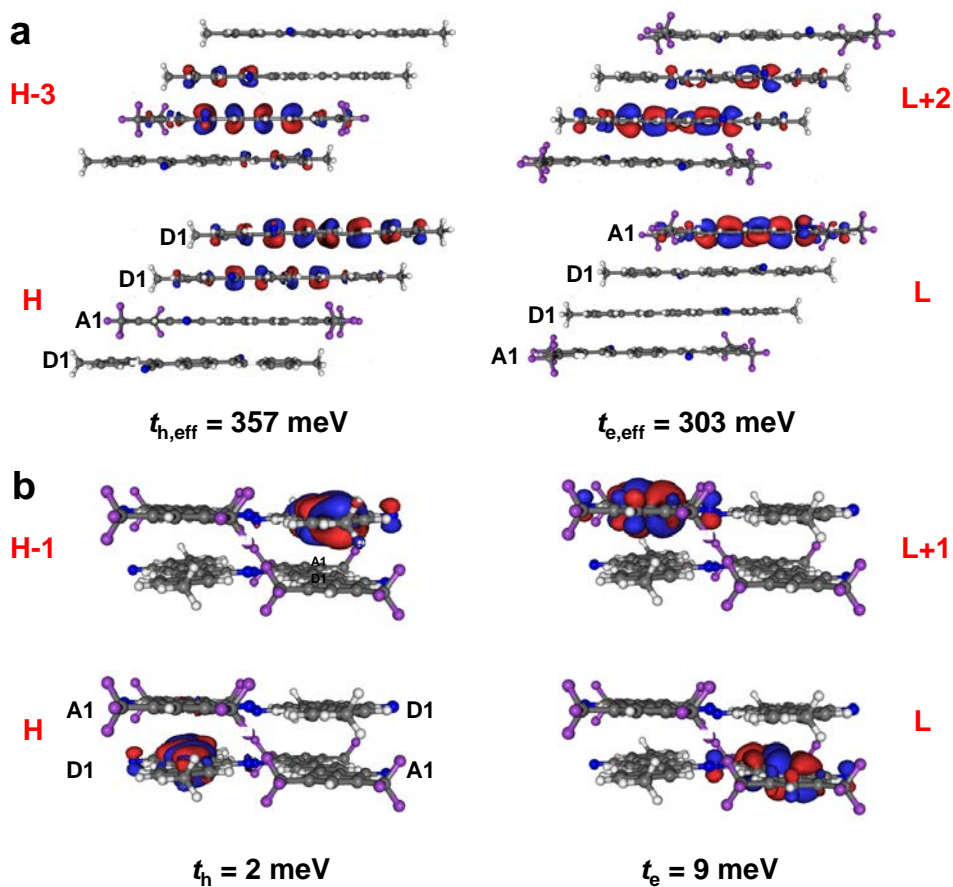


Figure 4-10. (a) DFT (CAM-B3LYP) calculated indirect electronic coupling of **D1-A1-D1-D1** and **A1-D1-D1-A1** tetramer stacks for p-channel and n-channel carrier, respectively. (b) DFT calculated direct electronic coupling between nearest inter stack **D1-D1** and **A1-A1** pairs.

4.4. Conclusions

I have presented charge-transfer (CT) complex with futuristic optoelectronic properties, which is accomplished through strategic donor (D) – acceptor (A) pair selection rule. Dicyanodistyrylbenzene (DCS) based D-A pair (i.e., **D1** and **A1**) engenders unusual 2-dimensional (2D) tight stacking molecular arrangement with characteristic 2:1 (**D1:A1**) mixed stack structure. In addition to the favorable stacking mode of CT cocrystal for reduced exciton trap density, notable electronic features (i.e., configuration interaction and moderate CT gap) lead to non-negligible oscillator strength and comparably low non-radiative deactivation rate; therefore, limited low emission efficiency of CT complex can effectively be surmounted. The unprecedentedly high emission quantum yield ($\Phi_F = \text{ca. } 60\%$), in combination to the peculiar ambipolar field-effect transport, enables us to develop the first CT based light-emitting organic field-effect transistors (LE-OFETs). The CT LE-OFET of this study revealed CT exciton formation from the molecular-level D-A heterojunction, manifesting CT electroluminescence with notable external quantum efficiency as high as 1.5%. However, low electrical performances arise from the large energetic separation between frontier molecular orbitals and work function of Au; thus, further device optimization steps considering lowering large contact barriers are on great demand.

4.5. References

- [1] (a) Yu, G.; Gao, J.; Hummelen, J. C.; Wudl, F.; Heeger, A. J. *Science* **1995**, *270*, 1789. (b) Goushi, K.; Yoshida, K.; Sato, K.; Adachi, C. *Nat. Photon.* **2012**, *6*, 253. (c) Alves, H.; Molinari, A. S.; Xie, H.; Morpurgo, A. F. *Nature Mater.* **2008**, *7*, 574. (d) Gutiérrez Lezama, I.; Nakano, M.; Minder, N. A.; Chen, Z.; Di Girolamo, F. V.; Facchetti, A.; Morpurgo, A. F. *Nat. Mater.* **2012**, *11*, 788. (e) Naab, B. D.; Himmelberger, S.; Diao, Y.; Vandewal, K.; Wei, P.; Lussem, B.; Salleo, A.; Bao, Z. *Adv. Mater.* **2013**, *25*, 4663. (f) Percec, V.; Glodde, M.; Bera, T. K.; Miura, Y.; Shiyankovskaya, I.; Singer, K. D.; Balagurusamy, V. S. K.; Heiney, P. A.; Schnell, I.; Rapp, A.; Spiess, H.-W.; Hudson, S. D.; Duan, H. *Nature* **2002**, *419*, 384. (g) Jonkheijm, P.; Stutzmann, N.; Chen, Z.; de Leeuw, D. M.; Meijer, E. W.; Schenning, A. P. H. J.; Würthner, F. *J. Am. Chem. Soc.* **2006**, *128*, 9535.
- [b] (a) Ferraris, J.; Cowan, D. O.; Walatka, V., Jr.; Perlstein, J. H. *J. Am. Chem. Soc.* **1973**, *95*. (b) Jérôme, D.; Mazaud, A.; Ribault, M.; Bechgaard, K. J. *Phys. Lett.* **1980**, *41*, L95. (c) Jérôme, D. *Chem. Rev.* **2004**, *104*, 5565. (d) Tokura, Y.; Koshihara, S.; Iwasa, Y.; Okamoto, H.; Komatsu, T.; Koda, T.; Iwasawa, N.; Saito, G. *Phys. Rev. Lett.* **1989**, *63*, 2405. (e) Tayi, A. S.; Shveyd, A. K.; Sue, A. C.-H.; Szarko, J. M.; Rolczynski, B. S.; Cao, D.; Kennedy, T. J.; Sarjeant, A. A.; Stern, C. L.; Paxton, W. F.; Wu, W.; Dey, S. K.; Fahrenbach, A. C.; Guest, J. R.; Mohseni, H.; Chen, L. X.; Wang, K. L.; Stoddart,

J. F.; Stupp, S. I. *Nature* **2012**, 488, 485. (f) Miller, J. S.; Calabrese, J. C.; Rommelmann, H.; Chittipeddi, S. R.; Zhang, J. H.; Reiff, W. M.; Epstein, A. J. *J. Am. Chem. Soc.* **1987**, 109, 769. (g) Saito, G.; Murata, T. *Phil. Trans. R. Soc. A* **2008**, 366, 139.

[3] (a) Mori, T. *Chem. Lett.* **2011**, 40, 428. (a) Das, A.; Ghosh, S. *Angew. Chem. Int. Ed.* **2014**, 53, 2038. (b) Zhang, J.; Geng, H.; Virk, T. S.; Zhao, Y.; Tan, J.; Di, C.-a.; Xu, W.; Singh, K.; Hu, W.; Shuai, Z.; Liu, Y.; Zhu, D. *Adv. Mater.* **2012**, 24, 2603. (c) Zhang, J.; Tan, J.; Ma, Z.; Xu, W.; Zhao, G.; Geng, H.; Di, C.; Hu, W.; Shuai, Z.; Singh, K.; Zhu, D. *J. Am. Chem. Soc.* **2013**, 135, 558. (d) Qin, Y.; Zhang, J.; Zheng, X.; Geng, H.; Zhao, G.; Xu, W.; Hu, W.; Shuai, Z.; Zhu, D. *Adv. Mater.* **2014**, 26, 4093. (e) Wakahara, T.; D'Angelo, P.; Miyazawa, K.; Nemoto, Y.; Ito, O.; Tanigaki, N.; Bradley, D. D. C.; Anthopoulos, T. D. *J. Am. Chem. Soc.* **2012**, 134, 7204. (f) Vermeulen, D.; Zhu, L. Y.; Goetz, K. P.; Hu, P.; Jiang, H.; Day, C. S.; Jurchescu, O. D.; Coropceanu, V.; Kloc, C.; McNeil, L. E. *J. Phys. Chem. C* **2014**, 118, 24688. (g) Yu, W.; Wang, X.-Y.; Li, J.; Li, Z.-T.; Yan, Y.-K.; Wang, W.; Pei, J. *Chem. Commun.* **2013**, 49, 54. (h) Zhu, W.; Zheng, R.; Zhen, Y.; Yu, Z.; Dong, H.; Fu, H.; Shi, Q.; Hu, W. *J. Am. Chem. Soc.* **2015**, 137, 11038. (i) Zhu, W.; Zheng, R.; Fu, X.; Fu, H.; Shi, Q.; Zhen, Y.; Dong, H.; Hu, W. *Angew. Chem. Int. Ed.* **2015**, 54, 6785. (j) Lei, Y.-L.; Jin, Y.; Zhou, D.-Y.; Gu, W.; Shi, X.-B.; Liao, L.-S.; Lee, S.-T. *Adv. Mater.* **2012**, 24, 5345. (k) Sun, Y.-Q.; Lei, Y.-L.; Sun, X.-H.; Lee, S.-T.; Liao, L.-S. *Chem. Mater.* **2015**, 27, 1157. (l) Park, S. K.; Cho, I.; Gierschner, J.; Kim, J. H.; Kim, J. H.; Kwon, J. E.; Kwon, O. K.; Whang, D. R.; Park,

J.-H.; An, B.-K.; Park, S. Y. *Angew. Chem. Int. Ed.* **2015**, Accepted.

[4] (a) Zhu, L.; Yi, Y.; Li, Y.; Kim, E.-G.; Coropceanu, V.; Brédas, J.-L. *J. Am. Chem. Soc.* **2012**, *134*, 2340. (b) Geng, H.; Zheng, X.; Shuai, Z.; Zhu, L.; Yi, Y. *Adv. Mater.* **2015**, *27*, 1443.

[5] (a) Sakai, M.; Sakuma, H.; Ito, Y.; Saito, A.; Nakamura, M.; Kudo, K. *Phys. Rev. B* **2007**, *76*, 045111. (b) Kawasugi, Y.; Yamamoto, H. M.; Tajima, N.; Fukunaga, T.; Tsukagoshi, K.; Kato, R. *Phys. Rev. Lett.* **2009**, *103*, 116801. (c) Kawasugi, Y.; Yamamoto, H. M.; Tajima, N.; Fukunaga, T.; Tsukagoshi, K.; Kato, R. *Phys. Rev. B* **2011**, *84*, 125129. (d) Kimata, M.; Ishihara, T.; Tajima, H. *J. Phys. Soc. Jpn.* **2012**, *81*, 073704. (e) Hasegawa, T.; Mattenberger, K.; Takeya, J.; Batlogg, B. *Phys. Rev. B* **2004**, *69*, 245115.

[6] Jones, II G. In *Photoinduced Electron Transfer Part A*, Fox, M. A.; Chanon, M., Eds.; Elsevier: Amsterdam, 1988; pp 245-268.

[7] (a) Park, S. K.; Varghese, S.; Kim, J. H.; Yoon, S.-J.; Kwon, O. K.; An, B.-K.; Gierschner, J.; Park, S. Y. *J. Am. Chem. Soc.* **2013**, *135*, 4757. (b) Wykes, M.; Park, S. K.; Bhattacharyya, S.; Varghese, S.; Kwon, J. E.; Whang, D. R.; Cho, I.; Wannemacher, R.; Lüer, L.; Park, S. Y.; Gierschner, J. *J. Phys. Chem. Lett.* **2015**, *6*, 3682.

[8] (a) Bartholomew, G. P.; Bu, X.; Bazan, G. C. *Chem. Mater.* **2000**, *12*, 2311. (b) Lim, S.-J.; An, B.-K.; Park, S. Y. *Macromolecules* **2005**, *38*, 6236.

[9] Park, S. K.; Kim, J. H.; Yoon, S.-J.; Kwon, O. K.; An, B.-K.; Park, S. Y. *Chem. Mater.* **2012**, *24*, 3263.

- [10] Sheldrick, G. M. *Acta Cryst.* **2008**, *A64*, 112.
- [11] Spek, A. L. *J. Appl. Cryst.* **2003**, *36*, 7.
- [12] Frisch, M. J.; Trucks, G. W.; Schlegel, H. B.; Scuseria, G. E.; Robb, M. A.; Cheeseman, J. R.; Scalmani, G.; Barone, V.; Mennucci, B.; Petersson, G. A.; Nakatsuji, H.; Caricato, M.; Li, X.; Hratchian, H. P.; Izmaylov, A. F.; Bloino, J.; Zheng, G.; Sonnenberg, J. L.; Hada, M.; Ehara, M.; Toyota, K.; Fukuda, R.; Hasegawa, J.; Ishida, M.; Nakajima, T.; Honda, Y.; Kitao, O.; Nakai, H.; Vreven, T.; Montgomery, Jr., J. A.; Peralta, J. E.; Ogliaro, F.; Bearpark, M.; Heyd, J. J.; Brothers, E.; Kudin, K. N.; Staroverov, V. N.; Kobayashi, R.; Normand, J.; Raghavachari, K.; Rendell, A.; Burant, J. C.; Iyengar, S. S.; Tomasi, J.; Cossi, M.; Rega, N.; Millam, J. M.; Klene, M.; Knox, J. E.; Cross, J. B.; Bakken, V.; Adamo, C.; Jaramillo, J.; Gomperts, R.; Stratmann, R. E.; Yazyev, O.; Austin, A. J.; Cammi, R.; Pomelli, C.; Ochterski, J. W.; Martin, R. L.; Morokuma, K.; Zakrzewski, V. G.; Voth, G. A.; Salvador, P.; Dannenberg, J. J.; Dapprich, S.; Daniels, A. D.; Farkas, Ö.; Foresman, J. B.; Ortiz, J. V.; Cioslowski, J.; Fox, D. J. *Gaussian 09, Revision A.02*, Gaussian, Inc., Wallingford CT, 2009.
- [13] (a) Briseno, A. L.; Tseng, R. J.; Ling, M.-M.; Falcao, E. H. L.; Yang, Y.; Wudl, F.; Bao, Z. *Adv. Mater.* **2006**, *18*, 2320. (b) Jiang, L.; Dong, H.; Meng, Q.; Li, H.; He, M.; Wei, Z.; He, Y.; Hu, W. *Adv. Mater.* **2011**, *23*, 2059. (c) Minemawari, H.; Yamada, T.; Matsui, H.; Tsutsumi, J. Haas, S.; Chiba, R.; Kumai, R.; Hasegawa, T. *Nature* **2011**, *475*, 364.
- [14] (a) An, B.-K.; Kwon, S.-K.; Jung, S.-D.; Park, S. Y. *J. Am. Chem. Soc.* **2002**, *124*,

14410. (b) An, B.-K.; Lee, D.-S.; Lee, J.-S.; Park, Y.-S.; Song, H.-S.; Park, S. Y. *J. Am. Chem. Soc.* **2004**, *126*, 10232. (c) An, B.-K.; Gierschner, J.; Park, S. Y. *Acc. Chem. Res.* **2012**, *45*, 544.

[15] (a) Rost, C.; Karg, S.; Riess, W.; Loi, M. A.; Murgia, M.; Muccini, M. *Appl. Phys. Lett.* **2004**, *85*, 1613. (b) Loi, M. A.; Rost-Bietsch, C.; Murgia, M.; Karg, S.; Riess, W.; Muccini, M. *Adv. Funct. Mater.* **2006**, *16*, 41. (c) Dinelli, F.; Capelli, R.; Loi, M. A.; Murgia, M.; Muccini, M.; Facchetti, A.; Marks, T. J. *Adv. Mater.* **2006**, *18*, 1416. (d) Capelli, R.; Toffanin, S.; Generali, G.; Usta, H.; Facchetti, A.; Muccini, M. *Nat. Mater.* **2010**, *9*, 496. (e) Kim, J. H.; Watanabe, A.; Chung, J. W.; Jung, Y.; An, B.-K.; Tada, H.; Park, S. Y. *J. Mater. Chem.* **2010**, *20*, 1062. (f) Oyamada, T.; Uchiuzou, H.; Akiyama, S.; Oku, Y.; Shimoji, N.; Matsushige, K.; Sasabe, H.; Adachi, C. *J. Appl. Phys.* **2005**, *98*, 074 506. (g) Nakanotani, H.; Saito, M.; Nakamura, H.; Adachi, C. *Adv. Funct. Mater.* **2010**, *20*, 1610.

[16] (a) Cicoira, F.; Santato, C. *Adv. Funct. Mater.* **2007**, *17*, 3421. (b) Hepp, A.; Heil, H.; Weise, W.; Ahles, M.; Schmechel, R.; von Seggern, H. *Phys. Rev. Lett.* **2003**, *91*, 157 406. (c) Swensen, J. S.; Soci, C.; Heeger, A. J. *Appl. Phys. Lett.* **2005**, *87*, 253511. (d) Zaumseil, Z.; Friend, R. H.; Sirringhaus, H. *Nat. Mater.* **2006**, *5*, 69. (e) Hotta, S.; Yamao, T.; Bisri, S. Z.; Takenobu, T.; Iwasa, Y. *J. Mater. Chem. C* **2014**, *2*, 965. (f) Nakanotani, H.; Kabe, R.; Yahiro, M.; Takenobu, T.; Iwasa, Y.; Adachi, C. *Appl. Phys. Exp.* **2008**, *1*, 091801.

Chapter 5.

Stimuli-Responsive Reversible Fluorescence Switching in a Crystalline Donor-Acceptor Mixture Film: Mixed Stack Charge-Transfer Emission vs. Segregated Stack Monomer Emission

5.1. Introduction

Multi-color photoluminescence (PL) switching on the basis of structural perturbation for organic π -conjugated materials has recently attracted enormous research interest and paved the way toward developing future applications such as optical recording and sensors.^[1] Various materials have been devised with fascinating approaches, showing actively controllable PL characteristics triggered by external stimuli (e.g., thermal stimuli, mechanical stimuli, and solvent vapor treatment). However, structural reorganizations are enabled by utilizing rather limited and specific intermolecular interaction motifs – e.g., local dipole alignment,^[1b] aurophilic interactions,^[1c] and conformational changes,^[1d] or by introducing co-/disassembling stacking modulators.^[1e] Moreover, in many cases PL changes are limited to rather small energetic shifts, which are based on transitions between excitonic and excimeric interactions. Furthermore, it is not feasible to predict the existence of multiple phases of the organic material itself and its luminescence alternations during the structural transformation. Accordingly, at this stage, I desire an intuitive and straightforward

guideline for both controlling and predicting luminescence changes based on anticipated structural rearrangement.

Multi-component charge-transfer (CT) complexes comprised of intermolecular donor-acceptor (D-A) pairs can resolve this issue. In these systems, predictable mixed stacking structures are provided, governed by the Coulombic interaction induced from the large energetic offset between donors and acceptors.^[2] This mixed arrangement, in turn, gives rise to distinguished emission energies originating from localized frontier molecular orbitals (MO), i.e., the highest occupied MO (HOMO) at donor, and the lowest unoccupied MO (LUMO) at acceptor, respectively; this enables the pronounced bathochromic shift of emission compared to the individual D/A materials. However, detrimental non-radiative deactivation of the CT state should be resolved; furthermore, facile phase transition between the mixed **D-A** phase (CT) and the demixed phase (individual **D/A**) will promote multi-color fluorescence switching based on the **D-A** complex.^[3,4] Among the recent advances in highly emissive **D-A** complex systems,^[5] I further gave attention to the CT system consisting of the isometrically tailored distyrylbenzene-based D-A pair.^[6] This D-A pair exhibited strong red PL and low internal conversion rates through establishing densely packed stacking structure; however, the intended loosely packed molecular arrangement is necessary for a stimuli-responsive feature. Therefore, it is expected that a high-contrast, multi-color switching system can be realized by using similar isometric chromophores for which **A1** has a noncentrosymmetric design for an attenuated intermolecular interaction

network. In this context, the PL switching between mixed and demixed (i.e., narcissistic self-sorting) phases is allowed,^[1e,7] meanwhile, the PL is defined by its CT and its individual D/A state during structural reorganization.

In this work, a novel strategy for establishing high-contrast, reversible PL switching media based on stimuli-responsive CT complexes is proposed. Facile stacking control between the mixed D-A CT complex and the demixed individual D/A phases can be attained by implanting the noncentrosymmetric **A1** in order to obtain the intended loosely packed structure, which can be characterized by distinct free volume and relatively weak intermolecular interactions (see **Figure 5-1a** for chemical structures of **D1** and **A1**). On the basis of the large energetic shift of the S_0 - S_1 transition during the phase change (**Figure 5-1b**), it is expected to achieve a programmable PL memory system that is controlled by polarity- or proticity-dependent solvent vapor annealing (SVA) as well as thermal/mechanical stimuli. In turn, these stimuli greatly modulate the intermolecular interactions based on electrostatic CT and H-bonding interaction motifs. An in-depth understanding of the unique PL switching mechanism induced from dynamic structural changes can be accomplished through a precise correlation of the chemical, structural, optical, and thermal properties.

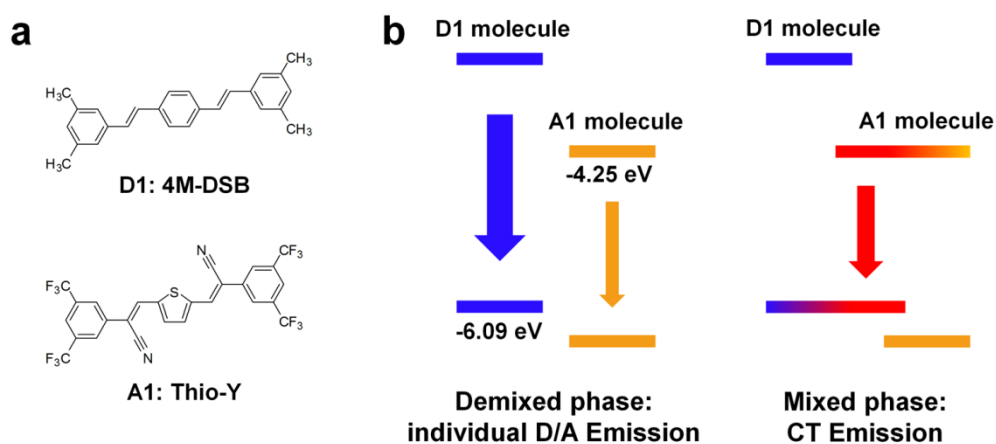
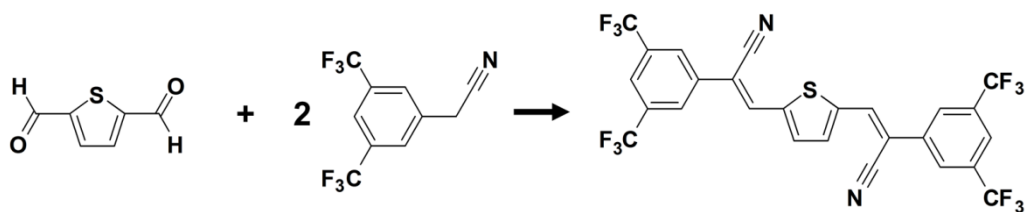


Figure 5-1. (a) Chemical structures of donor (**D1**: 4M-DSB) and acceptor (**A1**: Thio-Y). (b) Frontier molecular orbital diagrams of mixed and demixed phases.



5.2. Experimental

Synthesis The distyrylbenzene-based **D1** (4M-DSB) was synthesized by previous description, see **Scheme 3-1**.^[6] 3,3'-(1,4-phenylene)bis(2-(3,5-bis(trifluoromethyl)phenyl)acrylonitrile, i.e., dicyanodistyrylthiophene-based **A1** (Thio-Y), was synthesized by simple synthetic procedures, as previous reports, see **Scheme 5-1**.^[8] Thiophene-2,5-dicarbaldehyde (1.184 g, 0.0084 M) and 2-(3,5-bis(trifluoromethyl)phenyl)acetonitrile (4.277 g, 0.0169 M) were dissolved in 45 ml of t-butyl alcohol and 5 ml of tetrahydrofuran (THF). Tetrabutylammonium hydroxide (0.00169 M) was slowly added into the solution. The reaction was undergone in 50 °C, for 2 hours. The precipitated product was filtered, and purified by column chromatography. Further purification steps, i.e., recrystallization (yield 1.7 g) and sublimation (at ca. 173 °C, 5×10^{-6} Torr), were carried out before using the **A1**. ¹H NMR (300 MHz, CDCl₃) [δ ppm]: 8.10 (s, 4H), 7.95 (s, 2H), 7.93 (s, 2H), 7.78 (s, 2H).

Characterization UV/Vis absorption spectra were recorded using a Shimadzu UV-1650 PC spectrometer. PL spectra and absolute PL quantum yields were obtained using a Photon Technology International QM-40 spectrophotometer equipped with a 3.2-in. integrating sphere. Time-resolved PL lifetime measurements were carried out through time-correlated single photon counting using a Picoquant FluoTime 200 instrument. The AFM images were taken by a Bruker Nanoscope III multimode SPM with tapping

mode using RTESP cantilever. The FE-SEM images were obtained using a FEI Helios Nanolab 650. The powder XRD and SC-XRD analysis were carried out using a Bruker D8-Advance X-ray diffractometer and Bruker SMART-APEX II ULTRA, respectively. UPS was done on a KRATOS AXIS Nova instrument with vacuum deposited thin-film of **A1**. Thermogravimetric analyses were carried out using a TA Instruments Q-5000 IR, with a heating rate of 10°C/min. The 300 MHz ¹H NMR spectra were recorded using a Bruker Avance-300 in CDCl₃ solutions. The digital film images were taken using a Canon PowerShot SX40 HS digital camera under 365 nm UV irradiation by hand-held UV lamp. The differential scanning calorimetry (DSC) experiments were performed using a Perkin-Elmer DSC7 with scan rates of 1°C/min for **D1**, **A1**, and CT-P1 single-crystals and 2.5°C/min for **D1-A1** mixed powder samples.

Sample Preparation The nanoparticle suspension (THF:water, 0.2:9.8 v:v) of **D1**, **A1**, and **D1-A1** CT (**D1:A1**, with 1:1 stoichiometry) were produced with concentration of 2×10^{-5} mol L⁻¹. For nanoparticle suspension preparation, the stock solution of each compound or 1:1 mixed solution was injected into vigorously stirred water containing bial to generate uniform kinetically stable precipitates. Single crystals of **D1** and **A1** were obtained by solvent vapor diffusion method from a DCM/n-hexane and DCE/MeOH, respectively. Single crystals of CT-P1 were obtained by the same method using a mixed vapor of good solvents (i.e. DCM, CHCl₃, DCE, THF and CB) and MeOH as a poor solvent. CT-P1 crystals could also be prepared by recrystallization using DCM/MeOH with a small quantity of THF and EtOH as co-solvent. CT-P2

crystals were obtained by recrystallization using DCM and MeOH mixture. Spincoated films of **D1-A1** CT phases were obtained from the condition of 0.4 wt. % CHCl_3 solution with 1000 rpm/60 s. A 100 nm thick thin-film of **A1** was obtained on quartz plates by thermal vacuum deposition procedures under high vacuum condition (ca. 1×10^{-6} Torr) for UPS measurement.

Optical Memory demonstration: For optical memory demonstration, 3-components (**D1**, **A1**, and polymethylmethacrylate (PMMA)) blended solid-solution films were prepared. For this, 0.4 wt% of **A1**, and **D1** with 1:1 stoichiometry was dissolved in DCE, containing 1.0 wt% PMMA (average M_w of 15,000, purchased from Aldrich co.) as polymer binder material, and spincoated on quartz plates with 1500 rpm/60 s. To obtain blue emissive film, the film was placed on top of the solvent filled vial (MeCN, 5 min). To obtain patterned red emissive region, the film was placed on top of the solvent filled vial (DCE, 5min). For thermal writing process, hot metal stamps (185°C, 20s) were addressed onto the blue emissive MeCN SVA film. For piezo writing, I wrote letters gently using an ink-eliminated soft pen. For thermal erasing, the films were annealed using a hot plate (185°C, 20s).

Quantum-Chemical Calculation (Frontier) MO energies, vertical/adiabatic electron affinities (EA) and ionization potentials (IP) of the **D1** and **A1** were calculated by DFT (B3LYP functional and 6-311G* basis set as defined in the Gaussian 09 program package). The calculation of vertical EAs and IPs was carried out on the radical anions and cations imposing the neutral geometry, DCM as solvent by the

polarizable continuum model description. The calculation on adiabatic IPs and EAs was performed on the optimized geometries of the radical ions. Vertical transition energies of **D1** and **A1** were calculated by TD-DFT (B3LYP). The calculations on the **D1-A1** dimer pair were carried out on B3LYP geometry optimized molecules, where the intermolecular coordinates were taken from the single-crystal XRD analysis. For the TD calculations the coulomb attenuated method (CAM) variant of B3LYP functional was employed to account for long-range interaction; MO topologies were plotted using Molekel.

5.3. Results and Discussion

5.3.1. Optical Properties of CT Complex. The CT phenomenon between the distyrylbenzene-based donor (**D1**, 4M-DSB) and dicyanodistyrylthiophene-based acceptor (**A1**, Thio-Y) pair can be observed through UV/Vis absorption and PL spectroscopy (see **Figure 5-2** and **Table 5-1**). To avoid artifact such as high optical density in a single crystal, solid-state absorption were obtained using nanoparticle suspension representing solid-state CT. The **D1-A1** nanoparticle absorption reveals a new weak band at around 525 nm, which gives rise to PL at 660 nm. This low-lying state is well correlated with the (reported) experimental gap between the HOMO (**D1**) and LUMO (**A1**) energies (that is, -6.09 and -4.25 eV, respectively);^[6] this is

theoretically assigned to the $S_0 \rightarrow S_1$ transition, which has a pronounced CT character (see **Figures 5-2** and **5-3**, as well as **Tables 5-2** and **5-3**). The broad PL of the cocrystal and nanoparticle shows a strong bathochromic shift against the individual solid-state PL spectra of **D1** (467 nm) and **A1** (553 nm) crystals. This suggests significant potential for use in multi-color PL switching systems for which (de-)mixed phases can be controlled by external stimuli.

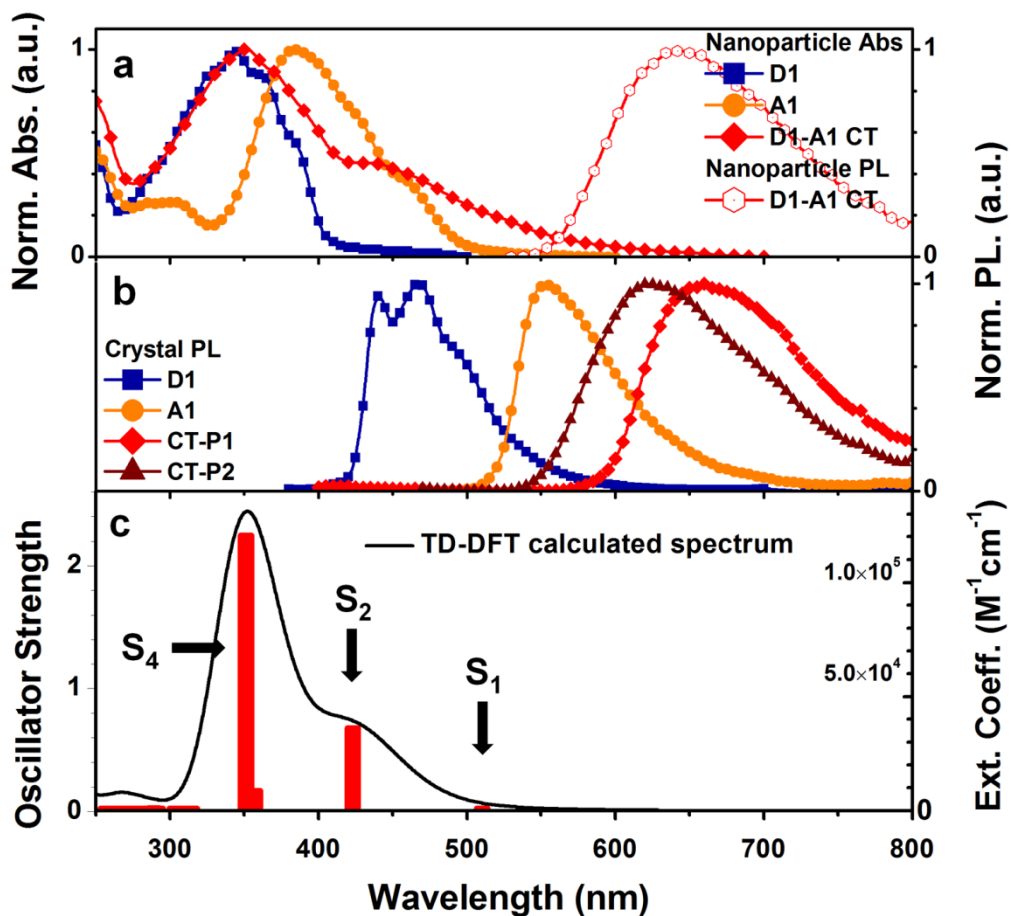


Figure 5-2. (a) Normalized UV/Vis absorption of **D1**, **A1**, and **D1-A1** nanoparticles, and normalized PL spectra of **D1-A1** nanoparticle. (b) Normalized PL spectra of **D1**, **A1**, **CT-P1**, and **CT-P2** single crystals. (c) Calculated absorption spectrum of **D1-A1** dimer by TD-DFT.

Table 5-1. Optical properties of CT complex and constituent compounds in the solid state: absorption (λ_{abs}) and emission (λ_{em}) wavelengths, absolute quantum yields (Φ_{F}), intensity-weighted average fluorescence lifetimes (τ_{F}), radiative rates (k_{r}), and non-radiative rates (k_{nr}).

	D	A	CT-P1	CT-P2
λ_{abs} [nm]	343	384	353, 444, 525 ^a	– ^b
λ_{em} [nm]	467	553	660	622
Φ_{F}	0.88	0.19	0.03	0.08
τ_{F} [ns]	1.47	2.65	3.62	3.10
k_{r} [ns ⁻¹]	0.601	0.070	0.009	0.026
k_{nr} [ns ⁻¹]	0.079	0.307	0.267	0.296

^a CT band observed from nanoparticle suspension absorption spectrum. ^b cannot be recorded owing to the high optical density, because CT-P2 only exists in the powder/crystal form.

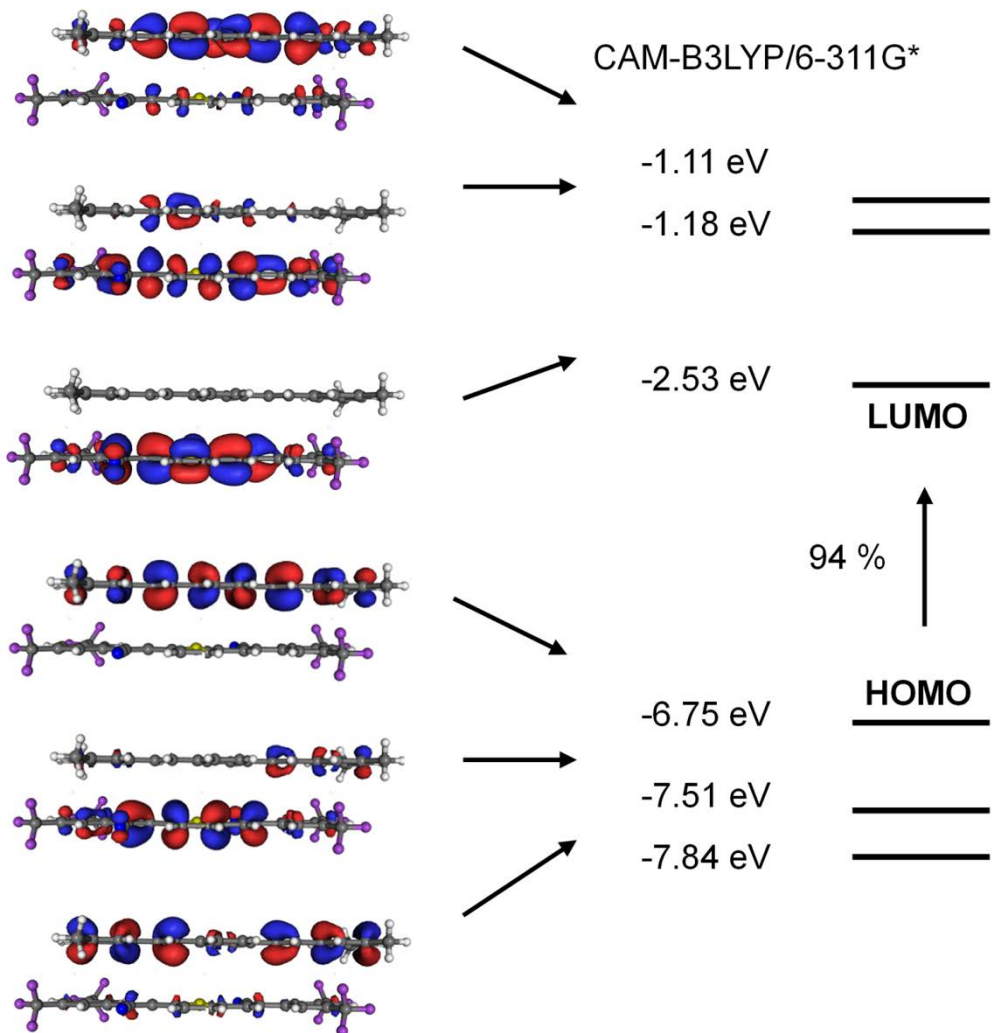


Figure 5-3. Calculated molecular orbital diagram for CT dimer pair by DFT(CAM-B3LYP/6-311G*).

Table 5-2. Experimental frontier MO energies as estimated by UPS and optical bandgap. Frontier MO energies, adiabatic and vertical electron affinities (EA) and ionization potentials (IP) of the **D1**, and **A1** molecules as calculated by DFT (B3LYP). Vertical transition energies $E_{\text{vert}}(S_0 \rightarrow S_1)$ as calculated by TD-DFT (B3LYP).

	D1 (4M-DSB)	A1 (Thio-Y)
<i>Experimental</i>		
HOMO	-6.09 eV	-6.78 eV
LUMO	-3.04 eV	-4.25 eV
<i>Calculation</i>		
HOMO ^a	-5.30 eV	-6.64 eV
LUMO ^a	-1.93 eV	-3.79 eV
EA _{adiab} ^b	2.44 eV	3.62 eV
EA _{vert} ^b	2.31 eV	3.45 eV
IP _{adiab} ^b	5.11 eV	6.20 eV
IP _{vert} ^b	5.23 eV	6.30 eV
$E_{\text{vert}}(S_0 \rightarrow S_1)$ ^a	3.16 eV (H→L)	2.73 eV (H→L)
^a in vacuo	^b in dichloromethane (PCM)	

Table 5-3. Vertical transition energies E_{vert} of 4M-DSB (**D1**), Thio-Y (**A1**) and **D1-A1** (1:1) as calculated by TD-DFT(CAM-B3LYP/6-11G*)//DFT(B3LYP/6-311G*).

E_{vert}	4M-DSB (D1)	Thio-Y (A1)	D1-A1 (1:1)
$S_1 \leftarrow S_0$	3.54 eV (f= 2.00) H→L: 93 % H-1→L+1: 5 %	3.00 eV (f= 1.52) H→L: 96 %	2.43 eV (f= 0.02) H→L: 94 % H-1→L: 3 %
$S_2 \leftarrow S_0$			2.93 eV (f= 0.68) H-1→L: 81 % H-2→L: 6 %
$S_3 \leftarrow S_0$			3.47 eV (f= 0.17) H-2→L: 49 % H→L+2: 31 % H→L+1: 9 % H-1→L: 6 %
$S_4 \leftarrow S_0$			3.53 eV (f= 2.25) H→L+2: 42 % H→L+1: 31 % H-2→L: 10 %

5.3.2. Structure Characteristics. I envisage that the noncentrosymmetric design of **A1** establishes the basis for programmable structure/PL switching. The molecular arrangement in the CT cocrystal was analyzed by single-crystal XRD (SC-XRD), which showed a dimer-pair brick-wall-like geometry with a 1:1 **D1-A1** mixed stack within its triclinic unit cell, as depicted in **Figure 5-4** and **Table 5-4**. The solved structure revealed two important structural features: weak intermolecular interactions and distinct free volume in the lattice. Upon solving the molecular stacking structure, it was clarified that inclusion of other component (most probably, solvent) occurred in the crystal structure, as analyzed from residual electron density other than **D1** and **A1** with 1:1 stoichiometry. This solvent inclusion was further confirmed by thermogravimetry analysis (TGA) and NMR spectroscopy. However, owing to the inevitable disorder of the solvent, the solvent-included structure (named CT-P1) could be roughly understood. The result, however, well reflects free volume, which acts as a solvent molecular inclusion site, provided by the curved molecular shape of **A1** (see **Figure 5-4c**). Furthermore, the loosely packed state was confirmed on the basis of a relatively large π -plane distance of approximately 3.5 Å and moderately weak -CN-induced intermolecular interactions (e.g., the -CN \cdots HC- interaction between two **A1** molecules, with 2 hydrogen bonds per molecule and a distance of 2.6 Å; **Figure 5-4b**).

In combination with the solvent-included form (CT-P1), I further found that the solvent-excluded form (CT-P2) can also be grown, and can give rise to emission property alternations (CT-P1: $\lambda_{em} = 660$ nm, $\Phi_F = 3.2\%$; CT-P2: $\lambda_{em} = 622$ nm, $\Phi_F =$

8.1%; see **Figures 5-5** and **5-6**). The packing structure of CT-P2 could be comprehended by comparing results from CT-P1. From powder XRD measurement, the main peak was found at 11.38° for CT-P1 and 11.72° for CT-P2 (**Figure 5-5a**). The main peak of CT-P1 was revealed to be (002) by SC-XRD simulation; thus d_{001} -spacing value was derived to be 15.55 Å. It is assumed that structural origin of CT-P2 should follow that of CT-P1; in that sense, d_{001} -spacing of CT-P2 could be estimated to 15.08 Å derived from (002) peak, indicating non-negligible contraction of lattice along such direction. Such lattice reorganization could also be well rationalized from the TGA and ^1H NMR analyses (**Figure 5-5b, c**). The weight loss at 139.6°C from TGA (estimated to ca. 17.5%) and observation of solvents peaks, i.e. THF and EtOH, assigned from ^1H NMR spectra (1 : 1 : 0.35, **D1** : **A1** : solvent; after sufficient ambient drying ca. 30 days) consistently indicated solvent inclusion occurred in case of CT-P1. By correlating SC-XRD results, arbitrary solvent molecules can easily be included at free volume site, particularly along *c*-axis direction of CT-P1. However, no sign of solvent inclusion in CT-P2 could be observed, therefore resulted in lattice reorganization along *c*-axis direction. To this end, concomitant luminescence property changes were derived, dictated by the structural perturbation.

The precise structure-property correlation from all combined structural, thermal, chemical, and spectroscopic analyses of CT-P2 could be summarized as follows: i) the elimination of included solvent molecules resulted in lattice reorganization, ii) the lattice reorganization shifted the **D1-A1** dimer pairs laterally so that the degree of π - π

overlap was comparably decreased, iii) therefore, the oscillator strength of the S_1 state will be enhanced, iv) and, resulted in increase of radiative constant ($k_r = 0.026 \text{ ns}^{-1}$). On the other hand, non-radiative constant ($k_{nr} = 0.296 \text{ ns}^{-1}$), also increased slightly, which might be the result from intramolecular contribution and/or increase in free volume. Meanwhile, the effect of solvatochromism could not be disregarded as well, which might also change luminescence characters by dipole interaction between solvent and constituting **D1-A1** pair.

Those structural features well reflect our intended sparsely packed molecular arrangement compared to the previously reported CT based on the centrosymmetric dicyanodistyrylbenzene based acceptor,^[6] which facilitates phase alteration in response to multiple stimuli, and thus leads to high-contrast luminescence switching behavior.

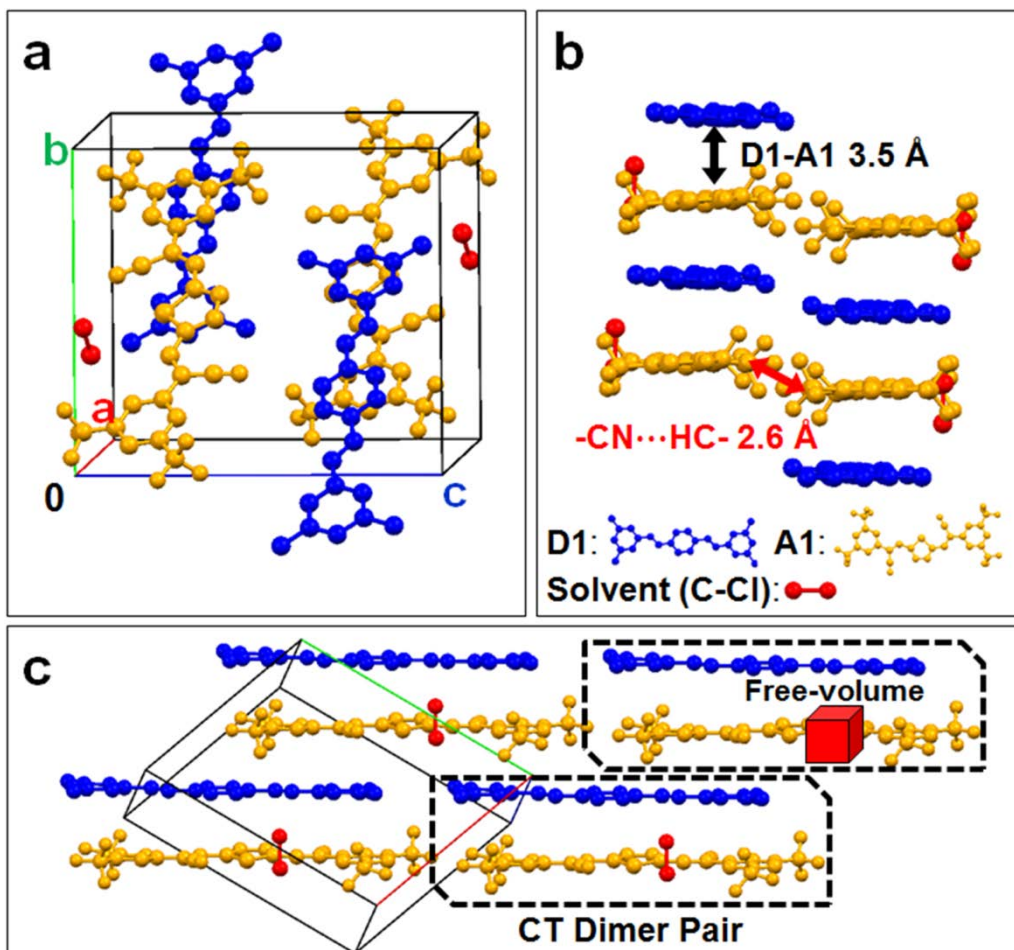


Figure 5-4. (a–c) Molecular arrangement of CT-P1 (solvent-included structure) from SC-XRD. **D1**: blue molecule; **A1**: yellow molecule; and solvent (C-Cl): red molecule. (b) Roll-angle view with information of the **D1-A1** $\pi-\pi$ distance (black arrow) and the **A1-A1** $-CN\cdots HC-$ distance (red arrow). (c) Slip-angle view showing dimer-pair brick-wall geometry. Black dotted box: **D1-A1** dimer pair; red cube: lattice free volume.

Table 5-4. Crystal data and structure refinement for CT-P1 cocrystal.

Empirical formula	C ₅₃ H ₃₆ Cl F ₁₂ N ₂ S
Formula weight	996.35
Temperature	173(2) K
Wavelength	0.71073 Å
Crystal system	Triclinic
Space group	P-1
Unit cell dimensions	a = 10.9520(3) Å α = 89.667(2)° b = 14.4295(4) Å β = 77.845(2)° c = 15.9432(4) Å γ = 70.3940(10)°
Volume	2314.49(11) Å ³
Z	2
Density (calculated)	1.430 Mg/m ³
Absorption coefficient	0.216 mm ⁻¹
F(000)	1018
Crystal size	0.23 x 0.20 x 0.13 mm ³
Theta range for data collection	1.31 to 27.49°
Index ranges	-14 ≤ h ≤ 14, -18 ≤ k ≤ 17, -20 ≤ l ≤ 19
Reflections collected	40436
Independent reflections	10596 [R(int) = 0.0446]
Completeness to theta = 27.49°	99.7 %
Absorption correction	None
Max. and min. transmission	0.9725 and 0.9520
Refinement method	Full-matrix least-squares on F ²
Data / restraints / parameters	10596 / 0 / 626
Goodness-of-fit on F ²	1.052
Final R indices [I > 2σ(I)]	R1 = 0.0943, wR2 = 0.2768
R indices (all data)	R1 = 0.1374, wR2 = 0.3197
Largest diff. peak and hole	1.015 and -1.574 e.Å ⁻³

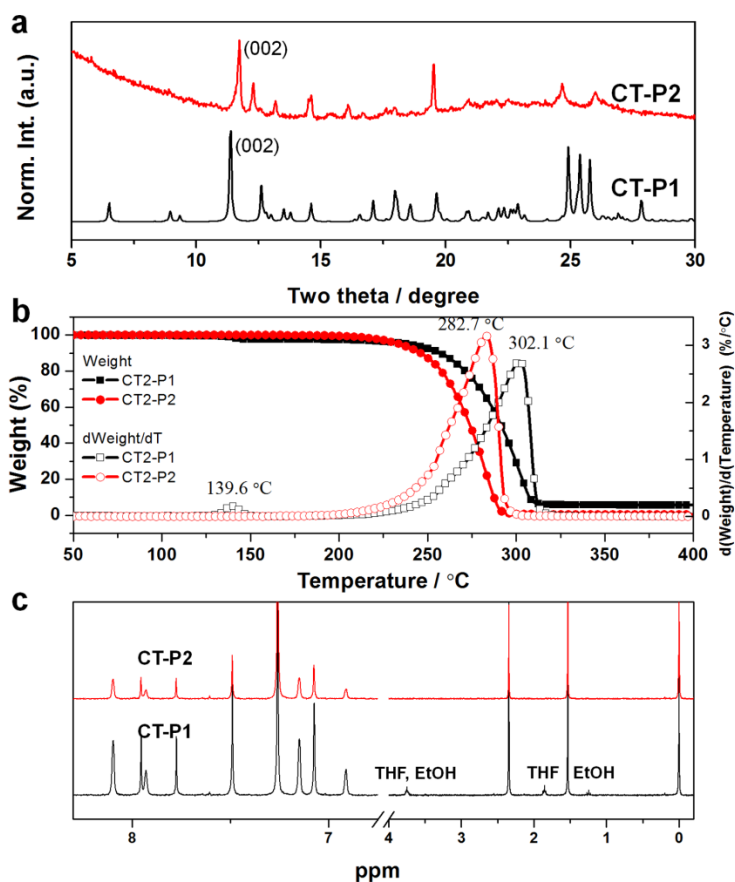


Figure 5-5. Powder XRD (a), TGA (b), and ^1H NMR (c) analyses of CT-P1 (black trace) and CT-P2 (red trace) single-crystalline powder obtained *via* recrystallization procedure. The main peak of CT-P1 is assigned to (002) at two theta value of 11.38° ; two theta position of CT-P2 (002) is assumed to be 11.72° due to the structure similarity (a). Inclusion of solvent molecules is only observed in case of CT-P1 by TGA analyses; additional ca. 2.6% weight loss at 139.6°C indicates solvent exclusion by lattice reorganization (b). Additional solvent peaks (THF and EtOH) are only detected in CT-P1 case from ^1H NMR; the stoichiometry of **D1:A1**:solvent are found to be ca. 1:1:0.35 (c).

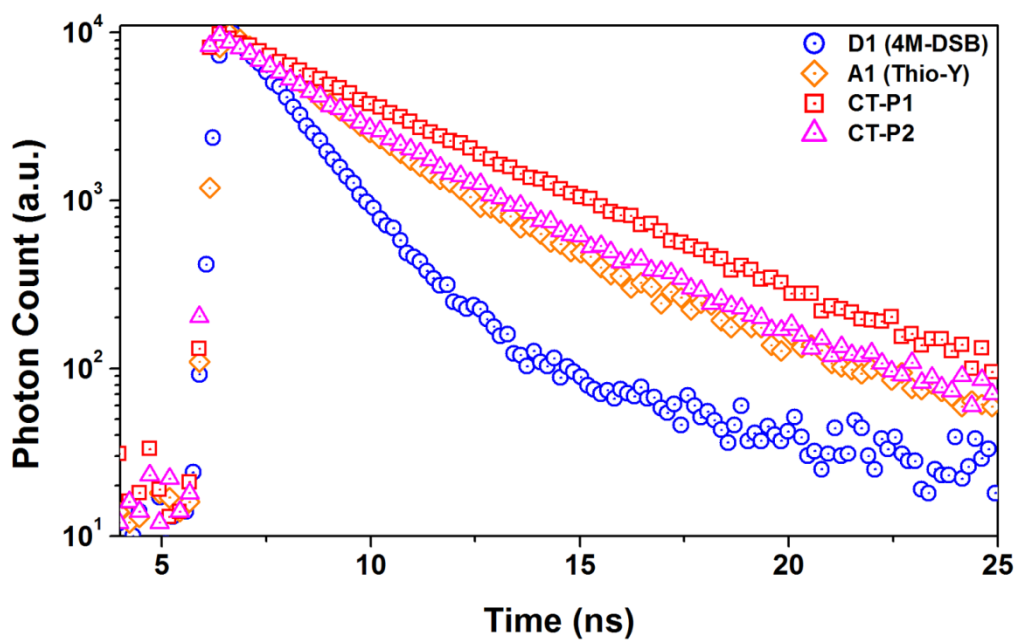


Figure 5-6. Solid-state PL lifetime spectra for **D1**: 4M-DSB (circle), **A1**: Thio-Y (diamond), CT-P1 (square), and CT-P2 (triangle), respectively.

5.3.3. Solvent Vapor Effect For a qualitative understanding of solvent property effects, and also for a demonstration of optical memory capabilities, I and coworkers performed SVA using a wide range of solvents, which were selected based on their proticity and empirical polarity values, $E_T(30)$.^[9,10] $E_T(30)$ values of the solvents are listed in **Figure 5-7**.^[9,10] The appropriately attenuated intermolecular interaction and its adequate free-volume indeed gave rise to superior external-stimuli responsive features. The pristine **D1-A1** spin-coated film shows PL resembling that of the **CT-P1** crystal ($\lambda_{em} = 658$ nm, black open/solid diamond spectra in **Figure 5-8a**); however, it exhibits abrupt solvent-dependent biphasic phase alteration during the SVA procedure (see **Figures 5-7** and **5-8a**).^[8] As visualized in the fluorescence images and spectra, the nonpolar solvent and polar protic solvent give rise to red emission ($\lambda_{em} = 619$ nm from 1,2-dichloroethane (DCE) SVA, which resembles the PL of CT-P2, red open/solid circle spectra of **Figure 5-8a**). On the other hand, the polar aprotic solvent results in blue fluorescence (e.g. acetonitrile (MeCN), $\lambda_{em} = 472$ nm, blue open/solid hexagon spectra of **Figure 5-8a**). This can be attributed to the mixed **D1-A1** CT formation that occurs when using the nonpolar or polar protic solvents; however, blue emission in the latter (polar aprotic) is greatly affected by the self-assembled structure of **D1** in the demixed phase. The out-of-plane XRD pattern of each film state supports this reconfiguration-based PL switching behavior – i.e., the appearance of the CT-P2 characteristic peak (red star) in the DCE SVA case, compared with the appearance of lamellar **D1** peaks (blue triangle) in the MeCN SVA case (**Figure 5-8b**). Notably, the

peculiar stacking features also rendered reversibility, showing consecutive switching behavior between the moderate red PL of the mixed CT phase (DCE SVA, λ_{em} of ca. 622 nm) and the bright blue PL of the demixed phase (MeCN SVA, λ_{em} of ca. 472 nm; **Figures 5-8c** and **5-9**).

The biphasic SVA dependence of molecular reorganization can be well explained by the nature of the intermolecular interactions and the role of the solvent.^[11] The binding affinity of D-A CT complexes with respect to solvent polarity is usually governed either by i) electrostatic interactions governing CT complexation, or by ii) CT complexation driven by the solvophobic effect. Electrostatic CT and H-bonding interactions become severely interrupted by a polar solvent owing to its ionic character in the former case,^[12] in the latter, however, those interactions can be promoted by polar protic solvents on the basis of strong H-bonding-induced solvent-solvent interactions.^[13] The current CT system exceptionally follows both principles, showing the polarity criterion of ca. $E_T(30) = 41-42$ by $E_T(30)$ for the former principle, and the hydrogen bonding capability of the solvent as a criterion in the latter case.^[11] Topological studies by FE-SEM and AFM also well reflect this situation (**Figure 5-10**). The mixture state of 2-dimensional **D1** crystals and 1-dimensional fibril supramolecular structures of **A1** is clearly manifested when SVA is carried out with polar aprotic solvent (MeCN) vapor (**Figure 5-10c, d**); however, bulk CT domains are immediately recovered by nonpolar (DCE) SVA (**Figure 5-10e, f**).



Figure 5-7. Digital images of CT spin-coated films taken under 365 nm UV irradiation.

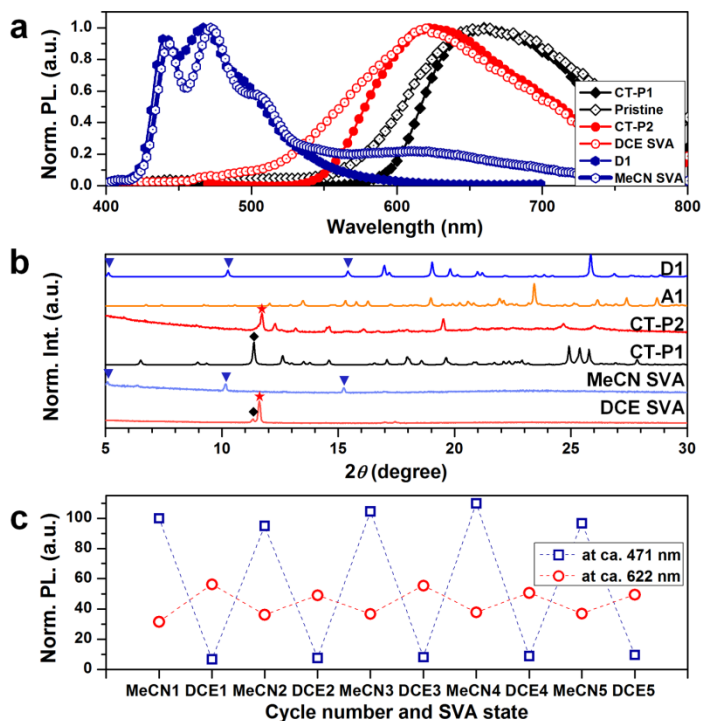


Figure 5-8. (a) Normalized PL spectra of pristine (black open diamond), DCE-SVA (red open circle), and MeCN-SVA (blue open hexagon) spin-coated films. Each state is compared with CT-P1 (black diamond), CT-P2 (red circle), and **D1** (blue hexagon), respectively. (b) XRD data of **D1**, **A1**, CT-P1, and CT-P2 single crystals, and spin-coated films of the DCE- and MeCN-SVA states. (c) The blue triangle, black diamond, and red star indicate characteristic peaks of **D1**, CT-P1, and CT-P2, respectively. The relative PL intensity transition during repetitive SVA processes using MeCN and DCE at ca. 471 nm (blue open square), and ca. 622 nm (red open circle).

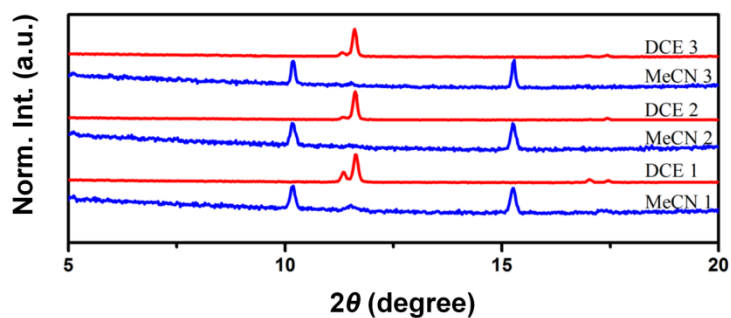


Figure 5-9. Out-of-plane XRD of **D1-A1** CT SVA film with consecutive MeCN \leftrightarrow DCE annealing procedures.

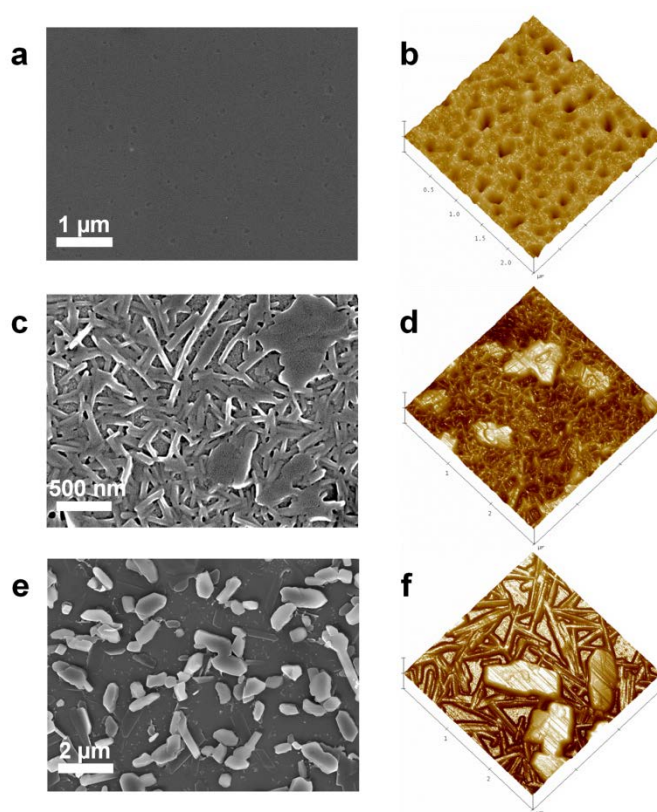


Figure 5-10. FE-SEM images and AFM images of pristine **D1-A1** spincoated film (a, b), MeCN SVA film (c, d), and DCE SVA film (e, f).

5.3.4 Multi-Stimuli Optical Memory Demonstration As well as the luminescence switching behavior *via* polarity- and proticity-dependent SVA (see entries ii and iii of **Figure 5-11**), the mixed CT phase can be triggered by thermal/mechanical stimuli, which enables us to design a multistimuli-responsive programmable fluorescence memory system (**Figure 5-11**). As depicted in entries iv and v of **Figure 5-11**, thermal and piezo writing on the blue emissive film indeed result in a red emission by mixed-phase formation.

This thermal (mechanical) stimulus-induced phase transition can be attained by overcoming the activation energy to form the thermodynamically favorable CT (mixed) phase *via* the diffusion of the thermally (mechanically) activated mobile **D1** molecules to the **A1** lattice (see **Figure 5-12**). DSC curves from mixture powder of **D1** and **A1** (ca. 1:1 stoichiometry) clearly reveal that molecular reorganization (from demixed to mixed phase) occur immediately after melting of **D1**, manifested by exothermal transition at 176.6°C (**Figure 5-12**, 1st cycle of powder mixture). Accordingly, melting transition of CT is observed at 206.0°C but any signal for melting of **A1** cannot be detected accompanied by (almost) full transformation from individually self-organized demixed phase to mixed CT phase in the first DSC heating regime; thus, the second cycle from the powder mixture exhibits very similar behavior to the first cycle of the CT-P1 single-crystal case. The fluorescent digital images of powder after heating procedure render straightforward evidence of the thermal-stimulus effect, see insets of **Figure 5-12**.

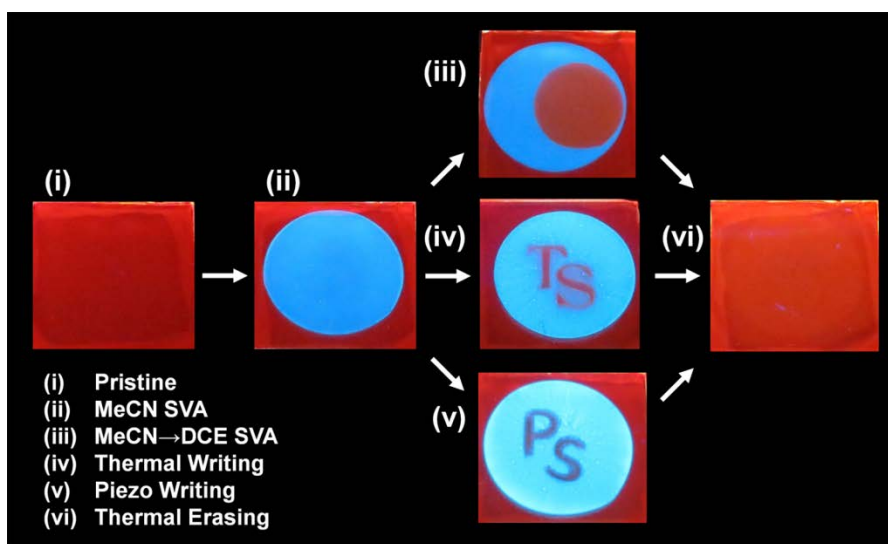


Figure 5-11. Optical memory demonstration of **D1-A1** CT spin-coated film consisting of three components (i.e., **D1**, **A1**, and PMMA), utilizing various external stimuli. The thermal erasing process that took place after piezo writing exhibited an inevitable stain.

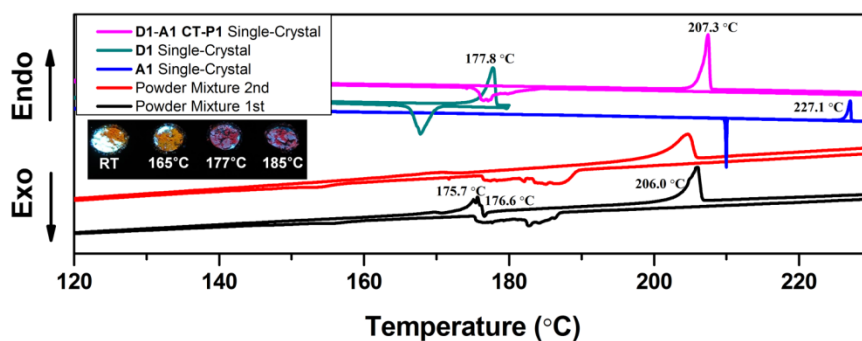


Figure 5-12. DSC curves of **D1-A1** mixture powder (black: 1st cycle, red: 2nd cycle), **A1** single-crystal (blue), **D1** single-crystal (turquoise blue), and CT-P1 single-crystal (magenta). The featured transition peaks are indicated above the curves. Inset digital images indicate fluorescence characters after applying 20 min thermal stimulus using DSC instrument.

5.4. Conclusions

In summary, stimuli-responsive reversible PL switching (red ↔ blue) system is successfully demonstrated by introducing a noncentrosymmetric acceptor (**A1**) to form a reconfigurable CT complex system. This PL switching approach provides an intuitive way of controlling optical properties by facile phase alteration, whose emission energy is highly predictable from frontier MOs of the constituent D/A molecules. Furthermore, I believe the molecular design rationale and crystal engineering strategy reported here might not only provide important insights for the supramolecular control of intermolecular interactions by the strategic selection of external triggers, but might also engender inspiration for controlling the nanostructure and/or phases of D-A heterosystems.

5.5. References

- [1] (a) Sagara, Y.; Kato, T. *Nat. Chem.* **2009**, *1*, 605. (b) Yoon, S.-J.; Chung, J. W.; Gierschner, J.; Kim, K. S.; Choi, M.-G.; Kim, D.; Park, S. Y. *J. Am. Chem. Soc.* **2010**, *132*, 13675. (c) Ito, H.; Muromoto, M.; Kurenuma, S.; Ishizaka, S.; Kitamura, N.; Sato, H.; Seki, T. *Nat. Commun.* **2013**, doi: 10.1038/ncomms3009. (d) Galer, P.; Korošec, R. C.; Vidmar, M.; Šket, B. *J. Am. Chem. Soc.* **2014**, *136*, 7383. (e) Fan, G.; Yan, D. *Sci.*

Rep. **2014**, *4*, 4933. (f) Yan, D.; Yang, H.; Meng, Q.; Lin, H.; Wei, M. *Adv. Funct. Mater.* **2014**, *24*, 587. (g) Luo, X. Li, J.; Li, C.; Heng, L.; Dong, Y. Q.; Liu, Z.; Bo, Z.; Tang, B. Z. *Adv. Mater.* **2011**, *23*, 3261. (h) Mutai, T.; Tomoda, H.; Ohkawa, T.; Yabe, Y.; Araki, K. *Angew. Chem. Int. Ed.* **2008**, *47*, 9522.

[2] Das, A.; Ghosh, S. *Angew. Chem. Int. Ed.* **2014**, *53*, 2038.

[3] (a) Kwon, M. S.; Gierschner, J.; Yoon, S.-J.; Park, S. Y. *Adv. Mater.* **2012**, *24*, 5487. (b) Kwon, M. S.; Gierschner, J.; Seo, J.; Park, S. Y. *J. Mater. Chem. C*, **2014**, *2*, 2552. (c) Luo, J.; Li, L.-Y.; Song, Y.; Pei, J. *Chem. Eur. J.* **2011**, *17*, 10515. (d) Liu, G.; Liu, J.; Liu, Y.; Tao, X. *J. Am. Chem. Soc.* **2014**, *136*, 590. (e) Das, A.; Molla, M. R.; Banerjee, A.; Paul, A.; Ghosh, S. *Chem. Eur. J.* **2011**, *17*, 6061. (f) Das, A.; Molla, M. R.; Maity, B.; Koley, D.; Ghosh, S. *Chem. Eur. J.* **2012**, *18*, 9849. (g) Park, J. S.; Yoon, K. Y.; Kim, D. S.; Lynch, V. M.; Bielawski, C. W.; Johnston, K. P.; Sessler, J. L. *Proc. Natl. Acad. Sci. USA* **2011**, *108*, 20913.

[4] (a) Wang, C.; Yin, S.; Chen, S.; Xu, H.; Wang, Z.; Zhang, X. *Angew. Chem.* **2008**, *120*, 9189. (b) Wang, C.; Guo, Y.; Wang, Y.; Xu, H.; Wang, R.; Zhang, X. *Angew. Chem. Int. Ed.* **2009**, *48*, 8962. (c) Rao, K. V.; Jayaramulu, K.; Maji, T. K.; George, S. J. *Angew. Chem. Int. Ed.* **2010**, *49*, 4218.

[5] (a) Wang, J.-Y.; Yan, J.; Ding, L.; Ma, Y.; Pei, J. *Adv. Funct. Mater.* **2009**, *19*, 1746. (b) Lei, Y. L.; Liao, L. S.; Lee, S. T. *J. Am. Chem. Soc.* **2013**, *135*, 3744. (c) Zhu, W.; Zheng, R.; Fu, X.; Fu, H.; Shi, Q.; Zhen, Y.; Dong, H.; Hu, W. *Angew. Chem. Int. Ed.* **2015**, *54*, 6785.

- [6] (a) Park, S. K.; Varghese, S.; Kim, J. H.; Yoon, S.-J.; Kwon, O. K.; An, B.-K.; Gierschner, J.; Park, S. Y. *J. Am. Chem. Soc.* **2013**, *135*, 4757. (b) Wykes, M.; Park, S. K.; Bhattacharyya, S.; Varghese, S.; Kwon, J. E.; Whang, D. R.; Cho, I.; Wannemacher, R.; Lürer, L.; Park, S. Y.; Gierschner, J. *J. Phys. Chem. Lett.* **2015**, *6*, 3682.
- [7] Safont-Sempere, M. M.; Fernández, G.; Würthner, F. *Chem. Rev.* **2011**, *111*, 5784.
- [8] (a) An, B.-K.; Gihm, S. H.; Chung, J. W.; Park, C. R.; Kwon, S.-K.; Park, S. Y. *J. Am. Chem. Soc.* **2009**, *131*, 3950. (b) Kim, J. H.; Chung, J. W.; Jung, Y.; Yoon, S.-J.; An, B.-K.; Huh, H. S.; Lee, O. W.; Park, S. Y. *J. Mater. Chem.* **2010**, *20*, 10103.
- [9] C. Reichardt in *Solvents and Solvent effects in Organic Chemistry*, 3rd ed., Wiley-VCH, Weinheim, **2003**, pp. 411-443.
- [10] Solvent abbreviation list: Ether: diethyl ether, DCM: dichloromethane, DCE: 1,2-dichloroethane, ACT: acetone, DMSO: dimethyl sulfoxide, MeCN: acetonitrile, IPA: isopropyl alcohol, EtOH: ethanol, MeOH: methanol.
- [11] G. A. Breault, C. A. Hunter, P. C. Mayers, *J. Am. Chem. Soc.* **1998**, *120*, 3402.
- [12] R. Foster, *J. Am. Chem. Soc.* **1960**, 1075.
- [13] M. S. Cubberley, B. L. Iverson, *J. Am. Chem. Soc.* **2001**, *123*, 7560.

Abstract in Korean

파이 공액 분자에 기반한 유기 반도체 재료는 화학적 다기능성, 작은 중량, 투명성, 저온 공정성, 유연성 등 무기 반도체 물질에서는 발현되기 어려운 다양한 이점들로 말미암아 전도 유망한 반도체 재료로 각광받고 있다. 고상 유기 반도체의 광-전자 (optoelectronic) 기능성은 이들의 전자적 (electronic) 특성뿐만 아니라 초분자적 분자 쌓임에 의해 결정됨은 잘 알려져 있다. 이러한 측면에서 유기 반도체의 구조-특성 상관관계 해석에 대한 급속한 발전이 이루어졌으며, 더 나아가 초분자 집합 조절을 통한 특성 제어 전략에 대한 연구는 최근 중요한 연구 분야로 자리매김 하고 있다. 한편, 전자 주개형 (electron donor) 물질과 전자 받개형 (electron acceptor) 물질의 복합체 및 계면은 광기전력 효과 (photovoltaic effect), 전하이동복합체적 (charge-transfer, CT) 특성에 인한 전하 수송 능력 향상, 들뜬 복합체 형성에 (exciplex) 의한 발광 특성 등 새로운 물리-화학적 기능성 발현으로 인하여 그 관심이 현저히 증진되고 있다. 특히 전자 받개 - 전자 주개로 구성된 전하이동복합체에 관한 연구는 이들의 금속성 전도도 특성으로 말미암아 오랜 기간 가장 활발한 진행을 보여온 연구 주제로써 자리매김 하였지만, 이들 중 전하이동의 정도가 낮은 중성형 (neutral)

전하이동복합체의 경우 특히 구조-특성적 상관관계에 관한 연구가 미흡한 실정이다. 중성형 전하이동복합체는 한편 특징적인 전자 및 구조적 특성에서 기인한 반도체적 특성과 독특한 발광적 특성을 발현함으로써 새로운 형태의 유기반도체 재료로써 고도의 활용 가능성을 보임은 분명하다.

본 저자 및 공동연구자들은 전도 유망한 파이 공액 분자형 유기 반도체 재료 중 특히 탄성 비틀림 특성으로부터 기인한 독특한 광-전자 특성을 보이는 다기능성 다이시아노다이스티릴벤젠 계 (dicyanodistyrylbenzene, DCS) 물질에 주목하였다. CN-TFPA라 명명 된 DCS계 물질은 π - π 상호작용과 시아노 작용기로부터 기인한 수소 결합성 상호작용의 정교한 균형으로 말미암아 수 밀리미터 스케일에 달하는 이차원적 n형의 초분자체를 이룸을 확인 할 수 있었으며, 이들의 전자 및 구조적 인자로 인한 높은 고상 형광 효율 ($\Phi_F \approx 80\%$) 및 유기 트랜지스터 제작을 통한 높은 n형 전하 이동도를 ($0.5 \text{ cm}^2 \text{ V}^{-1} \text{ s}^{-1}$) 유도 할 수 있었다. 이와 더불어 이차원적 초분자 특성으로 인한 그래핀 (graphene)과 같은 박리 및 전사의 가능성을 보여주었으며, 이를 통한 초박막 결정 유기 트랜지스터 소자 제작 및 소재 개발에 관한 새로운 아이디어를 제시 할 수 있었다.

CN-TFPA 분자는 독특한 초분자체적 광-전자 특성 이외에도 전하이동복합체 형성이 용이한 흥미로운 전자 받게 물질로써 복합체 형성

시 진보적 광-전자 기능성을 나타낼 수 있음을 확인 할 수 있었다. 양극성 (ambipolar) 전하 이동 현상 및 전하이동복합체적 발광 특성 발현을 위해 본 연구에서는 CN-TFPA와 분자 구조 차이가 (mismatch) 최소화 된 디스티릴벤젠 (distyrylbenzene, DSB) 형 전자 주개 분자인 4M-DSB를 디자인 하였으며 본 분자들의 자발적인 변갈아 쌓임 형 전하이동복합체 형성을 통해 상기의 특성을 성공적으로 구현 할 수 있었다. 초교환 기작 (superexchange mechanism) 에 의한 변갈아 쌓임 형태에서의 간접적인 전자 상호작용은 (indirect electronic coupling) 본 전하이동복합체에서의 양극성 전하 이동 특성 (p형 이동도 $6.7 \times 10^{-3} \text{ cm}^2 \text{ V}^{-1} \text{ s}^{-1}$; n형 이동도 $6.7 \times 10^{-2} \text{ cm}^2 \text{ V}^{-1} \text{ s}^{-1}$) 을 야기 할 수 있었다. 더 나아가 배치간 상호 작용으로써 (configuration interaction) 말미암은 특수한 전자적 특징 및 밀집된 분자 쌓임 특성에서 기인한 낮은 엑시톤 덧 밀도는 전하이동복합체에서는 구현이 어려운 30 - 40%의 높은 발광 양자 수득률을 보임으로써 전하이동복합체를 활용한 발광성 - 전하 전도성을 연결 할 수 있는 진보된 광-전자적 반도체 소재로써의 가능성을 확인 할 수 있었다.

진보된 광-전자 소재 및 소자 개발 의 다음 단계로써 증진된 형광 효율을 보이는 전하이동복합체를 활용한 전계 발광 트랜지스터 (light-emitting organic field-effect transistor) 적용가능성에 관한 연구를 진행하였다.

본 연구에서는 전자 받개형 DCS 분자인 CN-TFPA의 대응 분자로서 DCS계 전자 주개 물질인 2MDCS를 전자 및 구조적 특성을 고려하여 전략적으로 채택함으로써 60%에 달하는 높은 형광 효율을 보이는 전하이동복합체를 개발 할 수 있었다. 2:1의 화학량론적 전자 주개 - 전자 받개 비율로 이루어진 밀집된 분자 쌓임 구조는 초분자 신틸론 (supramolecular synthon)에 의해 이례적인 이차원적 전하이동복합체 성장을 보였으며, 본 전하이동복합체의 균형적인 양극성 전하 이동 특성으로 말미암아 유기 전계 트랜지스터 작동 하에서 외부 양자 효율이 1.5%에 달하는 전계 발광 트랜지스터적 특성을 구현 할 수 있었다. 본 번갈아 쌓임 형 전하이동복합체의 특수한 광-전자적 특성은 반도체성 전하이동복합체 소재의 미래적인 유기 광-전자 소자 적용가능성의 잠재력을 제시한다.

한편, 본 저자는 전하이동복합체를 활용한 자극 감응 형 멀티컬러 형광 변환 구현을 위한 연구를 진행하였다. 직관적인 적색 ↔ 청색의 고 대비 형광 변환 구현을 위해 전자 주개인 4M-DSB와 전자 받개인 Thio-Y를 선택함으로써 경계 분자 궤도의 (frontier molecular orbitals) 차이로 말미암아 전하이동복합체 형성 시 적색의 형광을 보이지만 전하이동복합체의 해체 시 전자 주개와 전자 받개의 형광, 특히 전자 주개의 청색 형광이 구현 될 수 있는 새로운 방식의 외부 자극 감응 형 형광 변환 시스템을 개발 할 수

있었다. 다이시아노다이스티릴싸이오펜 (Dicyanodistyrylthiophene) 형 전자 받개인 Thio-Y는 중심대칭성이 보이지 않는 유기 분자로서 전하이동복합체 형성 시 약화된 분자간 상호작용을 야기하여 외부 자극 감응성을 증진시키는 역할을 하게 된다. 이로 말미암아 정전기력에 (electrostatic) 기반한 전하이동복합체형 상호작용 및 수소결합성 상호작용은 극성의 반양성자성 용매 (polar aprotic) 증기에 의해 손쉽게 그 작용이 약화되어 전하이동복합체의 해체 및 단독 분자 형 초분자체의 형성을 보임을 확인 할 수 있었다. 한편 무극성 용매 (nonpolar solvent) 와 극성 양성자성 용매 (polar protic solvent) 의 경우 정전기력적 상호작용 유도 및 용매간 상호작용으로 말미암아 전하이동복합체 형성을 가역적으로 유도 할 수 있어 선택적 용매 활용을 통한 이상성 의존성 (biphasic dependence) 을 구현 할 수 있으며 이에 더 나아가 열, 압력을 활용한 가역적인 자발적 전하이동복합체 형성을 유도 할 수 있었다.

본 학위 논문에서는 다이시아노다이스티릴벤젠 계 초분자체 및 전하이동복합체의 구조-특성 간 상관관계 해석을 중점적으로 다루고자 하며, 특히 이들의 형광 특성 및 전하 수송 능력에 관한 분석을 구조 해석 기반의 양자화학 계산을 통해 진행하고자 하였다. 단일 성분 초분자체의 경우에서 살펴 볼 수 있듯 전하이동복합체의 분자 쌓임 구조는 구성 분자들의 전자적

특성과 함께 광-전자 기능성에 지대한 영향을 미침을 확인 할 수 있었다. 본 학위 기간을 통해 본 저자는 능동적 분자 / 초분자 매개변수의 조절을 통한 전하이동복합체의 전례 없는 광-전자 기능성을 구현하거나 이들 특성의 개선을 효과적으로 달성 할 수 있었으며, 일련의 연구 과정을 토대로 다이시아노다이스티릴벤젠 계 구성 분자와 다이스티릴벤젠 계 구성 분자로 이루어진 전하이동복합체의 광-전자 소재 및 소자로서의 높은 응용가능성을 확인 할 수 있었다.

주요어: 다이시아노다이스티릴벤젠, 다이스티릴벤젠, 초분자체, 전하이동복합체, 광-전자 특성, 전하 수송, 형광, 유기트랜지스터, 전계발광, 자극감응성.

학생 번호: 2010-20601

List of Publications

Original Papers

1. **Sang Kyu Park**, Jong H. Kim, Seong-Jun Yoon, Oh Kyu Kwon, Byeong-Kwan An, Soo Young Park “*High-Performance n-Type Organic Transistor with a Solution-Processed and Exfoliation-Transferred Two-Dimensional Crystalline Layered Film*” *Chem. Mater.* **2012**, *24*, 3263-3268.
2. Won Sik Yoon, **Sang Kyu Park**, Illhun Cho, Jeong-A Oh, Jong H. Kim, Soo Young Park “*High-Mobility n-Type Organic Transistors Based on a Crystallized Diketopyrrolopyrrole Derivative*” *Adv. Funct. Mater.* **2013**, *23*, 3519-3524. (Won Sik Yoon and Sang Kyu Park equally contributed to this paper)
3. Seong-Jun Yoon, Shinto Varghese, **Sang Kyu Park**, Reinhold Wannemacher, Johannes Gierschner, Soo Young Park “*Color-Tuned Highly Emissive Dicyanodistyrylbenzene Single Crystals: Manipulating Intermolecular Stacking Interaction for Spontaneous and Stimulated Emission Characteristics*” *Adv. Opt. Mater.* **2013**, *1*, 232-237.
4. **Sang Kyu Park**, Shinto Varghese, Jong H. Kim, Seong-Jun Yoon, Oh Kyu Kwon,

Byeong-Kwan An, Johannes Gierschner, Soo Young Park “*Tailor-Made Highly Luminescent and Ambipolar Transporting Organic Mixed Stacked Charge-Transfer Crystals: an Isometric Donor-Acceptor Approach*” *J. Am. Chem. Soc.* **2013**, *135*, 4757-4764.

5. Shinto Varghese, **Sang Kyu Park**, Santiago Casado, Roland Fischer, Roland Resel, Begona Milian-Medina, Reinhold Wannemacher, Soo Young Park, Johannes Gierschner “*Stimulated Emission Properties of Sterically Modified Distyrylbenzene-Based H-Aggregate Single Crystals*” *J. Phys. Chem. Lett.* **2013**, *4*, 1597-1602.

6. Jong H. Kim, Byeong-Kwan An, Seong-Jun Yoon, **Sang Kyu Park**, Ji Eon Kwon, Chang-Keun Lim, Soo Young Park “*Highly Fluorescent and Color-Tuned Exciplex Emission from Poly(N-vinylcarbazole) Film Containing Nanostructured Supramolecular Acceptors*” *Adv. Funct. Mater.* **2014**, *24*, 2746-2753.

7. Oh Kyu Kwon, Jung-Hwa Park, **Sang Kyu Park**, Soo Young Park “*Soluble Dicyanodistyrylbenzene-Based Non-Fullerene Electron Acceptors with Optimized Aggregation Behavior for High-Efficiency Organic Solar Cells*” *Adv. Energy Mater.* **2015**, *5*, 1400929.

8. Oh Kyu Kwon, Jung-Hwa Park, Dong Won Kim, **Sang Kyu Park**, Soo Young Park

“An All-Small-Molecule Organic Solar Cell with High Efficiency Nonfullerene Acceptor” *Adv. Mater.* **2015**, 27, 1951-1956.

9. Michael Wykes, **Sang Kyu Park**, Santanu Bhattacharyya, Shinto Varghese, Ji Eon Kwon, Dong Ryeol Whang, Ilhun Cho, Reinhold Wannemacher, Larry Lüer, Soo Young Park, Johannes Gierschner “*Excited State Feature and Dynamics in a Distyrylbenzene Based Mixed Stack Donor-Acceptor Cocrystal with Luminescent Charge Transfer Characteristics*” *J. Phys. Chem. Lett.* **2015**, 6, 3682-3687. (Michael Wykes, Sang Kyu Park, and Santanu Bhattacharyya equally contributed to this paper)

10. Shinto Varghese, **Sang Kyu Park**, Santiago Casado, Roland Resel, Reinhold Wannemacher, Larry Lüer, Soo Young Park, Johannes Gierschner “*Polymorphism and Amplified Spontaneous Emission in Dicyano-Distyrylbenzene Derivative with Multiple Trifluoromethyl Substituents: Intermolecular Interactions in Play*” *Adv. Funct. Mater.* **2015**, Accepted.

11. **Sang Kyu Park**, Ilhun Cho, Johannes Gierschner, Jin Hong Kim, Jong H. Kim, Ji Eon Kwon, Oh Kyu Kwon, Dong Ryeol Whang, Jung-Hwa Park, Byeong-Kwan An, Soo Young Park “*Stimuli-Responsive Reversible Fluorescence Switching in the Crystalline Donor-Acceptor Mixture Film: Mixed Stack Charge-Transfer Emission vs. Segregated Stack Monomer Emission*” *Angew. Chem. Int. Ed.* **2015**, Accepted.

12. Oh Kyu Kwon, Mohammad Afsar Uddin, Jung-Hwa Park, **Sang Kyu Park**, Thanh Luan Nguyen, Han Young Woo, Soo Young Park “A *High Efficiency Nonfullerene Organic Solar Cell with Optimized Crystalline Organizations*” *Adv. Mater.* **2015**, Accepted.

List of Presentations

International

1. **(Poster) Sang Kyu Park**, Jong H. Kim, Oh Kyu Kwon, Soo Young Park “*Organic Field Effect Transistor Comprising n-type 2D Crystalline Layer*” KJF 2010, Japan, 2010-08-22.
2. **(Oral)** Soo Young Park, Jong Hyun Kim, **Sang Kyu Park**, Seon Woo Yun “*Molecular Design and Synthesis of Highly Efficient n-Type OFET Material*” 94th Canadian Chemistry Conference and Exhibition, Canada, 2011-06-05.
3. **(Poster) Sang Kyu Park**, Jong H. Kim, Seong-Jun Yoon, Byeong-Kwan An, Soo Young Park “*Ambipolar Single Crystal Organic Field-Effect Transistors via Charge-Transfer Co-Crystal*” 2011 MRS Fall Meeting & Exhibit, US, 2011-11-28.
4. **(Poster)** Jin Hong Kim, **Sang Kyu Park**, Won Sik Yoon, Jong H. Kim, Soo Young Park “*Synthesis and Characterization of High-Performance n-Type Organic Semiconductor: Novel Dicyanodistyrylbenzene Derivative Forming Large 2D Single Crystal*” The International Symposium on Carbon Electronics 2013, Korea, 2013-05-06.

5. **(Poster) Sang Kyu Park**, Jong Hyun Kim, Seong Jun Yoon, Oh Kyu Kwon, Johannes Gierschner, Soo Young Park “*Tailor-Made Highly Luminescent and Ambipolar Transporting Organic Mixed Stacked Charge-Transfer Crystals: An Isometric Donor–Acceptor Approach*” The International Symposium on Carbon Electronics 2013, Korea, 2013-05-06.

6. **(Poster) Illhun Cho, Sang Kyu Park**, Soo Young Park “*Study of Heteroaromatic Fused-Ring System for Organic Electronics: Synthesis and Characterization of Indolo[3,2-b]indole-based Organic Semiconductors*” The International Symposium on Carbon Electronics 2013, Korea, 2013-05-06.

7. **(Poster) Won Sik Yoon, Sang Kyu Park**, Illhun Cho, Soo Young Park “*Energy Level Tailoring of Diketopyrrolopyrrole-based Small Molecules for Organic Field-Effect Transistor and Solar Cell Applications*” 2013 MRS Fall Meeting & Exhibit, US, 2013-12-06.

8. **(Poster) Sang Kyu Park**, Illhun Cho, Jin Hong Kim, Oh Kyu Kwon, Ji Eon Kwon, Soo Young Park “*Highly Luminescent and Ambipolar Transporting Organic Charge-Transfer Cocrystals: Isometric Cocrystals Comprising Distyrylbenzene and Dicyanodistyrylbenzene Derivatives*” 2014 MRS Fall Meeting & Exhibit, US, 2014-04-21.

9. **(Poster)** Jin Hong Kim, **Sang Kyu Park**, Jong Hyun Kim, Soo Young Park
“*Dicyanodistyrylbenzene-based Organic n-Type Semiconductor with Remarkable Electron Mobility*” 2014 MRS Fall Meeting & Exhibit, US, 2014-04-21.

10. **(Poster)** Oh Kyu Kwon, Jung-Hwa Park, **Sang Kyu Park**, Soo Young Park
“*Dicyanodistyrylbenzene-based non-fullerene electron acceptors containing naphthalimide substituent for organic solar cells*” ElecMol 2014 7th International Conference on Molecular Electronics, France, 2014-08-24.

11. **(Poster)** SangYoon Oh, **Sang Kyu Park**, Illhun Cho, Soo Young Park “*Stimuli-Responsive Photoluminescent Properties of Diaryl Substituted Fumaronitrile Derivatives*” KJF-ICOMEF 2014, Japan, 2014-09-21.

Domestic

1. **(Poster)** **Sang Kyu Park**, Jong Hyun Kim, Oh Kyu Kwon, Soo Young Park “*Highly Fluorescent and Semiconducting Supramolecular Nanowires*” 2010 한국고분자학회 춘계총회 및 연구논문 발표, 대한민국, 2010-04-08.

2. **(Poster)** **Sang Kyu Park**, Jong H. Kim, Seong-Jun Yoon, Soo Young Park
“*Fabrication of High Performance Single Crystalline Organic Field-Effect Transistors*”

via Solvent Annealing Technique” 대한화학회 제 107 회 총회 및 학술발표회, 대한민국, 2011, 2011-04-28.

3. (Poster) **Sang Kyu Park**, Byeong-Kwan An, Soo Young Park “*High-Performance n-type Organic Transistor with a Solution-Processed and Exfoliation- Transferred Two-Dimensional Crystalline Layered Film*” 2012 대한화학회 제 110 회 추계학술발표회, 대한민국, 2012-10-17.

4. (Poster) Jin Hong Kim, **Sang Kyu Park**, Soo Young Park “*Synthesis and Characterization of High-Performance n-Type Organic Semiconductor: Novel Dictanodistyrylbenzene Derivative Forming Large2D Single Crystal*” 2012 대한화학회 제 110 회 추계학술발표회, 대한민국, 2012-10-17.

List of Patents

Domestic

1. 박수영, **박상규**, 김종현 “유기물 반도체 물질, 이를 이용한 트랜지스터 소자 및 트랜지스터 소자의 제조방법” 대한민국, 등록번호 10-1401424
2. 박수영, **박상규**, 김종현 “유기물 반도체 물질, 이를 이용한 트랜지스터 소자 및 트랜지스터 소자의 제조방법” 대한민국, 등록번호 10-1408160